Metrology and mechanics for manufacturing space-based x-ray grating spectrometers

by

Jungki Song

B.S., Sogang University (2014)
M.S., Sogang University (2016)

Submitted to the Department of Mechanical Engineering
in partial fulfillment of the requirements for the degree of

Doctor of Philosophy in Mechanical Engineering

at the

MASSACHUSETTS INSTITUTE OF TECHNOLOGY

February 2021

© Massachusetts Institute of Technology 2021. All rights reserved.

Author . . . .
Department of Mechanical Engineering
Oct. 29, 2020

Certified by . . . .
Mark L. Schattenburg
Senior Research Scientist
MIT Kavli Institute for Astrophysics and Space Research
Thesis Supervisor

Accepted by . . . .
Nicolas Hadjiconstantinou
Professor of Mechanical Engineering
Chairperson, Committee on Graduate Students

Metrology and mechanics for manufacturing space-based x-ray grating spectrometers

by

Jungki Song

Submitted to the Department of Mechanical Engineering
on Oct. 29, 2020, in partial fulfillment of the
requirements for the degree of
Doctor of Philosophy in Mechanical Engineering

Abstract

Small errors in critical dimensions (CDs) or deformation of optical components can lead to severe performance degradation in high-resolution imaging and spectroscopy tools. Consistent innovations towards more precise optical elements and assembly procedures have led to high-resolution optical systems in many fields - including telescope, microscopy, lithography, and display technologies. A space x-ray telescope needs more stringent requirements as it observes distant space objects using a limited number of x-ray photons in a harsh space environment. The optical instruments for x-ray telescopes need to be high-resolution, efficient in collecting x-ray photons, and lightweight.

Optical elements in x-ray telescopes have large-apertures (typically around 1-2 m^2) which are realized by populating them with >1000 high-quality optical subelements (i.e., mirrors or gratings). In this thesis, we limit our attention to an x-ray grating spectrometer, one of the essential elements in x-ray telescopes. It is placed downstream of the focusing optics and prior to the x-ray detector to disperse nonmonochromatic x rays from distant sources for space-based x-ray spectroscopy. A critical-angle transmission (CAT) grating, a lightweight, freestanding, high-aspect ratio x-ray grating with 200-nm period and 4 μm depth, is a building block for grating spectrometers. More than 1000 high-quality CAT gratings need to be manufactured and precisely aligned within tolerance to build future CAT grating spectrometers.

This thesis attacks this manufacturing challenge through 1) inventing metrologies for characterizing CDs, 2) developing alignment processes, and 3) performing design and analysis of CAT grating structural supports. First, a metrology to characterize period variation of CAT gratings was developed. Metrology repeatability of 0.004 nm rms was achieved, successfully characterizing period variations of 0.018 nm rms (1 sigma) over large-area CAT gratings patterned with traditional interference lithography. The demonstrated metrology uncertainty and period variations fulfill the requirements for future x-ray telescope missions. Second, alignment metrology and protocols were developed, demonstrating an ability to align multiple CAT gratings to satisfy alignment requirements (<6 arcmin or 0.1 deg). The developed alignment

protocol is reliable and scalable for flight-level alignment, for which a large volume ($>$1000) of CAT gratings need to be aligned in a fast and accurate manner. Third, a metrology to characterize grating bar tilt variations was developed using small-angle x-ray scattering and a laser setup. The developed metrology demonstrated repeatability of $<$0.01 deg (1 σ) and accuracy of $\sim$0.08 deg (4.8 arcmin). It successfully characterized bar tilt angle variations from CAT gratings and results agree well with synchrotron measurements. It enabled us to close the loop in process optimization for CAT grating fabrication, and contributed towards suppressing bar tilt (or blaze) error within tolerance ($<$6 arcmin or 0.1 deg). Fourth, analytical and finite element studies were performed to design CAT grating structural supports that minimize x-ray blockage at a given stiffness. In-plane and out-of-plane stiffness of several 2D-lattice topologies were examined. A triangular lattice shows 23-580% on stiffness improvement (depending on mode of stiffness) over the current hexagonal lattice design for the same open area fraction. Adopting the new 2D lattice design is expected to increase open area fraction by $\sim$5% without compromising stiffness.

Thesis Supervisor: Mark L. Schattenburg
Title: Senior Research Scientist
MIT Kavli Institute for Astrophysics and Space Research

Acknowledgments

Four years ago, I came to MIT as a little kid obsessed with science and engineering. Now standing at the end of PhD as a more grown-up man, I can't believe how fast time went by, and how transformative the experience I had at MIT. Every moment at MIT was full of joy. And I am grateful to great leaders, great teachers, and great colleagues who shaped me to be who now I am along the journey for the last four years.

I would like to thank my advisor, Mark Schattenburg, for his encouragement, patience, and support throughout my PhD. Under his guidance, I had a privilege to spend countless hours studying and working independently to develop myself as an independent scientist. He supported whatever I did, and gave great advices and life lessons as needed. I thank Marty Culpepper for being a chair for this thesis. He asked hard but valuable questions such as "what do you want to do with your life?", "what is your contribution for Ph.D.?", which I haven't seriously thought about. I made big leaps forward to be a better man and a better scientist after his comments and questions. David Parks led me to the field of solid mechanics, which I had nearly zero experience before, and helped me build a strong foundation in the field of mechanics which I am proud of. He always welcomed me when I bumped into his office to ask questions to have discussions on mechanics and life.

Ralf Heilmann played an instrumental role in majority of this work. We had countless number of discussions in physics, engineering, and life which I truly enjoyed. He taught me everything I know about x-ray physics and gratings. I am grateful for the hospitalities his family offered to me in Thanksgivings. I would like to thank SNL CAT grating team, Alexander Bruccoleri, Anjelica Molnar-Fenton, Michael DeTienne, Brian Smallshaw for their hard work in preparing precious CAT grating samples and providing valuable feedbacks. SNL group members were another big part at MIT. I would like to thank Brandon Chalifoux, Mallory Whalen, and Youwei Yao, and Heng Zuo. It's been a privilege to be surrounded by you all!

Collaborators outside SNL provided great supports towards this work. Edward

Hertz and Jacob Hohl at Harvard-Smithsonian Center for Astrophysics were critical in developing alignment process for gratings. Herman Marshall and Alan Garner at MIT X-ray Polarimetry Beamline helped me run the x-ray beamline. Charlie Settens at shared x-ray facilities in MIT Materials Research Laboratory provided invaluable supports in using small-angle x-ray scattering tool. Mark Belanger at MIT Edgerton Center taught me how to make something useful out of a chunk of metal!

Generous funding supports have been provided by the NASA Research Opportunities in Earth and Space Science Strategic Astrophysics Technology grants (NNX15AC43G and NNX17AG43G).

I would like to thank friends who share delightful memories at MIT. I met too many good friends at MIT. All the memories I had with friends - chatting about science while taking a walk in Charles river, playing basketball every Friday, swimming, climbing white mountains, singing songs in choir, praying best wishes for each other's future - will be missed.

Lastly, I would like to thank my family. The love, pray, and support sent from Korea, 12000 km away from the other end of the planet, made my achievements possible.

Contents

List of Symbols **25**

1 Introduction **29**

1.1 Motivation 29

1.2 Thesis contribution 31

1.3 X-ray telescope 33

1.3.1 Arcus 34

1.3.2 Lynx 34

1.4 Grating basics 35

1.5 Critical-angle transmission (CAT) gratings 39

1.6 CAT grating spectrometer 47

1.7 Grating coordinates 49

1.8 Requirements for a CAT grating spectrometer 49

1.8.1 Ray tracing 51

1.8.2 Grating period 52

1.8.3 Alignment 53

1.8.4 Structural considerations 54

1.9 Thesis structure 58

2 Grating period metrology **61**

2.1 Working principle 63

2.2 Metrology tool construction 66

2.3 Sample preparation 66

2.4 System calibration 68
2.5 Results 69
2.6 Challenges in period measurement of CAT gratings 72
2.7 Conclusion 75

3 Grating alignment **77**
3.1 Prior art for grating alignment 78
3.2 Demonstration: first test 79
3.2.1 Repeatability and accuracy of angle measurements 80
3.2.2 Hardware 80
3.2.3 Procedure 81
3.2.4 X-ray verification 86
3.2.5 Results and Discussion 88
3.3 Demonstration: second test 90
3.3.1 Metrology tool construction 92
3.3.2 Hardware design 93
3.3.3 Procedure 95
3.3.4 X-ray verification 101
3.3.5 Results and Discussions 110
3.4 Alternative ways to measure roll misalignment 112
3.5 Conclusion 113

4 Grating bar tilt metrology **115**
4.1 Cause of profile tilt 118
4.2 Prior Art 120
4.3 Small angle x-ray scattering 120
4.4 Test grating fabrication 122
4.5 X-ray diffraction modelling 125
4.6 Metrology procedure 127
4.7 Results 132
4.7.1 Bar tilt measurements on test grating samples 132

4.7.2 Error analysis 133
4.7.3 Bar tilt measurements on CAT gratings 134
4.8 Conclusion 136

5 Design and analysis of CAT grating structural support 137
5.1 Problem formulation 140
5.2 Methodology 141
5.2.1 Constitutive relationship between average membrane stress and average (or uniform) strain 143
5.2.2 Constitutive relationship between average plate bending moment and average (or uniform) curvature 144
5.2.3 General constitutive relation of 2d-periodic lattice 144
5.2.4 Strain-energy based homogenization 145
5.3 Analytical 147
5.3.1 Calculation of strain energy 147
5.3.2 Full analytical solution 154
5.4 Numerical 158
5.5 Results and Discussion 159
5.6 Conclusion 172

6 Conclusion 175
6.1 Future work 179

A Example MATLAB scripts to calculate analytical solutions on stiffness of 2d periodic lattices 181
A.1 MATLAB script to calculate analytical solution on in-plane stiffness tensor for hexagonal lattice 182
A.2 MATLAB script to calculate analytical solution on out-of-plane stiffness tensor for hexagonal lattice 187

B Python scripts for simulation of in-plane and out-of-plane stiffnesses 193
B.1 Script for FE simulation of in-plane stiffness for triangular lattice . . 193

List of Figures

1-1 Four x-ray gratings aligned for test 1 (a), and test 2 (b). Please refer to chapter 3 for more details. 32

1-2 A schematic showing incident beam and multiple transmitted diffracted orders. Media below and above the gratings share same refractive indices. 36

1-3 A schematic demonstrating phase or amplitude modulation of the electric field of an incoming plane wave. 37

1-4 Scanning electron microscope images of intentionally cleaved CAT grating. Zoomed images show grating structure on L2 supporting structure (red dotted box) and freestanding grating membrane (orange dotted box). 40

1-5 Optical and scanning electron microscope images showing structural hierarchy of CAT gratings. Values on each figure exhibit length scale for aperture, level-2 supports, level-1 supports, and grating lines. . . 41

1-6 A schematic illustrating CAT grating principle. A hard x-ray (red) with a long penetration depth experiences phase modulation as it passes through the gratings. A soft x-ray (orange) reflects off the sidewall of the grating bars and diffracts to multiple orders. The diffracted orders near the angle of specular reflection blaze, resulting in enhanced diffraction efficiency. 43

1-7 A process flow for CAT grating fabrication. 45

1-8 (a) A schematic of the feedback-controlled interferometric lithography system used to define grating lines. (b) A phase distortion of gratings patterned on flat substrate due to interference of non-planar waves. (c) Parameters for interferometric arms that define periodicity of the gratings. The parameters are used when modelling phase distortion of the gratings. Images from Ref. [28] 46

1-9 An optical layout of the CAT grating spectrometer for Lynx. An array of CAT gratings (red) are assembled on a tilted Rowland torus and sit downstream from a focusing mirror assembly (grey) to diffract x-rays. X-rays travel through a long focal length and land on a detector array (orange) which also are assembled on the torus. Image from Ref. [39]. 48

1-10 (a) 3D-rendered optical layout of the CAT grating spectrometer for Arcus. (b) Hierarchy of optical channels consisting of SPO focusing mirror arrays and CAT grating windows. Images from Ref. [49]. . . . 50

1-11 Local coordinates and terminology for rotations of CAT grating . . . 51

1-12 A ray-trace simulation result on degradation of resolving power with increased grating period variations for chosen wavelengths of interest (1 nm: Black, 2.5 nm: blue, 5 nm: red). Image from [40]. 53

1-13 Degradation of resolving power (top) and effective area (bottom) with changing jitter in grating rotations (roll, pitch, and yaw from left to right) for chosen wavelengths (blue: 1.5 nm, orange 2.5 nm, green: 3.7 nm). Image from Ref. [38] 55

1-14 CAT grating imperfection observed during extensive testings. (a) Out-of-plane buckling of CAT grating membranes. Image from [48]. (b) An scanning electron microscope image of CAT grating membrane ripped off at the L2-grating membrane interface. 57

2-1 A schematic illustrating the working principle of the proposed metrology. Both angled-incidence and normal-incidence beams are illuminated in the same position on the grating as the gratings are scanned. Change of position of the returned beams are recorded with position sensitive detectors to deduce variations of grating parameters. 65

2-2 (a) A schematic of SLRT. Equation 2.1 follows a sign defined in local coordinates in the lower left corner. (b) A photograph of the SLRT. Inset in the upper right corner shows a photograph of two incident beams located on the same position of the grating surface. 67

2-3 (a) Inclined SEM image of cleaved 200-nm period reflection grating. (b) Photograph showing reflection grating mounted on rotation and translation stages for scanning. 68

2-4 Results on period measurement of reflection grating. (a) Period map showing both measured (color) and calculated (mesh) period variations. (b) Contour map for grating period variations from the center. (0,0) indicates wafer center. 'X' is the deduced center of interference fringes. 70

2-5 Measured roll angle variations from reflection grating. (a) Roll variation map showing both measured (color) and calculated (mesh) roll angle variations. 71

2-6 Representative images as observed from specularly reflected and back-diffracted return beams (a) non-symmetric shape, (b) fringes with non-symmetric beam intensity, (c) fringes too large to be captured by active detector area. 73

2-7 A concept for measurement of period variations and roll angles in transmission geometry. 73

2-8 Simulated diffraction efficiencies for 0th transmission and -1st diffracted order (193 nm, p-polarized) for 200-nm period, 6-μm deep silicon gratings. 74

3-1 A schematic for UV-based grating alignment setup using partial polarization property of HETGs. Image from Ref. [6]. 79

3-2 (a) An exploded view of a grating window with two grating holders. (b) A photograph of grating window after alignment and fixturing CAT gratings 82

3-3 (a) 3D model for two windows aligned on the window assembly frame. (b) A photograph of two windows (four CAT gratings) co-aligned on the grating assembly frame. Red line indicates scanned path for the SLRT. Areas illuminated in x-ray measurements are shaded in orange. Local coordinates are shown at the bottom left. 83

3-4 (a) Results of scanned line A-A' for alignment of two gratings on the window. Local coordinates are shown in blue. (b) Change of yaw, pitch, and roll angles along line scan A-A'. 84

3-5 Sequence of grating facet alignment. From 4-6, the gratings traveled to PANTER x-ray facility in Germany for x-ray verification. 85

3-6 Change of roll angle along the line scan. Areas shaded in grey indicate data not used for averaging. Noisy measurements in 80-90 mm and 115-118 mm spans correspond to buckled grating membranes [48] and thus were neglected when deriving roll angles. 86

3-7 Photograph of grating assembly mounted on the hexapod (a) and the upstream view of the grating assembly and SPO XOU pair (partially blocked by gratings in this view) each mounted on its hexapod (b). Inset in (b) shows pair of aligned SPO XOUs. 88

3-8 Roll alignment results measured using the SLRT (blue and orange) and x-ray (red). X13 was used as a reference for comparison 90

3-9 (a) A photograph of the GFAS. Optics are placed in an inverted configuration. UV source (not shown) is placed on another table to minimize thermal and vibration perturbations. (b) A zoomed image of a red dashed box. Facet frame is loaded beneath the support and gratings are sitting on the grating support, both inverted and nudged against three kinematic supports. (c) A zoomed image of the green dashed box. Four epoxy droplets were dispensed on the edges. 94

3-10 (a) 3D rendered model of Facet Frame. (b) Grating Facet. CAT grating was aligned and bonded at the mid-points of four flexures. (c) Grating window. (d) Four CAT gratings aligned mechanically and fixed on the grating window. 95

3-11 FLAT CAT grating alignment sequence. 1: Pick a reference grating, set "roll=0" reference in GFAS frame, bond reference grating to corresponding facet frame. 2: Load a facet frame to facet frame support. Load CAT grating to grating support. When loading the facet frame and gratings, nudge them against dowel pins for consistent positioning. Pull vacuums to hold grating tight. 3: Align CAT grating to "roll=0" reference set in sequence 1. 4: Translate the facet frame down toward the grating, place four thick shims between the grating and the facet frame to set "yaw=0" reference. Bond gap is set in this step. 5: Compensate for pre-characterized grating bar tilt angle[91] by rotating the grating with hexapod. 6: Dispense epoxy on four edges of the grating. 7: Cure epoxy with UV. 8: Post-thermal cure a grating facet at 55 degC for 15 min. 96

3-12 A schematic illustrating features of a produced grating facet. Grating is rolled to the reference coordinates set in GFAS frame. Tilted bars were compensated to be perpendicular to the surface of the facet frame. 98

3-13 A stand designed for kinematic alignment of CAT gratings. The window is placed to have 45 deg relative to the ground to provide consistent preload while mounting four CAT grating facets. 99

3-14 Exemplary scan data showing variations of yaw, pitch, and roll angles along line scans on X17 and X19. 100

3-15 An optical layout (a) and photograph (b) of the MIT X-ray Polarimetry Beamline. 102

3-16 A horizontal slit (a, b) and CAT gratings (c, d) mounted inside the grating chamber. 103

3-17 CCD images for 2nd diffracted orders from four CAT gratings. Blue and red dots indicate 'good' and 'bad' events, respectively. L1 diffracted orders are seen ∼120 pixels apart from the strong 0 order (in the vertical direction). Pixels are 20 μm wide along both x and y. 105

3-18 (a) Normalized flux for 2nd diffracted order of X19 along cross-dispersion direction. (b) Normalized flux for x-rays that didn't encounter gratings (gratings were out of the way from x-ray). 106

3-19 Histogram of 2nd diffracted order along cross-dispersion direction. Different virtual slits were chosen to plot histogram from left to right. Red arrows indicate position where the 2nd order image starts to emerge as translating the virtual slit. Green arrows indicate position where the image diminishes. 107

3-20 (a) Histogram of 2nd diffracted order along cross-dispersion direction with detected edges from slit (a) and histogram (blue) and Gaussian fit (red) after forcing counts within edges to have flat-top to prevent uncertainty from L2 shadowing. 108

3-21 A photograph showing an autocollimator installed and aligned to a 100-mm diameter mirror rigidly connected to grating stage to calibrate angular error motion of the stage. 109

3-22 A schematic showing pins inserted with an angle. 111

4-1 (a) Types of imperfections observed in high aspect ratio etching in semiconductor industry. (b) Overlay error caused by tilted etch profile. 116

4-2 A schematic for ideal grating (left) with bar tilt being uniform and parallel to the surface normal, and skewed grating (right) with with spatially varying bar tilt angle. 117

4-3 Potential causes for profile tilt. (a) Edge tilt caused by non-uniform plasma sheath at the edge of wafer. (b) Accumulation of charge on dielectric mask which repels positive SF_6 ions. (c) Non-uniform plasma density within the chamber. 119

4-4 Prior art in characterization of profile tilt. (a) Cross-sectional scanning electron microscope imaging of cleaved sample. (b) Image analysis on deep-etched grid patterns [7]. 121

4-5 CD-SAXS geometry defining the q vectors for the sample and the detector. The grating is oriented parallel to the rotation axis. Image from Ref. [92] 121

4-6 Front (a) and backside (b) mask design for test grating fabrication. . 123

4-7 Fabrication flow for test grating. 124

4-8 (a) A frontside photograph of the test grating (inset: SEM image of a single freestanding hexagonal membrane within the grating). (b) An inclined view of a cleaved test grating showing 3-4 μm of profile depth. 125

4-9 Prediction of 0th and +1st order DEs for straight bars (red in top graphs), skewed bars (blue in bottom graphs), and skewed bars rotated by skew angle (green in top graphs) as a function of incidence angle of x-rays onto grating bars (top) or grating surface normal (bottom) simulated with scalar diffraction theory (dashed line) and rigorous coupled wave analysis (RCWA) (solid line & circles). Insets inside the graphs are schematic for straight bars, skewed bars, and rotated skewed bars with a black arrow representing the direction of the surface normal. Results for both theories are insensitive to the bar-surface normal angle.127

4-10 Test grating mounted on rigid mount with front and back slits. Backside slit (not shown) is at the back of the grating. The grating is mounted on a laser reflection setup which measures relative angle between surface normal and slit axis. 128

4-11 (a) Height map of test grating mounted on the rigid jig. (b) Height variations along scans 1, 2. 129

4-12 (a) Experimental procedure. 1: Align the slit reference axis relative to x rays. 2: Measure bar tilt relative to x rays by performing variable-angle SAXS to record the change of DEs. 3: Align slit reference axis relative to the laser. 4: Measure surface normal relative to the laser. (b) 2D image of transmitted diffracted orders with different bar-to-x-ray angles. Each graph shows the spectrum and DEs from -5th to 5th orders. (c) Representative data (points) and Lorentzian fits (lines) from variable-angle SAXS. The surface normal was used as a reference for plotting. (d) Schematic showing arbitrary directions of the surface normal, grating bars, and the slit reference axis (to be aligned parallel to x rays and the laser in steps 1 and 3). The bar-normal angle (black solid angle) is characterized by combining two separate measurements using an x-ray beam (orange dotted angle) and a laser (green dotted angle). 131

4-13 Measured bar tilt variations along a line perpendicular to the grating bars for Pegasus- (a) and Rapier-etched (c) gratings. Scans 1 and 2 were performed 6 mm away from vertical chip edges [see insets in (a) and (c)]. Data from top patch were extrapolated (dashed lines) toward the center wide oxide mask for visual help. Surface normals were used as references for plotting. Graphical interpretations of bar tilt variations (exaggerated) for Pegasus- (b) and Rapier-etched (d) gratings. Relative plasma sheath thickness is deduced from the spatial variation of the bar tilt angle. 132

4-14 (a) Bar tilt variations of a square (32 mm × 32 mm) CAT grating relative to surface normal measured with the proposed metrology technique. Measurements were performed with both grating side (red) and the opposite side (purple) facing the x-ray source. Surface normals were used as references for plotting. Inset shows a square (32 mm × 32 mm) CAT grating etched with the Pegasus tool and mounted on a titanium frame. (b) Change of DEs of the consecutively blazed orders 4-6 along a scan line measured with an x-ray wavelength of 2.5 nm at a synchrotron facility. Inset shows the measured rectangular (8 mm × 32 mm) CAT grating etched with the Pegasus tool. 135

5-1 Representative volume elements for (a) hexagonal, (b) triangular, and (c) square periodic lattices. (d) Cross-section of the constituent beam. 139

5-2 A hexagonal lattice (left) and the corresponding RVE with the same size but consisting of homogeneous 'effective' materials (right). 146

5-3 (a) Unit cell for hexagonal lattice. Red dashed lines indicate boundary of the unit cell. A unit cell consists of three beams AO, BO, and CO which intersect at the point O. (b) A schematic showing deformation of Beam AO as displacement boundary conditions are applied for in-plane analysis. Local coordinate (x_a, y_a) and local basis vectors (m_j, n_j) are shown. Note that the beams are deformed such that the beam-ends are all rotated in the same manner as induced by periodic boundary condition. (c) A schematic showing local coordinates for beam AO used in out-of-plane analysis (before deformation). Unlike in-plane analysis, the local coordinates are placed at the beam end at the junction O. . 148

5-4 Visualization of in-plane deformation of 2d periodic lattices given different loading conditions (uniaxial strain, shear strain, and equibiaxial strain). 160

5-5 Visualization for out-of-plane deformation of 2d periodic lattices given different loading conditions (uniaxial curvature, twisting curvature, and equibiaxial curvature). 161

5-6 In-plane (top row) and out-of-plane (bottom row) stiffness derived from analytical (square) and finite element analysis (circle) for hexagonal, triangular, and square lattices. In-plane stiffness includes uniaxial, shear, and equibiaxial stiffness, and out-of-plane stiffness includes uniaxial, twisting, and equibiaxial stiffness (from left to right). Open area fraction was changed by changing beam length only while fixing thickness and width to be 500 and 96 μm. Young's modulus was assumed to be 169 GPa. 163

5-7 Contribution of stretching and in-plane bending of the beams on in-plane shear (membrane shear) stiffness for hexagonal, triangular, and square lattices. 164

5-8 Contribution of out-of-plane bending and twisting of the beams on twisting stiffness for hexagonal, triangular, and square lattices. 165

5-9 In-plane and out-of-plane stiffness of hexagonal, triangular, and square lattices modelled with Euler-Bernoulli (circle) and Timoshenko (X) beam elements using finite element analysis. 166

5-10 (a) Visualization of deformed hexagonal lattice when uniaxial curvature of 0.001 mm^{-1} is applied along x. (b) A schematic showing different deformation behaviors for beams modelled with Euler-Bernoulli (top) and Timoshenko (bottom) beam elements. Timoshenko beam transversely shears at the nodal junction, O, to release strain energy, resulting in lower stiffness compared to that modelled with Euler-Bernoulli beam element. 167

5-11 Visualization for in-plane and out-of-plane deformation of hexagonal lattice under different loading conditions (uniaxial strain, shear, equibiaxial strain, uniaxial curvature, twisting curvature, and equibiaxial curvature). 169

5-12 In-plane (top) and out-of-plane (bottom) stiffness modelled with nodal junction as a rigid point (X) and as a rigid body (square). 170

5-13 Full scale model of CAT gratings bonded to the frame with epoxy. (a) Meshed model of CAT grating attached to the frame with epoxy. Only the L2 hexagonal support and L3 aperture was included in the model with an assumption that thin CAT gratings and L1 membranes have negligible contribution to the overall stiffness of the structure. (b) Half geometrical and half meshed model to show detailed structures and mesh for titanium frame and epoxies. (c, d) Top (c) and inclined (d) view of deformed CAT grating facet when the whole assembly is uniformly heated by 30 degC. Color represents out-of-plane (z) displacement. 171

List of Tables

1.1 Alignment tolerances for CAT gratings. 55

2.1 Parameters used for SLRT 66

3.1 Angular misalignments between X14 and X10 recorded during each sequence of holder alignment. Units are in arcmin. 89

3.2 Measured stage roll error as stage was translated to positions for each grating. X19 is a reference. Units are in arcmin. 109

3.3 Measure roll angles as CAT grating facet was placed in different sections. S2 indicates section 2. X19 was kept placed in section 1 and used as a reference. Units are in arcmin. 110

3.4 Comparison of roll misalignments as measured from GFAS and MIT x-ray beamline. Each value indicate roll angle relative to X19. roll is positive counterclockwise when seen from grating side. Units are in arcmin. 111

3.5 Different measurements on roll misalignment depending on scan path. ±10 mm indicate line scans at ±10 mm away from the center along the cross-dispersion axis. X19 is a reference. Units are in arcmin. . . 112

5.1 Axial and bending displacements for beams AO, BO, CO in hexagonal lattice with beam length of 0.555 mm under in-plane shear of 0.0005. Negative axial displacements imply compression. All units in [μm]. . 164

5.2 Behavior of free variables for hexagonal lattice modelled with Euler-Bernoulli or Timoshenko beam elements. A uniaxial curvature of 0.001 mm^{-1} was applied along x. 167

List of Symbols

Lists of symbols used in chapter 5 are summarized. Symbols in other chapters are explained in detail in each chapter.

Symbol	Description
f	Optical (or open) area fraction
ρ	Areal density
b, t	Width and thickness of constituent beams
L	Length of constituent beams
L_{eff}	Effective length of constituent beams
E	Young's modulus of isotropically modelled crystalline silicon
G	Shear modulus of isotropically modelled crystalline silicon
$\underline{x}$ or x_β	Vector or tensor notation for coordinates (x,y) in global (lattice) coordinate within a representative volume element (RVE). For tensor notation, β can be replaced with any greek letters as needed
$\underline{x}_j$=(x_j, y_j)	Local (beam) coordinates for beam JO
$\underline{x}^J = (x^J, y^J)$	Coordinates at beam end J represented in global (lattice) coordinate

$\underline{u}$ or u_β	Vector or tensor notation for displacements (u,v) along x or y. For tensor notation, β can be replaced with any greek letters as needed
ϕ^J	Rotation of beam end J about z axis
w^J	Displacement of beam end J along z (out-of-page)
$\epsilon_{\alpha\beta}(\underline{x})$	Strain at $\underline{x}$ in RVE
$\epsilon^*_{\alpha\beta}$	Uniform strain applied at the boundary of RVE
$\bar{\epsilon}_{\alpha\beta}$	Average strain in RVE
$\kappa^*_{\alpha\beta}$	Uniform curvature applied at the boundary of RVE
n^{RVE}_α	Unit outward normal vector of RVE
$f_{\alpha\beta\sigma\gamma}(\underline{x})$	Elasticity tensor at $\underline{x}$ in RVE
$\sigma_{\alpha\beta}(\underline{x})$	Stress at $\underline{x}$ in RVE
$\bar{\sigma}_{\alpha\beta}$	Average stress in RVE
$\bar{C}_{\alpha\beta\sigma\gamma}$	Average elasticity tensor for RVE
$\bar{N}_{\alpha\beta}$	Average membrane stress for RVE
$\bar{M}_{\alpha\beta}$	Average plate bending moment for RVE
$C^{eff}_{\alpha\beta\sigma\gamma}$	Effective membrane stiffness of RVE
$D^{eff}_{\alpha\beta\sigma\gamma}$	Effective plate bending rigidity of RVE
$\bar{W}$	Average strain energy stored per unit volume in RVE
Ψ	Average strain energy stored per unit area in RVE
$R^j_{\alpha\beta}$	Operator to perform coordinate transformation from lattice coordinate to beam coordinate
$\theta^{J,j}_1$	Bending angle of the beam end J in local (beam) coordinate $\underline{x}_j$ (or slope at beam end J along local (beam) coordinate $\underline{x}_j$)
θ^J_1	Bending angle of the beam end J in lattice coordinate $\underline{x}$ (or slope at beam end J along lattice coordinate x)

$\theta_2^{J,j}$	Twisting angle of the beam end J in local (beam) coordinate $\underline{x}_j$ (or slope at beam end J along local (beam) coordinate y_j)
θ_2^J	Twisting angle of the beam end J in lattice coordinate $\underline{x}$ (or slope at beam end J along lattice coordinate y)
$\underline{m}^J = (m_1^J, m_2^J)$	A unit normal vector parallel to the longitudinal axis of the constituent beam JO
$\underline{n}^J = (n_1^J, n_2^J)$	An in-plane unit normal vector perpendicular to the longitudinal axis of the constituent beam JO
A_{cell}	Area of the unit cell
A_{beam}	Cross-sectional area of the constituent beams
I_b	Area moment of inertia for in-plane bending (bending about z)
I_t	Area moment of inertia for out-of-plane bending (bending about y_j)

Chapter 1

Introduction

1.1 Motivation

A plethora of new devices are being reported in the field of electronics, optoelectronics, and MEMS/NEMS. In the semiconductor industry, due to stalled progress in Moore's law, new types of device architectures have been (or will be) pursued either by stacking the electronics in 3D (FinFet, and Lateral/vertical gate-all-around, GAA), or adopting new materials and physics to build 'Beyond CMOS' structure such as superconducting electronics, neuromorphic computing units, resistive random access memory (RRAM), etc. [3, 1, 73]. However, it is worthwhile to ask the question "How many of these breakthroughs will remain laboratory toys and how many of them will move its way out to the world?". In order to answer these questions, there must be another line of effort on finding new metrology solutions and suitable process controls for these devices to escape out of the laboratory. Otherwise, those would remain as wishful thinking [2]. Similar issues exist in the field of x-ray astronomy as we build large-sized x-ray telescopes. As will be detailed in the following sections, some components in x-ray telescope (i.e., gratings) require high volume manufacturing to populate a large telescope aperture (>1 m). Though the quantities of devices to be produced

are much less than those in semiconductor industry (a few thousand devices required to be manufactured), development of metrology solutions is inevitable in order to build space-based x-ray grating spectrometers. For the most part of this thesis, my contributions towards developing measurement techniques will be discussed in order to realize an x-ray grating spectrometer, one of the essential modules in x-ray telescopes.

Gratings (or MEMS/NEMS devices alike) rely on their mechanical structures to operate, not on electrical or material properties. Therefore, understanding structural properties (mode shapes and amplitudes of deformations for x-ray gratings or their sub-structures under potential loading) are critical to maintain proper function. In an effort to build an x-ray telescope, a freestanding x-ray grating, a nano-sized device of interest in this thesis, needs to be mass-manufactured and assembled to cover large telescopic apertures. From after its fabrication to launch and decade-long operation in space, it will be subjected to many types external loads [72]. However, mechanical aspect of gratings are still at an early stage since most of the research effort has been invested in fabrication and process control of the gratings [4, 5, 10, 47, 9]. This thesis performed basic studies on its mechanical stiffness and search for better design space to make it stiffer but lighter.

Manufacturing of future x-ray telescopes is one of the most challenging precision engineering tasks in the current era, however, its impact is significant as it opens our eye beyond the currently observable universe. The field stands at the forefront of precision engineering and optical engineering requiring cross-disciplinary innovations as regard to mechanical engineering, electrical engineering, and physics (other fields that require similar levels of precision include semiconductor equipment, semiconductor manufacturing, and x-ray synchrotron optics [22] to the authors' knowledge). This thesis attacks this challenging task encompassing optics, metrology, and instrumentation aspect (chapter 2,3,4) of the manufacturing, and ends with mechanical aspect (chapter 5), all of which are critical contributions but still just a small step towards this daunting task. The author hopes this thesis will make our "eyes" closer to reality.

1.2 Thesis contribution

The contributions of this thesis are divided into three big themes, all of which aim to build high-performance space-based x-ray grating spectrometer (see section 1.2 for requirements), one of the essential components in future x-ray telescope missions: 1) inventions of metrologies for control of critical dimensions (CDs) (chapter 2, 4), 2) development of grating alignment process (chapter 3), and 3) design and analysis of structural supports for freestanding x-ray gratings (chapter 5).

First, a grating period metrology with 0.004 nm rms precision (20 ppm rms) was invented using a simple UV diffraction principle to characterize CD variations of 200-nm period x-ray gratings (chapter 2). The invented metrology satisfied $<$0.006 nm precision (requirements for future missions, see section 1.8) in measuring grating period variations caused from interference lithography step. Period variations of 0.018 nm (1 σ) were observed in 200-nm pitch gratings, which fulfil the resolving power requirements for future x-ray telescope missions ($>$3500 for Arcus and $>$5000 for Lynx). Please see figures 2-2 and 2-4 in chapter 2 for a photograph of the constructed metrology and the results of this research.

Second, a UV metrology and procedure were developed to align x-ray gratings with accuracy of $<$6 arcmin (chapter 3). The developed alignment process is intended to be fast ($<$one hour per grating), scalable, precise ($<$1.8 arcmin), and accurate ($<$3 arcmin) for high-volume ($>$1000) alignment of x-ray gratings to achieve effective area requirements ($>$350 cm^2 for Arcus and $>$4000 cm^2 for Lynx) for future x-ray telescope missions (see section 1.2). Since it is hard to attain all the aforementioned goals in a single experiment, two series of tests were performed: test 1 to develop alignment metrology, characterize its precision and accuracy, and demonstrate alignment of four x-ray gratings to satisfy alignment requirements (see section 1.8), and test 2 to improve design of alignment hardware (i.e., frames to bond gratings), modify alignment process to be scalable, and speed up the alignment process (a single day per grating for test 1 to $\sim$1 hr per grating for test2). Overall, speed of $\sim$one grating per hour,

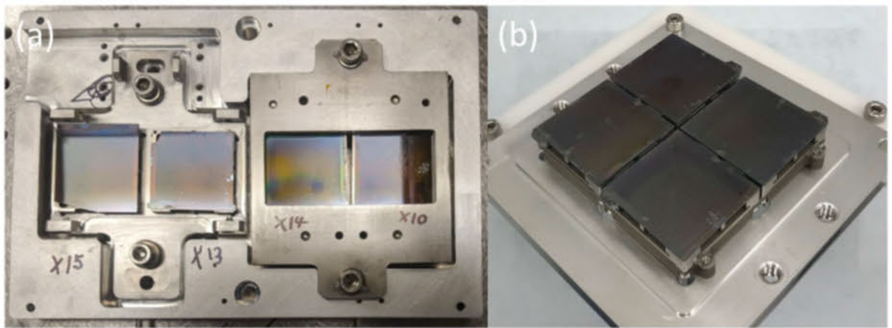

Figure 1-1: Four x-ray gratings aligned for test 1 (a), and test 2 (b). Please refer to chapter 3 for more details.

precision of 0.66 arcmin, and accuracy of 3.18 arcmin were achieved from best of both tests. Figure 1-1 shows photographs for four aligned x-ray gratings (see chapter 3 for more details).

Third, an x-ray based metrology was invented to characterize profile tilt of high-aspect ratio (~40 AR) x-ray gratings (chapter 4). The developed metrology demonstrated precision of <0.01 deg, and accuracy of $\sim$ 0.08 deg in characterizing profile tilt angle relative to a surface normal. It successfully characterized variations of profile tilt in x-ray gratings caused during deep reactive-ion etching (DRIE) step, provided feedbacks in developing new etch recipes to fabricate x-ray gratings with profile tilt varying less than 0.1 deg across $3x3cm^2$ area. The developed metrology and process are critical to achieve large effective area (>350 cm^2 for Arcus and >4000 cm^2 for Lynx) promised for future x-ray telescope missions. The proposed metrology is expected to replace cross-sectional SEM imaging commonly used in semiconductor manufacturing. It is nondestructive, fast (5-6 seconds of integration time per $10000\mu m^2$ field of view per sample vs 0.5-1 hrs per few μm^2 field of view per sample for SEM imaging), precise (~0.01 deg of precision vs 0.1 deg of precision for SEM imaging) and accurate (~0.08 deg of accuracy vs ~0.5 deg of accuracy for SEM imaging). Please see Fig. 4-14a in chapter 4 for the result of this research.

Forth, a better structural support for x-ray grating was designed by studying in-plane and out-of-plane stiffness's of several 2d periodic lattices (hexagon, triangle,

and square) using analytical and finite element tools. It was found that adopting triangular lattice will increase stiffness's by 23-580% (depending on loading modes) compared to current hexagonal lattice at the same optical area. Alternatively, replacing current hexagonal structural supports with triangular lattice is expected to increase optical area by 5% without compromising stiffness. It is expected to reduce chances on grating failures during assembly, launch, and operation, and is expected to have an economic impact of ~500,000 US dollars for 290 million US dollar x-ray grating spectrometer mission. Please see figures 5-6 and 5-12 for the results of this research.

1.3 X-ray telescope

An X-ray telescopes is a must-have-item in the field of x-ray astronomy. A number of high-priority questions in astrophysics had been addressed by high-resolution x-ray telescopes. The Chandra x-ray telescope, launched in 1999, is one of NASA's Great Obervatories[25], contributing to the first image of supernova remnant Cassiopeia A and the detailed structure of Crab Nebula [74, 100]. However, the Chandra observatory is outdated, relying on old technologies developed in 80 - 90s. Many important astrophysics questions of today imposes much more demanding requirements on x-ray telescopes. The main objective in x-ray telescope instrumentation is to achieve high resolution (both spectrally and spatially) and large collecting area in imaging/spectroscopy. Modern x-ray telescopes target sub-arcsecond imaging resolution and high spectral resolution across a large collecting area of >1 m^2 [31, 27].

A typical x-ray telescope is composed of three main elements; focusing optics, gratings (for high resolution spectroscopy mission in soft x-ray band), and detectors. All three components have to be advanced to push the boundary of performance limits. Recent developments of high resolution thin-shell x-ray mirrors [104], Silicon Pore X-ray Optics [26], and Critical-Angle Transmission Gratings [42, 46, 43, 48,

50, 49, 52] are key drivers in x-ray telescope instrumentation. Recently proposed x-ray telescope missions will utilize these groundbreaking technologies to build x-ray telescopes in the near future.

In this thesis, attention will be limited to a grating module which is placed downstream of the focusing optics. It is comprised of >1000 of high-quality gratings (differing between missions but ranging from 700 to 1000), precisely co-aligned relative to one another in their ideal configuration. Requirements on grating modules (i.e., critical dimensions (CDs) such as grating period and angles between grating bars and surface normal, grating alignment, optical area fraction) to be specified in this thesis (see section 1.7) were derived based on concept studies on optical layouts for the Arcus or Lynx missions, the future x-ray telescope missions. [40, 38].

1.3.1 Arcus

Research activities in this thesis were performed as a part of an effort towards Arcus[27], a medium-sized explorer (MIDEX) mission proposed to NASA with special focus on soft x-ray grating spectroscopy. It aims to achieve unprecedented sensitivity in the 12-50 bandpass, with spectral resolving power of >2500 and optical (or effective) area of >250 cm^2. It uses 12 m focal length grazing-incidence Silicon Pore X-ray Optics (SPOs) [26] to focus x-ray on CCD detectors. Downstream from the SPOs stand Critical-Angle Transmission (CAT) gratings to diffract soft x-rays with very high efficiency for high-resolution x-ray spectroscopy. The optical instrument will be loaded in a NGIS LEOStar-2 spacecraft and launched into a 4:1 lunar resonant orbit to observe a wide range of astrophysical sources [27].

1.3.2 Lynx

The majority of works from this thesis will be adopted in Lynx mission as well. Lynx is one of the four flagship-class missions being considered for the 2020 Astrophysics

Decadal Survey [31]. It promises sub-arcsecond on-axis imaging performance, arcsecond angular resolution over a large field of view (off axis), and high-resolution spectroscopy with resolving power of >5000 and effective area of 4000 cm^2 in the 0.2-2 keV band [39]. It has a 3-m diameter focusing mirror assembly with a 10-m focal length, downstream of which CAT grating assembly will be placed (retractable) to cover approximately two-thirds of the aperture for spectroscopy.

1.4 Grating basics

Diffraction gratings are one of the essential elements for nanoscale science, being used as nanoscale metrological standards, a high resolution spectroscopy, a monochromator, and many other optical instruments [85, 51]. It is a periodic structure (either along a single or multiple axes) that is typically used to spectrally resolve electromagnetic wave, electrons, and matter waves [42]. As the waves interact with gratings, they are split (or diffracted) into several (or numerous) waves travelling into directions where the rays with different path lengths constructively interfere with each other. As a plane wave with sufficient spatial and temporal coherence is incident on the grating with an angle θ_i, the direction of diffracted waves are derived according to the grating equation:

$$p(sin(\theta_i) - sin(\theta_m)) = m\lambda \quad (1.1)$$

where θ_m is a direction of mth diffracted order, λ is a wavelength of the incident wave, and p is a grating period (see Fig. 1-2). Angles are positive clockwise. The full-width half maximum (FWHM) of travelling diffracted waves depends on the design of 'slits' that repeats millions of times over the grating area. The ability to design and fabricate gratings (or slits) with varying size, materials, and geometry enables engineering the efficiency of diffraction peaks, enabling high resolution spectroscopy in x-ray astronomy.

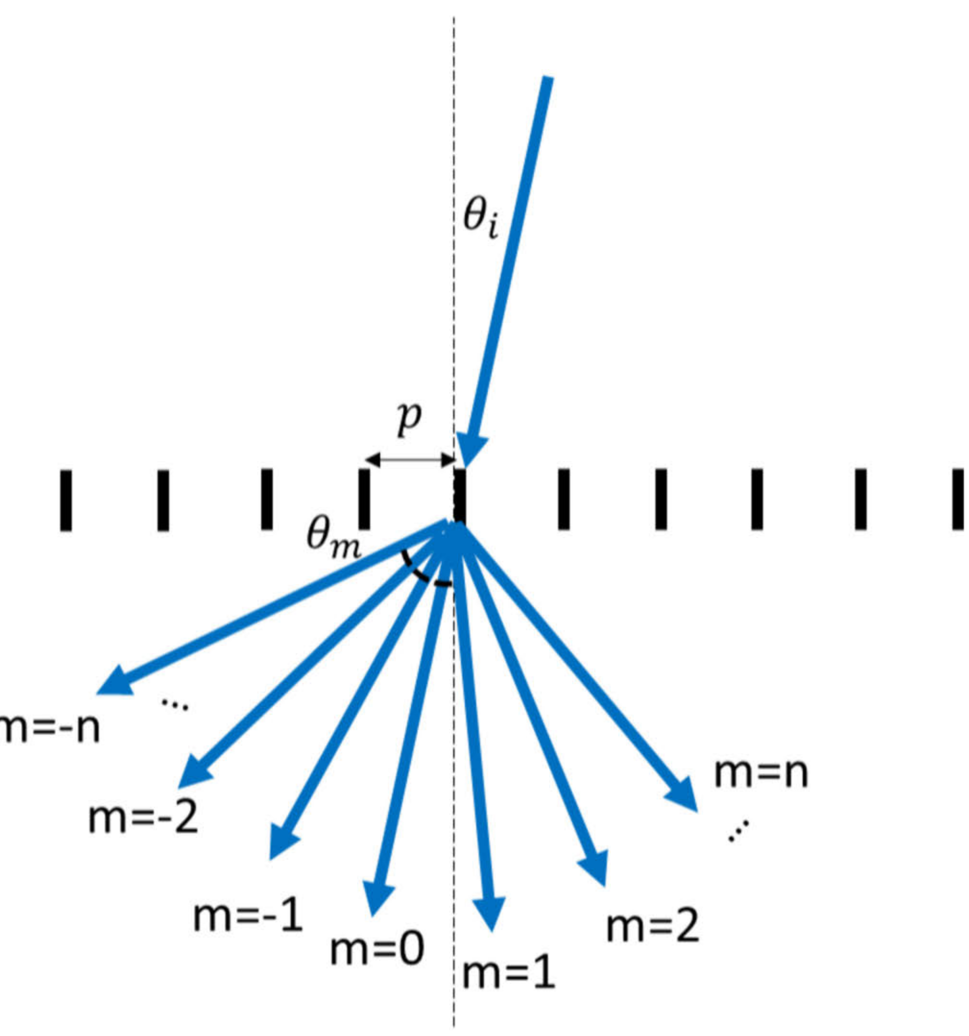

Figure 1-2: A schematic showing incident beam and multiple transmitted diffracted orders. Media below and above the gratings share same refractive indices.

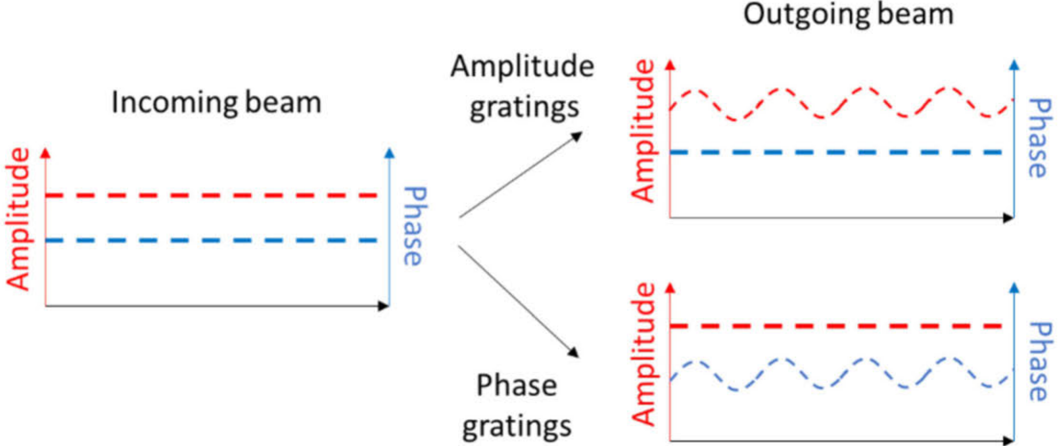

Figure 1-3: A schematic demonstrating phase or amplitude modulation of the electric field of an incoming plane wave.

Conceptually, gratings are categorized into amplitude and phase grating depending on whether it modulates amplitude or phase of the electric fields of the out-going beams. Figure 1-3 shows modulation of amplitude or phase as a monochromatic plane wave interacts with the grating. The mathematical expression on E-field amplitude modulation of the representative amplitude grating is as follows:

$$g_{amp}(x) = \frac{1}{2}[1 + m_{amp}cos(2\pi\frac{x}{p} + \phi)] \tag{1.2}$$

where p is a periodicity of the grating and m_{amp} is the contrast. Mathematical expression on E-field phase modulation of the representative phase grating is as follows:

$$g_{phase}(x) = exp[i\frac{m_{phase}}{2}sin(2\pi\frac{x}{p} + \phi)] \tag{1.3}$$

where p is a period and m_{phase} is the phase contrast.

In an x-ray band, total external reflection occurs when an x-ray reflects off an interface between air (or vacuum) and a material with index of refraction less than 1 at a glancing angle below critical angle. It is analogous to total internal reflection in other wavelength bands except that it happens at the exterior part of the material. Total external reflection occurs when a grazing angle (α) is below the critical angle,

$\alpha<\theta_c$ where θ_c is dependent on both materials and wavelength. For example, a critical angle is approximately $\sim$2 deg at λ=1.5 nm between Si/air interface, meaning that a grazing angle for an x-ray with 1.5 nm wavelength needs to be below 2 deg for total external reflection. This is one of the fundamental principles to build Wolter-type x-ray focusing optics and high-efficiency gratings. In the design of x-ray grating spectrometers, it is desirable to take advantage of total external reflection by aligning grating modules such that x-ray grazes at an angle below a critical angle at a designed wavelength. Another important concept in x-ray gratings is "blazing." "Blazing" occurs when certain diffracted orders are aligned with the angle of specular reflection, where the grating surface acts as a "mirror." Typically, it is desirable to blaze higher diffracted orders to achieve enhanced resolving power, however, it may lead to a reduced effective area if the grazing angle exceeds the critical angle.

Based on diffraction geometry, gratings can also be categorized as reflection and transmission gratings. High energy transmission gratings (HETG) built for the Chandra x-ray telescope are historic transmission gratings that achieved near $\sim$40% efficiency (sum of $\pm$ 1st orders) at a designed wavelength of $\lambda = 0.6$ nm [25, 83]. 200-nm pitch gold bars standing on polyimide support membrane delayed the phase of transmitting x rays by π to maximize diffraction efficiency of $\pm$ 1st orders. 0th order with π phase shift vanishes through destructive interference. However, for wavelengths other than 0.6 nm, the phase shift didn't work out as well for constructive interference. Efficiency loss from absorption of photons by the polyimide support reduced the operating bandwidth of the HETG in the soft x-ray band. Blazed reflection gratings are reflection-type gratings being proposed for x-ray spectroscopy for many decades [16, 45, 44, 30, 21]. Reflection gratings use conical or planar diffracted beams that reflects off the surface. A generalized grating equation for conical diffraction can be found in Ref. [41]. It has several advantages over traditional transmission gratings; it doesn't suffer from efficiency loss from absorption from the support and thus can operate in a wider bandwidth, and is oftentimes structurally stiffer compared to transmission gratings.

However, transmission gratings have many preferable characteristics compared to their reflective counterparts. It leaves the 0th order unaffected which can be used for x-ray imaging (for shorter wavelength) while diffracting x-ray with longer wavelengths for spectroscopy (CAT gratings enable both at the same time). Transmission gratings are inherently less sensitive to figure error, thereby requirement on surface flatness are less strict [52]. Reflection gratings are many centimeter long along the optical axis due to small graze angles while transmission gratings can be few μm thick. Lastly, since for reflection grating, x-rays are incident with grazing incidence angle, many number of gratings have to be stacked to populate a radial telescope aperture along the radial direction. Transmission gratings don't require stacking as x-rays are incident near normal (which means grazing incidence on grating bar sidewalls), requiring a much smaller number of gratings (30 times for 2 deg graze angle) to populate the telescopic aperture, leading to reduced weight. It drastically reduces the cost of stacking and aligning large number of gratings.

1.5 Critical-angle transmission (CAT) gratings

Until recently in the field of x-ray telescopes, transmission gratings have been rarely proposed for soft x-ray grating spectrometer missions ever since the HETG spectrometer [83] was deployed into space onboard the Chandra X-ray Observatory with its unparalleled 0.5 arcsec angular point spread function (PSF). To overcome the much higher "blur" of thin-foil x-ray mirror arrays employed for x-ray missions that require higher effective area than Chandra, the technology to blaze into high diffraction orders in transmission was lacking, and heavier, alignment-sensitive reflection gratings were the only option. Recent development of CAT gratings [42, 43, 52] has enabled the blazed transmission grating spectrometer, bringing innovations in the field of x-ray spectroscopy. State-of-the-art CAT gratings are comprised of is 200 nm-period, 4-6 μm deep freestanding ultra-high aspect ratio silicon grating, with sidewalls polished to roughness $<$1 nm, held in place by 5-μm period cross-support (level-1, L1) mesh

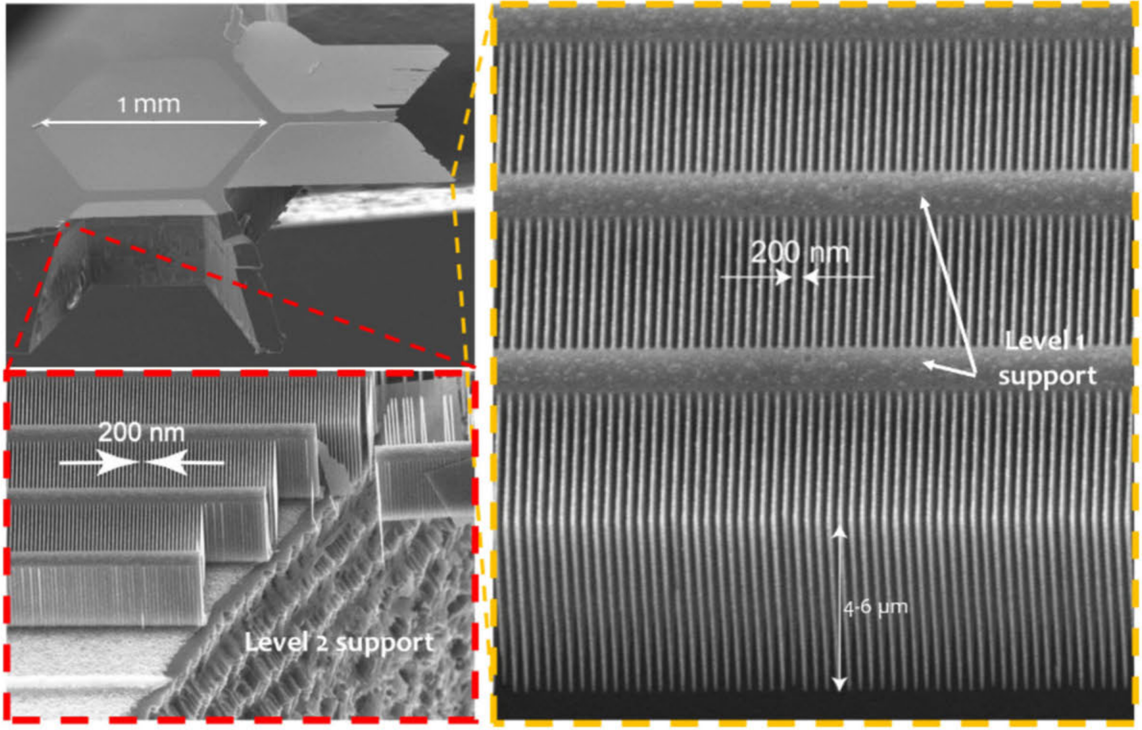

Figure 1-4: Scanning electron microscope images of intentionally cleaved CAT grating. Zoomed images show grating structure on L2 supporting structure (red dotted box) and freestanding grating membrane (orange dotted box).

running perpendicular to the gratings and a 1-mm period rigid hexagonal mesh (level-2, L2). It is sometimes called a "blazed transmission grating" in that it blazes certain diffracted orders with sidewalls acting as an array of 'nanomirrors'. It was devised to make use of good features from both reflection and transmission-type gratings. Figure 1-4 shows SEM images of cleaved CAT gratings. Zoomed images show grating bars sitting on L2 support (bottom left) and freestanding gratings bars (right).

As previously mentioned, since CAT gratings as freestanding structures are inherently weak, they are built with hierarchical structural supports for structural integrity along their fabrication, assembly, launch, and decade-long operations. Figure 1-5 shows a photograph of CAT gratings with zoomed SEM images to show overall structural hierarchy of CAT gratings along with their length scales. 5-μm period, 1-μm wide cross-supports (L1) connect to the gigantic (500-μm thick, 100-μm wide) 1-mm period hexagonal (L2) mesh at their ends. A hexagonal mesh repeats >26x27

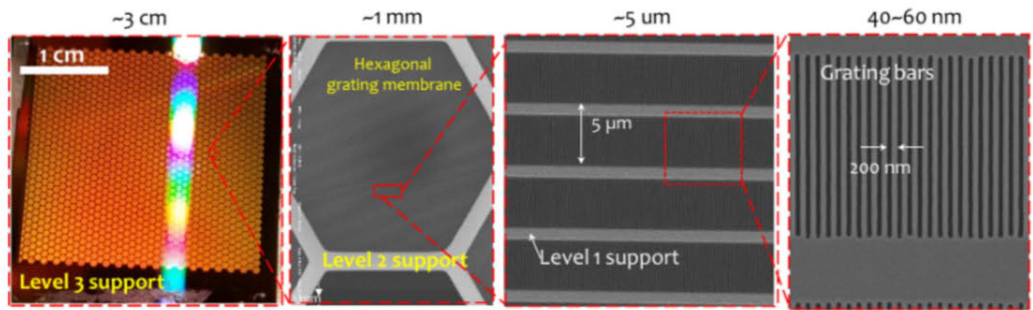

Figure 1-5: Optical and scanning electron microscope images showing structural hierarchy of CAT gratings. Values on each figure exhibit length scale for aperture, level-2 supports, level-1 supports, and grating lines.

times (depending on size of the grating) to populate an entire aperture of the single CAT grating. L2 supports are surrounded by rectangular level-3 (L-3) support. L3 support is used for handling or bonding gratings to metal frames for later assembly. A state-of-the-art CAT grating demonstrates the largest size of 30 x 31 mm.

Figure 1-6a shows working principle of the CAT grating. In the designed wavelength for soft x-rays (0.5-5 nm), x-rays reflect off smooth sidewalls of the grating bars and diffract towards the directions where path length differences between adjacent rays become integer multiple of the wavelength. The direction of mth diffracted order (β_m) follows the equation:

$$sin\alpha - sin\beta_m = \frac{m\lambda}{p} \tag{1.4}$$

where α is a grazing angle, λ the wavelength, and p the grating period. Blazing occurs for mth diffracted orders when it aligns with a direction of specular reflection ($\alpha = \beta_m$). Sidewalls act as an array of nanomirrors, similar to stacked reflection gratings [23]. Assuming a single reflection off the sidewall, geometrical optics suggest that the x-ray should be directed with angle $\alpha < tan^{-1}(b/d)$ in order to prevent multiple reflections (or scatterings) from sidewalls. As we increase the depth, d, and blaze at a smaller angle, wider x-ray band will be incident below critical angle,

but it indicates more challenging angular alignment requirements. Duty cycle of CAT grating is defined as b/p. Larger duty cycles lead to improved x-ray diffraction efficiency with more rays not blocked by the sidewalls, but it may lead to mechanically weak gratings. It is possible to blaze higher diffracted orders by varying the grazing angle as long as $\alpha < \theta_c$, but it will lead to efficiency loss as some portions of x-rays will not experience gratings (x-ray travels between grating bars uninterrupted) or some other portions of x-rays will experience multiple reflections. Figure 1-6 visualizes 0th order transmission and multiple diffracted orders, transmitted through a CAT grating and incident on the x-ray detector. The 0th order transmitted x-ray at short wavelengths (red) passes through the grating bars unperturbed and can be used for x-ray imaging, while x-ray photons at longer wavelength diffract (orange) as intended for x-ray spectroscopy.

Fabrication of large-area CAT grating with consistent high quality has been a big challenge over the last decade. Hurdles faced in process development and optimizations are described in detail from papers published by the Space Nanotechnology Laboratory [4, 5, 10, 47, 9, 46, 71]. In this thesis, lithography and high-aspect ratio etching steps will be discussed in detail, for which metrologies developed in this thesis played critical roles for process optimization. Figure 1-7 shows the overall fabrication process. It starts with silicon-on-insulator wafers with 4-μm thick <110> device layers and 500-nm thick buried oxide (F1). Grating lines are defined by lithographic patterning with traditional interference lithography (F2) followed by deep reactive-ion etching (DRIE) (F3) of a 4 μm thick <110> silicon-on-insulator (SOI) device layer. The grating lines are carefully aligned to the <111> crystalline direction for a short, crystal-lattice-orientation dependent KOH polishing of the sidewalls after deep reactive-ion etching. Once the gratings are engraved in the device layer, the device layer is filled with photoresist, flipped, and bonded to a carrier for back-side processing (F4). A pre-patterned 1-mm period hexagonal mesh (F2) is etched into the handle layer from the backside through deep reactive-ion etching (B1). Buried oxide (BOX) layer serves as an etch stop for both etches. BOX layer is removed

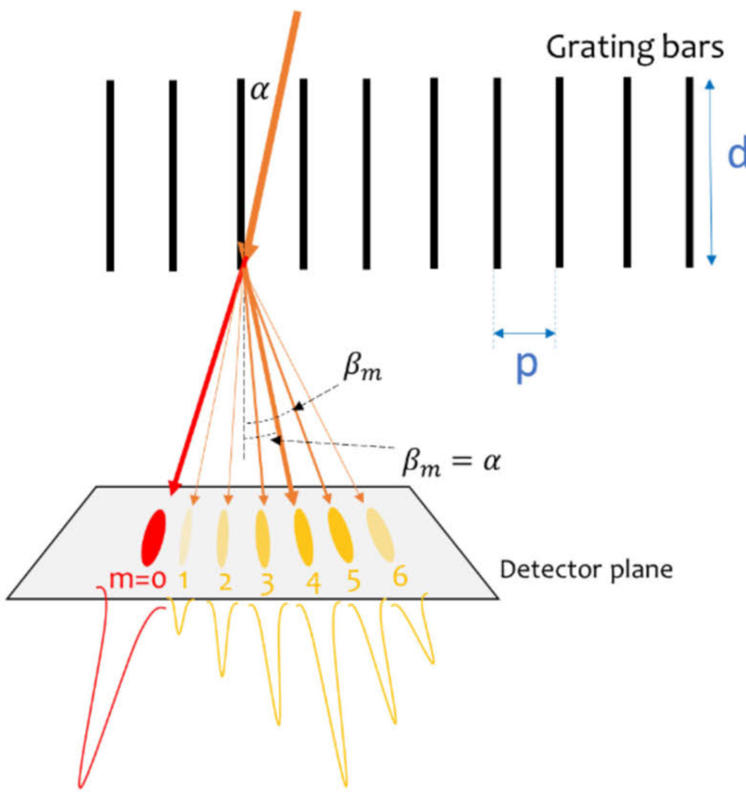

Figure 1-6: A schematic illustrating CAT grating principle. A hard x-ray (red) with a long penetration depth experiences phase modulation as it passes through the gratings. A soft x-ray (orange) reflects off the sidewall of the grating bars and diffracts to multiple orders. The diffracted orders near the angle of specular reflection blaze, resulting in enhanced diffraction efficiency.

afterward with wet HF (B2), and the gratings are de-bonded by cleaning photoresist, critical-point dry and ashing (B3).

Until recently, lithographic step (F2) defined grating lines utilizing standing-wave interference of two non-planar (spherical) beams. It was not until 1980s that interference lithography took over fabrication of fine pitched gratings from ruling engines, during which grating lines were engraved line by line using a diamond tip. For adoption of interferometeric lithography in grating fabrication, many technical problems including laser stability, beem steering stability, thermal stability, spatial phase locking of the interference fringes, and precise alignment of the interfering beams had to be solved to precisely define grating lines. Figure 1-8a shows a schematic of an Mach-Zehnder interference lithography tool being used to define grating lines for CAT gratings [97, 28]. While most of the engineering issues were resolved with traditional IL tool, there exists nonlinear phase of grating lines induced from interference of non-planar waves. Figure 1-8b shows a simulated phase discrepancy between 200-nm period linear gratings exposed by interfering two diverging spherical waves and a perfect linear grating. Figure 1-8c shows dimensional parameters (a,c) used for a simulation. Contours represent loci of equal phase discrepancy.

Great efforts were invested in developing Scanning Beam Interference Lithography [14, 13, 61, 62, 70, 105] to pattern perfect linear gratings free of phase distortion, however, for our current R&D effort in CAT grating fabrication towards Arcus, fabrication relies on Mach-Zehnder interference lithography due to cost issue in operating SBIL in a small univeristy laboratory, and IL tool is enough to satisfy spatial phase coherence requirements of grating period for near-future x-ray telescope missions. More recently, a 193 nm semiconductor scanner was adopted to pattern 200-nm period gratings and L1 cross-supports in a single step. Taking advantage of well-developed tool from semiconductor industry reduces time and effort spent for high volume manufacturing of CAT gratings. It is expected that large quantities of high-quality CAT gratings can be produced for more extensive testings. Another advantage of using the semiconductor scanner is that it may enable our grating allignment metrology easier.

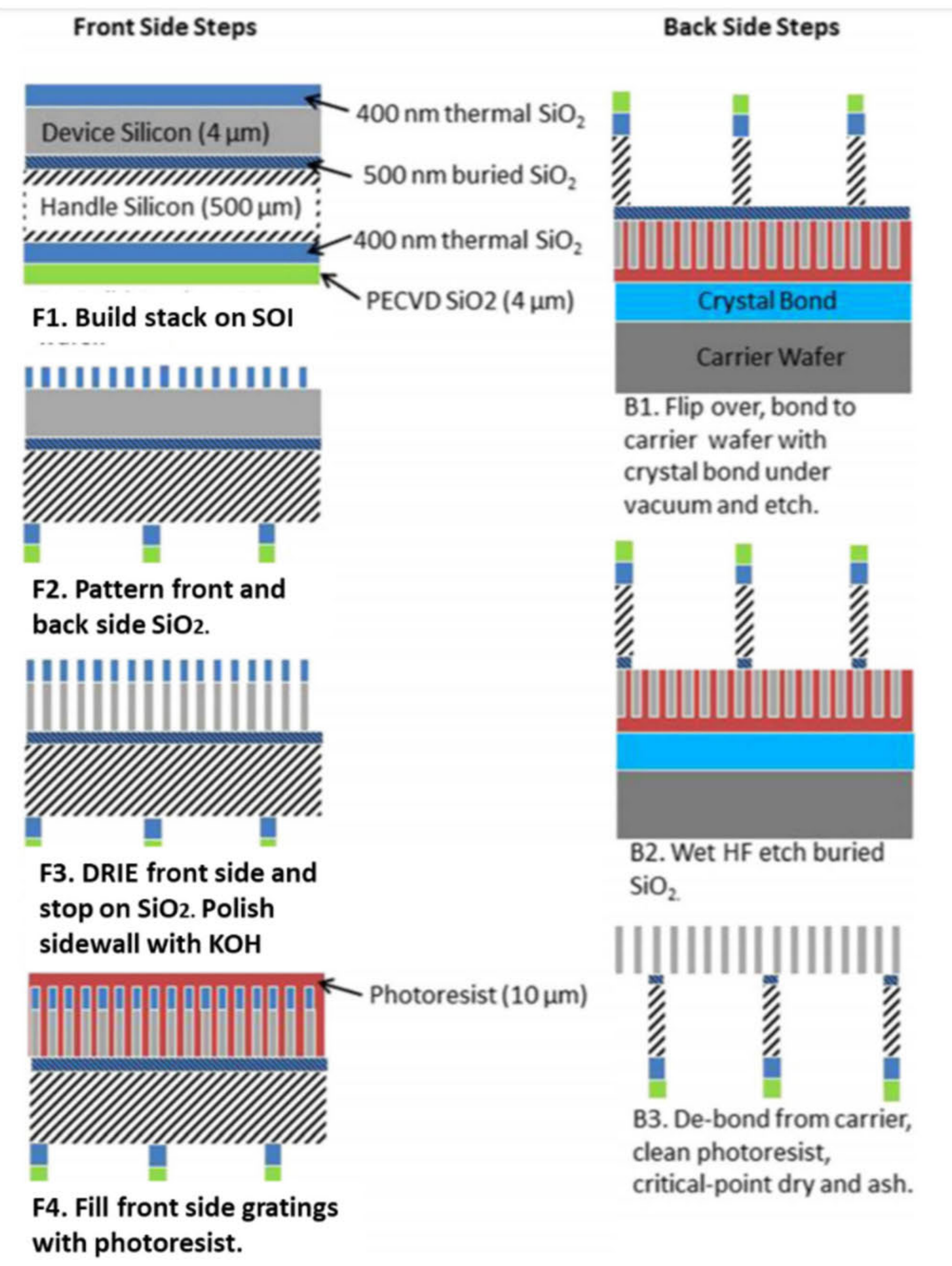

Figure 1-7: A process flow for CAT grating fabrication.

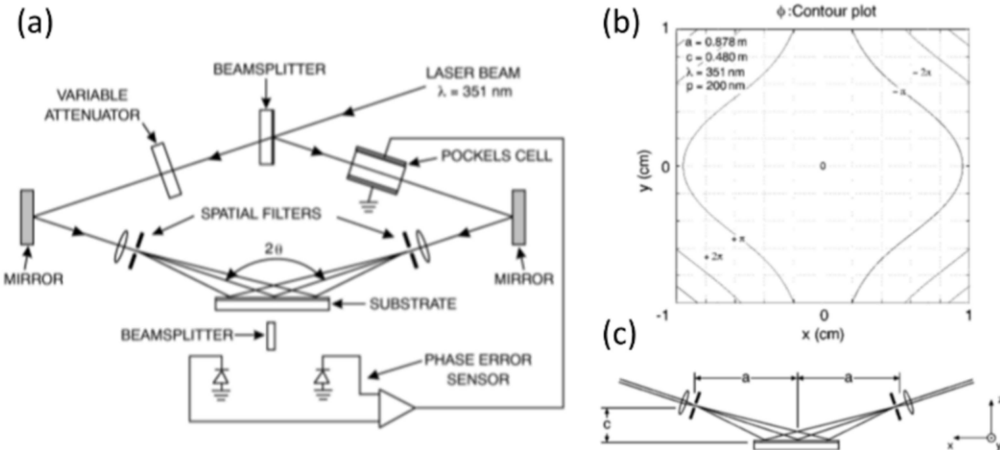

Figure 1-8: (a) A schematic of the feedback-controlled interferometric lithography system used to define grating lines. (b) A phase distortion of gratings patterned on flat substrate due to interference of non-planar waves. (c) Parameters for interferometric arms that define periodicity of the gratings. The parameters are used when modelling phase distortion of the gratings. Images from Ref. [28]

More will be discussed in chap. 3.

Deep etching of gratings (F3) on the device layer of the SOI wafer requires careful process optimization in order to achieve uniform, rectangular, and defect-free profiles across large areas. Deep reactive ion etching (DRIE) is used to etch high-aspect ratio grating bars (>40:1). DRIE etches the deep trenches by repeating passivation and etching steps in a time-multiplexed manner, in which the polymer layer is partially removed only at the base while sidewalls remain protected during each cycle of passivation and etch steps [102]. SF_6 and CF_4 are primary gas species for etching, and CHF_3, C_4F_8, and Ar are used as polymerization gases. Etch and passivation steps are alternated until the desired etch depth is reached. The buried oxide layer beneath the device layer serves as an etch stop. Careful balancing of etch parameters such as flow rates, chamber pressure, and applied RF power are critical throughout the deep etch process in order to control etch speed, selectivity, duty cycle, grating profile, and roughness of scallops [71]. However, etching millions of 100-nm wide (or thinner) grating bars evenly throughout 4 to 6 μm-thick device layer over large area (30 x 31 mm^2) is not a trivial problem, and it may be impossible to

find proper values for parameters if the etch chamber is poorly designed. Types of defects in high aspect ratio etching as shown in the semiconductor industry include, but not limited to, tapering, twisting, bowing, and underetching (see Chapter 4 for more details). In this thesis, only the profile tilt problem is tackled in high aspect ratio of CAT gratings. The journey of process optimization requires development of precision metrology to control etch parameters and find the best etch chamber design (see Chapter 4).

1.6 CAT grating spectrometer

Once high-quality CAT gratings are fabricated, they need to be properly aligned and assembled to build a CAT grating spectrometer. In a low-photon space environment, it is desirable to build focusing mirror arrays and the grating spectrometer to be as large as possible to maximize collecting efficiency. The grating spectrometer stands downstream of the focusing mirror arrays to diffract x-rays to analyze their spectrum. A large portion of the focusing lens aperture needs to be covered by gratings to maximize collecting efficiency of diffracted orders. Thus, large number of gratings needs to be precisely aligned and assembled to populate the large aperture of an x-ray grating spectrometer [52]. Herein, optical layouts for CAT grating spectrometers proposed for the Lynx and Arcus missions are introduced. Figure 1-9 shows an optical layout for Lynx CAT grating spectrometer, made out of a focusing mirror array, CAT grating array, and detector array. The spectrometer is designed such that CAT gratings tile the surface of the Rowland torus [8]. Dimensions of the torus are chosen such that the gratings are positioned close to the focusing mirrors to allow a longer travelling length for better spectral resolving power. The torus is tilted by angle α, close to the blaze angle for a targeted x-ray wavelength, such that gratings lie tangential to the curved torus surface (since gratings are flat, most of the area on the gratings don't fit on the curved toroidal surface, contributing the smearing of the diffracted peaks) [39]. The detector arrays are positioned on the curved Rowland

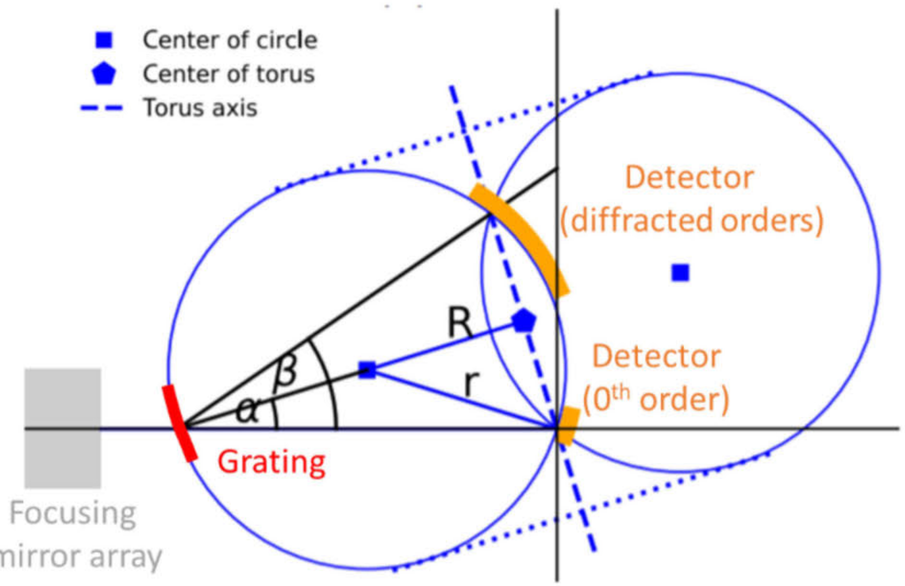

Figure 1-9: An optical layout of the CAT grating spectrometer for Lynx. An array of CAT gratings (red) are assembled on a tilted Rowland torus and sit downstream from a focusing mirror assembly (grey) to diffract x-rays. X-rays travel through a long focal length and land on a detector array (orange) which also are assembled on the torus. Image from Ref. [39].

toroidal focal surface. Multiple arrays of detectors are often required to image 0th order transmissions for high energy x-ray photons, and diffracted orders to enhance collecting efficiency for spectral analysis.

Figure 1-10 shows a schematic for the optical layout (a) and its structural hierarchy (b) proposed for the Arcus mission [49]. Research activities for metrology and structural design in this thesis were performed with the Arcus mission in mind. Arcus optics consists of four optical channels (two pairs of channels), each of which has 30-40 pairs of silicon pore optics (SPO) focusing optics and CAT grating windows (see Fig. 1-10b). Each CAT grating window has 4-6 co-aligned CAT gratings, making total of ∼190 CAT gratings per channel. In total, up to 700 CAT gratings are required to be assembled to build the CAT grating array. Four channels are placed in a configuration that takes advantage of the sub-aperturing effect (see Fig. 1-10a), covering a subset of full telescopic aperture. Sub-aperturing produces an anisotropic point spread function (PSF). Orienting the dispersion axis along the narrow direc-

tion of sub-apertured PSF helps to maximize spectral resolution [11]. Albeit it is not shown in the schematic, the CAT gratings are aligned with an angle, α, relative to the optical axis such that the gratings stand tangential to the tilted Rowland torus. 12 meters downstream of the optics stand two detector arrays on the Rowland toroidal focal surface, one receiving the 0th order transmitted image and the other receiving the blazed diffracted orders for spectral analysis (see Fig. 1-10a). Each pair of channels is oriented such that the dispersion axes from the channels fall within the same detector array (only 5 mm apart from each other in the cross-dispersion axis).

1.7 Grating coordinates

The terms yaw, pitch, and roll will be used throughout this paper. Figure 1-11 shows a local coordinate for the gratings used throughout this paper. Yaw angle is sometimes called blaze angle since x-rays are grazed below the critical angle at a given wavelength. Roll angle determines the dispersion axis of the gratings, where x is the dispersion axis, y the cross-dispersion axis, and z the optical axis.

1.8 Requirements for a CAT grating spectrometer

In order to achieve demanding requirements on resolution and collecting area for Arcus (or any other future missions), it is first required to produce large quantities ($>$1000) of high-quality CAT gratings. Development of metrology infrastructure to measure critical dimension (CD) variations of CAT grating is a key for quality control. Chapters 1 and 4 discusse metrologies developed for characterization of grating period and profile tilt, both of which have critical impact on spectrometer performance. Once the gratings are produced, it is required that the gratings be precisely aligned relative to one another, with the focusing mirror array, and the detector array in their ideal configurations to achieve promised performance. Understanding tolerances on each

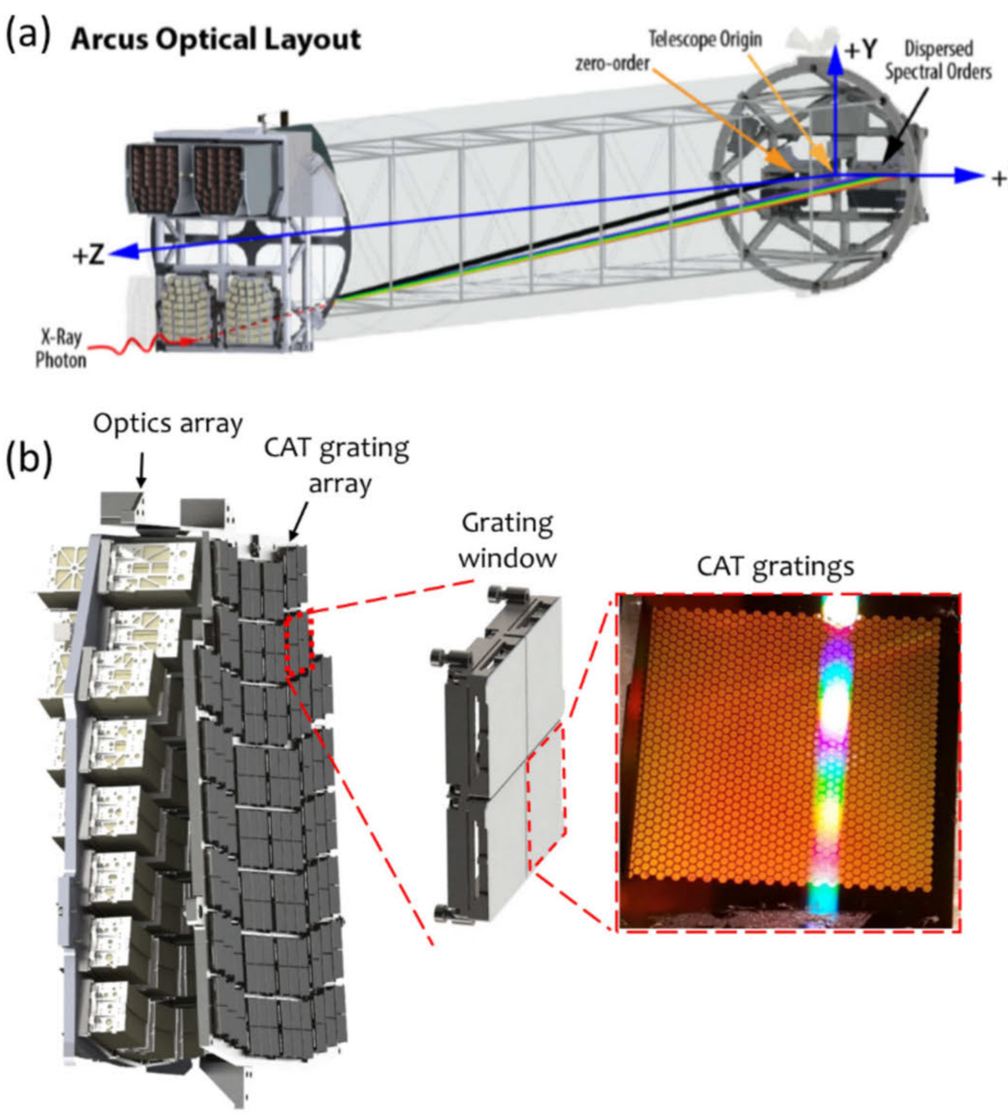

Figure 1-10: (a) 3D-rendered optical layout of the CAT grating spectrometer for Arcus. (b) Hierarchy of optical channels consisting of SPO focusing mirror arrays and CAT grating windows. Images from Ref. [49].

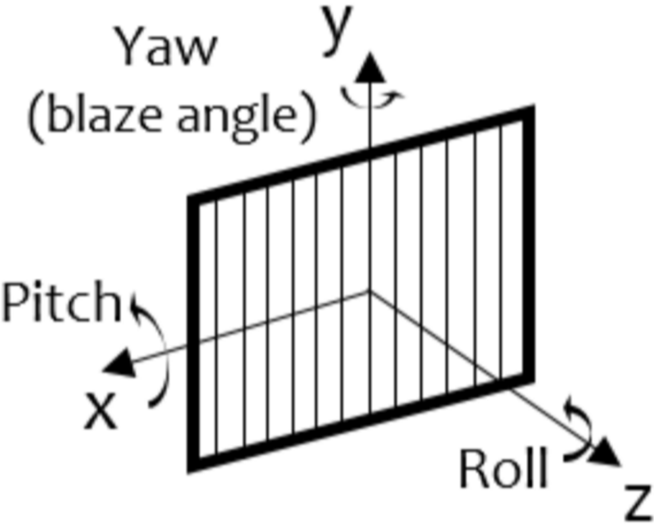

Figure 1-11: Local coordinates and terminology for rotations of CAT grating

degree of freedom for the three main components are critical to understand where labor and time need to be invested. Chapter 3 will discuss efforts towards fast and accurate alignment of CAT gratings. In this section I will identify critical dimensions and alignment parameters based on ray tracing simulation results. Lastly, structural requirements of the CAT gratings will be discussed; the grating as a thin optic can be fragile to certain loads, therefore, understanding mechanical aspects of CAT grating structure is critical for survival in a harsh space environment. Chapter 5 discusses a pioneering study performed to understand static stiffness of CAT gratings. Numeric values on each requirement shown in this section were derived from the concept study for the Arcus mission [40].

1.8.1 Ray tracing

For simple optical instruments, convolving object the with optical instrument PSF is sufficient to predict its performance. However, when it comes to building highly complex optical instruments, it is often necessary to perform a complex simulation to

understand tolerance for each degree of freedom of its sub-components [36, 40, 39]. In the field of x-ray telescope instrumentation, quantitative analysis for requirements on CD variations, alignments, and structural deformations are performed with ray tracing; a geometrical ray-tracing is well-suited for simulation of x-ray due to its short wavelength compared to the minimum feature size. It can track the influence of misalignments of sub-components, to predict the effect of jitter in CDs, and to analyze the effect of detector misplacement from the curved focal plane [37]. Ray-trace simulation of the grating spectrometer for Arcus was performed as follows: the photons are generated with an energy drawn from a specified spectrum. The focusing mirror array was modeled as an ideal mirror, with scattering angles drawn from a Gaussian distribution in and out of the plane of reflection. Input data on grating efficiency for different energies and blaze angles, transmission coefficient of filters, and quantum efficiency of the CCDs as a function of wavelength were used to model each optical sub-component. A random jitter to grating period, position or rotation of gratings were applied one by one (with other parameters fixed) to study effect of each degree of freedom.

1.8.2 Grating period

Photons diffracted from gratings with different pitches will diffract monochromatic x-ray to slightly different angles. As it travels towards a long telescopic focus ($\sim$12 m), small angle errors will be amplified over a long travelling distance and land photons in different positions on CCDs, smearing out the diffracted spots. Period variation has been a concern since the era of the Chandra x-ray telescope [20, 25] due to spectral resolving power being very sensitive to period error, and producing perfectly linear gratings across largea area had always been an issue [28, 14, 13, 61, 62, 70, 105] as described in the previous section. For Chandra, period variations were targeted to be better than 250 ppm, with metrology repeatability target of 50 ppm [20]. For future missions, requirement on resolving power $>$10000 for individual gratings imposes a

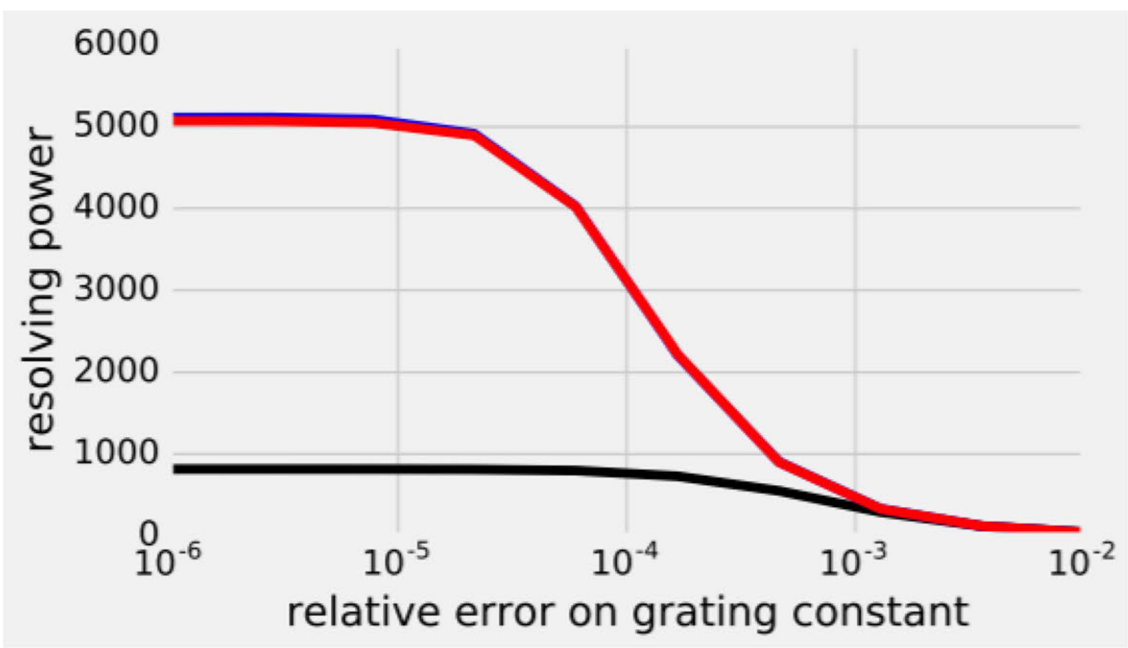

Figure 1-12: A ray-trace simulation result on degradation of resolving power with increased grating period variations for chosen wavelengths of interest (1 nm: Black, 2.5 nm: blue, 5 nm: red). Image from [40].

more stringent requirement of 0.01 nm rms (50 ppm) of period distortion over the active area of the grating. Fig. 1-12 shows ray tracing results for resolving power as random jitter is introduced to the grating period for different wavelengths (black: 1, blue: 2.5, red: 5.0 nm) [40]. The requirement was set to maintain resolving power better than 90% of ideal case. Metrology needs to consume no more than one-third of the required uncertainty, resulting in metrology uncertainty of 0.003 nm rms (15 ppm) for Arcus.

1.8.3 Alignment

As the CAT grating spectrometer composes of large numbers of gratings (>700 for Arcus), it is required to develop rapid, precise, and reliable alignment process for cost-effective assembly of grating hardware. Before diving deep into exploring alignment requirements, it is worthwhile to mention speed requirements let alone the alignment and reliability requirements, as slow grating alignment processes would result in high

labor costs and plenty of room for mistakes which may end up killing the mission. Considering a typical timeline imposed for grating alignment for previous missions, alignment process of a single grating should take less than 1 hr on average to finish on time. Alignment requirements are studied by investigating PSF of diffracted spots using ray tracing while varying each degree of freedom for the grating. Relative displacements or misalignments between individual gratings will land photons on different positions on detectors (or off of detector), reducing resolving power and collecting efficiency. A translation of a grating along the optical axis (z) is almost equivalent to having 'defocus' error (or placing gratings out of the Rowland torus) on diffracted orders. Shifting gratings along tangential directions of Rowland torus will have little effect on resolving power and effective area unless gratings or other optical components are shadowed by the supporting structures. Misalignments between gratings are more sensitive than displacements. Especially, roll angle rotates the diffracted spots around the telescopic focus; as distance between diffracted spot and telescopic focus gets higher for high orders, small roll error may cause diffracted orders to fall out of the detector (which reduces collecting power) or smear the line spread functions (which degrades resolution). Blaze error is less strict compared to roll error, however, it may reduce effective area when it leads to grazing angle exceeding critical angle, or it reduces resolving power if efficiency gets shifted to lower orders. Fig. 1-13 summarizes resolving power and effective area as a function of misalignments [39]. At current phase of Arcus, it is too early to decide final alignment requirements as instrument-level error budget may be updated in the future. Therefore, the alignment requirements were set using the tightest requirements reported so far [35]. Table 1.8.3 summarizes the requirements in 6 degrees of freedom.

1.8.4 Structural considerations

Though it often gets less attention than CD variations or alignment problems in the optoelectronics community, careful consideration on deformation of optical compo-

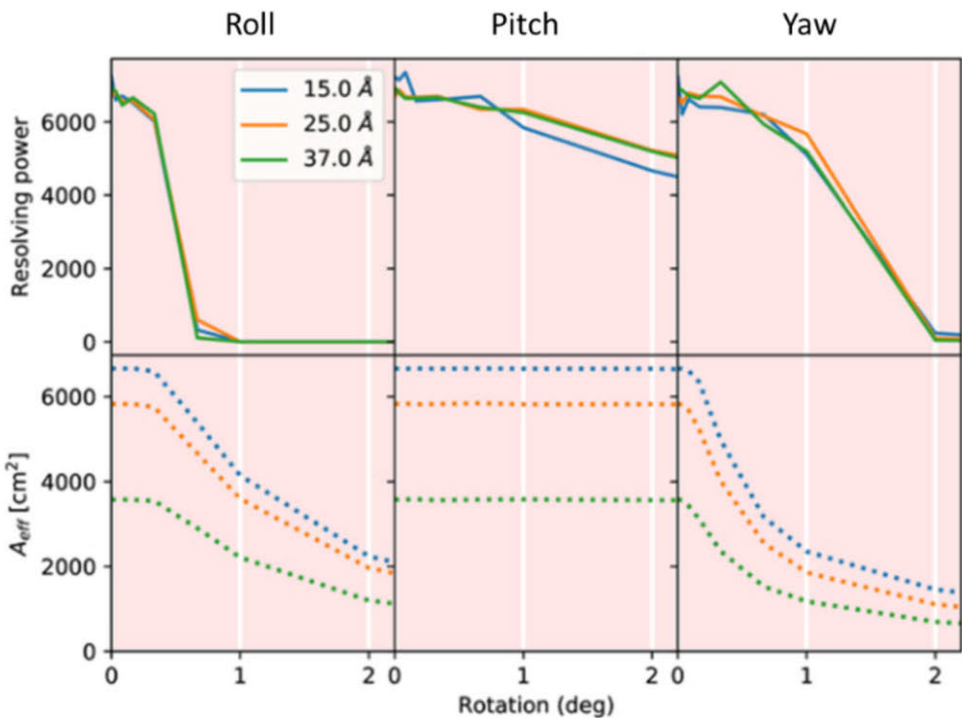

Figure 1-13: Degradation of resolving power (top) and effective area (bottom) with changing jitter in grating rotations (roll, pitch, and yaw from left to right) for chosen wavelengths (blue: 1.5 nm, orange 2.5 nm, green: 3.7 nm). Image from Ref. [38]

Table 1.1: Alignment tolerances for CAT gratings.

Degrees of freedom	**tolerance**
Translation along z	0.5 mm
Translation along x and y	5 mm
Rotation about x	6 degree
Rotation about y	6 arcmin
Rotation about z	6 arcmin

nents upon external loads are important for some applications as those do imply deleterious (or even worse) effects on optical performance. Especially for CAT gratings, since 1) the device is to be launched and operate in harsh space environment for several years and 2) it is inherently a flimsy structure with 4-um thick, 1-mm wide grating membrane strengthened by hierarchies of structural supports, it must be studied as a 'structure' from varieties of point of views (static loading, dynamics, shock, thermal, etc.). General Environmental Verification Standards [72] published by NASA Goddard provides a good guidance at the early stage of mission development when no specific launch loads (or vehicles) are solid yet. The manual suggests either finite element (FE) analysis or structural testing (or both) must be performed under expected structural loads, acoustic vibrations, random vibrations, and mechanical shock at every part, sub-system, and assembly level. Appropriate margins must be added to the expected loads for qualification. Probability levels and confidence intervals must be considered when testing probabilistic quantities such as flight loads and dynamic quantities (vibrations, etc.) [72]. Over the course of development, CAT gratings successfully passed environmental tests for launch vibrations and thermal cycling under vacuum without performance degradation [50, 49], However, its behavior under static loads (either from change of temperature or externally applied forces) has been under-studied. There are many possibilities that CAT gratings would suffer from static deformation; when bonding the gratings to the metallic frame, during epoxy curing, perturbation of temperature (either homogeneous or with gradients) in space, etc. A decade of process development has enabled manufacturing of high-quality CAT gratings with negligibly small number of defects, however, some types of static deformation were observed over the last decade as we developed alignment process, tried different recipes for research purposes, or processes were not fully controlled as CAT grating fabrication relies on 'beaker and tweezer' methods in a university laboratory setting. Figure 1-14 shows representative deformation (or failure) modes observed in some of the CAT gratings.

It is suspected that out-of-plane buckling visible in Fig. 1-14a occured from

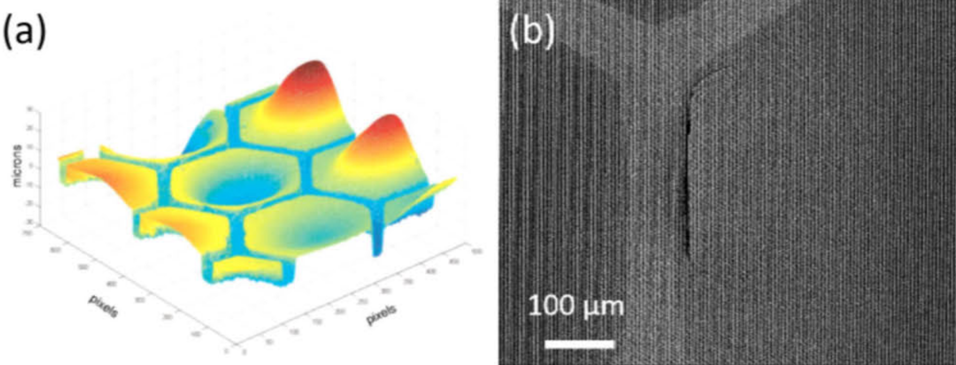

Figure 1-14: CAT grating imperfection observed during extensive testings. (a) Out-of-plane buckling of CAT grating membranes. Image from [48]. (b) An scanning electron microscope image of CAT grating membrane ripped off at the L2-grating membrane interface.

partial delamination of the device from the hexagonal mesh since the buried oxide (BOX) layer between L1 and L2 meshes was partially removed due to poor process control [48] (we "literally" rely on a beaker and tweezer for BOX etching). On the other hand, out-of-plane buckling may happen when the loads applied from bonding points on the L3 aperture transmits through hexagonal supporting structures (L2), causing local deformation of the L2 "beams." Such scenario may happen when the grating and its bonded frame experience uniform temperature change; CTE mismatch between silicon grating and titanium frame applies external load to the CAT grating supporting structure, and eventually to thin grating membranes (will be described in Chapter 5). The phenomena as described previously is simply a potential cause of the out-of-buckling based on thought experiments, and hasn't been confirmed yet experimentally. At above the yield strain, local deformations can also lead to ruptures (Fig. 1-14b) at the boundary of the thin "grating membrane." Though the described types of deformation are of great interest from a structural mechanics point of view, it is impracticable to perform extensive structural testings since the quantity of CAT grating is limited, leaving FE modelling the only option. However, modelling CAT gratings in FE software is computationally too expensive as it has myriad of hierarchical supporting structures. As the reader might have noticed, study of mechanical aspects of CAT grating stands at the early stage due to limit on both experimen-

tal and computational resources. Therefore, it is premature to specify requirements on mechanical properties of CAT gratings. A pioneering work on understanding mechanical properties of CAT gratings under static loadings will be discussed in Chapter 5.

1.9 Thesis structure

This thesis contributes to metrology and mechanical aspect of CAT gratings with the overarching goal of building a CAT grating spectrometer to satisfy challenging resolution and optical area requirements for future x-ray telescope missions.

Chapter 2 first reviews the metrology, scanning laser reflection tool (SLRT), developed for period measurements of HETG. Its ability to characterize grating period and roll variations on gratings patterned with interferometeric lithography will be reported.

Chapter 3 introduces developed metrologies and alignment procedures for fast and accurate alignment of CAT gratings. The story on two series of tests will be described, each with alignment goal, time spent, hardware design, metrology, and results. For each test, four CAT gratings were aligned to satisfy Arcus requirements. Inspection results along the alignment process will be discussed in detail. The alignment step shows a clear path towards parallelization for alignment of CAT gratings at a much larger scale.

Chapter 4 reports a metrology technique to characterize profile tilt of nanoscale gratings via x-ray diffraction. Since CAT grating fabrication shares similar issues in high aspect ratio etching as confronted in the semiconductor industry, several metrologies (including small-angle x-ray scattering) being used in industry are introduced. Physical models of CAT gratings are built based on scalar diffraction theory and rigorous coupled wave analysis (RCWA) to find the grating bar angle as we perform

small-angle x-ray scattering. Since x rays alone cannot characterize the bar-normal angle due to their low reflectivity at near-normal incidence, the surface normal is measured independently by reflecting a laser beam off the grating surface. A special rigid grating mount with slit reference axis are to be introduced to reference the two separate measurements.

Chapter 5 will present pioneering work to study mechanical properties of CAT gratings under static loads. It first reformulates complex CAT grating structural problems by neglecting unimportant structures (those contributing little to the mechanical behavior of the CAT gratings). Then it builds simplified models (both analytical and numerical) to understand the stiffness of hexagonal level-2 structure support. In-plane and out-of-plane stiffness of CAT grating were analyzed using both analytical and finite element methods. Since it is desirable to maximize open area fraction at a given stiffness, stiffness for other 2d periodic lattice topologies (triangle and square) were studied to optimize design of L2 supporting structure. Multiple simulations were performed to better simulate a real-world phenomena; modelling constituent "beams" of the periodic lattices with Euler-Bernoulli and Timoshenko beam, treating nodal junction as a rigid body, etc. The study presented in this chapter would later be a useful tool when people have more clear understanding of stiffness requirements or potential static loadings in the later phase of mission development.

Chapter 2

Grating period metrology

The ability to characterize spatial phase progression of gratings made possible the precision manufacturing of optical encoders, x-ray zone plates, holographic bragg reflector, and gratings for space-based x-ray spectroscopy [85, 51]. For optical encoders and x-ray gratings in particular which require large-area gratings, maintaining spatial phase coherence of the grating pitch over a large area is a key for the success of the product. For our application towards space x-ray grating spectrometers, it is required that period distribution of $>$1000 gratings falls within a 0.01 nm rms window over an aperture size of $>$1 m^2 (see section 1.8.2 in chapter 1). Thus, metrology to characterize period variations within a single grating and between multiple gratings is required for the mission success [89].

Traditionally, these components were patterned with interference lithography, however, the spatial phase of the grating lines exhibited non-linear phase progression due to interference of non-planar wavefronts. Phase distortion in traditional interference lithography was measured by interfering reflected beam and back-diffracted beam in a Littrow configuration to form Moiré pattern. However, Moiré-based characterization requires a precise mathematical model for grating period phase progression and a replicated reference grating for comparison [28], therefore cannot be applied to

measurements of gratings with an unknown mathematical model. Scanning beam interference lithography (SBIL) was built to overcome this problem by stitching grating lines - whether it being linear, curved, or chirped [14, 13, 61, 62, 70, 105]. As SBIL needs in situ measurement of 'image gratings', the interference fringes of two intersecting waves, several methods were employed using zone-plate [61] and beam-splitter [14] to successfully characterize gratings with high accuracy (down to uncertainty of 1 ppm) for real-time measurement of period distortion. Image metrologies are not suitable for fast characterization of large-area gratings since it characterizes fringes in image gratings, not a real grating - it is desirable to characterize grating period patterned on the substrate as grating period can be distorted locally when the substrate exhibits thickness variations or local warping. Additionally, instrumentation of zone-plate or beam-splitter based metrology would require expensive high-precision translation stages and thermal control unit to minimize air turbulence. In the semiconductor industry, CD-SEMs are often used to characterize periodicity or other critical dimensions (CDs) of nanostructures [73], however, the number of samples (or size of area) examined is limited due to its narrow field of view and slow speed. Moreover, there is a concern on SEM in that the scale is traceable to each SEM instrument, which depends on design of individual instrument - SI units for each SEM may be different as they experience different degrees of vibrations, drift, and thermal expansion along the course of measurements[15]. In this chapter, I propose a metrology concept that is straight-forward, low-cost and robust, featuring high sensitivity to tiny periodic variations. It is similar to a grating period metrology used in the development for the Chandra x-ray telescope [20], with modifications on its optical configuration to achieve improved accuracy. Section 2.1 introduces the working principle of the proposed metrology. Section 2.2 shows the constructed metrology tool in detail. Section 2.3 introduces image and fabrication process for calibration sample prepared with interference lithography. Section 2.4 shows calibration results for period measurement capability. Section 2.5 discusses measured period and roll variation maps from the calibration sample. Section 2.6 discusses limitations of the setup with suggestion of a better method.

2.1 Working principle

The proposed grating period metrology is based on simple reflection and diffraction of a UV beam [20]. Fig. 2-1 illustrates the working principle of the proposed metrology. As our 200-nm period gratings are illuminated with a UV laser (325 nm in wavelength) with non-zero incident angle (50-60 deg), it returns reflected (0th order) and back-diffracted (-1st order) beams. A normal incidence beam was also added to characterize local yaw and pitch of the grating more precisely, since the angled incidence beam is sensitive to z displacement of the grating. If there are local variations in grating period, surface tip/tilt, or grating line orientation at the illumination point, the return beams will change their propagating directions. If there are variations on surface height, the return beams shift along y in detector coordinates. With sufficient traveling length, slight changes of propagation directions are amplified to move spots on respective position sensitive detectors. Recording changes of beam spots position as the grating is scanned renders information on surface height variations, grating period variations, yaw, pitch, and roll angle variations with an appropriate mathematical model. For example, the back-diffracted beam spot will move along the dispersion direction only if grating period changes. It would move in the cross-dispersion axis when the grating rolls. In the real world, many parameters change simultaneously as the gratings are scanned, and motions of the beams are coupled with multiple parameters. For instance, movement of the back-diffracted spot along x (detector coordinate) is coupled with yaw, surface height change, and period variations; y-movement of back-diffracted spot is coupled with pitch and roll; x-movement of angled-reflected beam coupled with yaw and surface height change. Assuming small variations, the described geometry is represented by the following system of equations to first order:

$$\begin{bmatrix} dX_n \\ dY_n \\ dX_r \\ dY_r \\ dX_d \\ dY_d \end{bmatrix} = \Big[M \Big] \begin{bmatrix} dYaw \\ dPitch \\ dRoll \\ dp \\ dz \end{bmatrix} \tag{2.1}$$

where

$$[M] = \begin{bmatrix} 2R_n & 0 & 0 & 0 & 0 \\ 0 & -2R_n & 0 & 0 & 0 \\ 2R_r & 0 & 0 & 0 & -2sin\theta_i \\ 0 & -2R_r cos\theta_i & 0 & 0 & 0 \\ R_d \frac{cos\theta_d + cos\theta_i}{cos\theta_d} & 0 & 0 & \frac{R_d}{p}\frac{sin\theta_d + sin\theta_i}{cos\theta_d} & -\frac{sin(\theta_i - \theta_d)}{cos\theta_i} \\ 0 & -R_d(cos\theta_i + cos\theta_d) & -R_d(sin\theta_i + sin\theta_d) & 0 & 0 \end{bmatrix},$$

and $dX_n, dY_n, dX_r, dY_r, dX_d, dY_d$ indicate movements of the beams on the screens in x & y axes with n, r, and d referring to normal-reflected, angled-reflected, and diffracted beams, R_n, R_r, R_d the traveling length of the return beams, θ_i, θ_d the angle of incident beam and diffracted beam, $dYaw, dPitch, dRoll$ small variations of grating angles, and dp, dz slight variations of grating period and surface height. In this chapter, since period variations are of interest in this chapter, I limit my focus only on rows 1, 3, and 5 of the equation. As readers might already have noticed, it can be easily concluded that the proposed metrology can not only measure the grating period, but also rotations of the grating lines for precision alignment [89]. An ability to align grating roll angle will be presented in chapter 3 using rows 1, 2, 6 of the equation (see Chap. 3).

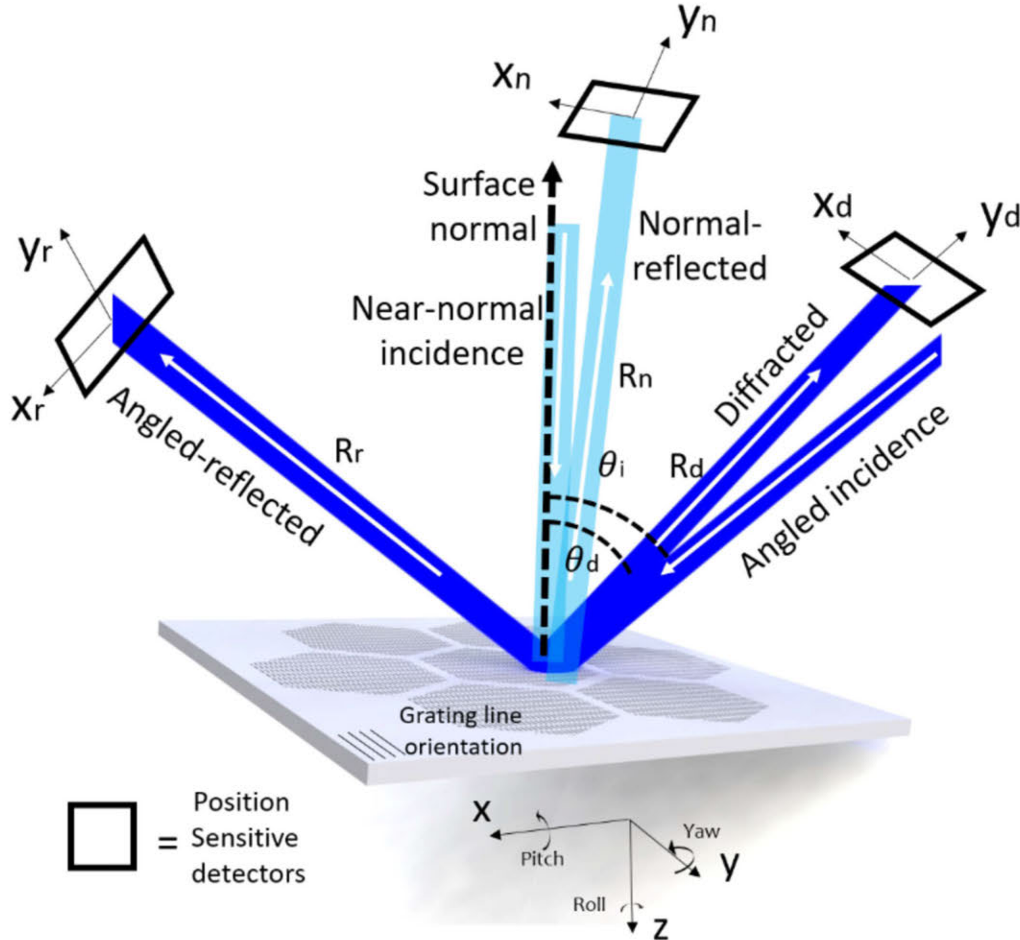

Figure 2-1: A schematic illustrating the working principle of the proposed metrology. Both angled-incidence and normal-incidence beams are illuminated in the same position on the grating as the gratings are scanned. Change of position of the returned beams are recorded with position sensitive detectors to deduce variations of grating parameters.

2.2 Metrology tool construction

Figure 2-2 shows a schematic and photograph of the proposed metrology tool, named the scanning laser reflection tool (SLRT). It has five main components: a 325 nm HeCd laser source, a high-precision XY stage, a 3-axis rotation stage, a grating mount, and three position-sensitive detectors (PSDs). The beam from the UV laser is split into two beams, which are reflected by mirrors (or beam splitters) to be incident upon the same location on the grating with different incident angles. 10× telescopes reduce the laser beam diameter to ∼150 um on the grating surface for both angled and normal incidence beams. The angled beam was partially masked so that the projected beam forms a similar (approximately circular) shape as the normal-incidence beam on the grating. PSDs find the center of gravity of the beams with sampling frequency of 1000 Hz averaged for 2 seconds. A 3-axis rotation stage is used to reduce grating tilt (yaw, pitch) about the axes of the raster scan. Imaging optics capture light scattered from the grating surface to locate the position of incident beams on the grating. The inset in the upper right corner in figure 2-2b shows two incident beams located on the grating surface. Table 2.2 summarizes the parameters used for SLRT. Calibration methods for the parameters are explained in detail in Ref. [89].

Table 2.1: Parameters used for SLRT

Parameters	**Value**
θ_i	57 degrees
θ_d	51.8 degrees
R_r	740 mm
R_n	620 mm
R_d	520 mm

2.3 Sample preparation

A reflection grating with nominal pitch of 200 nm was patterned using a Mach-Zehnder interferometer [89]. The interferometer and substrate holder were configured

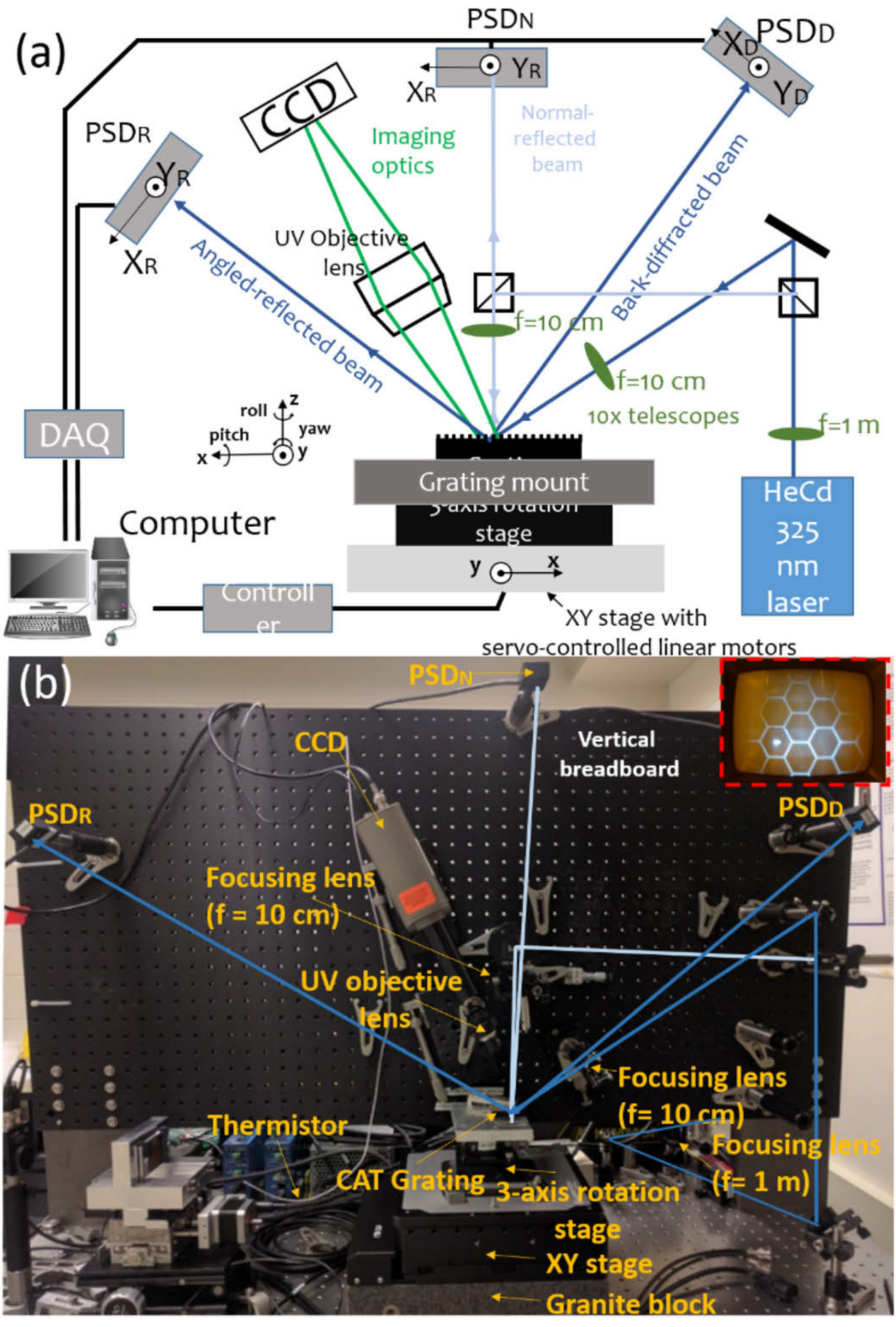

Figure 2-2: (a) A schematic of SLRT. Equation 2.1 follows a sign defined in local coordinates in the lower left corner. (b) A photograph of the SLRT. Inset in the upper right corner shows a photograph of two incident beams located on the same position of the grating surface.

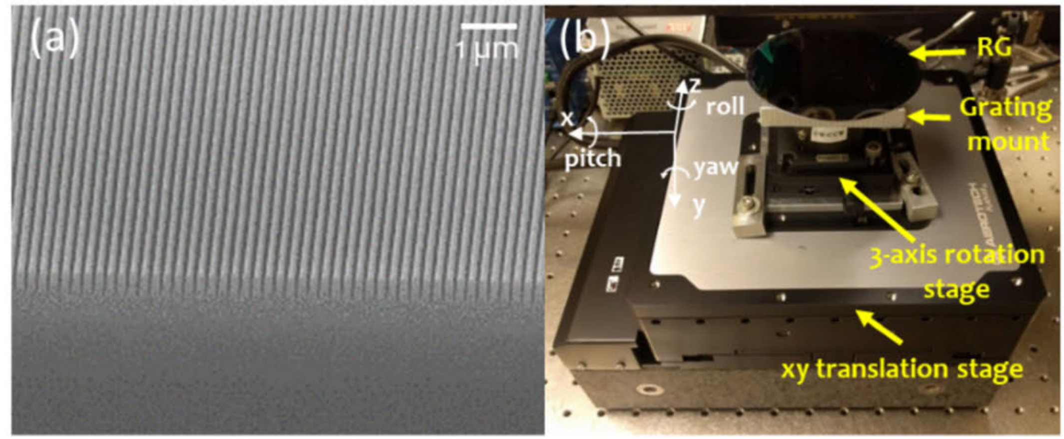

Figure 2-3: (a) Inclined SEM image of cleaved 200-nm period reflection grating. (b) Photograph showing reflection grating mounted on rotation and translation stages for scanning.

to have a=1.09 m, c=0.596 m (see Fig. 1-8c in Chapter 1) to generate interference fringes at the center of 100-mm silicon wafer. After patterning the grating lines, it was etched approximately 500 nm via reactive-ion etching. The sample was then cleaned of all organic materials via a mixture of sulfuric acid and hydrogen peroxide followed by a heated mixture of diluted peroxide and ammonium hydroxide. Fig. 2-3 shows a SEM image of a cleaved reflection grating. The fabricated reflection grating was bonded on the stage with three contact points, and a drop of acetone was used to release it after measurement.

2.4 System calibration

Detector position measurement noise was measured to be less than ± 0.58 μm rms. Path lengths for the three beams (R_r, R_n, R_d), and angles of incident and back-diffracted angles (θ_i,θ_d), were measured using a tape measure and fluorescent card. Three beams were aligned to be in the same dispersion plane. The measurement errors on path lengths and angles would have an effect on accuracy, and not on repeatability of the period measurement; for our application, since only the distribution in grating period is of interest, not on its mean value, small errors on those measurements are not

an issue. In the future, a specially fabricated reference grating with well-calibrated grating pitch can be placed next to the grating-to-be-scanned permanently if there are requirements on accuracy or variations between different gratings. Unlike image metrologies used for SBIL where either the beam splitter or the zone plate needs to translate with high precision, SLRT is robust against temporal variations of variables; since beam path lengths are very long, it is insensitive to temporal variations of the beam path from thermal expansion of the system, and wobbling motion of the stage can easily be corrected by recording change of beam spot positions of multiple beams (normal-reflected, angled-reflected, and back-diffracted beam) using eqn. 2.1. As only the positions for the centroids of the beam spots are important, not on the image, air turbulence is not a big concern, which is different from image metrologies. After calibrating the system configuration, overall period measurement repeatability was measured by raster scanning the center area (50 mm $\times$ 60 mm, 1 mm interval) of the single test reflection grating multiple times. The period repeatability is estimated to be 20 ppm (0.004 nm) rms which is sufficient to resolve grating period variation requirements for Arcus and Lynx. The derived period repeatability includes noise sources from contamination of the surface (which scatters the return beams) and repeatable mounting (the gratings were removed and remounted multiple times to simulate actual period measurements to be performed during mission development).

2.5 Results

Fig 2-4a shows measured (color) and expected (mesh) period variations of the test grating. A theoretical plot (mesh) for period variation was calculated using eqn. 1 in ref. [28] with parameters a, b, and c as described in the sample preparation section. The plots were shifted vertically for comparison. It is obvious from the results that the measured and expected period variations show good agreement with each other. Fig. 2-4b shows measured (noisy) and theoretical (smooth) contour maps for period variations of the test reflection grating. 'X' is deduced to be a center for

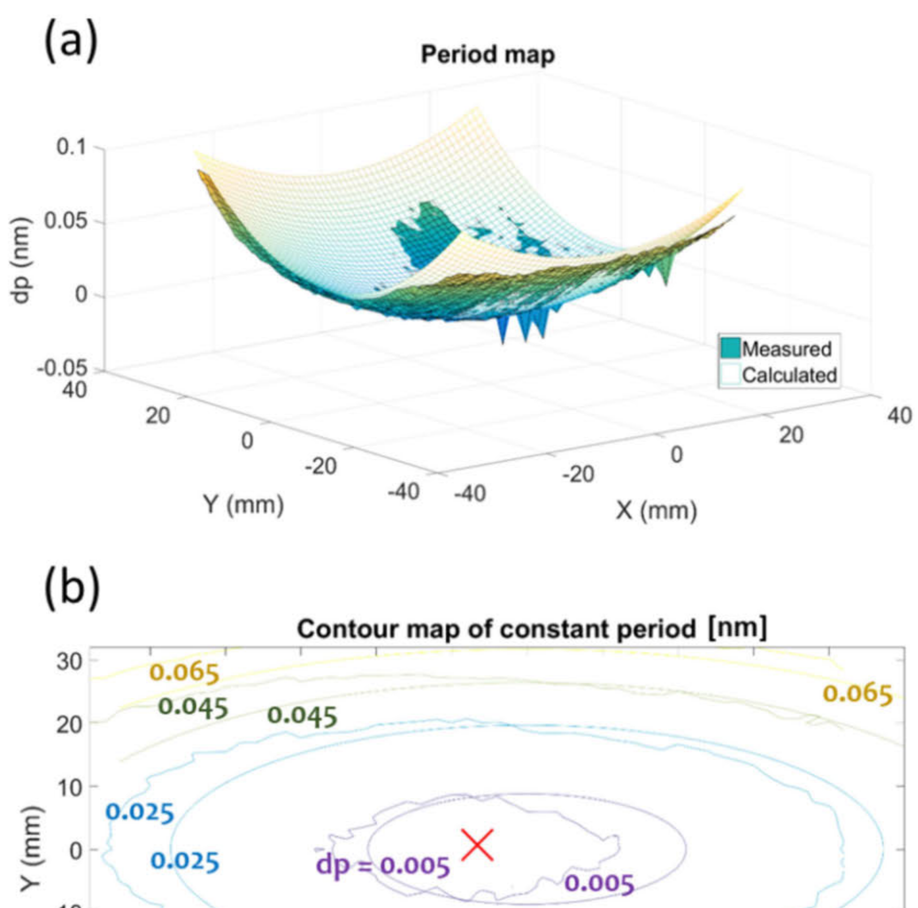

Figure 2-4: Results on period measurement of reflection grating. (a) Period map showing both measured (color) and calculated (mesh) period variations. (b) Contour map for grating period variations from the center. (0,0) indicates wafer center. 'X' is the deduced center of interference fringes.

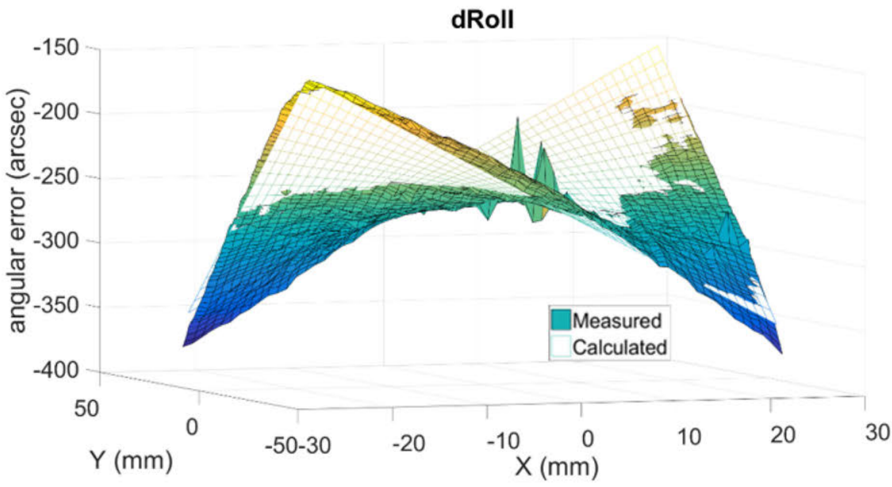

Figure 2-5: Measured roll angle variations from reflection grating. (a) Roll variation map showing both measured (color) and calculated (mesh) roll angle variations.

the interference fringes when illuminated with interference lithography. It is shown to be displaced by (-4,0) mm relative to the wafer center (0,0). This characterization helps to align interference fringes to the center of the substrate, minimizing period distortion in the region of interest (a rectangular area at the center of the wafer is used to fabricate CAT gratings); it is desirable to use center fringes for gratings since the period error increases more rapidly as distance from the center increases.

Figure 2-5 shows measured (color) and expected (mesh) roll variations for the test reflection grating. A theoretical roll angle variation was calculated using eqn. 2 from ref. [28]. Measured and calculated roll variations show good agreement, exhibiting hyperbolic distortion as expected. The PV of roll angle is ~200 arcsec (3 arcmin) for ~30 x 30 mm gratings, which is well within the tolerance budget (see chapter 1). Good agreement between measured and expected roll angle variations indicates the feasibility of the metrology for roll alignment, which will be discussed in detail in chapter 3.

2.6 Challenges in period measurement of CAT gratings

While the developed metrology successfully characterized period and roll variations of the test reflection grating with high accuracy, period measurement of CAT gratings adds another challenge due to an interplay between its structural complexity and the way position sensitive detectors (PSD) measures position of beam spots (similar issues will be discussed again in Chap. 3). First, different 'reflectivities' from hexagonal L2 support and grating membrane generate biased position signals since the PSD measures position by finding the "center of mass" of the beam - requiring that the beam footprint to be 'within' the grating hexagonal membranes without spilling over the hexagonal support to avoid position bias. Second, as the 1-mm period hexagonal CAT grating membrane exhibits slight out-of-plane buckling (typically 200 nm - 1000 nm in peak-to-valley); out-of-plane buckling induces return beams to form non-Gaussian profiles at the image plane of the detector, leading to biased position measurement of the beam spots. Fig. 2-6 shows typical shapes of the beam spots as captured with an image sensor. Non-symmetric beam profiles are detrimental to the accuracy of period measurement as it biases position signal. Lastly, fluctuations of surface height (z-displacement) due to local buckling of 1-mm period hexagonal grating membrane adds to errors when deriving period variations from eqn. 2.1; since measurement of grating period is coupled with yaw and surface height change (see eqn. 2.1), errors from measurements of other parameters accumulate when deducing period.

An easy way to avoid aforementioned issues is to measure grating period with a transmitted beam, as those issues arise due to 'reflected' beams being sensitive to tiny deformations of grating membranes. As the transmitted beam is much less sensitive to surface profile (yaw, pitch, and surface height variations), measurement of period variations and roll angle would be more straight-forward once the transmitted beams exhibit sufficient signal-to-noise (S/N) ratio. Fig. 2-7 shows simple concept for measurement of period variations of the gratings.

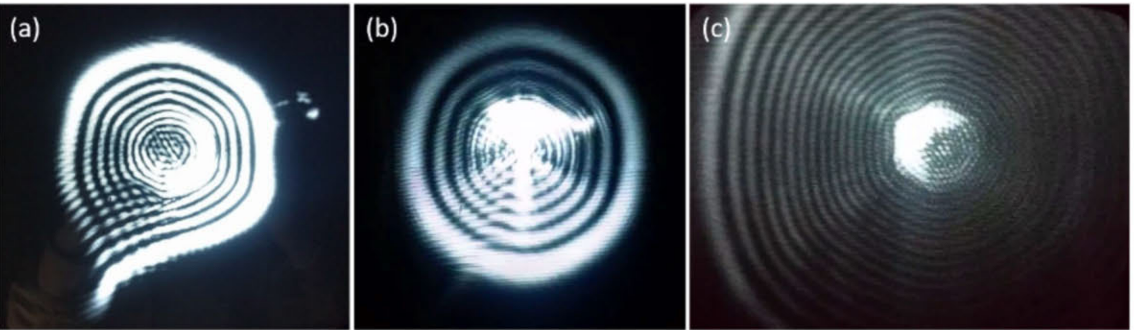

Figure 2-6: Representative images as observed from specularly reflected and back-diffracted return beams (a) non-symmetric shape, (b) fringes with non-symmetric beam intensity, (c) fringes too large to be captured by active detector area.

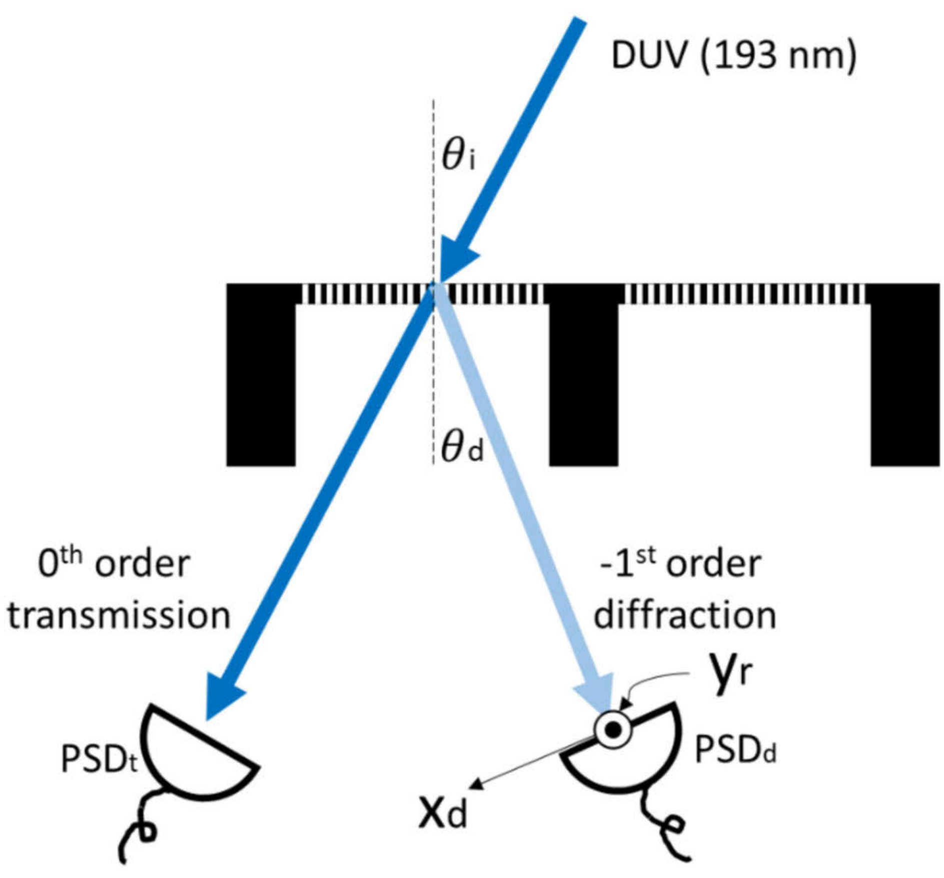

Figure 2-7: A concept for measurement of period variations and roll angles in transmission geometry.

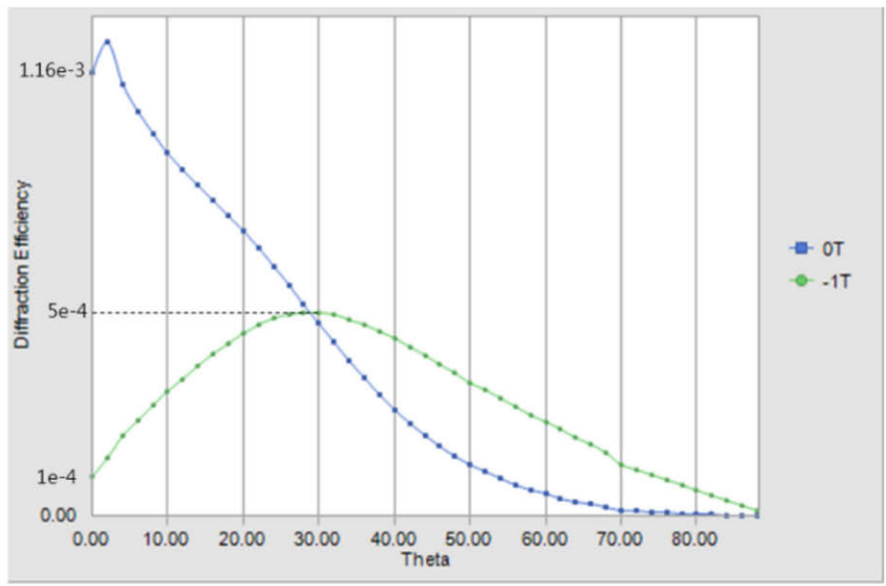

Figure 2-8: Simulated diffraction efficiencies for 0th transmission and -1st diffracted order (193 nm, p-polarized) for 200-nm period, 6-μm deep silicon gratings.

It is similar to the proposed metrology concept in Fig. 2-1 except that it uses transmitted diffracted orders; the PSD measures changes of beam positions along x & y to characterize grating period and angular variations. While only the in-plane diffracted order is shown in the schematic, adding oblique incident beam and observing conical diffracted order would help derive period variations from other parameters (yaw, pitch, and surface height change). In order that a beam transmits and diffracts through the 200-nm pitch gratings with sufficient signal, it is desirable to use a deep UV (DUV, wavelength shorter than 200 nm) to have sufficient transmission rate. While most of the DUV lines (i.e., ionizing radiations) are strongly absorbed by the atmosphere, the ArF characteristic line (193 nm) can propagate through a nitrogen environment (though it is strongly absorbed by oxygen), enabling measurements in non-vacuum environments with appropriate safety measures. Fig. 2-8 shows modeled 0th order transmission and -1st order diffraction efficiency (193 nm, E field parallel to the grating bar; p-polarized) for 6-μm thick gratings with varying incidence angle.

It is shown that -1st order would propagate at 27.7 deg from normal with 0.05% of diffraction efficiency at 30 deg incidence angle. Assuming photodetector sensitivity of 60 mA/W at 193 nm and S/N ratio of 5, 2 mW power of VUV needs to illuminate

the grating for reliable measurement, which would lead to only 1-5 deg C increase in peak temperature at the center of the circular beam spot (half the grating thickness with isotropic thermal conduction assumed). If diffracted beams from both in-plane geometry and conical diffraction geometry can be used, it is possible to characterize CAT grating period variations without suffering from L2-induced complications in theory. However, it requires large investments (ArF source, Nitrogen chamber, position sensitive detector for ArF line) with little gain, therefore is out of scope for this thesis.

2.7 Conclusion

New metrology to characterize period variations of gratings was developed including concept development, construction, characterization, and application to flight grating prototypes. The developed metrology successfully characterized CAT grating period variations patterned with traditional interference lithography, which is instrumental for development of CAT grating spectrometers for the Arcus and Lynx missions. The period variations were observed to be $<$0.018 nm (90 ppm; 1 sigma) for 30 x 30 cm size gratings (corresponds to resolving power of $>$10000), which is sufficient for Arcus and Lynx missions. A period repeatability of 0.004 nm rms (20 ppm rms) was achieved for the developed instrument which is small enough to resolve IL-patterned grating period variations. Considering that the derived period repeatability includes noise sources from contamination of the surface and yet-to-be non-repeatable mounting, more improved precision is expected once more serious engineering efforts are to be invested in the future. Complications from buckled hexagonal grating membranes are expected to be managed by transmitted diffracted orders, however, it is not of a impending concern since there had been no signs of degradation on grating period post lithographic processing (from fabrication all the way to assembly) as observed from x-ray resolving power measurements.

Chapter 3

Grating alignment

This chapter discusses results of tests (test 1 and test 2) performed in order to demonstrate our ability to align gratings to satisfy mission requirements [27, 31]. Demonstrating an ability to align several CAT gratings to meet tolerance in a reasonable amount of time is critical to build a CAT grating spectrometer. The metrologies designed for alignment in this chapter share the same working principle as the one described in chapter 2, with additional automated angular rotation capability and a bonding station designed for alignment and bonding in a single setup. Four CAT gratings were aligned for each test to form a Grating Assembly (GA). Roll angle was the primary target for alignment for both tests. Alignment requirements for CAT gratings are summarized in chapter 1. The work in this chapter was performed in collaboration with the Harvard-Smithsonian Center for Astrophysics and the MIT Polarimetry beamline facility.

This chapter is divided into two sub-chapters, each of which introduces objectives for the test, hardware, metrology, alignment procedure, x-ray verification test, and alignment results. For both tests, inspections of quantities such as angular drift or grating distortions were performed during critical steps to fully understand the effect of each step on the GA. The alignment results were confirmed with x-ray (reference)

measurements to verify the feasibility of the developed metrology, hardware, and alignment protocols. Time spent to align four CAT gratings was recorded for each test to assess scalability of each test for high volume alignment (>1000) of CAT gratings in a limited time duration of mission schedule.

In test 1, CAT gratings were aligned to satisfy Arcus alignment requirements using simple hardware and the SLRT. However, a discrepancy was observed for measured roll angles between SLRT and x-ray methods, but within the alignment budget. In test 2, refinements were made in all aspects of the test - including alignment protocol, metrology, hardware, and x-ray verification test - to tackle issues studied in test 1. More details will be articulated in sub-chapters for each test.

3.1 Prior art for grating alignment

During the Chandra era, the partial polarization property of fine-pitched transmission gratings was used to align high energy transmission gratings (HETGs)[6]. Fig. 3-1 shows a schematic of the metrology tool used to align multiple grating facets for Chandra. A photoelastic modulator (PEM) and lock-in amplifier were used to "detect a signal proportional to the sine of twice the angle between the grating lines and the axis of the PEM" for alignment [6]. However, this alignment technique could be of limited use for CAT gratings due to structural differences; for example, parasitic partial polarization from the integrated cross-support mesh (L1) and stress birefringence in the buried oxide layer have the potential to degrade the accuracy of this method. In this chapter, new metrology concepts are suggested to measure roll angles via recording change of propagation directions for specularly reflected and diffracted beams. It is potentially better suited for CAT gratings as it is assessed to be relatively free of complications from the L1 support mesh and internal stress in the BOX layer.

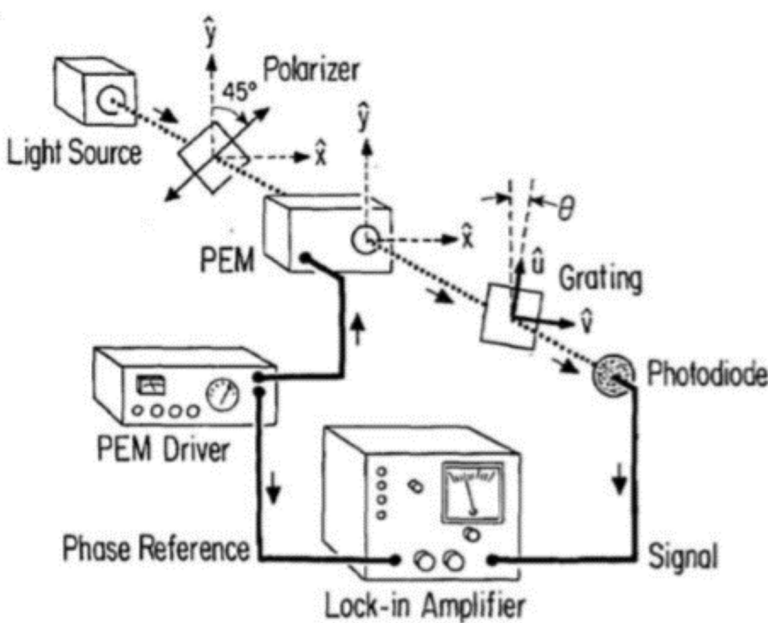

Figure 3-1: A schematic for UV-based grating alignment setup using partial polarization property of HETGs. Image from Ref. [6].

3.2 Demonstration: first test

The objective of the first test was simple: to align four gratings to satisfy the challenging mission alignment requirements under feedback from a metrology tool. CAT gratings used for test 1 are labeled X10, X13, X14, and X15. We designed four grating holders, two windows, and one grating assembly frame. Four CAT gratings were bonded to four grating holders to form four grating facets, two pairs of grating facets were aligned on a window, and two windows were aligned on the window alignment frame. No active effort was made to align yaw and pitch; those were aligned mechanically on the flat surface of the window as the gratings are fixed after roll alignment. The roll angles measured with the proposed metrology were verified with x-rays at the PANTER x-ray testing facility in Germany. The same SLRT was used for grating metrology (see 2-2 in Chap. 2) for test 1. Grating roll angle is derived by using rows 1,2,6 of the eqn. 2.1.

3.2.1 Repeatability and accuracy of angle measurements

Measurement repeatability of angular misalignment between the CAT gratings was determined by scanning along line A-A' (see Fig. 3-2b) multiple times (>3) (the grating alignment assembly was remounted between the measurements), and it was found to be 0.06, 0.11, and 0.67 arc min rms for yaw, pitch, and roll, respectively. Accuracy of SLRT in roll measurement, on the other hand, depends on the quality of CAT gratings (i.e., out-of-plane buckling amplitudes) as discussed in section 2.6 of Chap. 2. For planar reflection gratings free of complications from membrane buckling, the system achieves high accuracy as demonstrated by the near perfect agreement between measured and theoretically predicted roll angle variations in Fig. 2-5 of Chap. 2. For high-quality CAT gratings with out-of-plane buckling amplitudes of less than 100-200 nm PV, accuracy on angle measurements is evaluated to be ± 0.1, ± 0.8, and ± 1.1 arcmin for yaw, pitch, and roll, respectively which are in tolerance. For low-quality CAT gratings with buckling amplitude of few microns, accuracy is assessed to be out of tolerance budget as will be detailed in Results and Discussion section for test 2.

3.2.2 Hardware

Four grating holders, two grating windows, and one window assembly frame were designed for test 1. Figure 3-2a shows a schematic for one of the grating windows with two grating holders (X10 and X14) bonded to it. CAT gratings with size of 30×31 mm^2 were used for test 1. CAT gratings were bonded at the center of four flexures that run parallel to each edge of the grating to compensate for CTE mismatch between the grating and the titanium support frame. 0.03 mm diameter wires were temporarily placed between the frame and the grating to set the bond thickness for attachment to the integral flexure support [90]. In this way, yaw and pitch angles between the gratings were aligned kinematically. The CAT gratings were bonded such that the grating lines are facing downward. The wires were carefully removed after a

24-hour cure at room temperature. Roll angle of CAT gratings are adjusted manually with fasteners and Belleville washers working as pivot points. Spring plungers provide pre-load to the frame against the micrometer for manual roll adjustments. The fixture screws are tightened once the alignment is complete. Fig. 3-2b shows the grating window with the two CAT gratings aligned relative to each other. Micrometers, spring plungers, and pivot fasteners were all removed after fixturing the gratings with the fixture screws.

Figure 3-3 shows a schematic and photograph of two grating windows aligned on the window assembly frame. According to the state-of-the-art layout of the CAT grating spectrometer, it is required to align CAT gratings on a curved Rowland toroidal surface, however in test 1, a window assembly frame was designed to be flat for simplicity. One window (right) is to be fixed first and the second window (left) will be aligned relative to the first one manually using the micrometer and spring plunger. Two blocks holding the micrometer or spring plunger are used for alignment temporarily and removed. Figure 3-3b shows grating windows fixed on the window assembly frame, along with scan lines (red) and area illuminated with x-ray (orange) for roll measurements (discussed later).

3.2.3 Procedure

Holder alignment

The SLRT was used to scan across line A-A' (see Fig. 3-2b, note that the readers are looking at the flipped side of a grating window) of two adjacently located CAT gratings to measure variations of angles (yaw, pitch, and roll) along the line. Figure 3-4 shows exemplary angular variations for yaw, pitch, and roll across a line A-A' after adjusting roll between gratings X14 and X10.

Misalignments between gratings were derived by line-averaging and subtracting

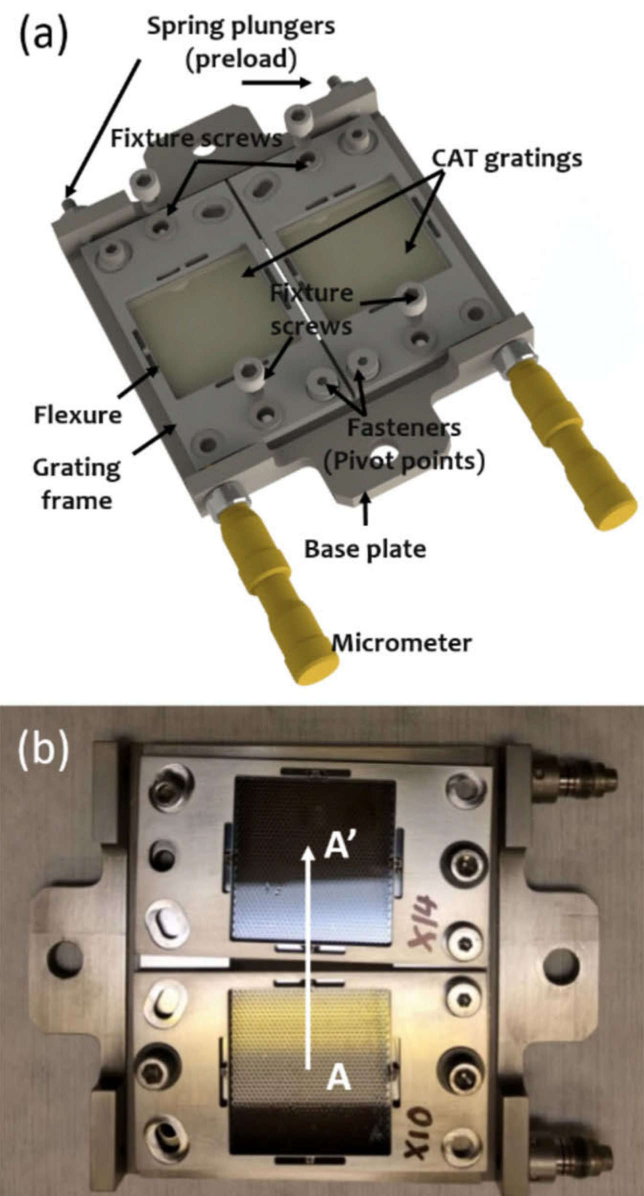

Figure 3-2: (a) An exploded view of a grating window with two grating holders. (b) A photograph of grating window after alignment and fixturing CAT gratings

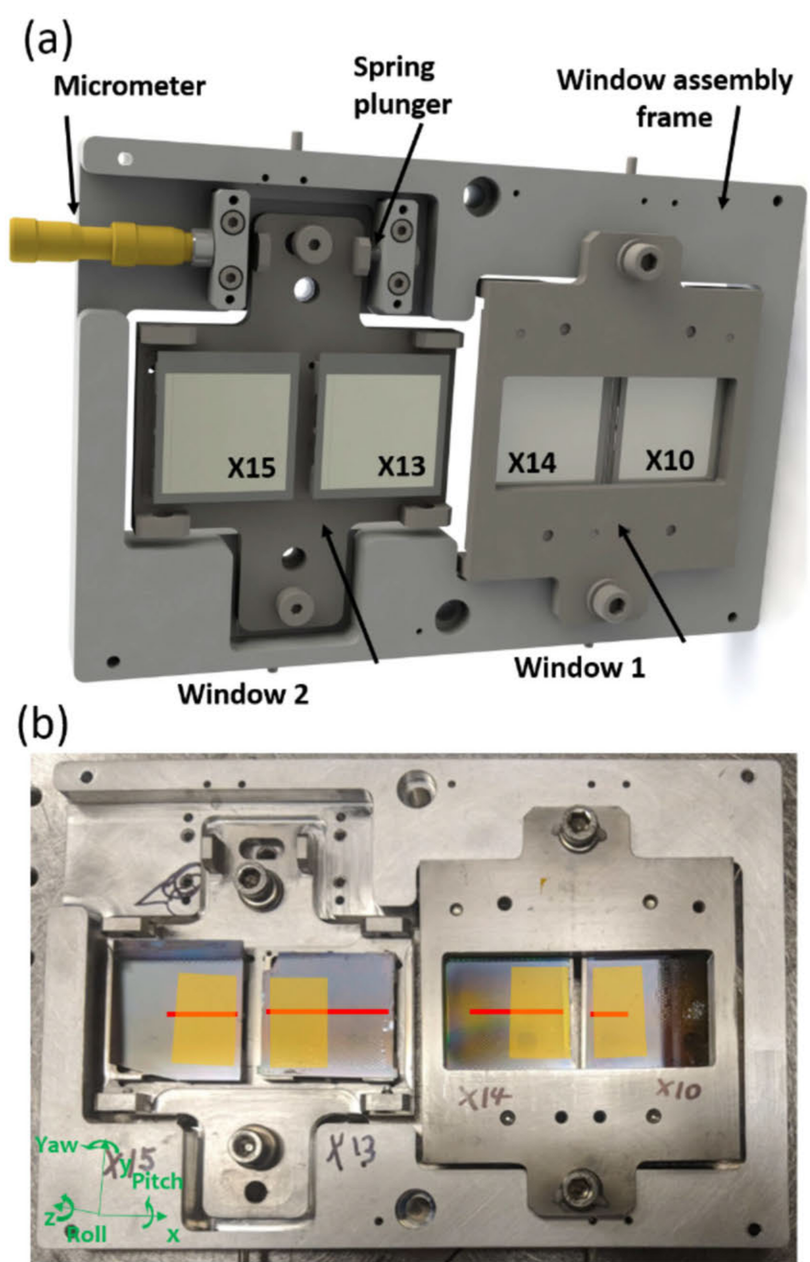

Figure 3-3: (a) 3D model for two windows aligned on the window assembly frame. (b) A photograph of two windows (four CAT gratings) co-aligned on the grating assembly frame. Red line indicates scanned path for the SLRT. Areas illuminated in x-ray measurements are shaded in orange. Local coordinates are shown at the bottom left.

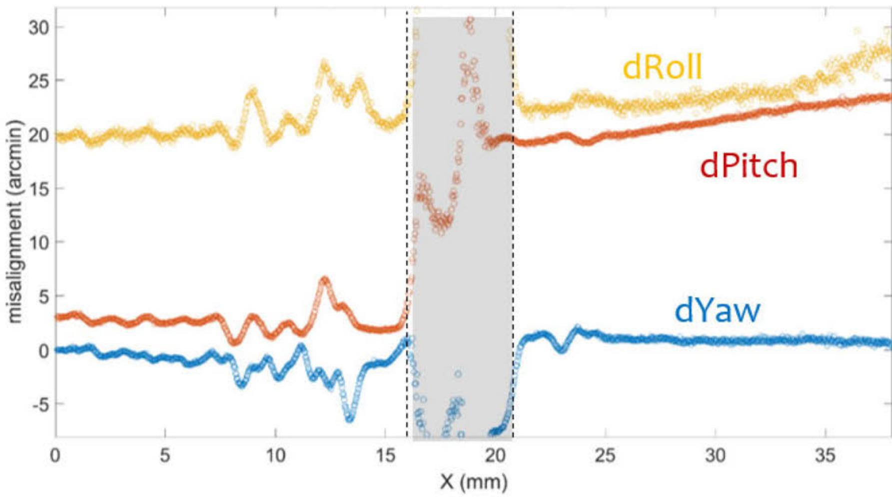

Figure 3-4: (a) Results of scanned line A-A' for alignment of two gratings on the window. Local coordinates are shown in blue. (b) Change of yaw, pitch, and roll angles along line scan A-A'.

the data from each grating. Due to manual adjustment and narrow alignment budget, roll angle was measured and adjusted multiple times along the alignment process. Figure 3-5 summarizes the alignment (or travel) log at each step.

Angular misalignments were measured after every step to detect potential mechanical drift from each step. First, the grating holders were rotated in roll using micrometers for alignment. Preloads were kept small and micrometers were retracted several times during alignment to minimize distortion of the holder. Second, the holders were locked in position with fixture screws and all other fasteners were removed. Third, spring plungers and micrometers were removed. Fourth, the fixture screws were torqued again (300-500 N-mm) as a last check before packing the grating. Fifth, the grating was flown to PANTER to measure roll angle with x-rays (reference measurement). Sixth, the window was sent back to MIT to check alignment status after travel. The window was packed inside double ziplock bags in a clean room environment before travel to prevent contamination and environmental shock.

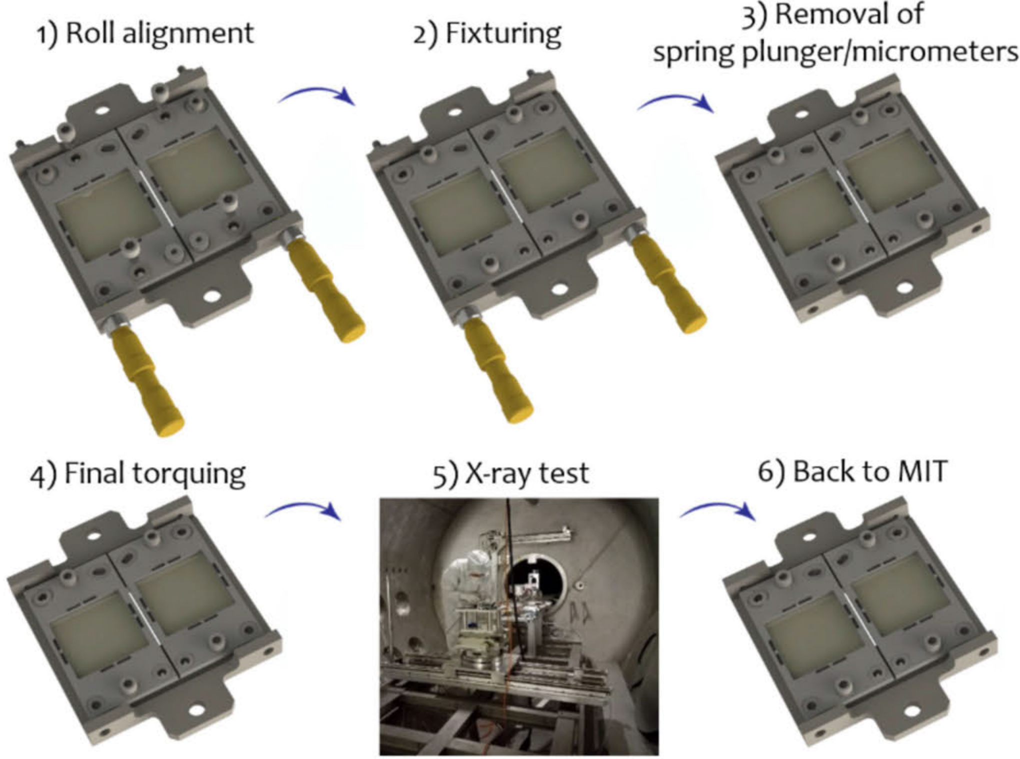

Figure 3-5: Sequence of grating facet alignment. From 4-6, the gratings traveled to PANTER x-ray facility in Germany for x-ray verification.

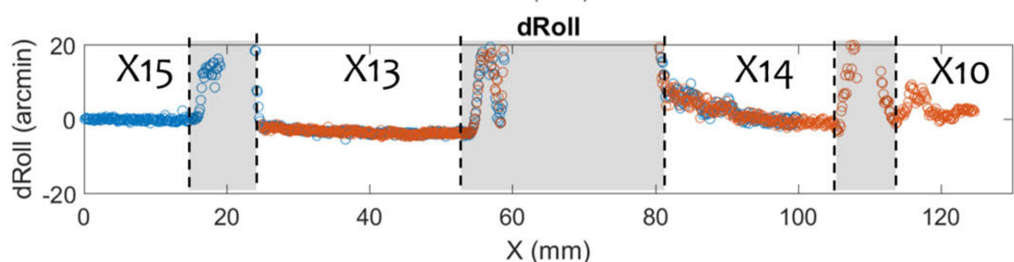

Figure 3-6: Change of roll angle along the line scan. Areas shaded in grey indicate data not used for averaging. Noisy measurements in 80-90 mm and 115-118 mm spans correspond to buckled grating membranes [48] and thus were neglected when deriving roll angles.

Window alignment

The second window was prepared by aligning and bonding X13 and X15 on it. A grating holder design for the second window was modified, but its main feature is the same as shown in Fig. 3-2a. More details of the design of grating holder (termed 'facet frame' in test 2) for the second window will be discussed in test 2. After preparing two windows with two grating holders aligned on each, they were manually aligned again on the window assembly frame using a spring plunger and micrometer. Similar degrees of mechanical drift were observed as those studied in facet alignment (see Results and Discussion section). Figure 3-6 shows change of roll angle across the gratings after completion. Due to limited stage travel, the windows were scanned twice and stitched at each step (red and blue in Fig. 3-6). After aligning windows to satisfy alignment requirements, all the holders and windows were carefully tacked with epoxy to prevent mechanical drift during travel. More details on window-level alignment are explained in Ref. [90].

3.2.4 X-ray verification

Reference roll measurements were performed using x rays at the PANTER x-ray facility in Germany after facet and window alignment. The facility is equipped with an electron bombardment x-ray source, ~120 m long vacuum pipe, and two hexapods

separated by ~591 mm along the optical axis, each mounted with a pair of silicon pore optics (SPO) x-ray optical unit (XOU) and grating assembly, and a Princeton Instruments x-ray integrating CCD camera (1300 × 1340, 20 μm pixels) at the downstream end of the chamber. The gratings were placed between the SPO XOU and CCD camera to disperse x-rays. The distance from the gratings to the focus of the XOUs was determined to be ~12736 mm. Figure 3-7 shows grating assembly mounted on the hexapod and an upstream view of the grating assembly and SPO XOUs as seen from near the XOU focus. The grating assembly was initially aligned in pitch and yaw to the upstream SPO XOU pair (mounted on a separate hexapod) by eye in air using the back reflection of an alignment laser beam originating from the x-ray source. After pumpdown, gratings were translated laterally (in the plane perpendicular to the optical axis) to center them on the converging x-ray. Precise locations of several slits were established after centering to selectively illuminate gratings. Best focus of the co-aligned XOUs in the dispersion direction was found to be 2.1 arcsec (FWHM, no gratings in the beam).

At Mg-Kα radiation (1.253 keV, 0.989 nm), the zeroth order peaks when grating bar sidewalls are parallel to the x-ray. A zeroth order yaw scan was performed with all four gratings illuminated at once to find "yaw=0" reference where intensity peaks. For test 1, since CAT gratings were aligned on a flat surface, performing the zeroth order yaw scan for each grating will result in different "yaw=0" reference due to converging x-rays. It is not expected to be seen for test 2 since the gratings are aligned along the Rowland torus thanks to improvements on window design (to be described later). After finding the yaw reference, the grating assembly was rotated by half the angle of a diffraction order for blazing. The CCD was translated to the location of the 8th order Mg-Kα, and fixed in place for the entire measurement. X-ray data was accumulated, and the centroid of the single grating line spread function was calculated. Diffraction peaks in 8th order were measured from each grating one by one using a movable slit. Roll misalignment between gratings rotates the dispersion axis around the zeroth order. For small roll angles, roll angles between

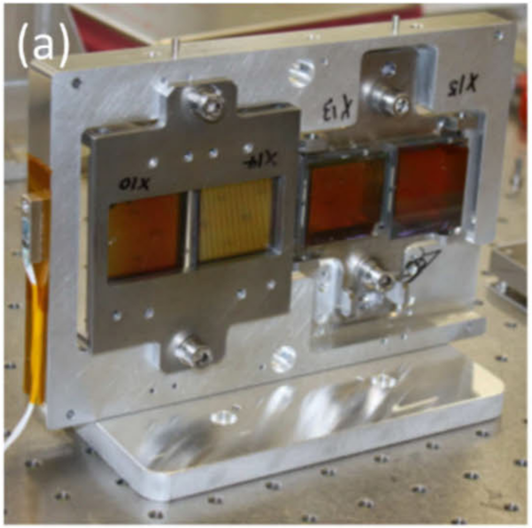

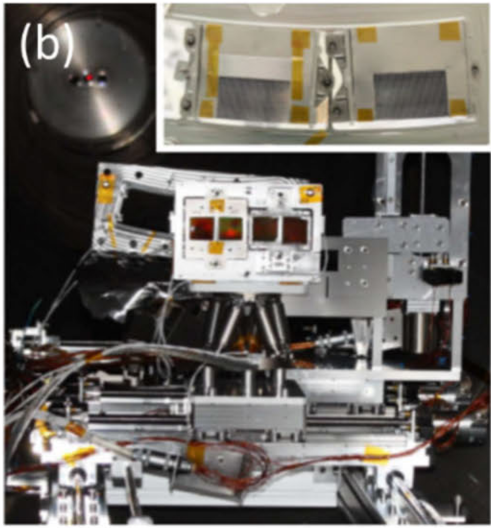

Figure 3-7: Photograph of grating assembly mounted on the hexapod (a) and the upstream view of the grating assembly and SPO XOU pair (partially blocked by gratings in this view) each mounted on its hexapod (b). Inset in (b) shows pair of aligned SPO XOUs.

CAT gratings are measured by $dRoll = arcsin(\Delta y/D)$ where dRoll is misalignment, Δy is offset of the centroid of 8th order diffracted peak from the gratings in the cross-dispersion direction, and D is the dispersed distance ($\sim$504 mm) for 8th order. The roll misalignment of each grating was computed with X13 as a reference.

3.2.5 Results and Discussion

Table 3.1 summarizes the measured angular misalignments of X14 relative to X10 after each step in holder alignment. Local coordinates are defined at the bottom left corner of Figure 3-2. All three angles drift during each step, except that only roll drifted after removing spring plungers and micrometers. Changes in angles at each step were small enough not to fall outside of the tolerance window. However, the changes lengthened the alignment process as it necessitated checking roll angles between gratings after each step. The fact that the alignment process relies on manual micrometer also made it slow since the gratings had to be "roll and scan" multiple times until all four gratings satisfied alignment requirements before beginning the

Table 3.1: Angular misalignments between X14 and X10 recorded during each sequence of holder alignment. Units are in arcmin.

Sequence	**dYaw**	**dPitch**	**dRoll**
After roll adjustment	-0.9	8.8	3.8
Fixturing	2.0	14.1	4.8
Removal of spring plungers/micrometers	2.0	14.0	3.4
Final torquing	2.5	10.6	0.08
X-ray testing	N/A	N/A	3.6
Back at MIT	2.2	18.5	3.3

fixturing step (step 2 in Fig. 3-5). Overall, it took ~1 week to align four CAT gratings.

Figure 3-8 summarizes the relative roll angles and uncertainties for SLRT measurements (0.7-1.1 arcmin assuming high-quality CAT gratings used for test 1) and x-ray measurements (std = 1.4 arcmin) [49]. Data was referenced to X13 for comparison. Regardless of the long travel delay before and after x-ray measurements, roll angles measured with the SLRT are similar in trend, but differ from each other (0.08 and 3.3 arcmin before and after x-ray testing). This is assessed to be due to non-repeatability in the scanned path for test 1 (it was later modified for test 2 to be a repeatable scan path). It is encouraging that both measurements indicate the roll angle was aligned within the tolerance window (<6 arcmin), implying the potential of UV-based SLRT for aligning gratings without relying on time-consuming x-ray alignment. However, little is known on the cause for difference between the two measurements. It is unlikely that the roll angle drifted mechanically during travel since it was repeatedly seen that the hardware doesn't drift once it is mechanically fixed (either with screws, epoxy or both) (will be mentioned again in test 2). It is suspected that the SLRT measurement is not accurate enough - enough to satisfy Arcus requirement with high-quality CAT gratings, but not enough to have strong correlation with x-ray measurements - due to complexities arising from buckled grating membrane and L2 complexities (please see chap. 2 for more details). The CAT gratings used for this study exhibited buckled membranes with spatially varying mag-

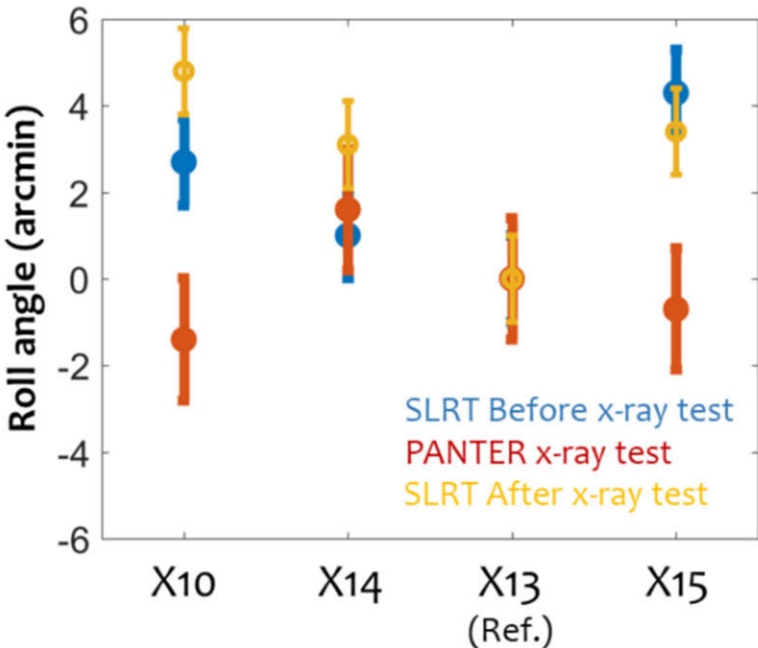

Figure 3-8: Roll alignment results measured using the SLRT (blue and orange) and x-ray (red). X13 was used as a reference for comparison

nitude (100-200 nm PV) evenly distributed over its aperture, contributing to biased position measurement along the scan. In Figure 3-6 for example, noisy data in ranges of 80-90 and 115-118 mm correspond to buckled membranes. Different reflectivities between L2 hexagonal support and grating membranes are another biasing factor as the position sensitive detector measures center of mass of the beam profile [89].

3.3 Demonstration: second test

Although four CAT gratings were aligned to satisfy the requirement in test 1, the process still requires advancements to be adopted for flight assembly:

1) it takes long to align and bond gratings (~1 wk to align four CAT gratings).

2) it lacks active control on alignment of yaw & pitch.

3) hardware used in test 1 served as a simple grating holder with no considerations on structural efficiency (i.e., x-ray blockage and weight).

4) x-ray verification test performed at PANTER test is costly, hard-to-access, and time-consuming.

Test 2 was designed to address all these problems in a holistic approach as follows:

1) Develop a new alignment protocol that is simpler, more automated, and scalable.

2) Design flight-like hardware with reduced x-ray blockage and weight.

3) Replace PANTER x-ray test protocol with new protocol using more easily accessible x-ray setup near MIT.

4) Make an active effort to align yaw angle to compensate for grating bar tilt angle [91] caused during DRIE etching (note that grating bars are drawn to be tilted relative to the surface of the grating in Fig. 3-11 and 3-12).

Test 2 was designed to achieve all four goals, however, point #4 is less important compared to points #1-3 since actual flight CAT gratings will be manufactured to be close to tilt-free.

For test 2, the SLRT was modified to build a Grating Facet Assembly Station (GFAS, Fig. 3-9) that can load, align, and bond a CAT grating to a facet frame in a single setup (Fig. 3-10a,b). Due to our past limited capacity in producing high-quality CAT gratings, test 2 was performed with relatively low-quality CAT gratings. CAT gratings used for test 2 are labeled X17, X19, X21, and X22. Unlike a flat grating window for test 1, new grating window was designed to be curved such that two sections are inclined by 9 arcmin in yaw to follow the Rowland torus. For the new alignment procedure, a CAT grating was aligned and bonded to its corresponding facet frame using the GFAS hexapod to form a grating facet. The computer-controlled hexapod enabled quick alignment since the gratings don't need

to be 'rolled and scaned' multiple times as was manually done in test 1. CAT gratings are bonded to have consistent angular orientation with respect to the facet frame. The grating facet is later kinematically aligned on the grating window by simply mounting it on the window while nudging it against the mechanical reference structures. In this way, it is possible to simplify the time-consuming two-step alignment procedure (holder and window alignment) described in test 1 to facilitate production. The whole alignment process can be designed to speed up the process by parallelizing (rate-limiting) alignment & bonding steps (i.e., the step producing grating facets) with multiple GFAS's. New x-ray measurement protocol was developed at MIT X-ray Polarimetry Beamline to verify roll angles measured with GFAS. Having an easily accessible x-ray beamline near MIT campus is of great merit towards development of CAT grating spectrometers in the future.

Although test 2 improved grating alignment techniques from all aspects, the test was only partially successful since it was performed with low-quality CAT gratings. As implied in test 1, using CAT gratings with lower quality (e.g., buckling amplitudes of 4-5 μm, pinched bars, etc.) led to larger disagreement between UV and x-ray measurements in the end. The limitations of roll accuracy in GFAS measurements will be discussed, along with a new measurement technique to circumvent this issue.

3.3.1 Metrology tool construction

To accommodate the need to align and bond CAT gratings and facet frames in a single setup, some modifications were made to the SLRT to build a Grating Facet Alignment Station (GFAS). GFAS is similar to SLRT except it has an inverted geometry. It is also equipped with grating support, hexapod, facet frame support, and UV fiber bundles for curing CAT gratings to facet frames while measuring angular orientation with the UV laser. Figure 3-9 shows photographs of the GFAS. A hexapod is used when scanning the gratings or adjusting angular orientaion of the gratings. The grating support places a CAT grating in a repeatable position. The facet frame support

loads and registers a facet frame near the surface of the grating for bonding. The UV fiber bundles cure epoxy after alignment. Similar to the SLRT, the lasers (normal and angled) are incident on the gratings, and 3 PSDs measure changes of positions as gratings are scanned. The facet frame is inverted and loaded to the facet frame support, then brought down to the grating using a vertical stage for bonding (see Fig. 3-9b). The facet frame is placed to the same repeatable position using three dowel pins. A CCD is installed at the top side of the facet frame support to center a CAT grating to the facet frame. A CAT grating is fixed in place by vacuum-pull through tiny holes under the edges of the grating (under where the epoxy is dispensed, see Fig. 3-9c). Note that the CAT grating is sitting inverted (grating side downward), nudging against the three points kinematic supports (see Fig. 3-9c) for repeatable positioning. As will be discussed in the procedure section, positioning grating and facet frame in a consistent location is critical to achieve consistent angular orientation of gratings relative to the frames. Four-pole UV fiber bundles are installed in the facet frame support to illuminate a calibrated dose of UV to cure the epoxy. The same geometrical parameters were used for GFAS as shown in Table 2.2.

3.3.2 Hardware design

The hardware used for test 1 served as a simple testbed to align roll angles without consideration of structural efficiency; those structures are bulky and leave too much dead zones (i.e., areas blocking x rays). As ∼1000 CAT gratings are needed to build a CAT grating spectrometer, even a small portion of dead zones are scaled by X1000, significantly reducing the performance. As part of an effort for test 2, a more flight-like facet frame and grating window were designed (see Figure 3-10). A CAT grating was re-designed to be 26×27 mm^2 in size, with 2 mm edges to better match the aperture size of state-of-the-art focusing optics [26]. Figure 3-10a shows a flexured Ti facet frame. Grating bonds are placed at four bonding points in the middle of four flexures to produce a grating facet (see Figure 3-10b). Note that, unlike the grating

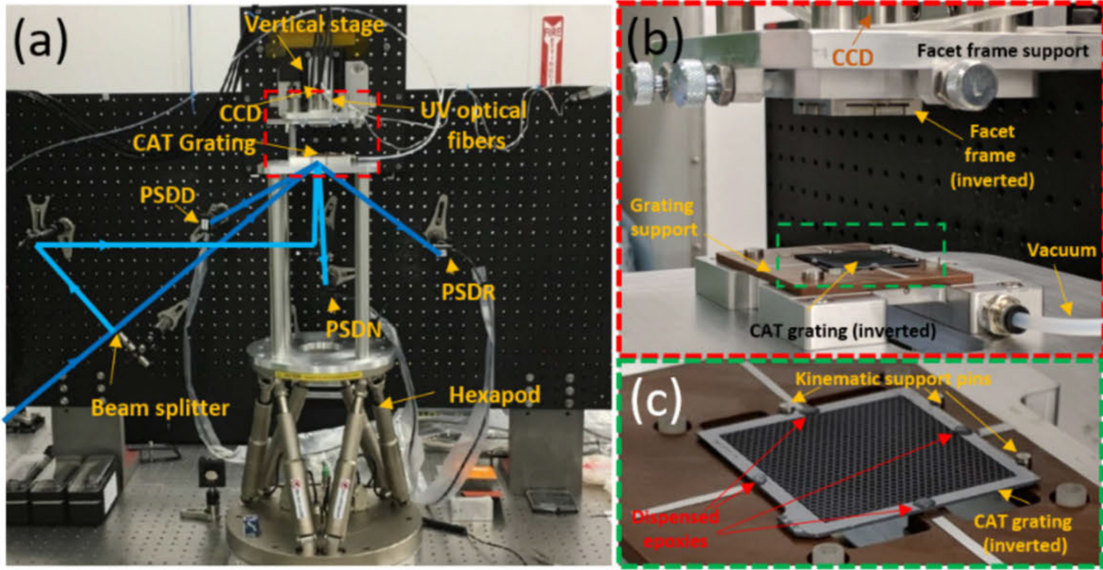

Figure 3-9: (a) A photograph of the GFAS. Optics are placed in an inverted configuration. UV source (not shown) is placed on another table to minimize thermal and vibration perturbations. (b) A zoomed image of a red dashed box. Facet frame is loaded beneath the support and gratings are sitting on the grating support, both inverted and nudged against three kinematic supports. (c) A zoomed image of the green dashed box. Four epoxy droplets were dispensed on the edges.

holder in test 1, structures of the facet frame all fall under the edges of the grating membrane to avoid unintended x-ray blockage. The rigid support beams beneath the flexures are used as a mechanical reference when nudging the grating facet on the window (see Figure 3-10a). Figure 3-10c shows a photograph of a grating window with four sections (two leveled and two inclined). Six dowel pins were arbor-pressed for kinematic alignment of grating facet. Right two sections (green) were machined to be skewed by $\sim$9 arcmin relative to the left two sections (blue) such that grating vectors are tangential to the tilted Rowland torus at their center area. Produced grating facets are mounted on the window while being pushed against kinematic support pins to kinematically align roll angle. Pins 1-4 set roll angles between gratings and pins 5 and 6 simply constrain translation. Roll angles for gratings are to be aligned kinematically since the grating facets have consistent roll angles relative to their frame from previous alignment step. Gratings aligned in top and bottom sections share the same pins to minimize roll error. Figure 3-10d shows a grating window populated

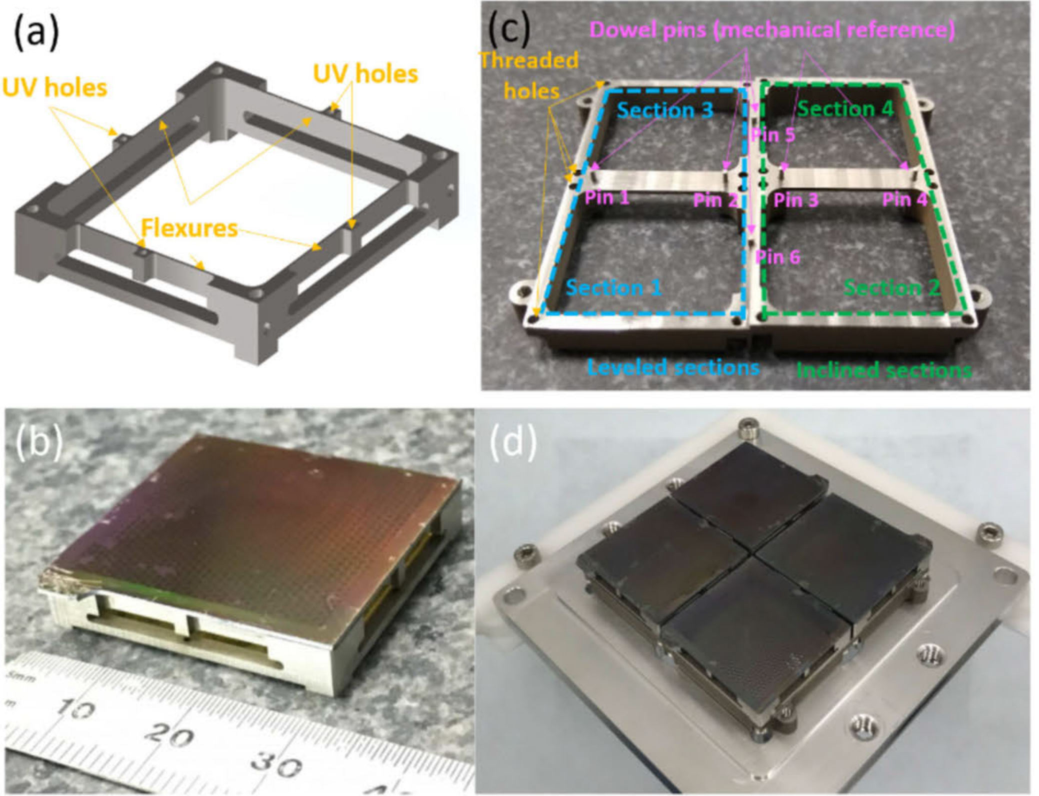

Figure 3-10: (a) 3D rendered model of Facet Frame. (b) Grating Facet. CAT grating was aligned and bonded at the mid-points of four flexures. (c) Grating window. (d) Four CAT gratings aligned mechanically and fixed on the grating window.

with four 'pre-aligned' grating facets.

3.3.3 Procedure

Alignment & bonding step

For test 2 alignment, many details in the GFAS and associated hardware must come into play in harmony to achieve alignment accuracy. It is a challenge to write down the procedure in a line in an orderly manner. Thereby, I recommend reading sections 3.3.1 to 3.3.3 at least twice to gain a clear picture in mind on how alignment is performed.

Figure 3-11 shows the detailed alignment and bonding procedure. First, a ref-

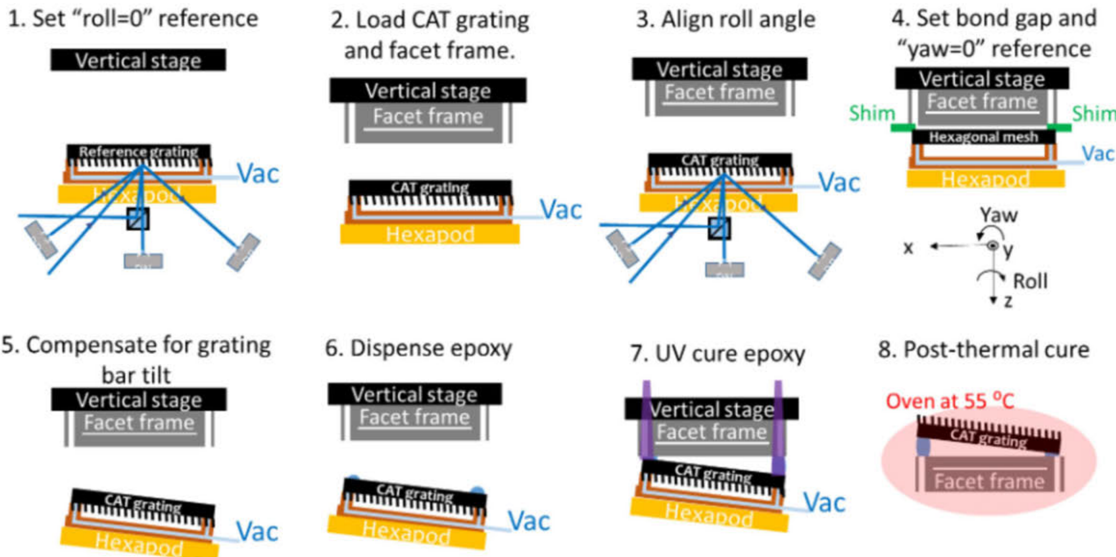

Figure 3-11: FLAT CAT grating alignment sequence. 1: Pick a reference grating, set "roll=0" reference in GFAS frame, bond reference grating to corresponding facet frame. 2: Load a facet frame to facet frame support. Load CAT grating to grating support. When loading the facet frame and gratings, nudge them against dowel pins for consistent positioning. Pull vacuums to hold grating tight. 3: Align CAT grating to "roll=0" reference set in sequence 1. 4: Translate the facet frame down toward the grating, place four thick shims between the grating and the facet frame to set "yaw=0" reference. Bond gap is set in this step. 5: Compensate for pre-characterized grating bar tilt angle[91] by rotating the grating with hexapod. 6: Dispense epoxy on four edges of the grating. 7: Cure epoxy with UV. 8: Post-thermal cure a grating facet at 55 degC for 15 min.

erence grating is picked and placed on the grating support while nudging against its kinematic support pins, then scanned with the GFAS to set the "roll=0" reference in GFAS frame (sequence 1). Light vacuum is pulled throughout the alignment process to hold the grating tight in position. No significant distortion of gratings was observed from light vacuum. 'Scan' in this section indicates a scan along the center of the grating from one end to the other along the dispersion direction. Repeatability in placing CAT gratings in grating supports was assessed by scanning the reference grating multiple times. Sequence 1 was repeated multiple times throughout the alignment procedure to make sure that there is no temporal change in the "roll=0" reference. A facet frame was loaded to the facet frame support, nudging against three dowel pins, and lowered to bond the reference grating to the facet frame. All subsequent CAT gratings were oriented to have roll angle match the "roll=0" reference such that CAT gratings have consistent angular orientation relative to the frame.

Second, a facet frame and subsequent CAT grating is loaded; both are mounted while nudging against the kinematic support pins (sequence 2) for consistency. Eyeballing with the CCD, the CAT grating is centered on the facet frame with $<$100 um accuracy (remember that the lateral translation degrees of freedom for the grating are relaxed ($\sim$1 mm) as shown in Chap. 1).

Third, the CAT grating is rolled using the hexapod (sequence 3) to "roll=0" set in sequence 1. In this sequence, CAT gratings are rolled and scanned several times to asymptotically approach the reference. However, the time it takes to do trial-and-error is significantly reduced as angles are adjusted with a precision-controlled hexapod.

Fourth, the facet frame is translated down toward the grating. Four 200-μm thick shims are placed at the gap between the grating and the frame to control bond gap (sequence 4). It should be emphasized that the 'shimming' process sets the "yaw=0" reference of the grating relative to the surface of the facet frame for later grating bar tilt compensation. Since angular error of the vertical translation

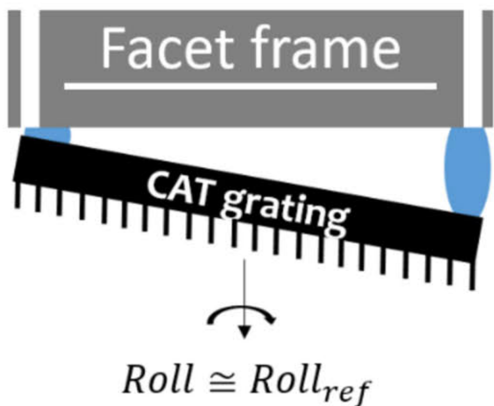

Figure 3-12: A schematic illustrating features of a produced grating facet. Grating is rolled to the reference coordinates set in GFAS frame. Tilted bars were compensated to be perpendicular to the surface of the facet frame.

stage was characterized to be negligibly small (<0.05 deg) compared to targeted tilt compensation value (typically 0.3-0.5 deg [91]), tilt reference was set just once with the reference grating.

Fifth, the frame is raised up out of the way, and grating bar tilt angle (characterization performed based on Ref. [91]) is compensated using the hexapod (sequence 5).

Sixth, a drop of epoxy is dispensed to the bonding spots on grating edges, the grating is lowered to the frame to have edges contact with the epoxy, and the epoxy is cured with UV (sequence 6, 7). The UV cure herein is intended for fast curing of epoxy for rapid alignment (to have it light-fixed to the frame for removal and proceed to subsequent grating-frame pair), not for achieving maximum strength of the epoxy. After curing, the vacuum is turned off, the produced grating facet is removed from the GFAS and undergoes a post-UV thermal cure (55 degC for 15 min) to achieve full epoxy bonding strength (sequence 8). Figure 3-12 schematically represents the grating facet after the alignment procedure is complete. The produced grating facets have consistent roll angle relative to the facet frame. The grating is bonded while being held in a rotated orientation to compensate for tilted grating bars so that grating bars are perpendicular to the top surface of the facet frame.

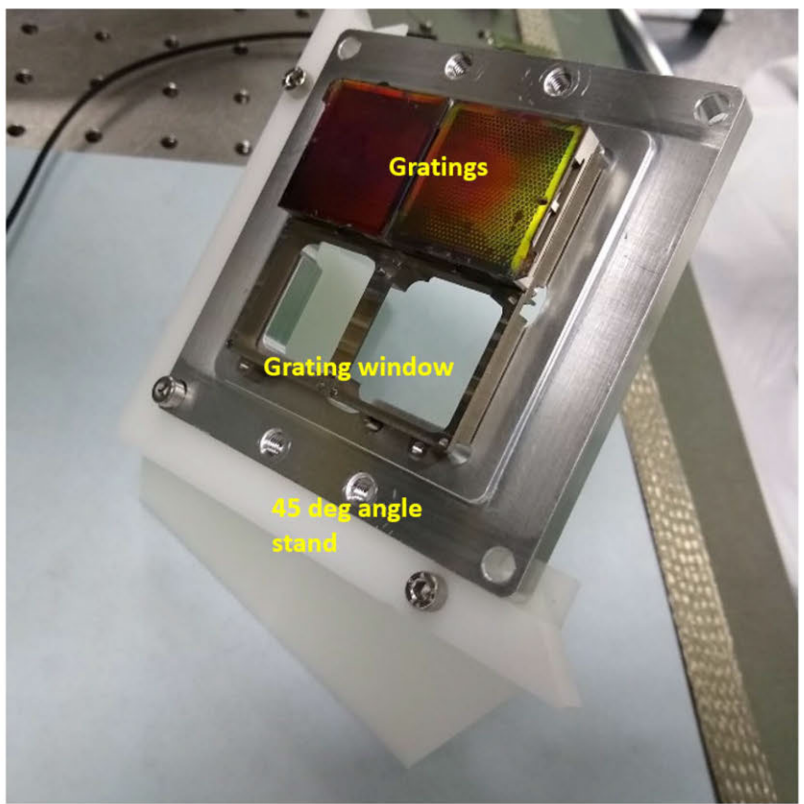

Figure 3-13: A stand designed for kinematic alignment of CAT gratings. The window is placed to have 45 deg relative to the ground to provide consistent preload while mounting four CAT grating facets.

Mounting step

The produced grating facets are placed on a 45 deg bracket, one by one, to achieve consistent pre-load between the grating facet and the pins (Fig. 3-13). Four screws are tightened from the back of the window. Fig. 3-14 shows representative scan data for two adjacent gratings X17 and X19 (X19 on the leveled section and X17 on the inclined section) after mounting on the window. Yaw angle shows 10-15 arcmin of difference due to the 'inclined section'. Roll misalignment between gratings is calculated by subtracting the line-averaged roll angle for X19 from X17 (X19 is the reference).

Several tests were performed in order to understand whether kinematic alignment strategy using arbor-pressed pins produces 'well-aligned' grating windows: 1) Study

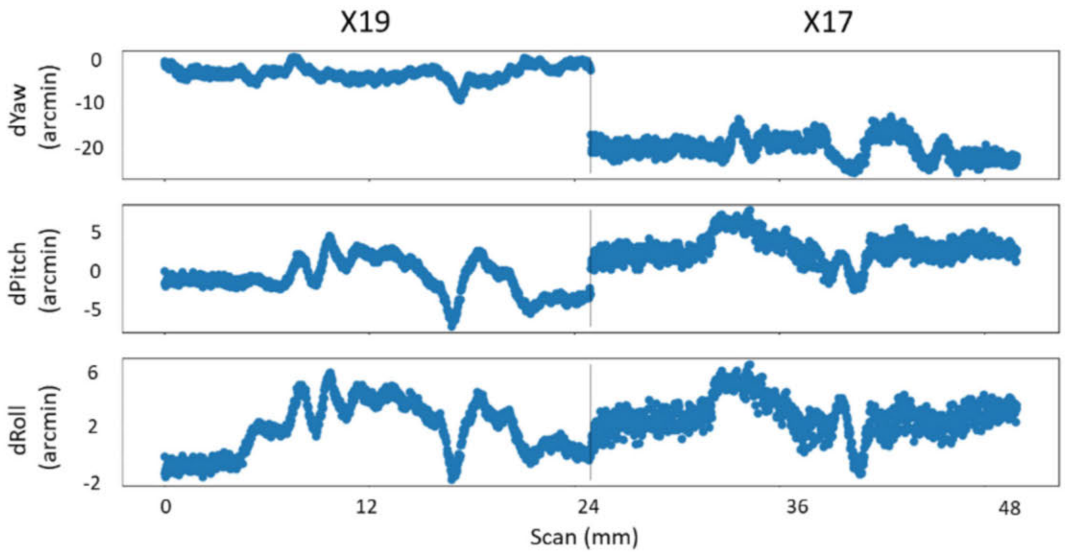

Figure 3-14: Exemplary scan data showing variations of yaw, pitch, and roll angles along line scans on X17 and X19.

of distortion of CAT gratings during mounting on window were performed, and 2) appropriateness of arbor-pressed pins for kinematic alignment was examined - it may result in mis-aligned gratings (regardless of success in alignment & bonding step) if the pins were pressed inappropriately. This was verified by mounting the grating facet on different sections and evaluating change of roll angles as mounted in different sections. Detailed results will be presented in the Result and Discussion section. Overall, time spent on alignment and bonding of CAT gratings on facets had significantly reduced - four gratings were aligned in 1.5 days compared to a week spent for test 1. However, while producing grating facet still (sequences in Fig. 3-11) took a large portion of time and effort; mounting and kinematically aligning a grating facet on the window is a relatively fast and easy task (took less than an hour). Building multiple GFAS's will help parallelize the rate-limiting alignment & bonding step for large volume alignment (>1000) once flight alignment starts for future x-ray grating spectrometer missions.

3.3.4 X-ray verification

Though PANTER facility served well for x-ray verification tests, long travel time to Germany and restrictions of time slot significantly slows research progress for roll alignment. It would be better to have an x-ray testing facility near MIT to speed up the development process for roll alignment. The MIT X-ray Polarimetry Beamline is suited for our purpose, with a long beamline (~8 m) generating a pencil beam, Manson source with interchangeable anodes (boron, sapphire, copper, etc.) to produce several characteristic x rays, and a Princeton Instruments CCD camera (20 μm pixel, 1340 x 1300 pixels) co-mounted with a shutter. Bremsstrahlung generated x-rays while bombarding the target with electrons are filtered using a laterally graded multi-layer mirror; narrow spectrum of each characteristic x-ray can be produced by spectrally filtering the x-ray through properly positioning multi-layer mirror with calibrated spacings. Polarized x-rays are produced by aligning the incident angle of x-rays at the Brester angle, however, it is not of interest in this thesis since no noticeable difference in diffraction efficiencies are observed between two orthogonally polarized x rays. A horizontal slit (2 cm-long, 1-mm wide) is placed ~8 m downstream of the source, gratings 0.7 m from the slit, and camera 1.8 m from the grating. Figure 3-15 shows a schematic and photograph of the x-ray beamline. Unlike the PANTER test facility, it is not equipped with a focusing SPO XOU.

Translation/rotation stages for the graded multi-layer mirror, slit, gratings, and camera driven by stepper motors are available for operation in vacuum. Camera shutter closes during 15 seconds of readout after exposure. Figure 3-16 shows slit and gratings mounted inside the grating chamber. It is worthwhile to emphasize that the slit, gratings (L2 mesh of CAT grating to call it more in detail), and CCD camera are not necessarily installed to be parallel to each other, which would help prevent obscuration from L2 shadowing during data analysis (to be discussed later). A hundred millimeter diameter mirror is rigidly mounted to the grating stage to calibrate wobbling motion of the stage using an autocollimator (to be discussed later).

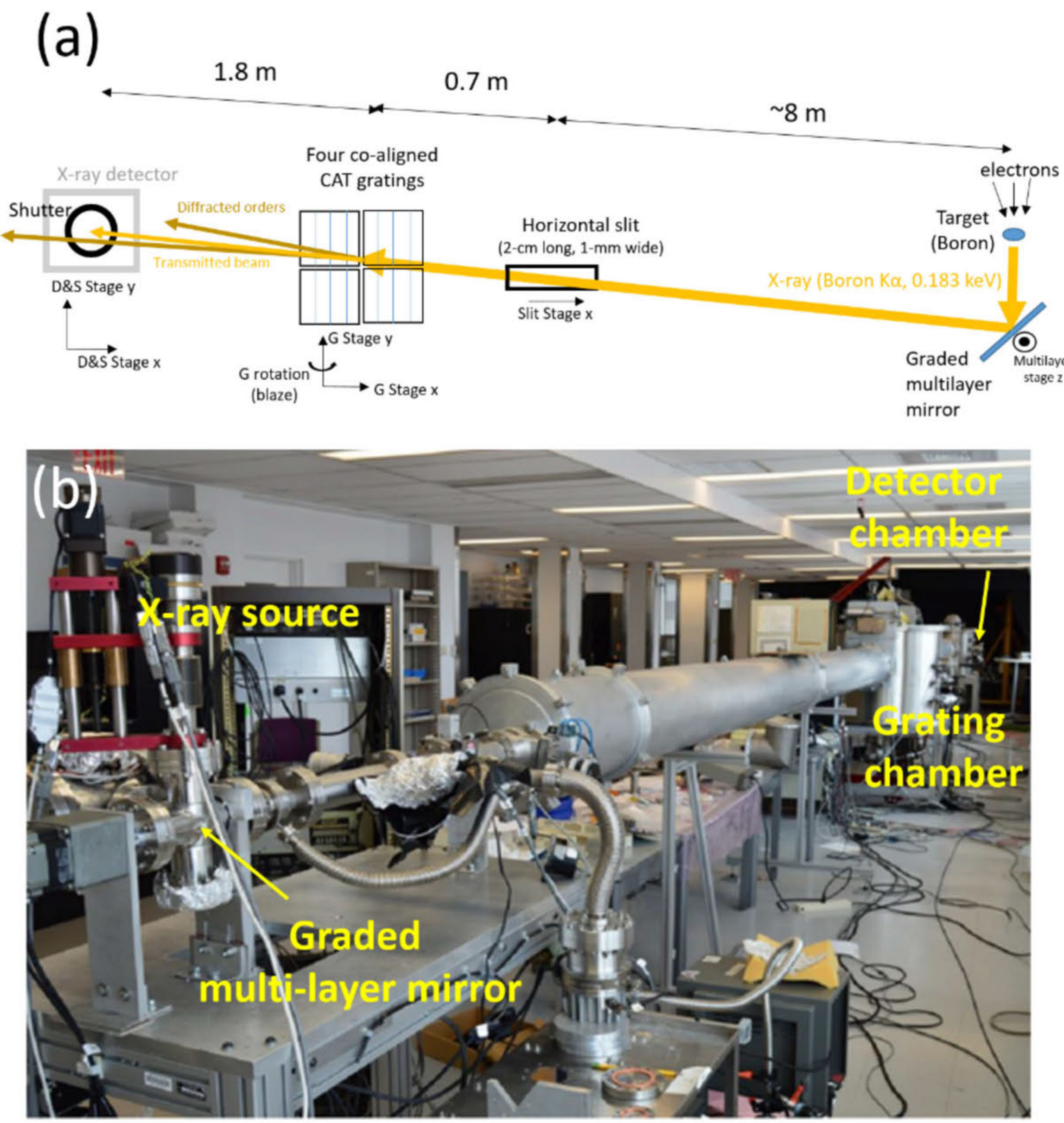

Figure 3-15: An optical layout (a) and photograph (b) of the MIT X-ray Polarimetry Beamline.

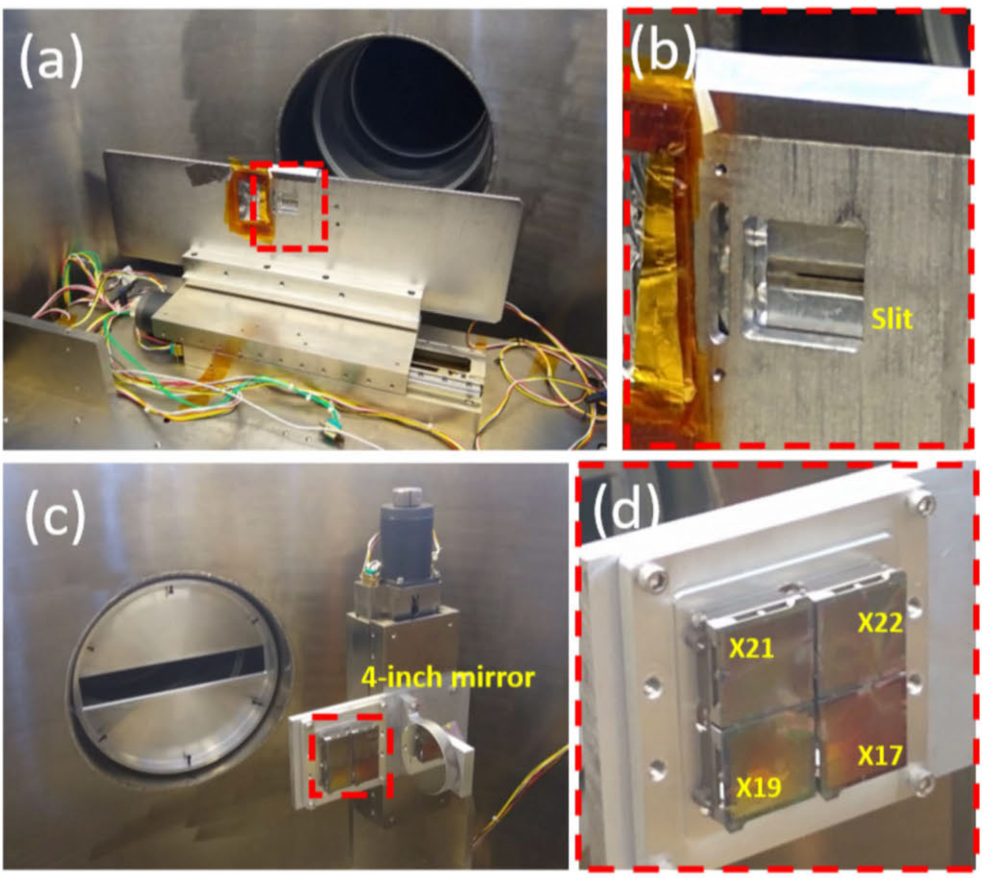

Figure 3-16: A horizontal slit (a, b) and CAT gratings (c, d) mounted inside the grating chamber.

Boron Kα (6.77 nm, 0.183 keV) was used as an anode to illuminate CAT gratings. Gratings were blazed by 2 deg and the CCD camera was translated 13.0 cm away from the 0th transmitted order to observe the 2nd diffracted order. All four CAT gratings were illuminated with x rays for 45 seconds, collecting 100 frames (total of 4500 seconds) by translating the gratings subsequently using the grating xy translation stages. Since the facility lacks an XOU focusing unit, it needs to accumulate x-rays for a long time (2 hrs) to detect the beam centroid with high fidelity. The CCD camera was kept in the same position throughout the scans to observe displacement of the 2nd diffracted order in the cross-dispersion direction. Similar to test 1, roll angles between gratings are measured by $dRoll = arcsin(\Delta y/D)$ where dRoll is misalignment, Δy is offset of the centroid of 2nd order B Kα diffracted 'image' (not a peak) from the gratings in the cross-dispersion direction, and D is the dispersed distance ($\sim$130 mm) for 2nd order. Pixel size and range of travel (13 cm maximum from 0th order) limit an angular resolution to be 0.5 arcmin (1/12 of tolerance budget). A total of 8000-13000 'good events' were detected from each grating, with number varying due to different blaze conditions incurred by different bar-normal angles (see Chap. 4) and different duty cycles for grating bar and L1 structures. Good events are algorithmically determined from the raw image by assessing photon energy, pile-up of the pixel, etc. Fig. 3-17 shows images of 2nd diffracted orders from each grating. Diffraction from L1 cross-support is shown as well $\sim$120 pixels apart in cross-dispersion direction (considering 0.776 deg between L1 diffracted orders and 1.8 m of traveling length from gratings to camera). Of note, all the images for horizontal slits are shown to be tilted relative to detector horizontal axis as described in the previous paragraph.

Roll misalignments are measured by finding the centroid along y (cross-dispersion direction), and dividing it by the rotation arm (13.0 cm). However, unlike x-ray verification tests at PANTER for which converging x-ray were used with gratings placed completely out-of-focus, shadowing from L2 hexagonal support is clearly visible in the pencil beam. Figure 3-18 is drawn by summing events along x from columns

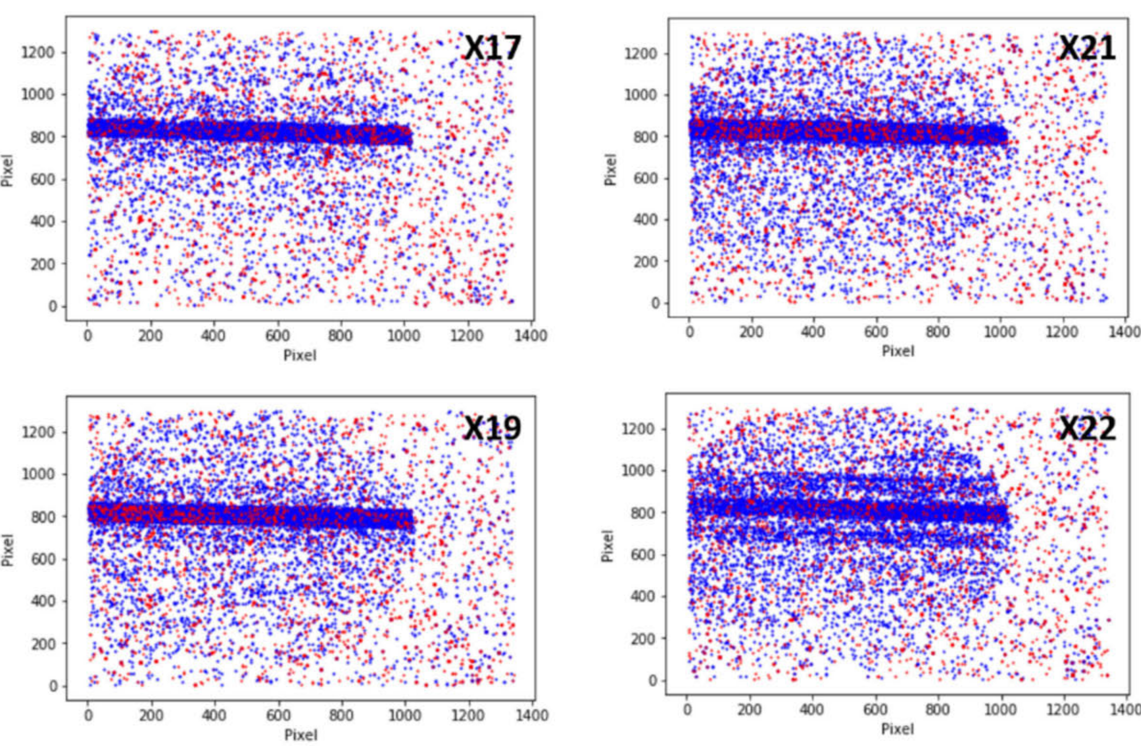

Figure 3-17: CCD images for 2nd diffracted orders from four CAT gratings. Blue and red dots indicate 'good' and 'bad' events, respectively. L1 diffracted orders are seen ~120 pixels apart from the strong 0 order (in the vertical direction). Pixels are 20 μm wide along both x and y.

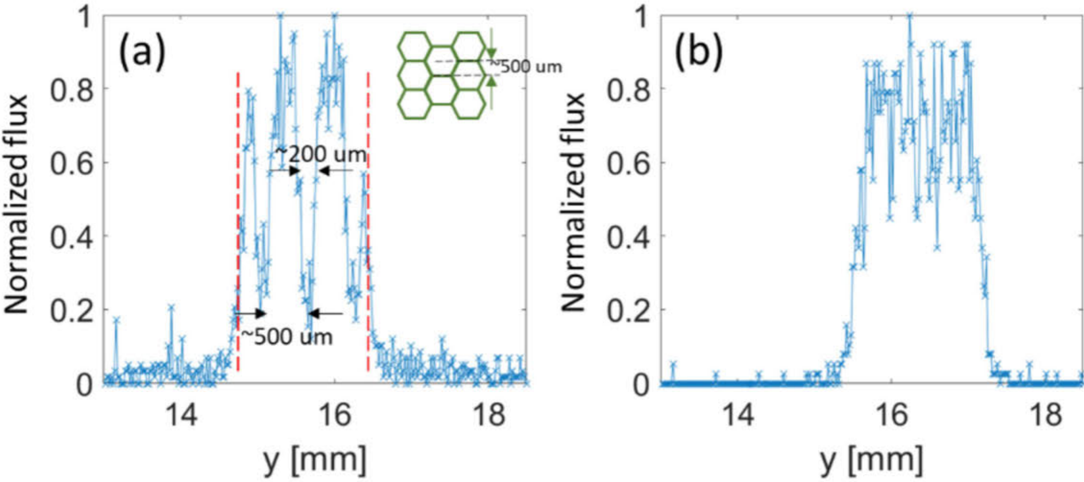

Figure 3-18: (a) Normalized flux for 2nd diffracted order of X19 along cross-dispersion direction. (b) Normalized flux for x-rays that didn't encounter gratings (gratings were out of the way from x-ray).

350 to 750, and plotting the histogram along y. A small region of interest near the slit image (rows 650-925) was chopped along y for better visibility (all subsequent histograms will show only the same rows). Figure 3-18a is a representative plot clearly showing shadowing effect from L2 structural support with periodicity and FWHM of $\sim$500 μm and 150-200 μm wide trough. Inset shows designed dimensions for hexagonal structural support which is in line with length scales observed from Figure 3-18a. Such fast variations of intensity are not shown from a 'no grating' image (Fig. 3-18b), which clearly indicates x rays are blocked by L2 hexagonal mesh. In the worst case scenario, the centroid of 2nd diffracted orders can shift along y by $\sim$200 μm if the edge of x-ray footprint coincidently overlaps with edge of L2, which will lead to $\sim$6 arcmin degradation in roll measurement accuracy.

In order to circumvent this L2 shadowing problem, an analysis strategy was devised to take advantage of the fact that the horizontal slit is not necessarily parallel to the hexagonal mesh; certain strips (or subsets) of slit (call it 'virtual slits') along the long axis are likely to be not shadowed by hexagonal mesh. Two analysis methods were devised employing 'virtual slits'. First, sort out virtual slits that are not shadowed by hexagonal mesh at their edges, then detect top and bottom edges of those virtual

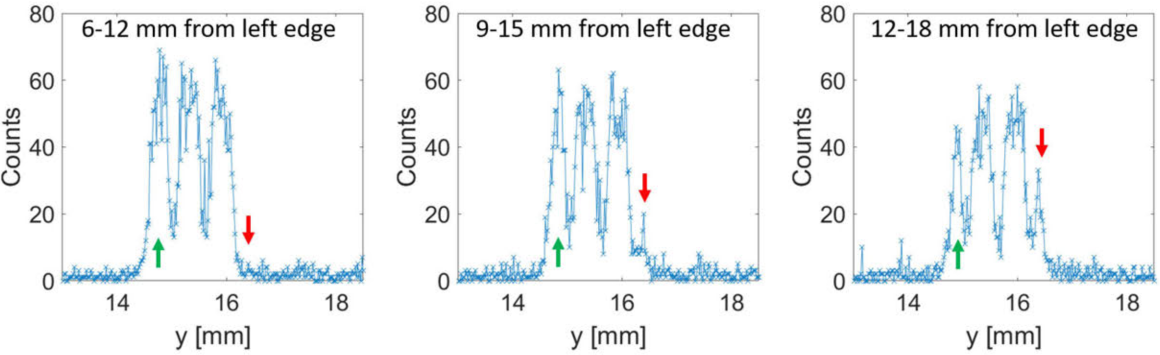

Figure 3-19: Histogram of 2nd diffracted order along cross-dispersion direction. Different virtual slits were chosen to plot histogram from left to right. Red arrows indicate position where the 2nd order image starts to emerge as translating the virtual slit. Green arrows indicate position where the image diminishes.

slits to calculate centroid of each grating.

Figure 3-19 shows number of x-ray photons along y for three 6-mm wide virtual slits - left edges of virtual slits were translated by 6, 9 to 12 mm from the left edge of the actual slit. Thanks to slit not parallel to hexagonal mesh, translating virtual slit along the long axis has the same effect as convolving $rect(y - y')$ with $G2(y)$ with varying y' ($rect$ function represent binary slit transmission function and $G2(y)$ indicates intensity modulation for 2nd diffracted order). As virtual slit is translated from left to right (Fig. 3-19), a peak emerges at y=16.4 mm (red arrow) while the peak at y=14.8 mm (green arrow) reduces in its width.

This implies that both edges of the slit footprint was not shadowed by hexagonal mesh for virtual slits 9-15 mm and 12-18 mm. It should be ensured to find a virtual slit that is free from L2 shadowing for 'all four gratings' to deduce roll misalignment accurately. However, it is laborious to find 'free' virtual slits or those may not exist.

Second method subdivides the full image into several vertical strips, make x-ray counts within the slit area to be flat-top, and fitting the histogram with a symmetric function (e.g., Gaussian, etc.) to find the mean (centroid) for each virtual slit, and average means for all the virtual slits. For method 2, it is not required to find 'free' virtual slits as uncertainties from L2 shadowing (if any) are reduced by smearing

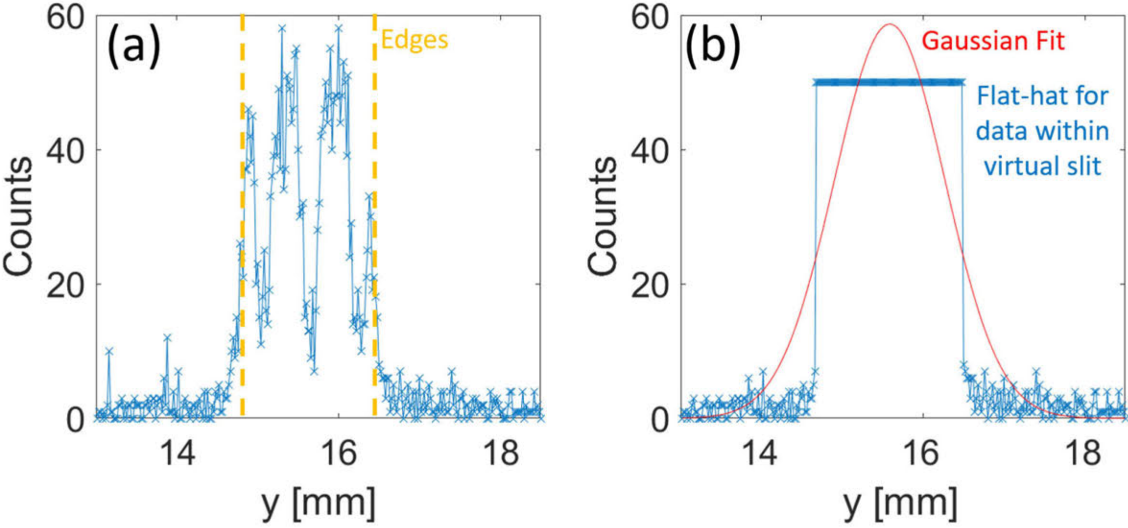

Figure 3-20: (a) Histogram of 2nd diffracted order along cross-dispersion direction with detected edges from slit (a) and histogram (blue) and Gaussian fit (red) after forcing counts within edges to have flat-top to prevent uncertainty from L2 shadowing.

them out through averaging over multiple virtual slits. Figure 3-20 shows the process of detecting slit edges, forcing counts within the slit to have a flat-top (to remove obscuration from L2-induced fluctuation), and Gaussian fitting.

Error from stage wobble was compensated after deducing roll errors. Figure 3-21 shows the autocollimator aligned to the 100-mm mirror that is rigidly connected to the gratings and grating stage. The angular error with rotation about y axis (call it stage roll error) is our only interest as it is the only stage error that has strong correlation with roll misalignments as measured from x-ray testing. The stage was found to be repeatable (<3 arcsec PV) as it was moved to different positions for all four gratings multiple times. Thereby, stage roll error was measured with the assumption that the stage behaves repeatably in vacuum (for x-ray measurement) and in air (for autocollimator testing). Table 3.2 summarizes stage roll error. Stage roll is positive clockwise.

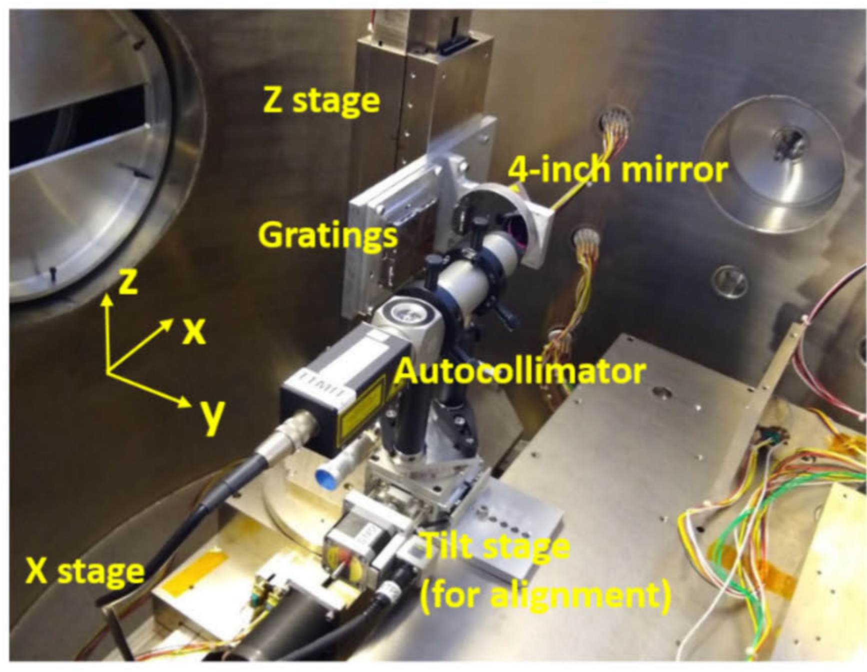

Figure 3-21: A photograph showing an autocollimator installed and aligned to a 100-mm diameter mirror rigidly connected to grating stage to calibrate angular error motion of the stage.

CAT grating facet	Stage roll error
X17	0.73
X19 (Ref.)	0
X21	0.68
X22	1.34

Table 3.2: Measured stage roll error as stage was translated to positions for each grating. X19 is a reference. Units are in arcmin.

Table 3.3: Measure roll angles as CAT grating facet was placed in different sections. S2 indicates section 2. X19 was kept placed in section 1 and used as a reference. Units are in arcmin.

Section	**X17**	**X21**	**X22**
S2	4.4	8.4	8.3
S3	-1.2	-2.1	-2.8
S4	0.3	-0.6	0.1

3.3.5 Results and Discussions

Table 3.3 summarizes relative roll angles between four CAT gratings after mounting on the window. Roll repeatability was measured to be 0.56 arcmin (1 σ) by mounting and removing the same grating facet in the same section multiple times. As described in the Procedure section, three gratings (X17, X21, X22) were swapped to be mounted on all sections 2-4 while keeping X19 (reference) mounted in section 1 to study feasibility of kinematic alignment strategy using dowel pins - if it works well for our purpose, roll angle should be the same regardless of which section each grating is mounted. It is shown from Table 3.3 that all three gratings are misaligned when they are mounted in section 2 (some variations were seen between section 2 and 3, but the values stay within alignment tolerance).

It is suspected that pin 4 was inserted into the hole with an angle (see Fig. 3-22). As pins 1-4 were machined along a single straight path using high-precision mill, error from machining is unlikely to be the culprit due to very low non-straightness error ($\sim$0.3 μm in $\sim$6 cm travel along the window) of modern milling machines. In the end, the gratings were mounted as follows: X19 (reference) on section 1, X17 on section 2, X21 on section 3, X22 on section 4. The roll misalignments between gratings in their final configuration are summarized in column 1 of Table 3.4).

Distortion of CAT gratings was measured using Fizeau interferometer after mounting, removing, and re-mounting it on the window. No noticeable distortions of CAT gratings were observed while mounting, removing, and re-mounting CAT gratings on

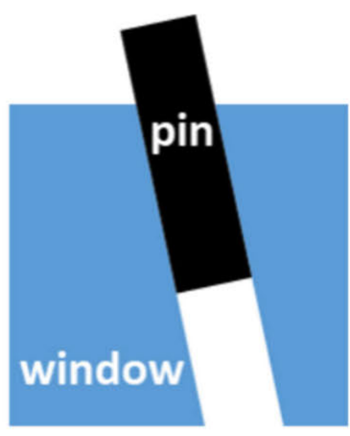

Figure 3-22: A schematic showing pins inserted with an angle.

Table 3.4: Comparison of roll misalignments as measured from GFAS and MIT x-ray beamline. Each value indicate roll angle relative to X19. roll is positive counterclockwise when seen from grating side. Units are in arcmin.

Roll measurement	GFAS before x-ray test	X-ray measurements			GFAS after x-ray test
		Method 1	Method 2	stage corrected	
X17	4.4	-11.6	-10.3	-9.9	4.5
X21	-2.1	-9.2	-9.8	-8.5	-2.1
X22	0.1	-6.8	-6.4	-5.5	0.11

the window. Table 3.4 summarizes roll misalignments measured with the GFAS and the x-ray beamline. Column 4 shows roll errors after compensating for stage roll error (Table 3.2). Roll angles measured before and after x-ray measurement (column 1 and 5) imply no angular drift or damage during packaging, testing, and travel between GFAS and x-ray facility (∼5 miles distance). However, the results show large differences for measured roll angles between the two different techniques.

Roll angles measured using x-ray are considered reference for the following reasons: 1) X-ray is a direct way of measuring roll angles as CAT gratings are to be used for x-rays, 2) Data analysis techniques for x-ray measurements derive roll errors without obscuration from L2 shadowing, 3) The UV technique, on the other hand, is an indirect way of measurement and highly depends on sample quality (i.e., buckling,

Table 3.5: Different measurements on roll misalignment depending on scan path. ±10 mm indicate line scans at ±10 mm away from the center along the cross-dispersion axis. X19 is a reference. Units are in arcmin.

CAT Grating facet	**-10 mm**	**center scan**	**10 mm**
X17	2.9	4.5	5.6
X21	-1.7	-2.1	-4.5
X22	2.4	0.1	-3.2

bar pinching) since it records position changes of the reflected beams, not transmitted beams. A roll accuracy with GFAS is assessed to be degraded due to measurement uncertainty arising from low-quality gratings (see section 2.6 in Chap. 2). Table 3.5 supports this argument as it shows roll angles measured with GFAS are dependent on chosen scan path.

3.4 Alternative ways to measure roll misalignment

It is concluded from two series of tests that UV-based metrology may be unreliable for alignment of CAT gratings as its accuracy depends on sample quality. It is unlikely that flight-quality CAT gratings have similar or worse quality, however, more work needs to be done as even a single mistake may impact performance of multi-billion USD x-ray telescope missions. Utilizing transmitted orders is an alternative way to measure roll angles more accurately without being affected from grating quality (i.e., buckling, bar pinching, etc.). Transmitted diffracted orders are sensitive to roll angle, but are much less sensitive to yaw & pitch than reflected orders. Recording change of positions for transmitted diffracted orders is expected to measure roll angle more accurately independent of sample quality. However, diffraction efficiency of transmitted diffracted orders is near zero above 200 nm wavelength, necessistating 193 nm ArF laser. However, instrumentation and operation of ArF line based metrology is not a simple task as it ionizes air (see section 2.6 in Chap. 2). Here, a simpler method using visible laser is suggested instead. It has not been available until recently before adoption of a 193 nm semiconductor scanner to pattern 200-nm grating lines

and 5-μm support mesh (L1) together with a well-defined photomask. A visible laser (either red or green) has higher transmission and diffraction efficiencies compared to ArF lines, not to mention ease of operation. L1 diffracted orders could be used to align grating lines as it has exact, and 'fixed' 90 deg angle with gratings patterned with a precise photomask. Recording change of position of L1 diffracted orders along the cross-dispersion direction will result in precise measurement of roll angles. The effect of yaw and pitch on L1 diffracted order is much smaller than roll, and thus is expected to have negligible effect in roll measurement.

3.5 Conclusion

UV-based metrologies and protocols for alignment of CAT gratings are reported. Fast and precise alignment of CAT gratings is one of the most fundamental techniques required to build CAT grating spectrometers for future x-ray missions. Two series of tests were performed in order to develop fast and accurate protocols for alignment of CAT gratings. Metrologies, hardware, alignment procedures, and x-ray verification tests were developed for each test to fulfill its own objective. In a first test, four CAT gratings were successfully aligned to satisfy alignment requirements for the Arcus mission using SLRT. Roll angles between CAT gratings were verified with x-rays in the PANTER facility. SLRT precision of 0.66 arcmin and accuracy of 3.18 arcmin were achieved with 'high-quality' CAT gratings. In a second test, alignment speed was improved (1wk for test 1 vs a single day for test 2) by modifying SLRT to build GFAS and designing new alignment protocols. A new measurement protocol was developed for x-ray verification test using a pencil beam at MIT X-ray Polarimetry Beamline to replace the high-cost and not-easily-accessible PANTER x-ray facility. Although CAT gratings were aligned out of the Arcus alignment budget for test 2 due to relatively low-quality CAT gratings used, test 2 has its own value in that alignment speed was improved by 5x using an automated tool (i.e., GFAS) and new alignment protocol, an x-ray testing protocol was developed using more easily accessible x-ray facility

near MIT campus, and problem with SLRT was found - SLRT measurement is highly sensitive to CAT grating quality - that would have prevented accurate alignment for future missions. With the shift from interference lithography to the 193 nm semiconductor scanner, CAT gratings with consistent angles between grating lines and L1 supports will be produced, which enables simpler alignment using transmitted diffracted orders of a visible laser from L1 cross-support.

Chapter 4

Grating bar tilt metrology

CAT grating bars are high aspect ratio structures etched with the well-known Bosch deep reactive-ion etching process (DRIE) (see Chap. 1). Along with cryogenic reactive-ion etching, the DRIE process is commonly used for the fabrication of high aspect ratio structures including 3D very large scale integration (3DVLSI), through-silicon vias (TSV), and x-ray diffractive elements [87, 67, 91]. However, etching millions of 100-nm wide (or thinner) grating bars evenly throughout the 4 to 6 μm-thick device layer is not a trivial problem; since we want uniform etching over large area of CAT gratings (with size up to 3 x 3 cm^2 for Arcus or much larger for Lynx), it is desirable to have a state-of-the-art etch chamber and well-optimized etch recipe. Similar problems occur in semiconductor industry when fabricating 3D NAND structures, etching 2.5 million tiny holes through the 128-256 layers of deposited thin films [64]. Figure 4-1a shows representative defects observed in high aspect ratio etching. Spectroscopic ellipsometry [79, 58], which is used to build physical models of the structures by measuring polarized light, is typically used in the semiconductor industry for detecting defects. Figure 4-1b illustrates a well-known overlay error in IC chip fabrication. It occurs when profiles tilt (see Figure 4-1a) over the course of etching.

Similar kind of problems occur in etching CAT grating bars. Figure 4-2 visu-

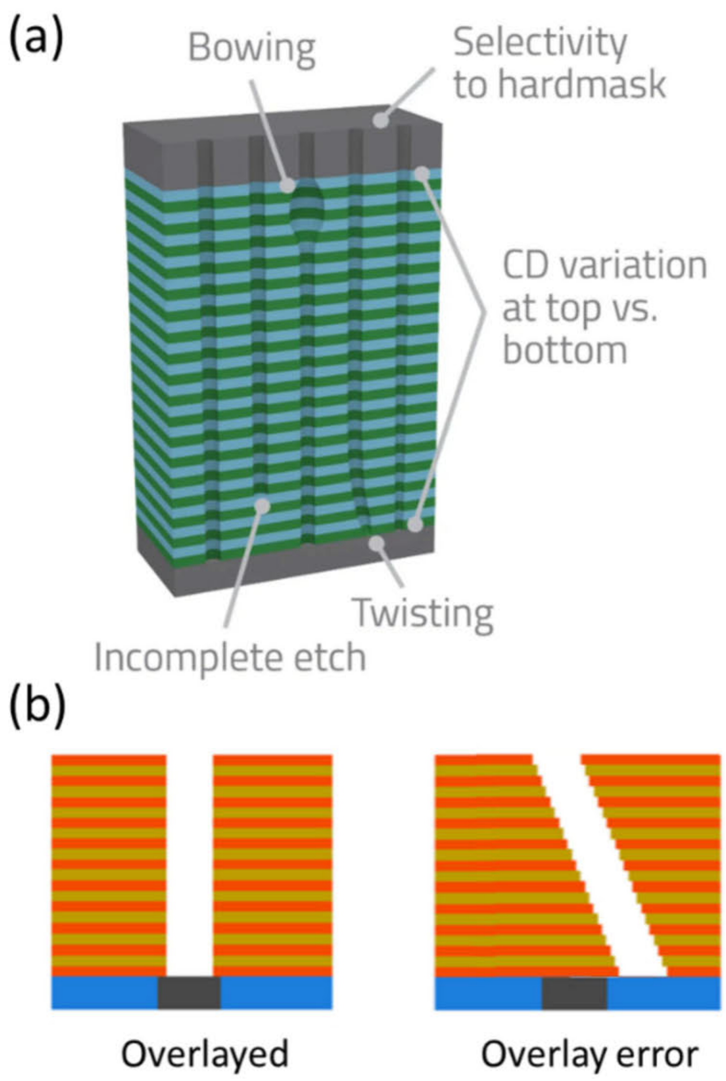

Figure 4-1: (a) Types of imperfections observed in high aspect ratio etching in semiconductor industry. (b) Overlay error caused by tilted etch profile.

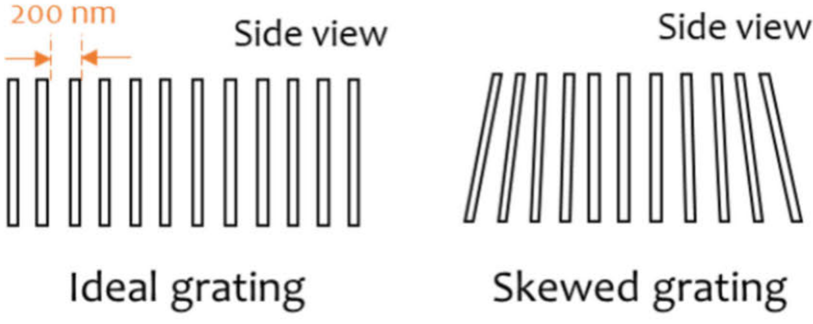

Figure 4-2: A schematic for ideal grating (left) with bar tilt being uniform and parallel to the surface normal, and skewed grating (right) with with spatially varying bar tilt angle.

alizes 'straight' gratings with uniform bar direction parallel to the surface normal and 'skewed' gratings with bar direction varying across the gratings. Similar to a schematic for 'skewed' gratings, CAT grating bars are not only skewed but also have spatial variations of skewing angle along the dispersion direction of the gratings. In an actual astronomical CAT grating application, a readout camera would cover several diffraction orders at once, which means that every part of the grating will contribute to the effective area of the instrument. However, if the bar tilt variations become too large, photons may end up in orders that miss the readout, or the critical angle may be exceeded, also leading to a loss of effective area. It is therefore of interest to keep the profile tilt within a certain range, depending on the specific instrument design and desired grating size. For CAT gratings, only etch angle variations along the grating dispersion direction are important; along the perpendicular direction observed efficiency variations are insignificant (see Fig. 1-13 in Chap. 1).

In an actual CAT grating alignment, a laser-based technique is used instead of time-consuming x-ray alignment (see Chap. 3), using surface normal as a reference instead of actual grating bar angle (laser is not sensitive to a grating bar angle); it is not feasible to align gratings by directly measuring bar angle during assembly since directly aligning bar angle need time-consuming x-ray measurement in a vacuum environment (which is highly unlikely in terms of time, cost, and labor). Therefore, it is preferable to first have information on how skewed each grating is relative to

surface normal, and then use it for later assembly using a laser in an atmospheric environment.

In this chapter, a metrology technique to characterize profile tilt of nanoscale gratings is presented using x-ray diffraction and laser reflection. This technique is used to close the loop with DRIE processing parameters, and enables fast and precise alignment of blaze angle for CAT gratings for assembly (see Chap. 3). The chapter is organized as follows: Section 4.1 introduces potential causes of profile tilt. Section 4.2 shows previous metrologies to characterize profile tilt. Section 4.3 discusses small-angle x-ray scattering (SAXS), the primary technique used for characterization of nansostructures in this work and in the semiconductor industry. Section 4.4 illustrates the preparation process for test grating samples to characterize the developed metrology. Section 4.5 presents modelling results on x-ray diffraction of CAT gratings. Section 4.6 illustrates overall metrology procedures. Section 4.7 shows characterization results for test grating, error analysis, and measurement results for CAT gratings. Section 4.8 discusses conclusion from this chapter.

4.1 Cause of profile tilt

Profile tilt is thought to be caused by non-normal bombardment of etch species onto sample surfaces due to a non-uniform plasma sheath. Figure 4-3 shows reported causes of profile tilt. Edge discontinuities in the etch target plane can induce gradients in the plasma sheath near substrate edges to cause 'edge tilt'[7] (see Figure 4-3a). Another possible cause for a non-uniform plasma sheath is positive surface charging of a non-conducting etch mask which can repel positive etch species to cause a convex profile tilt[81] (see Figure 4-3b). Additionally, non-uniform concentration of etch species in the plasma chamber can induce varying sheath thickness across the sample, resulting in a continuous change of profile tilt angle across the sample [7] (see Figure 4-3c). Recent development of a dual-source etch chamber design and installation of a

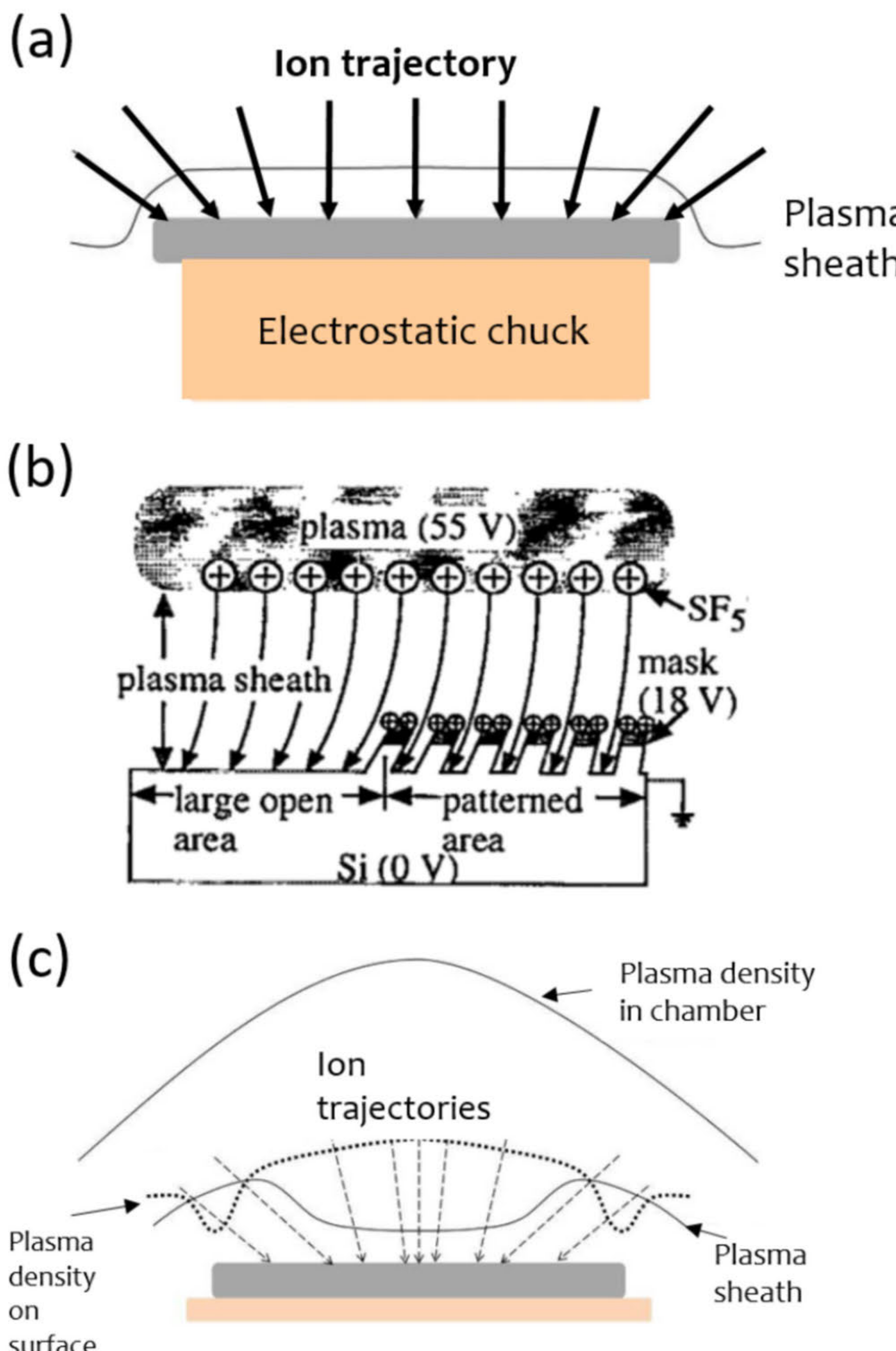

Figure 4-3: Potential causes for profile tilt. (a) Edge tilt caused by non-uniform plasma sheath at the edge of wafer. (b) Accumulation of charge on dielectric mask which repels positive SF_6 ions. (c) Non-uniform plasma density within the chamber.

ceramic ring around the sample have improved plasma density uniformity to reduce tilt variation.

4.2 Prior Art

Previously, destructive and laborious cross-sectional scanning electron microscopy (SEM) imaging was used to characterize profile tilt variations (see Figure 4-4a) [7]. However, SEM images are easily distorted by aberrations from the electron lens, mechanical drift, and sample charging [77, 76]. An exact knife-edge cross-sectional image is required to characterize profile tilt relative to the surface normal with high accuracy. Slow scan speed and sometimes the deposition of a conducting metal layer for imaging can be other drawbacks. Another characterization method uses front and backside alignment of a grid pattern with subsequent deep etching [7] (see Figure 4-4b, left). Profile tilt was measured by analyzing misalignments between the grid mask pattern and the shadow of the deep-etched profile using an optical microscope (see Figure 4-4b, right). However, it cannot be used for real-time process monitoring as it requires a carefully designed test sample. Overall, the slow, destructive, and unreliable nature of previous measurement techniques limit their applicability for process control of profile tilt in high volume manufacturing.

4.3 Small angle x-ray scattering

Small angle x-ray scattering was used as the key technique towards characterization for bar tilt of CAT gratings. It can be categorized as one of coherent lensless x-ray diffractive imaging (CDI) techniques. Since the first adoption of CDI technique [82, 68], it had evolved to a variety of forms depending on the object of interest. For example, forward-scattering CDI, Bragg CDI, scanning diffraction microscopy (ptychography) [56, 12], and small angle x-ray scattering (SAXS) to name a few. SAXS

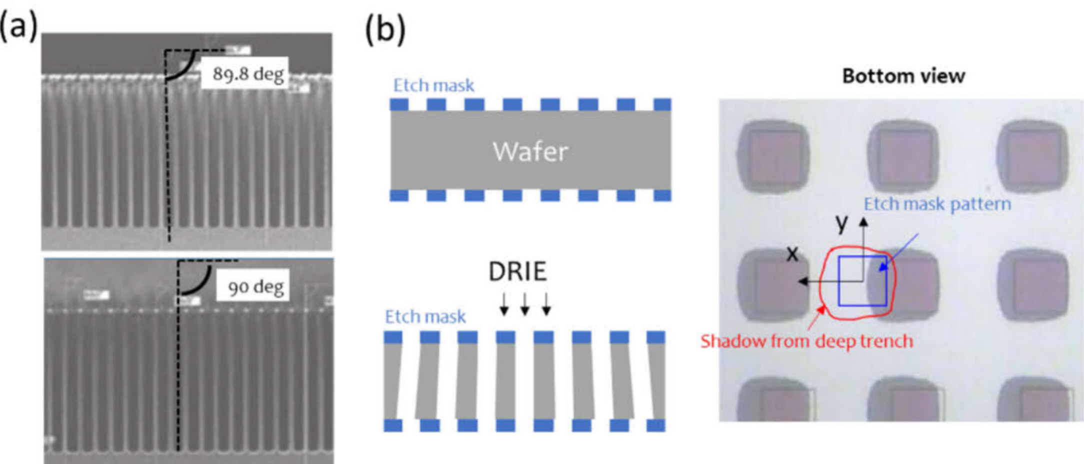

Figure 4-4: Prior art in characterization of profile tilt. (a) Cross-sectional scanning electron microscope imaging of cleaved sample. (b) Image analysis on deep-etched grid patterns [7].

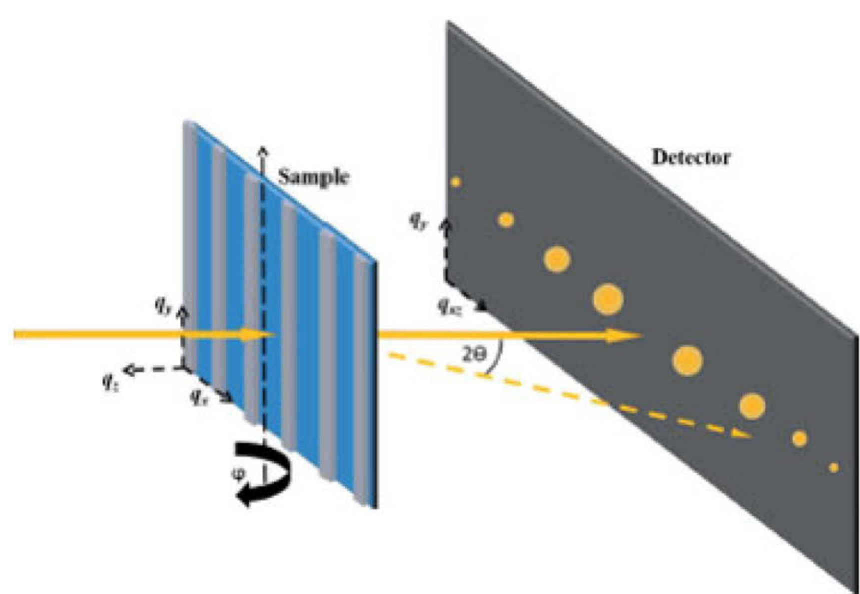

Figure 4-5: CD-SAXS geometry defining the q vectors for the sample and the detector. The grating is oriented parallel to the rotation axis. Image from Ref. [92]

is similar to forward-scattering CDI. It is a variable-angle transmission scattering technique for which the meausrements are performed with varying sample tilt to find both horizontal and vertical information of the sample. Fig. 4-5 shows measurement geometry and q (momentum) vectors for CD-SAXS [92]. Application of small angle scattering (SAS) as a metrology for process monitoring in semiconductor industry can be found in Ref. [101]. In the first trial, people actually used small-angle neutron scattering (SANS) instead of SAXS. It is similar to SAXS in technique, but differs in physics since neutrons interact with atomic nuclei while x-ray interacts with the electrons. Since x-ray interacts with the "electron cloud" of the constituting atoms, it is not only sensitive to geometry but also to change in atomic composition. Ref. [88] shows a good example of high sensitivity of CD-SAXS technique by demonstrating that CD-SAXS can detect tiny defects or line edge roughness in a line grating samples patterned by nanoimprint lithography. X-ray is now dominant technique in SAS, finding applications for measurement of sidewall angle [57] and shape determination [92, 99] of the photoresist. Long penetration depth and short wavelength of x-rays is another advantage towards high-resolution 3D imaging. In these days, CD-SAXS is being used for process monitoring of vertically stacked electronics such as 3D NAND, FinFet, and Memory devices [86]. Characterization of fin pitch after pitch quad process, sidewall roughness, line edge roughness, corner rounding, BOX recess of fins, and amount of remaining materials after CMP are among many parameters measurable with CD-SAXS in process development for FinFet. Along with CD-SEM and scatterometry, it is now being considered one of the key metrologies for process monitoring of three-dimensional nanoscale devices with varying material compositions [73].

4.4 Test grating fabrication

Two test gratings were prepared to study the performance of the proposed metrology. Both were patterned with the same etch mask but etched with different deep reactive-

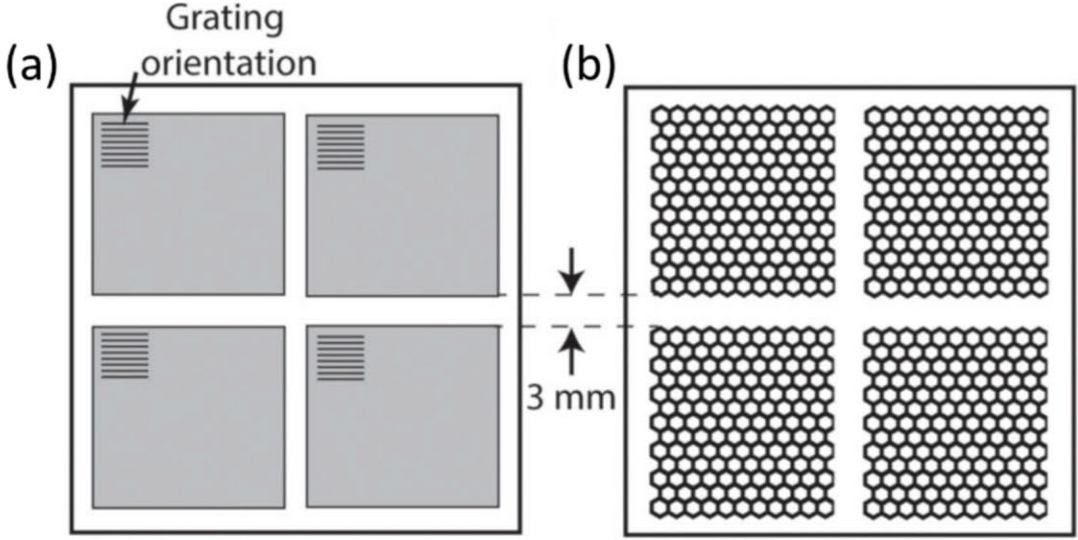

Figure 4-6: Front (a) and backside (b) mask design for test grating fabrication.

ion etch tools (single source plasma "Pegasus" tool and dual-source plasma "Rapier" tool [7]). Using test gratings simplify characterization of the metrology since it is much easier to fabricate (fairly simple fabrication as compared to CAT grating fabrication process). Figures 4-6a and 4-6b show the design of etch masks for front and back sides of a bulk silicon wafer. They consist of four rectangular grating patches, 26 $\times$ 27 mm in size, patterned on an $\sim$55 mm square chip with 3 mm gaps between patches. The design of each patch is identical to those used in Chap. 3, comprised of a large array of 1-mm pitch, 100-μm wide hexagonal structural supports on the back side, and 200-nm period grating bars mechanically supported by 5 μm-period cross-supports on the front side.

Figure 4-7 shows the fabrication process of the test gratings. 300 nm of oxide was patterned on the front side of bulk silicon wafers and diced to a size of 55 $\times$ 55 mm. Then, the chips were bonded to 100 mm (Pegasus) or 150 mm (Rapier) carrier wafers (step 1, Fig. 4-7), and the grating bars were deep reactive-ion etched to a depth of 3–4 um with the Pegasus and Rapier tools. Next, the grating front side was filled with Protek-SR, and the chip was flipped and bonded to 100 mm carrier wafers for back side etching on a Pegasus etcher (step 2, Fig. 4-7). The back side pattern was etched until the bulk silicon under the grating bars became thin enough

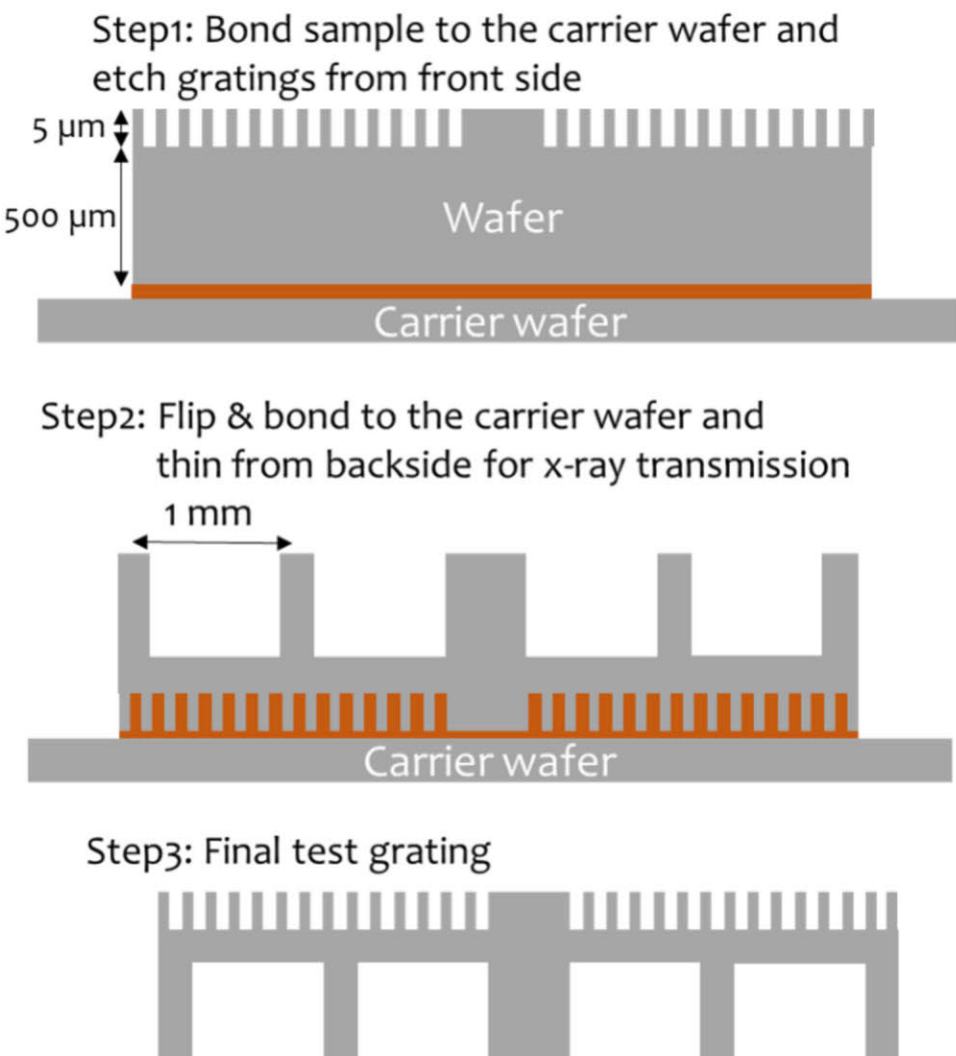

Figure 4-7: Fabrication flow for test grating.

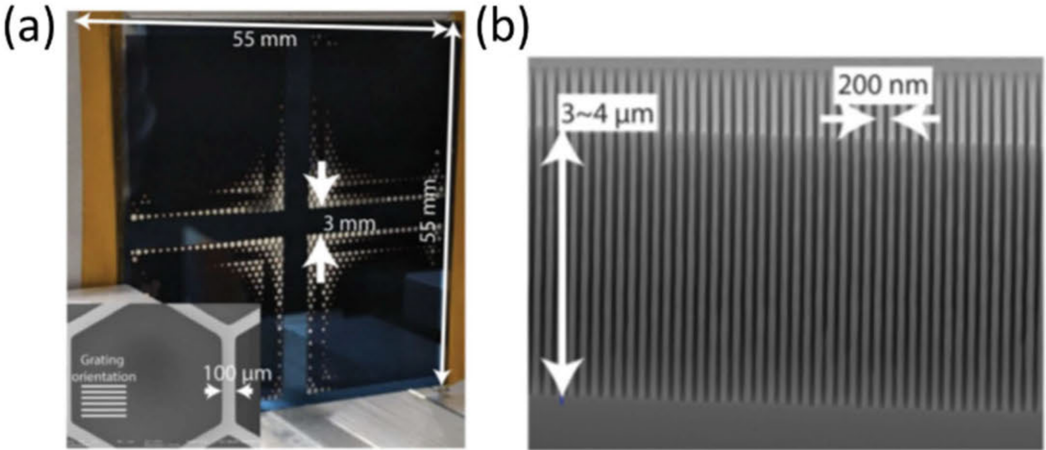

Figure 4-8: (a) A frontside photograph of the test grating (inset: SEM image of a single freestanding hexagonal membrane within the grating). (b) An inclined view of a cleaved test grating showing 3-4 μm of profile depth.

(less than the x-ray absorption length or around 70 μm) to enable observation of transmitted diffraction orders from x-ray illumination. Final test gratings show the bars etched in the front side and hexagonal arrays etched from the back side (step 3, Fig. 4-7). Figure 4-8a shows a photograph of a test grating sample. The center region near the gap between grating patches was inadvertently over etched due to nonuniform etch rate during DRIE. The inset in Fig. 4-8a is a top view image of the 1-mm pitch, 100-μm hexagonal mesh with the grating bars running horizontally on the page (not resolved). Figure 4-8b shows an inclined SEM image of the grating bars from a cleaved test grating.

4.5 X-ray diffraction modelling

While CAT gratings can be approximated as amplitude gratings in parts of the soft x-ray regime [42, 43], it is more reasonably modeled as a phase grating in the hard x-ray region (Cu $K\alpha$, 8.04 keV) due to its long penetration depth in silicon. Following the discussion in Ref. [33], the relative DEs of CAT gratings can be approximated by the Fourier transform of the complex scalar field modulation. The same scalar

theory was used to obtain analytical expressions for absolute diffraction efficiencies (DEs) of x-ray transmission gratings in the HETGS instrument of the Chandra x-ray telescope [29, 84]. In this thesis, I used a numerical approach, including the Radon transform [82] and Discrete Fourier Transform (DFT), to calculate DEs. First, a Radon transform was performed to calculate path length modulations, $PL(x')$, for each incidence angle. Next, the complex scalar field modulation was derived using the term $e^{iq\Delta nPL(x')}$, where q is the wavenumber, n the refractive index contrast, and x' is a 1-D projected axis at the given incident angle. Then, DEs were calculated from the modulus squared of the DFT of the complex scalar field. Rigorous coupled wave analysis (RCWA) is a more precise method to predict DEs. It slices the grating into stratified layers and solves Maxwell's equations to calculate the fields within each "slice" while matching the boundary conditions. The transmitted fields and resulting DEs are derived using a transfer matrix method [103, 69]. Straight bars with bar direction parallel to the surface normal (see red grating bars inside top graphs, Fig. 4-9) and skewed bars with bar direction skewed by -0.286 deg relative to the surface normal (see blue grating bars inside bottom graphs, Fig. 4-9) were considered as illustrative examples. For simulation of skewed bars with scalar theory, grating depth was corrected by a factor of $1/cos(-0.286deg)$. In RCWA, skewed bars were approximated by slicing grating bars into 10 equal stratified layers (see blue grating bars in bottom graphs, Fig. 4-9), shifting the grating bar region laterally in each subsequent layer by 2 nm. Fig. 4-9 shows modelling results for 0th and +1st order DEs as a function of incidence angle of x-rays onto grating bars (top) or grating surface normal (bottom) for straight (red) and skewed (blue) bars based on scalar diffraction theory (dashed line) and RCWA (solid line). Tilt is positive clockwise. DE for -1st order almost perfectly overlaps with +1st order DE, and thus was not plotted. Regardless of skewed or straight bars, modelling indicates that both 0th and $\pm$1st orders go to extrema (0th order DE minimized, $\pm$1st orders DE maximized) when the incident x rays propagate parallel to the grating bars. For straight bars, surface normal, grating bars, and x rays are all parallel to one another at DE extrema at tilt = 0 deg (see red plots in top graphs, Fig. 4-9). For skewed bars, DEs also

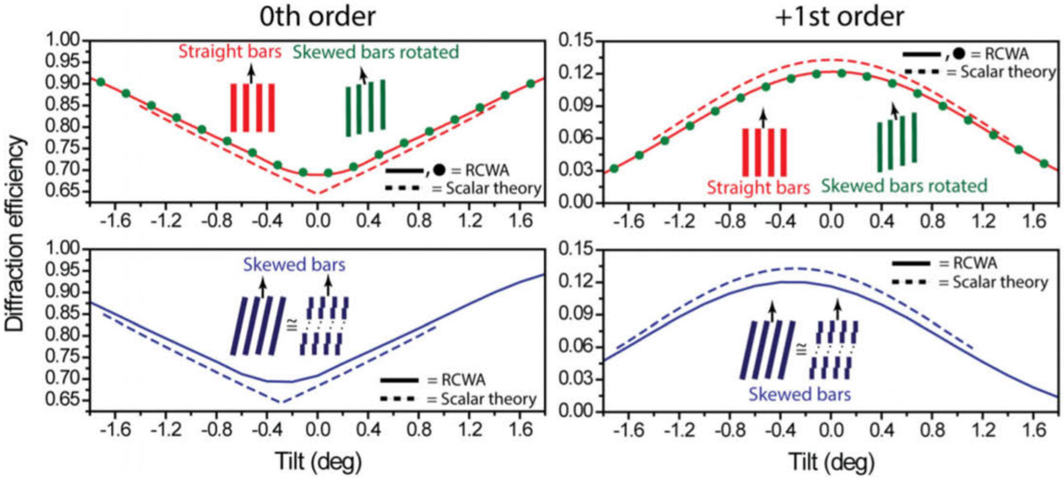

Figure 4-9: Prediction of 0th and +1st order DEs for straight bars (red in top graphs), skewed bars (blue in bottom graphs), and skewed bars rotated by skew angle (green in top graphs) as a function of incidence angle of x-rays onto grating bars (top) or grating surface normal (bottom) simulated with scalar diffraction theory (dashed line) and rigorous coupled wave analysis (RCWA) (solid line & circles). Insets inside the graphs are schematic for straight bars, skewed bars, and rotated skewed bars with a black arrow representing the direction of the surface normal. Results for both theories are insensitive to the bar-surface normal angle.

reach their extrema when x rays are incident parallel to the bars (at tilt=-0.286 deg), but with surface normal inclined by +0.286 deg (see blue plots in bottom graphs, Fig. 4-9). Rotating the skewed bars by their skew angle (green) leads to almost perfect overlap with the results for straight bars (see green circles in top graphs, Fig. 4-9), demonstrating the sensitivity of our method to measure the angle between grating bars and x rays, but not bar-surface normal angle (i.e., angle between grating bars and the surface normal).

4.6 Metrology procedure

Small angle x-ray scattering (SAXS) technique and simple laser reflection principle were used using different experimental setups to characterize bar-surface normal angle. According to x-ray diffraction modelling, 0th and $\pm$ 1st order DE predict extrema (0th order DE minimized, $\pm$1st order DE maximized) when local grating bars are par-

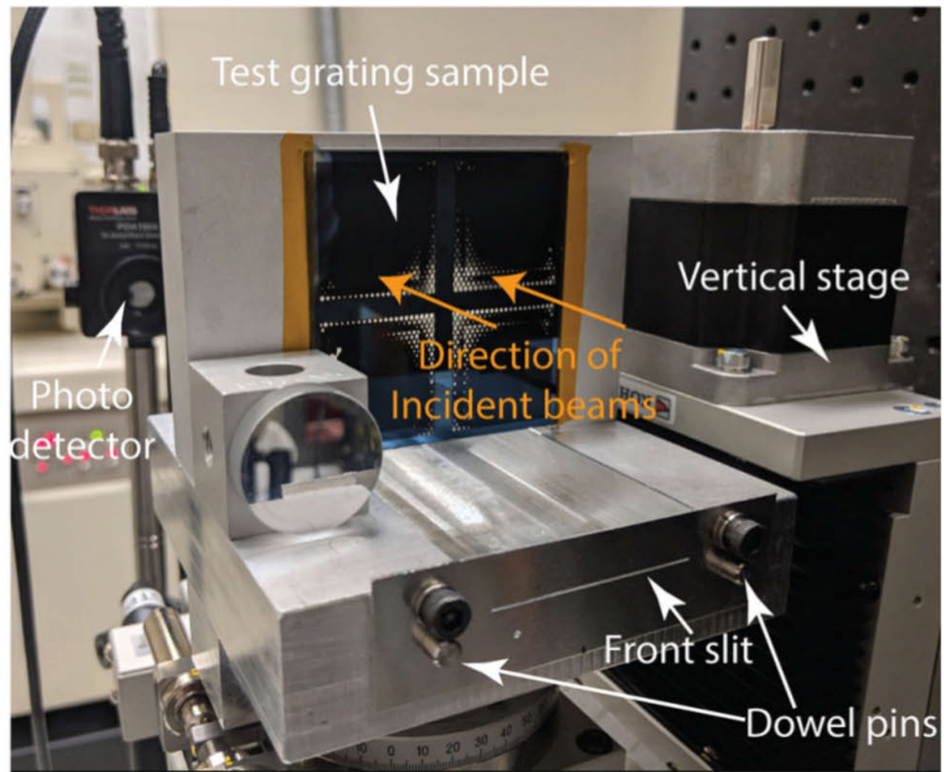

Figure 4-10: Test grating mounted on rigid mount with front and back slits. Backside slit (not shown) is at the back of the grating. The grating is mounted on a laser reflection setup which measures relative angle between surface normal and slit axis.

allel to the incident x-ray beam. Since x rays alone cannot characterize bar-surface normal angle due to their extremely low reflectivity at near-normal incidence, the surface normal was measured independently by reflecting a laser beam off the grating surface. A special rigid grating mount with slit reference axis was designed to reference the two separate measurements. Fig. 4-10 shows a photograph of CAT grating mounted on a custom-designed grating mount. It has two slits (300-μm wide, 3 cm long) rigidly aligned $\sim$100 mm apart from each other along the beam propagation direction using a pair of dowel pins to serve as a reference axis (or plane).

Figure 4-11a shows interferometric data on surface height variations of the test gratings mounted on the custom-designed jig. Surface height variations along line 1 and 2 were measured to be $\sim$18 μm across the 55 mm square sample, which effectively tilt the grating bar only on the order of $\sim$0.01 deg along the scanned lines (see Fig. 4-11b). There were no discernible temporal angular drifts during two separate

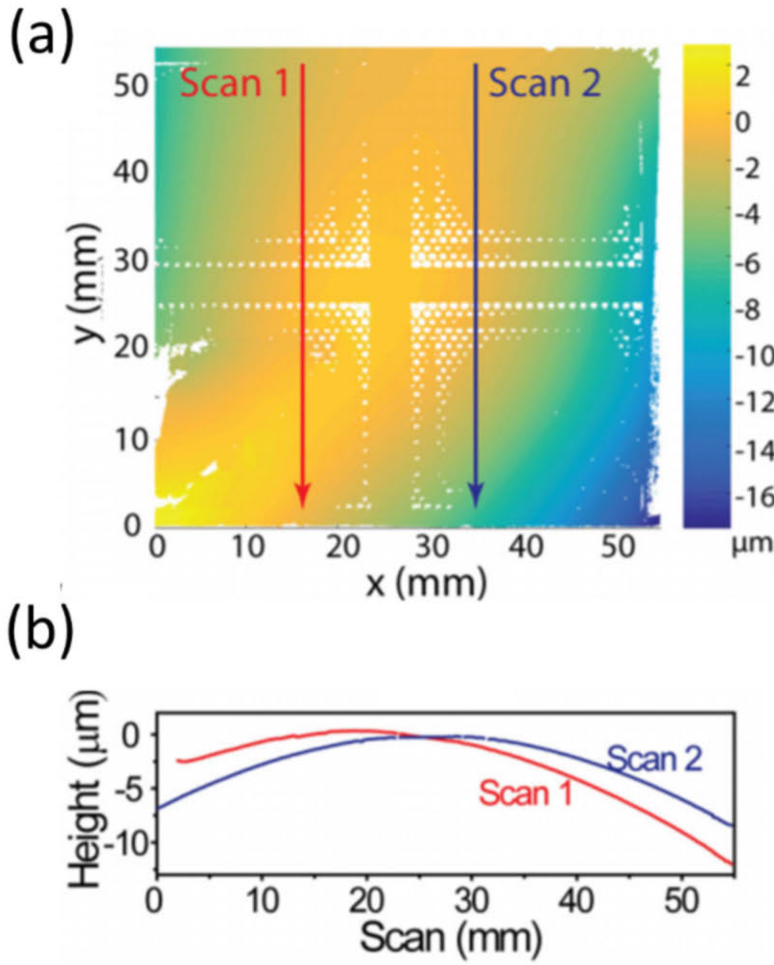

Figure 4-11: (a) Height map of test grating mounted on the rigid jig. (b) Height variations along scans 1, 2.

measurements once the grating is fixed in the jig.

Fig. 4-12a shows an overview of the experimental procedure. First, the slit reference axis was aligned with a collimated x-ray beam by performing a tilt-scan around the slit reference axis (step 1, Fig. 4-12a). The inset in step 1 of Fig. 4-12a shows a typical intensity signal during the alignment step. After alignment, the grating mount was translated vertically using a high-precision vertical stage (<10 arcsec of angular error) to allow x rays to be incident on the grating surface. The SAXS system was used to perform SAXS with changing incidence angles (0.4 deg step, 0.3 s integration time) to find the bar tilt angle relative to the x rays (or relative

to the slit reference axis, since the latter was aligned with the x rays in step 1) (step 2, Fig. 4-12a). The SAXS system is equipped with microfocus x-ray source with Cu Kα radiation, Kirkpatrick-Baez type multilayer focusing optics, two pairs of horizontal and vertical slits to control focal spot size, and a Pilatus 300k detector (487 $\times$ 719 pixels, 172 um pitch). Transmitted diffracted orders were imaged on 2D detector arrays located 1.5 m downstream from the sample (0.0065 deg of angular resolution). Fig. 4-12b shows an image of the transmitted diffraction peaks and the corresponding 1-D projection onto the grating dispersion axis. Fig. 4-12c shows measured change of DEs for 0th and $\pm$1st orders (points) and the corresponding Lorentzian fits (solid lines). Directions of grating bars are found by averaging the angles of the extrema in the 0th and 1st order DEs (see red dotted line in Fig. 4-12c) when the grating bars in the x-ray beam spot are parallel to the incident x rays. After x-ray measurements, the slit reference axis was aligned to a laser beam (step 3, Fig. 4-12a) following the same procedure as shown in step 1 but using the laser. Then, the grating mount was translated vertically so the laser is incident on the grating surface. The direction of the surface normal relative to the laser beam (or to the slit reference axis, since it was aligned to the laser in step 3) was measured using the reflection principle. Steps 1 & 2 together characterize the bar angle relative to the slit reference axis (orange dotted angle in Fig. 4-12d). Steps 3 & 4 together characterize the surface normal relative to the slit reference axis (green dotted angle in Fig. 4-12d). Putting it all together, the bar-surface normal angle (black solid angle in Fig. 4-12d) is deduced. Spatial variation of bar tilt angle in the test grating sample was measured by repeating a variable-angle SAXS (step 2, Fig. 4-12a) at several points along the direction perpendicular to the grating lines. Surface normal was determined only once (step 3 & 4, Fig. 4-12a) since mechanical distortion of the fixed test grating is negligibly small compared to etch angle distribution (see Fig. 4-11).

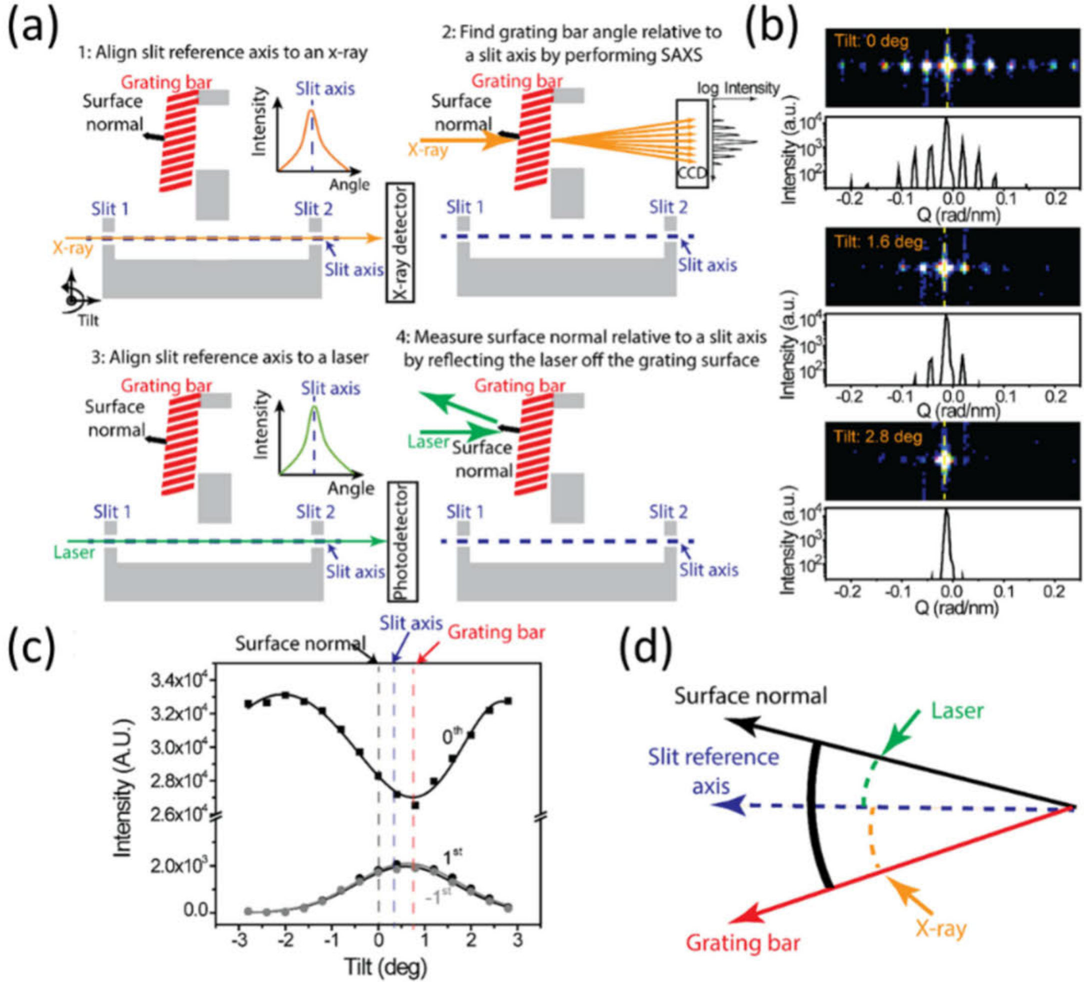

Figure 4-12: (a) Experimental procedure. 1: Align the slit reference axis relative to x rays. 2: Measure bar tilt relative to x rays by performing variable-angle SAXS to record the change of DEs. 3: Align slit reference axis relative to the laser. 4: Measure surface normal relative to the laser. (b) 2D image of transmitted diffracted orders with different bar-to-x-ray angles. Each graph shows the spectrum and DEs from -5th to 5th orders. (c) Representative data (points) and Lorentzian fits (lines) from variable-angle SAXS. The surface normal was used as a reference for plotting. (d) Schematic showing arbitrary directions of the surface normal, grating bars, and the slit reference axis (to be aligned parallel to x rays and the laser in steps 1 and 3). The bar-normal angle (black solid angle) is characterized by combining two separate measurements using an x-ray beam (orange dotted angle) and a laser (green dotted angle).

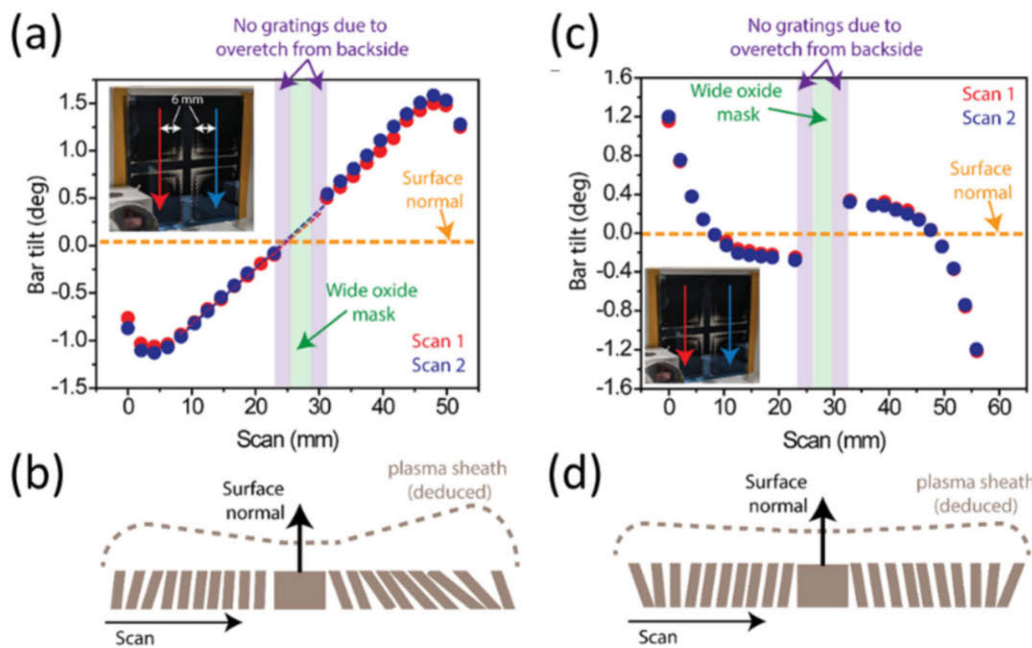

Figure 4-13: Measured bar tilt variations along a line perpendicular to the grating bars for Pegasus- (a) and Rapier-etched (c) gratings. Scans 1 and 2 were performed 6 mm away from vertical chip edges [see insets in (a) and (c)]. Data from top patch were extrapolated (dashed lines) toward the center wide oxide mask for visual help. Surface normals were used as references for plotting. Graphical interpretations of bar tilt variations (exaggerated) for Pegasus- (b) and Rapier-etched (d) gratings. Relative plasma sheath thickness is deduced from the spatial variation of the bar tilt angle.

4.7 Results

4.7.1 Bar tilt measurements on test grating samples

Figs. 4-13a and 4-13c show bar tilt angle variations from two test gratings etched with Pegasus and Rapier tools. Two line scans were performed (see insets in Figs. 4-13a and 4-13b). Bar angle is positive counterclockwise relative to surface normal as seen from left edge in insets in Fig. 4-13. Figs. 4-13b and 4-13d are graphical representations of bar angle variations for Pegasus- and Rapier-etched gratings, respectively. Dashed lines indicate relative variation of plasma sheath thickness deduced from the bar tilt angle variations.

Edge effects are clearly visible near <10 mm from top and bottom edges of both samples likely due to non-perpendicular electric field caused by termination of the plasma sheath. Linear change of bar tilt angle is visible near the central region (5 - 47 mm) in the Pegasus-etched gratings (0.6 deg/mm, see Fig. 4-13a) while the Rapier-etched gratings (see Fig. 4-13c) show nearly constant bar tilt near the central region (10-25 mm and 33-45 mm). A very similar trend of tilt was reported by the plasma etcher manufacturer (Fig. 8 in Ref. [7]). It was claimed that the more advanced Rapier tool generates a more uniform plasma density, resulting in uniform profile tilt [7]. An asymmetric plasma sheath can be deduced for the Pegasus-etched grating from the asymmetric bar angles around the surface normal in the Pegasus data (Figs. 4-13a and 4-13c) while a symmetric plasma sheath is deduced for the Rapier-etched grating. A sudden jump of bar tilt angle is clearly observed in the Rapier sample (Fig. 4-13c) across the wide gap masked with a non-conducting oxide mask. It is speculated that positive charging of the non-conducting, wide (∼3 mm) oxide etch mask strip repels positive SF_6 ions during the etching steps, causing convex bar angle distributions [81]. A similar phenomenon can be deduced from the Pegasus data (see Fig. 4-13a) since, by linearly extrpolating the data set from a left data set (scan 6-22 mm), it doesn't line up with data from its right data set (scan 31-46 mm); the right data set is shifted positive relative to extrapolated data from a left data set (see linearly extrapolated lines in Fig. 4-13a). It is suspected that surface charge from the wide oxide mask contributes to bar angle variations in addition to what is expected from non-uniform plasma density alone.

4.7.2 Error analysis

Accuracy and repeatability

Repeatability in characterizing bar-normal angle by SAXS was measured to be <0.01 deg (1σ). Accuracy is estimated to be ∼0.08 deg, which is sufficiently low to align CAT gratings to satisfy alignment requirements (see Chap. 1). Both repeatability

and accuracy were derived by root-sum-square (RSS) of uncertainties from x-ray and laser measurements. The main factor limiting the accuracy of measurements is due to yet-to-be-optimized laser measurements ($\sim$0.07 deg), which can be improved with additional effort as an actual flight mission is in place. The error from x-ray measurements comprise only a small portion of the error budget ($<$0.03 deg).

Error due to non-rectangular grating profile

Non-rectangular and asymmetric grating profiles could shift extrema of 0th and $\pm$1st DEs from 'nominal' grating bar direction and bias the measurement results. However, assuming that bar shapes are uniform across the grating, this bias can be corrected in the assembly process by aligning CAT gratings to blaze certain diffraction orders.

4.7.3 Bar tilt measurements on CAT gratings

The developed metrology technique was applied to characterize variations of bar-normal angle in freestanding CAT gratings. Insets in Figs. 4-14a and b show a square (32 mm $\times$ 32 mm) and a rectangular (8 mm $\times$ 32 mm) CAT grating, respectively. These gratings were etched with the same Pegasus tool and thus the same trend of linear bar tilt variations is expected. Fig. 4-14a shows bar tilt variations ($\sim$0.06 deg/mm) of the square CAT grating measured from both sides along the same points using the proposed metrology technique. Measurements from both sides show good agreement with each other. Since thin, freestanding CAT gratings can display slight out-of-plane buckling of the freestanding membrane within a hexagonal cell (see Chap. 1), there can be subtle discrepancies between front- and back-side measurements (see Fig. 4-14a) if the measurement positions do not overlap perfectly (curvature of the sample will mechanically tilt the bar angle). Synchrotron measurements were performed at beamline (6.3.2) in Advanced Light Source (ALS) at Lawrence Berkeley National Laboratory (LBNL) with help from Dr. Eric Gullikson and ALS funding.

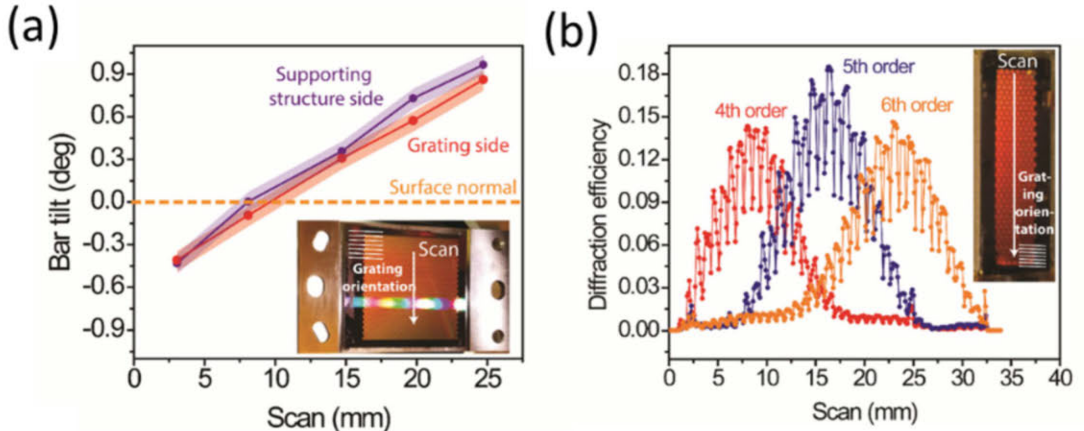

Figure 4-14: (a) Bar tilt variations of a square (32 mm × 32 mm) CAT grating relative to surface normal measured with the proposed metrology technique. Measurements were performed with both grating side (red) and the opposite side (purple) facing the x-ray source. Surface normals were used as references for plotting. Inset shows a square (32 mm × 32 mm) CAT grating etched with the Pegasus tool and mounted on a titanium frame. (b) Change of DEs of the consecutively blazed orders 4-6 along a scan line measured with an x-ray wavelength of 2.5 nm at a synchrotron facility. Inset shows the measured rectangular (8 mm × 32 mm) CAT grating etched with the Pegasus tool.

Bar tilt variations of CAT gratings, measured with the proposed metrology technique, agree with observations from synchrotron data. Fig. 4-14b is an example synchrotron data set taken at an x-ray wavelength of 2.5 nm for a rectangular CAT grating (see inset in Fig. 4-14b). The data shows the DEs of diffraction orders 4-6 along a line scan. The illumination angle, relative to the surface normal, was kept constant during the scan such that x-rays are incident on the bar sidewalls at a small grazing angle, nominally optimizing diffraction into 5th order. The fast variations in the DEs (about one cycle every 0.87 mm) are due to partial blockage of the ~0.15 mm x 0.35 mm beam footprint by the hexagonal support grid. The slowly varying envelope is due to a gradual change in the tilt angle of the illuminated grating bars as the sample is translated along the scanned line. The deduced bar tilt angle change as a function of beam footprint position is on the order of 0.05 deg/mm and in good agreement with the observation from Pegasus-etched test gratings (see Figs. 4-13a and 4-14a).

4.8 Conclusion

The metrology to characterize bar-normal angle for CAT grating is reported. It demonstrates repeatability of <0.01 deg (1 σ) and accuracy of $\sim$0.08 deg (4.8 arcmin) at a fast scan speed ($\sim$ 5 sec of integration time per point per sample), with a clear path towards better accuracy and speed with more investment. The accuracy achieved with the metrology technique falls within the blaze window of 6 arcmin (see section 1.7.3 in Chap. 1) for the proposed Arcus mission. Comparison of bar tilt angle variations for CAT gratings with synchrotron measurements shows very good agreement. These results were used to find the best commercial DRIE chamber, and optimize process parameters for DRIE etching for improved quality control of CAT grating fabrication. It successfully characterized bar-normal angles of CAT gratings enabling precision assembly of a CAT grating spectrometer (see Chap. 3). The proposed method can be expanded to characterize cross-sectional profiles of other nanostructures with appropriate x-ray diffraction modelling. The long penetration depth of x rays is ideal to characterize profile tilt of nanoscale features even on relatively thick substrates. Recent surge in physics-driven deep learning approach relaxes the needs for precise physical model, flux (or source intensity), expanding applications of x-ray imaging. Performing emulation experiment in a visible wavelength regime helps accelerate research progress in x-ray regime [34].

Chapter 5

Design and analysis of CAT grating structural support

In the field of optomechanics, tiny strains or deformation of the optical component can lead to severe degradation of optical performance. Therefore, unlike conventional mechanical engineering disciplines, optomechanics concerns strain more than stress, and with strain requirement being more demanding (∼0.001 of yield strain as compared to ∼0.01 of yield strain for typical mechanical engineering applications) [96]. Thereby, it is needed to understand stiffness of the optical components to estimate its deformation given expected external loads (i.e., mounting constraints, thermal expansion, and acceleration).

Although the transmission geometry of CAT grating brings many benefits (relaxed alignment requirements and low mass) [50], a CAT grating as a 'freestanding' structure requires careful mechanical analysis to maintain its structural integrity during assembly, launch, and decade-long operation in harsh space environment. Out-of-plane buckling of the CAT grating membrane is one of the distortion modes [48] that can sometimes lead to performance degradation.

Taking a closer look at CAT grating structural hierarchy, it can be assumed

that stiffness (i.e., axial, shear, bending, and twisting) are dominated by hexagonal level-2 structural support; the L1 and grating 'membrane' are ∼100x thinner than the hexagonal structural support. Thus, given external loads or displacements, the bulky, rigid hexagonal structural support takes the great part of the load while thin, flimsy level-1 and grating 'membrane' just conform to however the hexagonal support moves.

Since the length scale of a single hexagonal 'unit cell' (∼1 mm) is an order of magnitude smaller than the aperture of the state-of-the-art CAT grating (∼ 30 mm), it is reasonable to analyze the representative volume element (RVE) of the periodic hexagonal lattice with periodic boundary conditions [17, 59] to simplify the problem. Using strain-energy based homogenization [53, 93, 54, 55], the RVE of hexagonal lattice can be considered as a thin continuous 2-dimensional meta-material having macroscopic 'effective properties' which depend on the dimensions of its members, the applied loading, and the properties of the constituent materials.

With previous assumptions in mind, the following question arises: 'Is the hexagonal periodic lattice the optimal lattice topology to maximize stiffness given a certain targeted open area fraction?'.

Effective mechanical properties of 2d-periodic lattices have attracted a lot of interest in the aerospace community to study mechanical performance of sandwich structures [63, 98, 32, 54, 65, 19, 95]. However, only the in-plane stretching/shear or out-of-plane compression were of major interest since the honeycomb core in a sandwich structure was strengthed by facesheets that are placed far from the neutral axis to resist out-of-plane bending/twisting. However, for thin optical components, out-of-plane bending and twisting stiffness of 2d-periodic lattice need to be considered since those usually deform through bending and twisting and can't be strengthened with facesheets.

In this chapter, three basic 2d periodic lattices (square, triangle, and hexagon) were studied, and their averaged (or effective) stiffness tensors were derived both

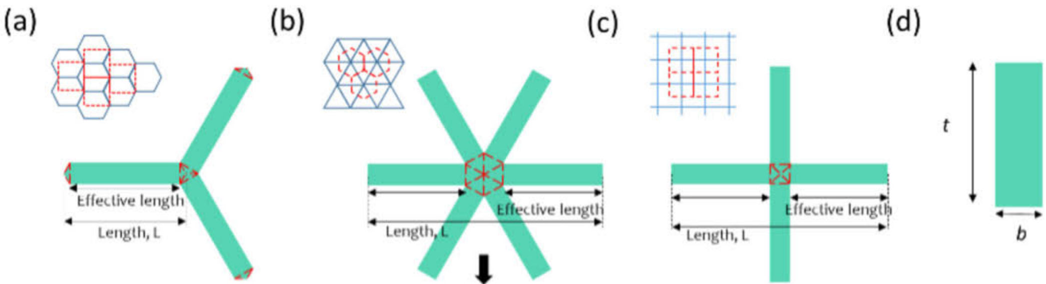

Figure 5-1: Representative volume elements for (a) hexagonal, (b) triangular, and (c) square periodic lattices. (d) Cross-section of the constituent beam.

analytically and numerically. Not restricting our attention to in-plane mechanical properties, out-of-plane bending and twisting properties of 2d periodic lattices were derived with a general continuum approximation. To the author's knowledge, it is the first study to analyze out-of-plane response of 2d periodic lattices. Results from analytical solutions and finite element analysis show close agreement with each other when the same Euler Bernoulli assumption is used. The Timoshenko beam element was also used to better approximate the 'stocky' beam when out-of-plane bending behavior is considered. Results show significant difference for out-of-plane stiffness (D_{11} or D_{66}) when modeled with Euler or Timoshenko beam theory. Noting that material from intersecting beams overlaps at the nodal junctions, another set of finite element simulations was performed, treating nodal junction as a rigid body while constituent beams with 'effective' length were clamped to the nodal junction. As low-density (or high open area fraction) lattices are of interest in this thesis, only 5-10% of differences in stiffnesses are shown between the results where lattices with 'full' beam length were considered and those treating nodal junction with beams with 'effective' length attached to it. This differs from results usually achieved in metamaterial community, where high-density meta-materials are of great interests for structural applications [75].

5.1 Problem formulation

Figure 5-1(a-c) shows representative volume elements (RVEs) of 2d periodic lattices (square, triangle, and hexagon). Simple Euler-Bernoulli and Timoshenko beam theory were used to model the RVEs. Figure 5-1d shows cross-section of the constituent beams. The area within the red dotted lines are termed 'nodal junction' where the material from intersecting beams overlaps. As opposed to additive manufacturing community whose primary interest is on high-density metamaterials [94, 66], space optical components needs to be low density (or light-weight). For our application, 2D lattices with low density (or high open area fraction) are of main interest as we desire to minimize blockage of x-rays; the structural support only needs to be strong enough for structural integrity during manufacturing, launch, and operations.

Optical area fraction, $f = 1 - \rho$ where ρ is an areal density of the unit cell, is introduced as a measure to quantify area fraction where photons can transmit without being blocked by the structural support. Optical area fraction of the RVEs are derived as follows:

$$\begin{aligned} f_{Hex} &= 1 - \frac{2}{\sqrt{3}}\frac{b}{L} + \frac{1}{3}(\frac{b}{L})^2 \\ f_{Tri} &= 1 - 2\sqrt{3}\frac{b}{L} + 3(\frac{b}{L})^2 \\ f_{Sqr} &= (1 - b/L)^2 \end{aligned} \tag{5.1}$$

where b and L are defined in Fig. 5-1.

The state-of-the-art CAT grating uses a hexagonal lattice with optical area fraction of 0.82, and it is planned to dial it up to 0.9 for future x-ray telescope missions. For 2d-lattices with large optical area fraction, the amount of material in the nodal junction is negligibly small compared to those inside the constituent beams. Therefore, it may be enough to neglect material overlap at the junction, modelling RVEs

with constituent beams with 'full' length being rigidly adjoined at the nodal 'point' (to be called 'nodal point model' in the thesis). On the other hand, if material overlap at the nodal junction is to be considered, a nodal junction can be considered 'rigid', with adjoining beams with 'effective' length, L_{eff} attached to the junction (see Fig. 5-1a-c) (called 'rigid body nodal junction model'). For both cases, the RVEs react to the external load 'only' by deformation of adjoining beams (axial stretching, bending, and twisting).

As CAT gratings are fabricated with a standard 500-μm thick silicon-on-insulator wafer, material and thickness of the periodic lattices are fixed. Narrowing the width of the lattice is discouraged as it would reduce process window for deep-reactive ion etching (the beam can be tapered during etching) to define the periodic lattice [9]. Therefore, we performed a parametric study with length L of the beams only to study 'effective' mechanical properties of 2d periodic lattices as a function of open area fraction f. As the Zener anisotropy index of cubic-symmetric crystalline silicon is small (1.56), base material for adjoining beams is assumed to be isotropic silicon for simplicity [78]. Since 2d lattice topology with 3, 6 fold symmetries are mathematically isotropic, hexagonal and triangular lattices are considered transversely isotropic while square lattice is considered cubic symmetric. As only small strain or deformation of optical components are concerned, linear elastic behavior of constituent material is assumed.

5.2 Methodology

A hexagonal lattice is used as an example to explain the procedure (Fig. 5-1a). Considering a uniform strain, $\epsilon^*_{\alpha\beta}$ applied across the boundary of the RVE of a hexagonal lattice, displacement at the boundary is given as (with index notation):

$$u_\alpha = \epsilon^*_{\alpha\beta} x_\beta \tag{5.2}$$

where x_β indicates coordinates along 1 (x direction) or 2 (y direction), and α, $\beta = 1$ (x direction) or 2 (y direction).

The average strain is defined as:

$$\bar{\epsilon}_{\alpha\beta} = \frac{1}{A} \int_A \epsilon_{\alpha\beta}(\underline{x})\, dA \tag{5.3}$$

where A is an area of the RVE, and $\epsilon_{\alpha\beta}(\underline{x})$ is a strain that is spatially varying within the RVE.

Using work-energy balance (i.e., work done by the boundary traction and body force equals the total elastic energy stored in the body), and substituting equation 5.2 into equation 5.3 and using the divergence theorem, it is concluded that average strain is equal to the assumed uniform strain $\epsilon^*_{\alpha\beta}$:

$$\begin{aligned} \bar{\epsilon}_{\alpha\beta} &= \frac{1}{2A} \int_{\partial R} [u_\alpha n^{RVE}_\beta + u_\beta n^{RVE}_\alpha]\, dL \\ &= \frac{1}{2A} \int_{\partial R} [\epsilon^*_{\alpha\sigma} x_\sigma n^{RVE}_\beta + \epsilon^*_{\beta\sigma} x_\sigma n^{RVE}_\alpha]\, dL \\ &= \frac{1}{2A} \int_A [\epsilon^*_{\alpha\sigma} \delta_{\sigma\beta} + \epsilon^*_{\beta\sigma} \delta_{\sigma\alpha}]\, dA = \epsilon^*_{\alpha\beta} \end{aligned} \tag{5.4}$$

where ∂R is a boundary of the RVE and n^{RVE}_α (or n^{RVE}_β) is a unit outward normal vector of RVE.

Plane stress condition is assumed since in-plane length scale for the RVEs of interest is larger than its thickness. With assumed uniform strain, the stress within the RVE is represented as:

$$\sigma_{\alpha\beta}(\underline{x}) = f_{\alpha\beta\sigma\gamma}(\underline{x}) \epsilon^*_{\sigma\gamma} \tag{5.5}$$

where $f_{\alpha\beta\sigma\gamma}(\underline{x})$ is an elasticity tensor that is spatially varying over the domain of the RVE.

Using equations 5.4-5.5, average stress can be calculated:

$$\bar{\sigma}_{\alpha\beta} = \frac{1}{A}\int_A \sigma_{\alpha\beta}(\underline{x})\, dA = \frac{1}{A}\int_A f_{\alpha\beta\sigma\gamma}(\underline{x})\, dA\epsilon^*_{\sigma\gamma} = \bar{C}_{\alpha\beta\sigma\gamma}\epsilon^*_{\sigma\gamma} \tag{5.6}$$

where $\bar{\sigma}_{\alpha\beta}$ and $\bar{C}_{\alpha\beta\sigma\gamma}$ are averaged stress and averaged (or effective) elasticity tensor in the plane stress condition. It has to be emphasized that the linear relationship between averaged stress and averaged strain (eqn. 5.6) holds only when uniform strain is applied across the RVE (since average strain is treated as constant in eqn. 5.6 only when it is uniform across RVEs).

5.2.1 Constitutive relationship between average membrane stress and average (or uniform) strain

For in-plane analysis, given a uniform strain $\epsilon^*_{\alpha\beta}$, the applied displacement boundary condition is constant along the thickness direction. Therefore, similar to the way plate or membrane structures are described, it is desirable to obtain a thickness-averaged stress-strain relationship. Integrating equation 5.6 along the thickness, the constitutive equation between average membrane stress and averaged (or uniform) strain is obtained:

$$\bar{N}_{\alpha\beta} = \int_{-\frac{t}{2}}^{\frac{t}{2}} \bar{\sigma}_{\alpha\beta} dz = \int_{-\frac{t}{2}}^{\frac{t}{2}} \bar{C}_{\alpha\beta\sigma\gamma}\epsilon^*_{\sigma\gamma} dz = \bar{C}_{\alpha\beta\sigma\gamma} t \epsilon^*_{\sigma\gamma} \tag{5.7}$$

where $\bar{N}_{\alpha\beta}$ is an averaged membrane stress, and $C^{eff}_{\alpha\beta\sigma\gamma}$=$\bar{C}_{\alpha\beta\sigma\gamma}t$ indicates the 'effective' membrane elasticity tensor that is desired to compute from in-plane analysis.

5.2.2 Constitutive relationship between average plate bending moment and average (or uniform) curvature

Out-of-plane analysis is performed to obtain the stress-strain relationship between plate bending moment $M_{\alpha\beta}$ and applied uniform curvature $\kappa^*_{\sigma\gamma}$. Suppose that a uniform curvature $\kappa^*_{\sigma\gamma}$ is applied over the boundary of the RVE for a hexagonal lattice. Based on the kinematic assumption for Kirchoff plate that 'straight lines initially normal to the mid-plane remain straight and normal after deformation', a strain field is described to be linearly varying through thickness:

$$\epsilon_{\sigma\gamma} = z\kappa^*_{\sigma\gamma} \tag{5.8}$$

Note that, for out-of-plane analysis, $\epsilon^*_{\sigma\gamma}$ is a function of z only. Therefore, the linear relationship between average stress and average strain still holds according to equation 5.6 (z variable is not involved in areal-integration).

Integrating equation 5.6 along the thickness, the constitutive relation between plate bending moment $M_{\alpha\beta}$ and applied uniform curvature $\kappa^*_{\sigma\gamma}$ is derived as follows:

$$\bar{M}_{\alpha\beta} = \int_{-\frac{t}{2}}^{\frac{t}{2}} \bar{\sigma}_{\alpha\beta} z dz = \int_{-\frac{t}{2}}^{\frac{t}{2}} \bar{C}_{\alpha\beta\sigma\gamma}\kappa^*_{\sigma\gamma} z^2 dz = \bar{C}_{\alpha\beta\sigma\gamma}\frac{t^3}{12}\kappa^*_{\sigma\gamma} \tag{5.9}$$

where $\bar{M}_{\alpha\beta}$ is an average plate bending moment $D^{eff}_{\alpha\beta\sigma\gamma}$=$\bar{C}_{\alpha\beta\sigma\gamma}\frac{t^3}{12}$ indicates 'effective' plate bending rigidity of the RVE that is desired to derive from out-of-plane analysis.

5.2.3 General constitutive relation of 2d-periodic lattice

Putting equations 5.7 and 5.9 together, a generalized constitutive relation between averaged stress and applied strain for an 'effective' cubic-symmetric material (when

axis is aligned with the principal direction of the RVE) is derived:

$$\begin{bmatrix} N_{11} \\ N_{22} \\ N_{12} \\ M_{11} \\ M_{22} \\ M_{12} \end{bmatrix} = \begin{bmatrix} \bar{C}_{1111}t & \bar{C}_{1122}t & 0 & 0 & 0 & 0 \\ \bar{C}_{1122}t & \bar{C}_{2222}t & 0 & 0 & 0 & 0 \\ 0 & 0 & \bar{C}_{1212}t & 0 & 0 & 0 \\ 0 & 0 & 0 & \bar{C}_{1111}\frac{t^3}{12} & \bar{C}_{1122}\frac{t^3}{12} & 0 \\ 0 & 0 & 0 & \bar{C}_{1122}\frac{t^3}{12} & \bar{C}_{2222}\frac{t^3}{12} & 0 \\ 0 & 0 & 0 & 0 & 0 & \bar{C}_{1212}\frac{t^3}{12} \end{bmatrix} \begin{bmatrix} \epsilon_{11} \\ \epsilon_{22} \\ 2\epsilon_{12} \\ \kappa_{11} \\ \kappa_{22} \\ 2\kappa_{12} \end{bmatrix} \tag{5.10}$$

where each component of the stiffness tensor represents 'effective' stiffness of assumed RVE with a homogeneous effective medium. $\bar{C}_{1111}t$, $\bar{C}_{2222}t$ indicate membrane axial stretching stiffness along x, y directions, $\bar{C}_{1122}t$ indicates membrane shear stiffness, $\bar{C}_{1111}\frac{t^3}{12}$, $\bar{C}_{2222}\frac{t^3}{12}$ indicate plate bending rigidity, and $\bar{C}_{1122}\frac{t^3}{12}$ indicates plate twisting rigidity for the RVE of interest. Note that the above equation 5.10 holds only when homogeneous (or uniform) displacement boundary conditions are applied. The equation applies to isotropic material as well since isotopic material is a subset of cubic-symmetric material. For an 'effective' isotropic lattice such as hexagon and triangle, $\bar{C}_{1111}$=$\bar{C}_{2222}$ and 2$\bar{C}_{1212}$=$\bar{C}_{1111}$-$\bar{C}_{1122}$.

5.2.4 Strain-energy based homogenization

Since it is non-trivial to derive $\bar{C}_{\alpha\beta\sigma\gamma}$ by spatially averaging the elasticity tensor $f_{\alpha\beta\sigma\gamma}(\underline{x})$ across the RVE (it requires solving complex 2-d elasticity problem), an alternative approach based on strain-energy based homogenization [53, 54, 55, 63, 93] is used to obtain the stiffness components in equation 5.10. For this method, an RVE with same size but consisting of a homogeneous 'effective' medium is considered. A new RVE is comprised of an 'effective' material such that it stores the same strain energy as the original RVE when the same displacement or traction boundary conditions (or both), $u(x)$ and $t(x)$ are applied (see Fig. 5-2). For our purpose, the homogeneous displacement boundary condition is applied to calculate the strain energy; uniform

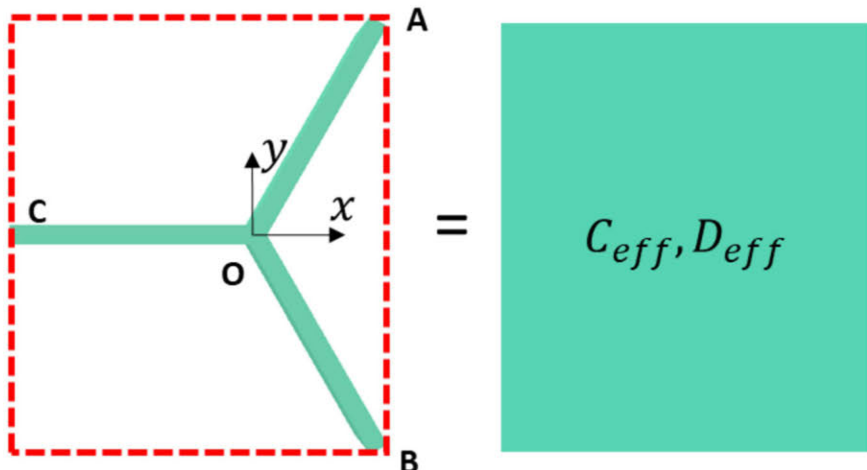

Figure 5-2: A hexagonal lattice (left) and the corresponding RVE with the same size but consisting of homogeneous 'effective' materials (right).

strain, $\epsilon^*_{\sigma\gamma}$, for in-plane analysis and uniform curvature $\kappa^*_{\sigma\gamma}$ for out-of-plane analysis.

Average strain energy stored in an RVE is:

$$\bar{W} = \frac{1}{2}\bar{\sigma}_{\alpha\beta}\epsilon^*_{\alpha\beta}, \tag{5.11}$$

For in-plane analysis, given a constant strain, thickness-integrated strain-energy (i.e., areal strain energy density) for the given RVE is

$$\Psi = \int_{-\frac{t}{2}}^{\frac{t}{2}} \bar{W} dz = \int_{-\frac{t}{2}}^{\frac{t}{2}} \frac{1}{2}\bar{\sigma}_{\alpha\beta}\bar{\epsilon_{\alpha\beta}} dz = \frac{t}{2}\bar{C}_{\alpha\beta\sigma\gamma}\epsilon^*_{\alpha\beta}\epsilon^*_{\sigma\gamma} \tag{5.12}$$

Calculating the second derivative of the thickness-integrated strain-energy with respect to averaged strain, $\bar{\epsilon}_{\alpha\beta}$ (or uniform strain $\epsilon^*_{\alpha\beta}$), the stiffness components relating membrane stiffness and in-plane strain are derived (see equation 5.7):

$$\frac{\partial^2\Psi}{\partial\bar{\epsilon_{\alpha\beta}}\partial\bar{\epsilon_{\sigma\gamma}}} = \bar{C}_{\alpha\beta\sigma\gamma}t = C^{eff}_{\alpha\beta\sigma\gamma} \tag{5.13}$$

Similarly for out-of-plane analysis, given a constant curvature, thickness-integrated

strain energy (i.e., areal strain energy density) for the given RVE is:

$$\Psi = \int_{-\frac{t}{2}}^{\frac{t}{2}} \bar{W} dz = \int_{-\frac{t}{2}}^{\frac{t}{2}} \frac{1}{2} \bar{\sigma}_{\alpha\beta} \bar{\epsilon_{\alpha\beta}} dz = \int_{-\frac{t}{2}}^{\frac{t}{2}} \frac{1}{2} \bar{C}_{\alpha\beta\sigma\gamma} \kappa^*_{\alpha\beta} \kappa^*_{\sigma\gamma} z^2 dz = \frac{t^3}{24} \bar{C}_{\alpha\beta\sigma\gamma} \kappa^*_{\alpha\beta} \kappa^*_{\sigma\gamma} \quad (5.14)$$

By performing second-order differentiation of areal strain energy density Ψ with respect to averaged (or uniform) curvature $\bar{\kappa}_{\alpha\beta} = \kappa^*_{\alpha\beta}$, the stiffness components relating plate bending moment and curvature are derived (see equation 5.9):

$$\frac{\partial^2 \Psi}{\partial \bar{\kappa_{\alpha\beta}} \partial \bar{\kappa_{\sigma\gamma}}} = \bar{C}_{\alpha\beta\sigma\gamma} \frac{t^3}{12} = D^{eff}_{\alpha\beta\sigma\gamma} \quad (5.15)$$

Taken together, for any given 2-d periodic lattice, a general constitutive relation (equation 5.10) relating membrane stress with in-plane strain and plate bending rigidity with curvature can be derived.

5.3 Analytical

5.3.1 Calculation of strain energy

In order to calculate stiffness components for the chosen RVEs, it is required to first calculate the strain energy as displacement boundary conditions are applied. Herein, I describe a method to calculate strain energy of RVEs analytically. The hexagonal lattice will be used as an example to illustrate the calculation procedure of strain energy with a simple Euler beam theory. A nodal junction is treated as 'rigid' point, and only the energy contribution from beam deformation is assumed. Fig. 5-3a shows RVE of hexagonal lattice with beam end A,B,C, and rigid nodal point O.

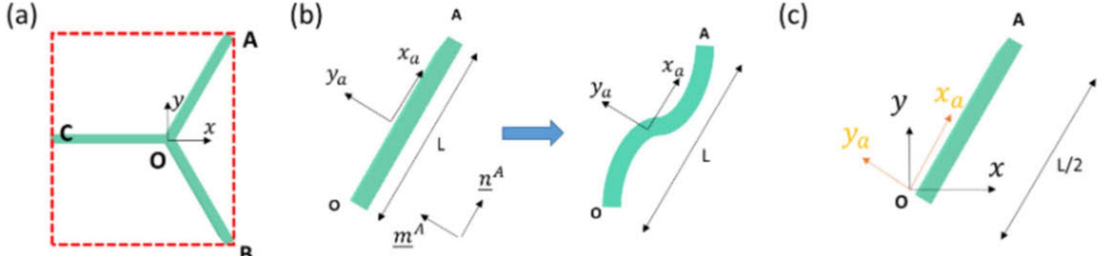

Figure 5-3: (a) Unit cell for hexagonal lattice. Red dashed lines indicate boundary of the unit cell. A unit cell consists of three beams AO, BO, and CO which intersect at the point O. (b) A schematic showing deformation of Beam AO as displacement boundary conditions are applied for in-plane analysis. Local coordinate (x_a, y_a) and local basis vectors (m_j, n_j) are shown. Note that the beams are deformed such that the beam-ends are all rotated in the same manner as induced by periodic boundary condition. (c) A schematic showing local coordinates for beam AO used in out-of-plane analysis (before deformation). Unlike in-plane analysis, the local coordinates are placed at the beam end at the junction O.

In-plane case

Given a uniform strain $\epsilon^*_{\alpha\beta}$, displacements at the boundaries are obtained according to equation 5.2:

$$u^J_\alpha(x_\beta) = \epsilon^*_{\alpha\beta} x^J_\beta \tag{5.16}$$

where J can be A,B,C (see Fig. 5-3). It is assumed that the boundary conditions for each constituent beam are considered clamped at both ends to adjoining rigid nodal junctions. The beams are considered to stretch or bend transversely to accommodate the displacement field applied at the boundary (A,B,C). Free variables $\underline{u}^O$=(u^O, v^O, ϕ^O) are introduced at the nodal junction, where u^O and v^O are displacement along x and y, and ϕ^O is a rotation around z of the nodal junction point O. These free variables spontaneously find their positions to minimize the total strain energy once virtual uniform strain $\epsilon^*_{\alpha\beta}$ is applied (as discussed later). From the periodicity of hexagonal lattice, rotation degree of freedom ϕ is equal at all the nodes A,B,C,and O (3-fold symmetry of the hexagonal lattice also support this fact since the lattice is rotationally invariant by 60 degrees):

$$\phi^O = \phi^A = \phi^B = \phi^C \tag{5.17}$$

Therefore, each constituent beam deflects in such a way that it is odd-symmetric about the center of the beam. Fig. 5-3b shows beam AO as an example to visualize its configuration before and after deformation. For each constituent beam JO, relative displacement between node J and nodal junction O is derived using equation 5.16 and free variable (u^O, v^O):

$$\Delta \underline{u}^{JO} = (u^J - u^O, v^J - v^O) \tag{5.18}$$

Local coordinate (x_j, y_j) and local orthonormal basis vector (m_j, n_j) are introduced for each constituent beam (see Fig. 5-3b). Right image of Fig. 5-3b visualizes beam AO deformed once virtual strain is applied. Note that the rotation of the beam end in the deformed configuration is the same based on periodic boundary condition. Projecting relative displacements $\Delta \underline{u}^{JO}$ onto local basis vectors, axial stretching Δu_{JO}^{axial} and transverse bending deflection Δu_{JO}^{bend} for beam JO are derived:

$$\begin{aligned} \Delta_{JO}^{axial} &= \Delta \underline{u}^{JO} \cdot \underline{n}_j \\ \Delta_{JO}^{bend} &= \Delta \underline{u}^{JO} \cdot \underline{m}_j \end{aligned} \tag{5.19}$$

Along with beam dimensions (length, thickness, and width L, t, and b) and material property (Young's modulus E), the axial stretching energy is:

$$U_{JO}^{axial} = \frac{1}{2} \frac{Ebt}{L} (\Delta_{JO}^{axial})^2 \tag{5.20}$$

The boundary conditions of beam JO represented in the local axes $(x_j,\, y_j)$ where

j=a, b, c; see Fig. 5-3b) are:

$$
\begin{aligned}
v'(x_j = \frac{L}{2}) = \phi^O \\
v'(x_j = -\frac{L}{2}) = \phi^O \\
v(x_j = \frac{L}{2}) = \frac{\Delta_{JO}^{bend}}{2} \\
v(x_j = -\frac{L}{2}) = -\frac{\Delta_{JO}^{bend}}{2}
\end{aligned}
\tag{5.21}
$$

Based on boundary conditions given above and following Euler-Bernoulli beam theory, bending energy is calculated as:

$$
U_{JO}^{bend} = \frac{1}{2}\int_{-\frac{L}{2}}^{\frac{L}{2}} EI_b \frac{\partial^2 v(x_j)}{\partial x_j^2} dz = \frac{6EI_b(L\phi - \Delta_{JO}^{bend})^2}{L^3} \tag{5.22}
$$

where $I_b = \frac{tb^3}{12}$.

Summing axial and bending energy of all the adjoining beams, total strain energy stored in the RVE is expressed as:

$$
U_{JO} = \sum_J U_{JO}^{axial} + U_{JO}^{bend} \tag{5.23}
$$

where J=A,B,C.

Dividing U by the area of unit cell A_{cell}, areal strain energy density $\Psi=\frac{U}{A}$ is derived. The resulting Ψ is the same entity as shown in equation 5.12, but derived with simple beam theory.

Thus far, the derived areal strain energy density Ψ is dependent on free variables $\underline{u}^O$=(u^O, v^O, ϕ^O). The free variables can be found by principle of energy minimization of the RVE; as virtual strain $\epsilon_{\alpha\beta}$ is applied, the free variables find their positions to

minimize the total strain energy of the RVE.

$$\frac{\partial \Psi}{\partial \underline{u}^O} = 0 \tag{5.24}$$

Since free variables are expressed as a function of axial or bending stiffness, areal strain energy density is derived as:

$$\Psi = f(E, \underline{x}^J, \underline{u}^O) = f(\underline{x}^J, \frac{Ebt}{L}, \frac{3EI_b}{L^3}) \tag{5.25}$$

where $\underline{x}^J$ indicates nodal coordinate at the beam-end J, $\frac{Ebt}{L}$ and $\frac{3EI}{L^3}$ are axial and bending stiffness. Using equation 5.13, analytical solution for elasticity component for in-plane mode, $C^{eff}_{\alpha\beta\sigma\gamma}$=$C_{\alpha\beta\sigma\gamma}t$ is derived.

Out-of-plane case

Out-of-plane displacement at the boundary is approximated using a Taylor series, $w = w(0) + \frac{\partial w}{\partial x}x + \frac{\partial w}{\partial y}y + \frac{1}{2}\frac{\partial^2 w}{\partial x^2}x^2 + \frac{1}{2}\frac{\partial^2 w}{\partial y^2}y^2 + \frac{\partial^2 w}{\partial x \partial y}xy$. The origin for the RVE is placed at the nodal junction. Neglecting rigid-body translation and rotation terms, the out-of-plane displacement and tip/tilt at the boundary are approximated as

$$w^J = \frac{1}{2}\kappa^*_{11}(x^J)^2 + \frac{1}{2}\kappa^*_{22}(y^J)^2 + \kappa_{12}x^J y^J = P^J_{\alpha\beta}\kappa^*_{\alpha\beta} \tag{5.26}$$

$$\frac{\partial w}{\partial x}(\underline{x}^J) = \kappa^*_{11}x^J + \kappa^*_{12}y^J \tag{5.27}$$

$$\frac{\partial w}{\partial y}(\underline{x}^J) = \kappa^*_{22}y^J + \kappa^*_{12}x^J \tag{5.28}$$

where $\kappa^*_{\alpha\beta} = \begin{bmatrix} \kappa^*_{11} & \kappa^*_{12} \\ \kappa^*_{21} & \kappa^*_{22} \end{bmatrix}$ indicates uniform curvature applied across the boundary, $P^J_{\alpha\beta} = \begin{bmatrix} \frac{1}{2}(x^J)^2 & \frac{1}{2}x^J y^J \\ \frac{1}{2}x^J y^J & \frac{1}{2}(y^J)^2 \end{bmatrix}$ is a tensor introduced to simplify expression for eqn. 5.26, $\underline{x}^J$

$= (x^J, y^J)$ the coordinates at the end of beam J, and w^J the out-of-plane displacement of the beam end J. J can be A,B,C for the hexagonal lattice (see Fig. 5-3). Similar to in-plane analysis, beam ends are assumed to be clamped to the adjacent rigid nodal junction at both ends. With no in-plane displacements of beam ends, each constituent beam is considered to bend and twist out of the page to accommodate the displacements at the boundary. Warping of the rectangular cross-section was neglected for simplicity.

Free variables $\underline{w}^O=(\frac{\partial w}{\partial x}|_O, \frac{\partial w}{\partial y}|_O, w^O)$ are introduced at the nodal junction, where w_O is an out-of-plane displacement and $\theta_1^O=\frac{\partial w}{\partial x}(\underline{x}^O)$ and $\theta_2^O=\frac{\partial w}{\partial y}(\underline{x}^O)$ are slopes along x and y at the nodal junction O (See Fig. 5-3c). These free variables at node O find its way to minimize the total strain energy once (virtual) uniform curvature $\kappa^*_{\alpha\beta}$ is applied (discussed later). Since warping at the beam-ends is neglected, the periodic boundary condition doesn't impose any kinematic constraint, thereby energy contribution from constrained warping is neglected (i.e., as neighboring RVEs can be rigidly rotated and translated to attach to the original RVE, periodic boundary condition doesn't apply kinematic constraints at the beam-ends).

Introducing local coordinate (x_j, y_j) for each constituent beam, the boundary conditions are represented in local coordinates with coordinate transformation as follows:

$$\theta_\alpha^{J,j} = R^j_{\alpha\beta}\frac{1}{2}(\kappa^*_{\beta\gamma} + \kappa^*_{\gamma\beta})x^J_\gamma \tag{5.29}$$

where $R^j_{\alpha\beta}$ is an operator to perform coordinate transformation of beam JO from global (or lattice) coordinates (x,y) to local coordinates $(x_j,\ y_j)$, $\theta_1^{J,j}=\frac{\partial w}{\partial x_j}(\underline{x^J})$ and $\theta_2^{J,j}=\frac{\partial w}{\partial y_j}(\underline{x^J})$ bending and twisting angles of the beam at J in local coordinate $\underline{x}_j=(x_j,$ $y_j)$. x^J_γ are coordinates at the beam-end J.

The boundary conditions of beam JO are represented in the local axis as:

$$
\begin{aligned}
\frac{\partial w}{\partial x_j}(x_j = L/2) = \theta_1^{J,j} \\
\frac{\partial w}{\partial x_j}(x_j = 0) = \theta_1^{O,j} \\
w(x_j = L/2) = \frac{1}{2}\kappa_{11}^*(x^J)^2 + \frac{1}{2}\kappa_{22}^*(y^J)^2 + \kappa_{12}^* x^J y^J = P_{\alpha\beta}^J \kappa_{\alpha\beta}^* \\
w(x_j = 0) = w^O
\end{aligned}
\tag{5.30}
$$

Based on boundary conditions given above and following Euler-Bernoulli beam theory, bending energy is calculated as:

$$
U_j^{bend} = \frac{1}{2}\int_0^{\frac{L}{2}} EI_t((w(x_j))'')^2 dx_j \tag{5.31}
$$

where $I_t = \frac{bt^3}{12}$ (please note that the moment of inertia, I_t, are different for in-plane and out-of-plane cases).

Neglecting energy contribution from constrained warping, the twisting energy is:

$$
U_j^{twist} = \frac{\beta G t w^3}{L}(\theta_2^{J,j} - \theta_2^{O,j})^2 \tag{5.32}
$$

where β is a torsional constant for rectangular beam, G is a shear modulus, $\theta_2^{J,j} = \frac{1}{2}R_{\alpha\beta}^j(\kappa_{\beta\gamma}^* + \kappa_{\gamma\beta}^*)x_\gamma^J$ and $\theta_2^{O,j} = R_{2\beta}^j \theta_\beta^O$.

Summing bending and twisting energy of all the adjoining beams:

$$
U = \sum_j U_j^{bend} + U_j^{twist} \tag{5.33}
$$

Dividing U by area of the unit lattice A, areal strain energy density $\Psi=\frac{U}{A}$ is derived. The resulting Ψ is the same entity as shown in equation 5.14, but derived using Kirchoff plate approximation for RVE and Euler beam theory for each constituent beam. Note that strain energy from the rigid nodal entity and constrained warping

was neglected.

Similar to in-plane analysis, free variables $\underline{w}_O$ spontaneously find their optimal values to minimize total strain energy of the RVE once virtual uniform curvature $\kappa^*_{\alpha\beta}$ is applied.

$$\frac{\partial \Psi}{\partial \underline{w}^O} = 0 \tag{5.34}$$

Therefore,

$$\Psi = f(E, \underline{x}^J, \underline{w}^O) = f(\underline{x}^J, \frac{\beta G t w^3}{L}, \frac{3EI_t}{L^3}) \tag{5.35}$$

where $\underline{x}^J$ indicates nodal coordinates at the beam-end J, $\frac{3EI_t}{L^3}$ and $\frac{\beta G t w^3}{L}$ are bending and twisting stiffness. Using equation 5.15, the analytical solution of elasticity component for out-of-plane mode, $D^{eff}_{\alpha\beta\sigma\gamma}$=$\bar{C}_{\alpha\beta\sigma\gamma}\frac{t^3}{12}$ is derived.

5.3.2 Full analytical solution

The same procedure described in the previous section is applied to the chosen RVEs. Hexagonal lattice is used as an example to derive the full analytical solution. Analytical expressions for all the lattices are identical except that number of beams J, coordinates of the beam ends, and coordinate transformation operators, $R^j_{\alpha\beta}$ are different. MATLAB scripts to perform calculations of full analytical solution on in-plane and out-of-plane stiffness tensors are provided in Appenidx A.

In-plane result

Total strain energy for a given 2d lattice is calculated by 5.20, 5.22, and 5.23. Areal strain energy density Ψ is derived by dividing total strain energy with area A. Free

variables are calculated using equation 5.24:

$$\begin{bmatrix} 3L & \sum_J m_1^J & \sum_J m_2^J \\ \frac{12EI_b}{L^2}\sum_J m_1^J & \sum_J(\frac{EA_{beam}}{L}(n_1^J)^2 + \frac{12EI_b}{L^3}(m_1^J)^2) & \sum_J(\frac{EA_{beam}}{L}n_1^J n_2^J + \frac{12EI_b}{L^3}m_1^J m_2^J) \\ \frac{12EI_b}{L^2}\sum_J m_2^J & \sum_J(\frac{EA_{beam}}{L}n_1^J n_2^J + \frac{12EI_b}{L^3}m_1^J m_2^J) & \sum_J(\frac{EA_{beam}}{L}(n_2^J)^2 + \frac{12EI_b}{L^3}(m_2^J)^2) \end{bmatrix} \begin{bmatrix} \phi \\ u_1^O \\ u_2^O \end{bmatrix}$$
$$= \begin{bmatrix} \sum_J(\epsilon_{\alpha\beta}x_\beta^J m_\alpha^J) \\ \sum_J(\frac{EA_{beam}}{L}\epsilon_{\alpha\beta}x_\beta^J n_\alpha^J n_1^J + \frac{12EI_b}{L^3}\epsilon_{\alpha\beta}x_\beta^J m_\alpha^J m_1^J) \\ \sum_J(\frac{EA_{beam}}{L}\epsilon_{\alpha\beta}x_\beta^J n_\alpha^J n_2^J + \frac{12EI_b}{L^3}\epsilon_{\alpha\beta}x_\beta^J m_\alpha^J m_2^J) \end{bmatrix} \tag{5.36}$$

Axial and bending stiffness tensors are calculated using equation 5.13. The results are:

$$C_{\sigma\gamma\delta\kappa}^{Axial,eff} = \frac{1}{A_{cell}}\sum_J(\frac{EA_{beam}}{L}x_\delta^J n_\kappa^J(x_\gamma^J n_\sigma^J - \frac{\partial u_\alpha^O}{\partial \epsilon_{\sigma\gamma}}n_\alpha^J)) \tag{5.37}$$

$$C_{\sigma\gamma\delta\kappa}^{Bend,eff} = \frac{1}{A_{cell}}\sum_J(\frac{12EI_b}{L^3}x_\delta^J m_\kappa^J(x_\gamma^J m_\sigma^J - \frac{\partial u_\alpha^O}{\partial \epsilon_{\sigma\gamma}}m_\alpha^J - L\frac{\partial \phi}{\partial \epsilon_{\sigma\gamma}})) \tag{5.38}$$

where $\frac{\partial u_\alpha^O}{\partial \epsilon_{\sigma\gamma}}$ and $\frac{\partial \phi}{\partial \epsilon_{\sigma\gamma}}$ are derived by performing first order differentiation of eqn. 5.36 with respect to the applied strain.

The effective in-plane stiffness tensor is derived by summing axial and bending elasticity components:

$$C_{\sigma\gamma\delta\kappa}^{eff} = C_{\sigma\gamma\delta\kappa}^{Axial,eff} + C_{\sigma\gamma\delta\kappa}^{Bend,eff} \tag{5.39}$$

Out-of-plane result

Based on boundary conditions in eqn. 5.30, a beam displacement is kinematically defined as follows:

$$w(x_j) = w^O + \frac{L\theta_1^{O,j}}{2}(\frac{x_j}{L/2}) + (3P_{\alpha\beta}^J\kappa_{\alpha\beta}^* - 3w^O - L\theta_1^{O,j} - \frac{L}{4}R_{1\beta}^j(\kappa_{\beta\gamma}^* + \kappa_{\gamma\beta}^*)x_\gamma^J)(\frac{x_j}{L/2})^2 + (\frac{L}{4}R_{1\beta}^j(\kappa_{\beta\gamma} + \kappa_{\gamma\beta}^*)x_\gamma^J - 2P_{\alpha\beta}^J\kappa_{\alpha\beta}^* + 2w^O + \frac{L\theta_1^{O,j}}{2})(\frac{x_j}{L/2})^3$$

where $P_{\alpha\beta}^J = \begin{bmatrix} \frac{1}{2}(x^J)^2 & \frac{1}{2}x^Jy^J \\ \frac{1}{2}x^Jy^J & \frac{1}{2}(y^J)^2 \end{bmatrix}$.

Calculating a second derivative of w with respect to x_j,

$$\begin{aligned}(w(x_j))'' = \frac{8}{L^2}(3P_{\alpha\beta}^J\kappa_{\alpha\beta}^* - 3w^O - L\theta_1^{O,j} - \frac{L}{4}R_{1\beta}^j(\kappa_{\beta\gamma}^* + \kappa_{\gamma\beta})x_\gamma^J) + \\ \frac{48}{L^3}(\frac{L}{4}R_{1\beta}^j(\kappa_{\beta\gamma}^* + \kappa_{\gamma\beta}^*)x_\gamma^J - 2P_{\alpha\beta}^J\kappa_{\alpha\beta}^* + 2w^O + \frac{L\theta_1^{O,j}}{2})x_j \\ = M^J + N^Jx_j\end{aligned} \tag{5.40}$$

Bending strain energy is calculated from equation 5.31

$$U_j^{bend} = \frac{1}{2}\int_0^{\frac{L}{2}} EI_t(M^J + N^Jx_j)^2dx_j = \frac{EI_t}{2}((M^J)^2(L/2) + M^JN^J(L^2/4) + \frac{(N^J)^2}{3}(L^3/8)) \tag{5.41}$$

Twisting strain energy is calculated from equation 5.32.

$$U_j^{twist} = \frac{\beta Gtb^3}{L}(\frac{1}{2}R_{2\beta}^j(\kappa_{\beta\gamma}^* + \kappa_{\gamma\beta}^*)x_\gamma^J - \theta_{2,j}^O)^2 \tag{5.42}$$

Taken together, total strain energy is calculated by eqn. 5.33. Areal strain energy density Ψ is derived by dividing total strain energy with area A.

Free variables are found using equation 5.34, resulting in system of equations:

$$\begin{bmatrix} 6 & \frac{L}{2}\sum_J R_{11}^J & \frac{L}{2}\sum_J R_{12}^J \\ \frac{24EI_t}{L^2}\sum_J R_{11}^J & \sum_J(\frac{2GJ_b}{L}(R_{21}^J)^2+\frac{8EI_t}{L}(R_{11}^J)^2) & \sum_J(\frac{2GJ_b}{L}(R_{21}^J R_{22}^J)+\frac{8EI_t}{L}(R_{11}^J R_{12}^J)) \\ \frac{24EI_t}{L^2}\sum_J R_{12}^J & \sum_J(\frac{2GJ_b}{L}(R_{21}^J R_{22}^J)+\frac{8EI_t}{L}(R_{11}^J R_{12}^J)) & \sum_J(\frac{2GJ_b}{L}(R_{22}^J)^2+\frac{8EI_t}{L}(R_{12}^J)^2) \end{bmatrix} \begin{bmatrix} w_O \\ \frac{\partial w}{\partial x}|_O \\ \frac{\partial w}{\partial y}|_O \end{bmatrix}$$
$$= \begin{bmatrix} \sum_J 2P_{\alpha\beta}^J \kappa_{\alpha\beta}^* - \sum_J \frac{L}{4}(R_{1\beta}^j(\kappa_{\beta\gamma}^*+\kappa_{\gamma\beta}^*)x_\gamma^J \\ \sum_J \frac{24EI_t}{L^2}(P_{\alpha\beta}^J\kappa_{\alpha\beta}^* R_{11}^j - \sum_J \frac{2EI_t}{L}R_{11}^j R_{1\beta}^j(\kappa_{\beta\gamma}^*+\kappa_{\gamma\beta}^*)x_\gamma^J + \sum_J \frac{\beta Gtb^3}{L}R_{21}^j R_{2\beta}^j(\kappa_{\beta\gamma}^*+\kappa_{\gamma\beta}^*)x^J \\ \sum_J \frac{24EI_t}{L^2}(P_{\alpha\beta}^J\kappa_{\alpha\beta} R_{12}^j - \sum_J \frac{2EI_t}{L}R_{12}^j R_{1\beta}^j(\kappa_{\beta\gamma}^*+\kappa_{\gamma\beta}^*)x_\gamma^J + \sum_J \frac{\beta Gtb^3}{L}R_{22}^j R_{2\beta}^j(\kappa_{\beta\gamma}^*+\kappa_{\gamma\beta}^*)x^J \end{bmatrix} \tag{5.43}$$

where β=0.293 (torsional stiffness constant for rectangular beam cross-section with aspect ratio of 5:1), $P_{\alpha\beta}^J = \begin{bmatrix} \frac{1}{2}(x^J)^2 & \frac{1}{2}x^J y^J \\ \frac{1}{2}x^J y^J & \frac{1}{2}(y^J)^2 \end{bmatrix}$ and $\kappa_{\alpha\beta}^* = \begin{bmatrix} \kappa_{11}^* & \kappa_{12}^* \\ \kappa_{21}^* & \kappa_{22}^* \end{bmatrix}$.

Axial and bending stiffness tensors are calculated using equation 5.15. The results are:

$$D_{\sigma\gamma\delta\kappa}^{Bend,eff} = \sum_J [\frac{EI_t}{2}(L\frac{\partial M^J}{\partial\kappa_{\delta\kappa}}\frac{\partial M^J}{\partial\kappa_{\sigma\gamma}^*} + \frac{L^2}{4}\frac{\partial M^J}{\partial\kappa_{\delta\kappa}^*}\frac{\partial N^J}{\partial\kappa_{\sigma\gamma}^*} + \frac{L^2}{4}\frac{\partial M^J}{\partial\kappa_{\sigma\gamma}^*}\frac{\partial N^J}{\partial\kappa_{\delta\kappa}^*} + \frac{L^3}{12}\frac{\partial N^J}{\partial\kappa_{\delta\kappa}^*}\frac{\partial N^J}{\partial\kappa_{\sigma\gamma}^*})] \tag{5.44}$$

where $\frac{\partial M^J}{\partial\kappa_{\delta\kappa}^*} = \frac{8}{L^2}(3P_{\kappa\delta}^J - \frac{L}{4}(R_{1\kappa}^j x_\delta^J + R_{1\delta}^j x_\kappa^J) - 3\frac{\partial w^O}{\partial\kappa_{\kappa\delta}^*} - R_{1\beta}^j\frac{\partial\theta_\beta^O}{\partial\kappa_{\kappa\delta}^*})$ and $\frac{\partial N^J}{\partial\kappa_{\delta\kappa}^*} = \frac{48}{L^3}(\frac{L^2}{8}(R_{1\kappa}^j x_\delta^J + R_{1\delta}^j x_\kappa^J) - 2P_{\kappa\delta}^J + 2\frac{\partial w^O}{\partial\kappa_{\kappa\delta}^*} + \frac{L}{2}R_{1\beta}^j\frac{\partial\theta_\beta^O}{\partial\kappa_{\kappa\delta}^*})$ (derived by second-order differentiation of M^J andN^J in 5.40 with respect to $\kappa_{\kappa\delta}^*$). $\frac{\partial w^O}{\partial\kappa_{\delta\kappa}^*}$ and $\frac{\partial\theta_\beta^O}{\partial\kappa_{\delta\kappa}^*}$ are derived by first-order differentiation of 5.43 with respect to $\kappa_{\delta\kappa}^*$.

$$D_{\sigma\gamma\delta\kappa}^{Twist,eff} = \sum_J(\frac{2\beta Gtb^3}{L}(\frac{1}{2}(R_{2\kappa}^j x_\delta^J + R_{2\delta}^j x_\kappa^J) - R_{2\beta}^j\frac{\partial\theta_\beta^O}{\partial\kappa_{\sigma\gamma}^*})(\frac{1}{2}(R_{2\kappa}^j x_\delta^J + R_{2\delta}^j x_\kappa^J) - R_{2\beta}^j\frac{\partial\theta_\beta^O}{\partial\kappa_{\delta\kappa}^*})) \tag{5.45}$$

Effective out-of-plane stiffness tensor is derived by summing axial and bending

elasticity component:

$$D^{eff}_{\sigma\gamma\delta\kappa} = D^{Bend}_{\sigma\gamma\delta\kappa} + D^{Twist}_{\sigma\gamma\delta\kappa} \tag{5.46}$$

5.4 Numerical

Elasticity components (or stiffness) in eqn. 5.10 can be obtained through numerical simulation on a single unit cell with commercial Abaqus/standard software. First, the 2d-lattices were modeled using only the beam elements, neglecting material overlap at the nodal junction. Euler and Timoshenko (B33 and B31 for Abaqus element library) beam elements were used for each constituent beam, JO. As Zener anisotropy index of cubic-symmetric crystalline silicon is small (1.56), a base material was modeled as an isotropic linear silicon material with Young's modulus of 169 GPa and Poisson ratio of 0.265 for simplicity. For in-plane analysis, periodic boundary condition, eqn. 5.17, was applied by coupling rotational degree of freedom at each node. Same boundary condition, eqn. 5.16, used for derivation of analytical solution was applied to the boundary (or beam-ends). The following three different displacement boundary conditions were applied to the boundaries (the beam-ends) to obtain in-plane elasticity components ($C_{1111}t = C_{2222}t$, $C_{1122}t$, $C_{1212}t$ in 5.10):

1) Uniaxial strain, ϵ^*_{11} or ϵ^*_{22}, along one of the principal directions (x or y).

2) Pure shear, ϵ^*_{12}

3) Equibiaxial strain, $\epsilon^*_{11} = \epsilon^*_{22} \neq 0$

For out-of-plane analysis, no periodic boundary conditions were applied since warping of the beams was neglected for simplicity. The same boundary condition, eqn. 5.26, used in derivation of analytical solution was applied to the boundary (or beam-ends). The following three different displacement boundary conditions were applied to the boundaries (the beam-ends) to obtain out-of-plane elasticity components ($C_{1111}\frac{t^3}{12} = C_{2222}t\frac{t^3}{12}$, $C_{1122}\frac{t^3}{12}$, $C_{1212}\frac{t^3}{12}$ in 5.10):

1) Uniaxial curvature, κ^*_{11} or κ^*_{22} along one of the principal directions (x or y).

2) Pure twisting, κ^*_{12}

3) Equibiaxial curvature, $\kappa^*_{11} = \kappa^*_{22} \neq 0$

Another set of simulations were performed to understand the effect of a nodal junction. Here, a nodal junction was treated as a rigid 'body' and the adjoining beams with 'effective' length were rigidly attached to the nodal junction (see Fig. 5-1). A discrete rigid element (type R2D2 or R3D3 from Abaqus library) and the Timoshenko beam elements (B21 for in-plane analysis, B31 for out-of-plane analysis from Abaqus library) were used. For rigid nodal junctions, all degrees of freedom at the nodes are constrained to the reference point at its centroid. The adjoining beams were connected to the edges of the rigid body using 'Tie node' constraints and 'BEAM MPC (multi-point constraint)' as offered in Abaqus/Standard to couple both translational and rotational degrees of freedom of the connecting points. For all the simulations, Python scripts were written to perform a parametric study of RVEs with varying beam length. Python scripts for FE studies on in-plane and out-of-plane stiffness of RVEs are included in Appendix B.

5.5 Results and Discussion

A parametric study on length L was performed using both analytical solution and finite element simulation. For each RVE, lengths of the constituent beams were varied such that the open area fraction of the lattices fall within the range of 0.82-0.92 as calculated from eqn. 5.1. For the hexagonal lattice, beam length was varied from 0.555-1.255 mm with 0.05 mm of interval, square lattice from 1 to 2.1 mm with 0.079 mm of interval, triangular lattice from 1.7 to 3.6 mm with 0.136 mm of interval. A current state-of-the-art CAT grating is designed with hexagonal lattice and optical area fraction of 0.82 (corresponding to 0.555 mm of beam length). In

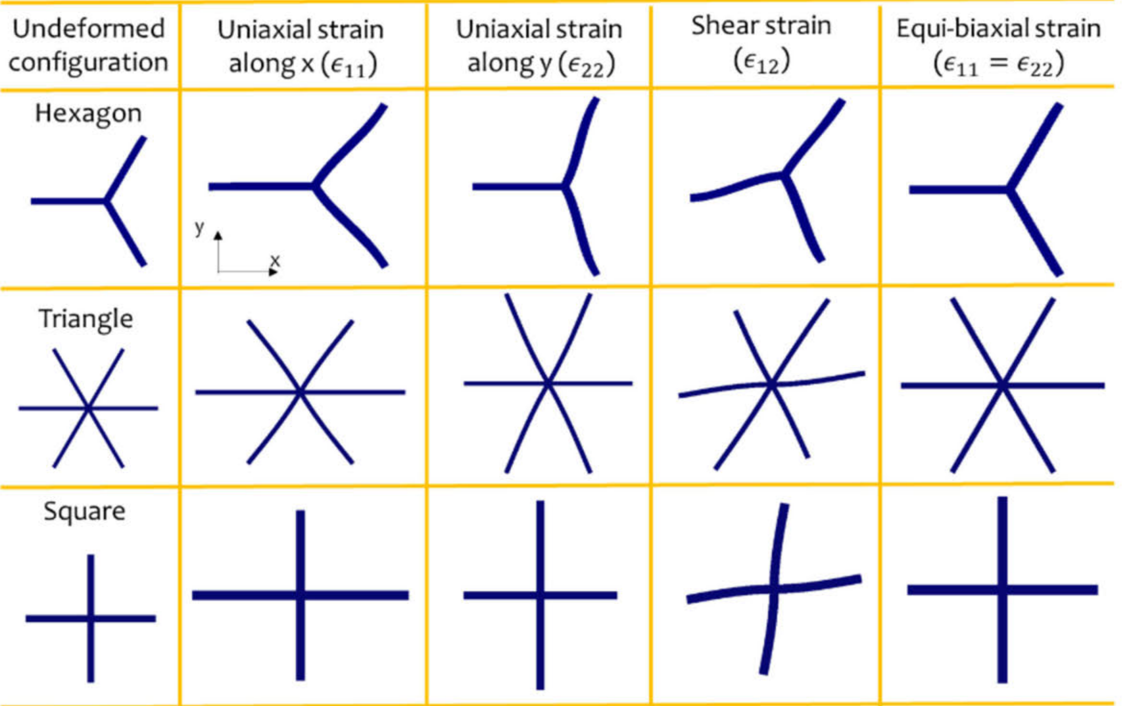

Figure 5-4: Visualization of in-plane deformation of 2d periodic lattices given different loading conditions (uniaxial strain, shear strain, and equibiaxial strain).

this study, parameter space with open area fraction larger than the state-of-the-art was examined to explore how in-plane and out-of-plane stiffness of different lattice topologies behave. Thickness was fixed to be 500 μm considering standard 100-mm wafer thickness used in the semiconductor industry. Width of the beams were fixed to be 0.096 mm, the same as current design of CAT grating, since narrowing it further would cause fabrication challenge.

First, analytical and finite element (FE) analysis were performed on the rigid point model, treating nodal junction as a rigid 'point'. Figures 5-4 and 5-5 visualize the deformed periodic RVEs as captured in Abaqus software when uniform strain or curvature are applied to the boundary of the 'nodal point model'. Thickness of the beam was scaled by 0.2 for visual clarity. It is observed that the RVEs simply expand isotropically when equibiaxial strain is applied.

Figure 5-6 shows analytical ('square') and FE simulation ('circle') results for several modes of stiffness for hexagonal, triangular, and square lattices as a function

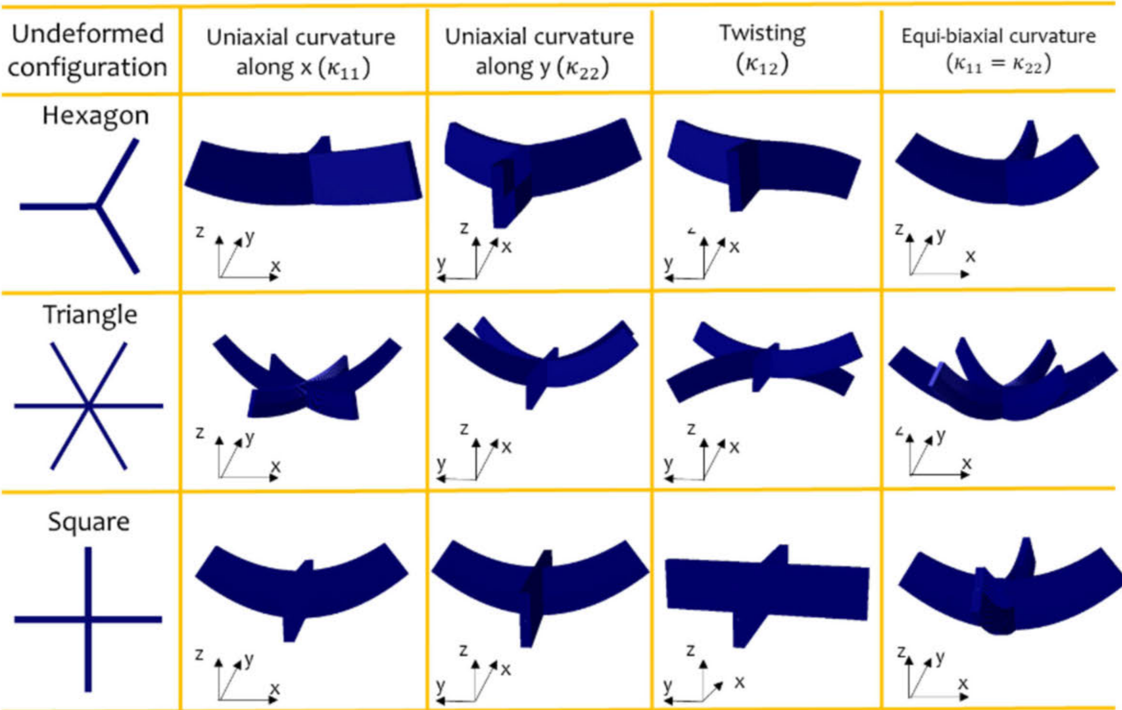

Figure 5-5: Visualization for out-of-plane deformation of 2d periodic lattices given different loading conditions (uniaxial curvature, twisting curvature, and equibiaxial curvature).

of open area fraction. Stiffnesses for in-plane stretch along x or y (top left), in-plane shear (top middle), equibiaxial stretch (top right), out-of-plane bending along x or y (bottom left), twisting (bottom middle), and equibiaxial bending (bottom right) are shown. For FE simulations, the Euler-Bernoulli elements (B23, B33 in Abaqus elements library for in-plane and out-of-plane analysis, respectively) with longitudinal length of 10 μm were used. For all modes of stiffness, the results show nearly perfect agreement ($<$1% of errors) (the results are identical when FE results are simulated with 1 beam element for each constituent beams). Considering the in-plane stretching or bending along the principal directions (top left, bottom left), the square lattice (pink) exhibits the highest stiffness as the lattice responds to the external load only by 'stretching'. However, the square lattice is highly compliant to in-plane shear (top middle) or twisting (bottom middle) since the lattice resists them purely with bending or twisting of the constituent beams. A triangular lattice, on the other hand, shows high stiffnesses for all the loading modes since more than one of the constituent beams needs to stretch to accommodate the applied external loads. A hexagonal lattice shows reasonably high stiffness for all external loads, however, the stiffnesses are all less than those for the triangular lattice (triangular lattice defeats hexagonal lattices for all rounds).

The above statements on lattice behavior - whether it is stretching-dominated, bending-dominated, or twisting-dominated - are manifested by looking into stiffness contributions from deformation (stretching, bending, and twisting) of the constituent beams as driven in the analytical solution (see eqn. 5.39 and 5.46). Figure 5-7 explicitly shows stiffness contributions for the in-plane shear case as an example. Insets in each plot shows deformed geometry of the RVEs with the shortest beam lengths. It is shown that the stiffness is dominated by bending (blue) of the constituent beams for hexagonal and square lattices (stretching contribution is zero for square lattice) while stretching (red) of the beams plays a major role for the triangular lattice. Looking into more details on the behavior of hexagonal lattice upon in-plane shear loads, Figure 5-7 visualizes the hexagonal lattice after in-plane shear strain of 0.001 is applied;

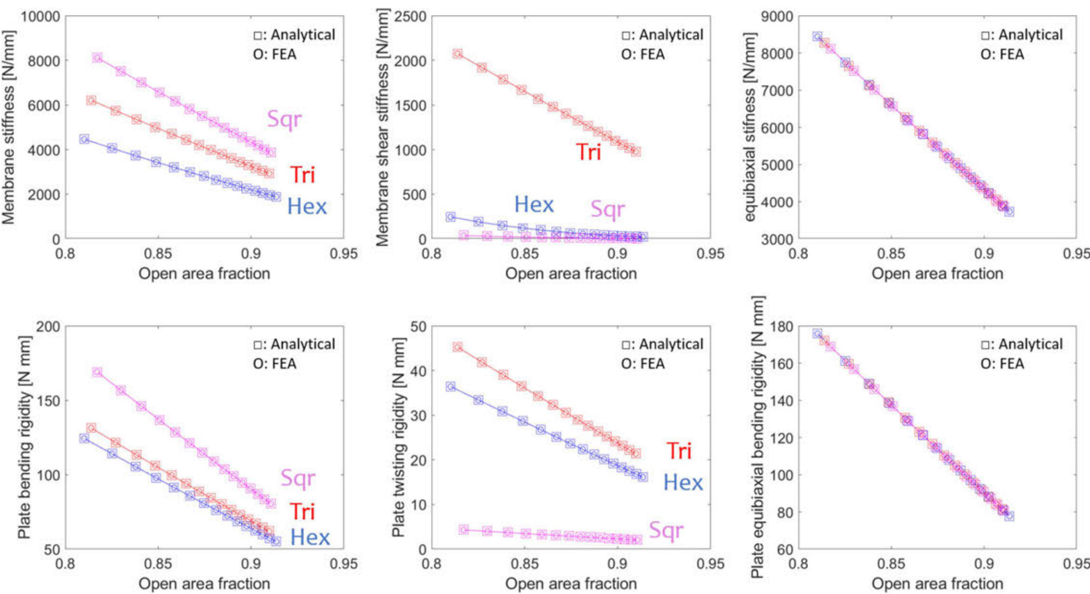

Figure 5-6: In-plane (top row) and out-of-plane (bottom row) stiffness derived from analytical (square) and finite element analysis (circle) for hexagonal, triangular, and square lattices. In-plane stiffness includes uniaxial, shear, and equibiaxial stiffness, and out-of-plane stiffness includes uniaxial, twisting, and equibiaxial stiffness (from left to right). Open area fraction was changed by changing beam length only while fixing thickness and width to be 500 and 96 μm. Young's modulus was assumed to be 169 GPa.

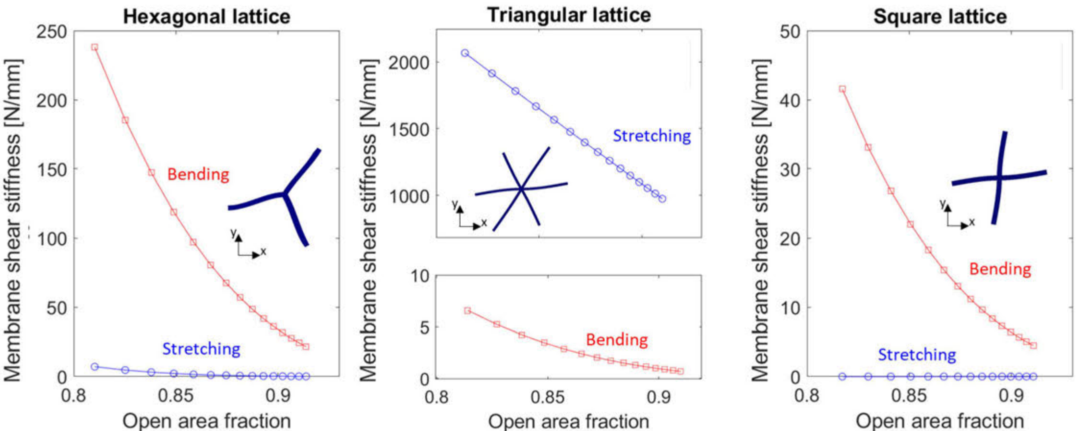

Figure 5-7: Contribution of stretching and in-plane bending of the beams on in-plane shear (membrane shear) stiffness for hexagonal, triangular, and square lattices.

Table 5.1: Axial and bending displacements for beams AO, BO, CO in hexagonal lattice with beam length of 0.555 mm under in-plane shear of 0.0005. Negative axial displacements imply compression. All units in [μm].

Beam	**Axial displacement**	**Bending displacement**
AO	0.0067	-0.1349
BO	0	0.2698
CO	-0.0067	-0.1349

the free variables are derived to be $(u_O, v_O, \phi) = (0, 0.131\ \mu m, 0)$ from eqn. 5.24. Axial stretching and bending displacements for beam AO, BO, CO are summarized in Table 5.1 (see eqn. 5.19). It is shown that all beams stretch very little (6.7 nm for 0.555 mm length beam at the largest), while the beams undergo bending displacement of 130-260 nm, indicating the strain energy (and thus stiffness) is dominated by 'bending' of the constituent beams.

Figure 5-8 shows stiffness contributions for the twisting case as another example. It is shown that the stiffness is dominated by bending (pink) of the constituent beams (note that the beams were bent along the thickness, unlike along the width for in-plane cases) for hexagonal and triangular lattices while twisting of the beams (black) played a dominant role for the square lattice (bending contribution is zero for square lattice). This result is manifest from the deformed geometries for RVEs shown in insets, as the constituent beams are bent only for hexagonal and triangular lattices

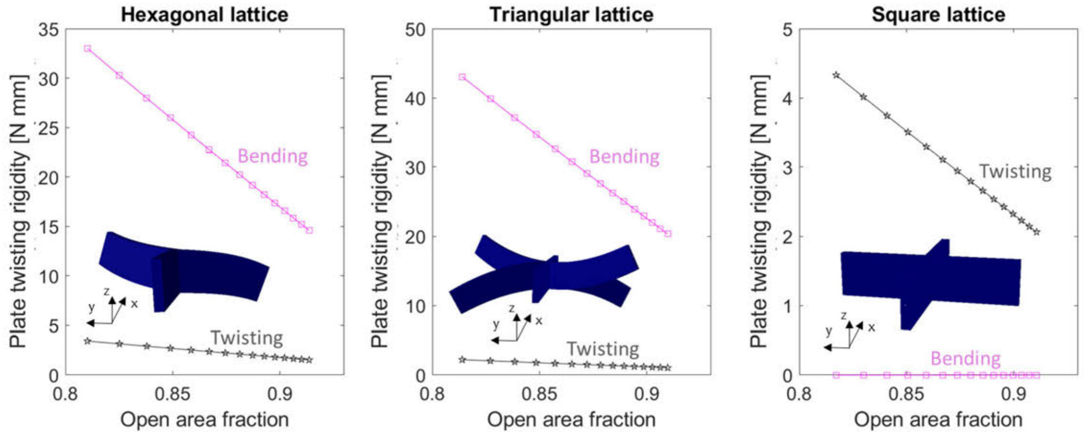

Figure 5-8: Contribution of out-of-plane bending and twisting of the beams on twisting stiffness for hexagonal, triangular, and square lattices.

while the square lattices underwent twisting only.

Interestingly, it was shown that all the lattices exhibit the same stiffness against equibiaxial strain (top right, Fig. 5-6) or curvature (bottom right, Fig. 5-6), meaning that the lattices behave the same independent of lattice topologies when equibiaxial loads are applied. Optical area fraction is the only independent variable for equibiaxial stiffness.

For some simulation cases (i.e., hexagonal lattice with area fraction of 0.82), the constituent beams fall out of the 'slender' regime, and the Euler beam approximation might not be appropriate for modelling. Timoshenko beam elements (B21 for in-plane analysis and B31 for out-of-plane analysis in Abaqus elements library) were used as alternatives to better approximate the real-world behavior. Figure 5-9 plots FE results simulated with Timoshenko (x) and Euler-Bernoulli (circle) beam elements. For in-plane stiffness (top row), the results are almost identical since the beam bends along the short side (b). However, since the beam bends along the long side (thickness) for out-of-plane analysis, the beams may want to transversely shear in a favorable way to minimize strain energy. As expected, significant deviations are observed in out-of-plane stiffness for the hexagonal lattice (see bottom left, bottom middle plots in Fig. 5-9) when Timoshenko beam element was used. More details on lattice behavior can

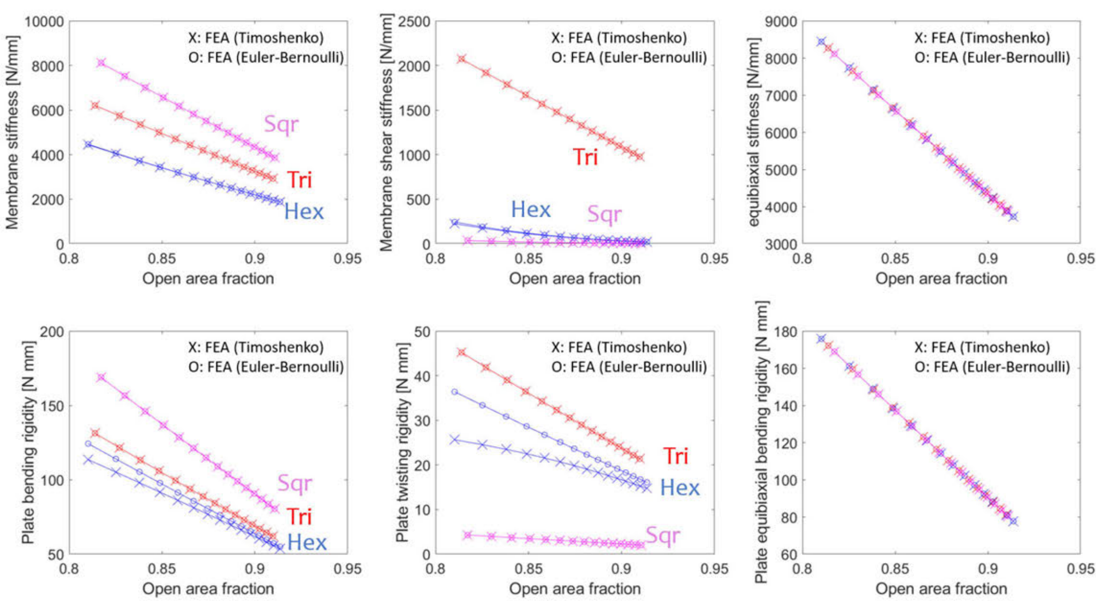

Figure 5-9: In-plane and out-of-plane stiffness of hexagonal, triangular, and square lattices modelled with Euler-Bernoulli (circle) and Timoshenko (X) beam elements using finite element analysis.

be analyzed by finding the behavior of the free variables for a representative example. Figure 5-10a shows the deformed shape of a hexagonal lattice made out of three 0.555 mm-long constituent beams when curvature of 0.001 mm^{-1} was applied along x. Table 5.2 summarizes the behavior of free variables ($\frac{\partial w}{\partial x}|_O$, $\frac{\partial w}{\partial y}|_O$, w_O) of the lattice modelled with Eurler-Bernoulli or Timoshenko beam elements. It is interpreted that the the nodal point rotated further toward negative slope when modelled with Timoshenko elements while it stayed in the same 'zero' position along the thickness direction. This implies that the beam transversely sheared at the nodal point to accommodate the curvature, which in turn reduced the stiffness in out-of-plane bending (bottom left in Fig. 5-9). Fig. 5-10b visualizes this result; the beam CO transversely sheared at rigid nodal point ('O'), and the other beams AO and BO transversely sheared in an opposite way for compatibility.

For triangular and square lattices on the other hand, stiffnesses were calculated to be the same regardless of types of beam elements being used. It is estimated to

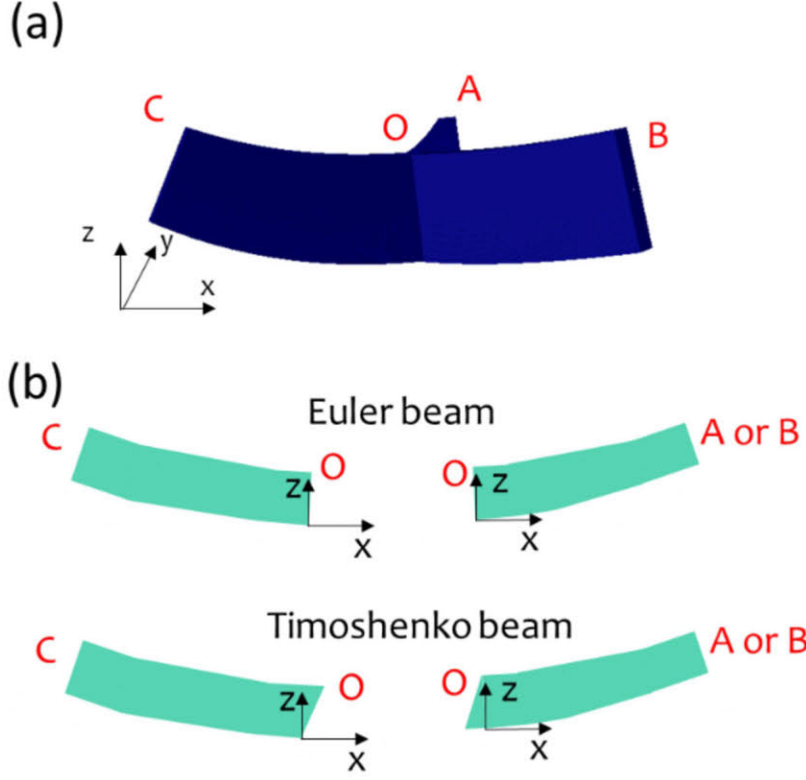

Figure 5-10: (a) Visualization of deformed hexagonal lattice when uniaxial curvature of 0.001 mm^{-1} is applied along x. (b) A schematic showing different deformation behaviors for beams modelled with Euler-Bernoulli (top) and Timoshenko (bottom) beam elements. Timoshenko beam transversely shears at the nodal junction, O, to release strain energy, resulting in lower stiffness compared to that modelled with Euler-Bernoulli beam element.

Table 5.2: Behavior of free variables for hexagonal lattice modelled with Euler-Bernoulli or Timoshenko beam elements. A uniaxial curvature of 0.001 mm^{-1} was applied along x.

Free variables	**Euler-Bernoulli**	**Timoshenko**
$\frac{\partial w}{\partial x}\vert_O$	$-6.5e^{-5}$	$-1.37e^{-4}$
$\frac{\partial w}{\partial y}\vert_O$	0	0
w_O	0	0

be due to the symmetry of the lattice; there is no room for the Timoshenko beam to transversely shear since the nodal point is at the centroid of the lattice (all the constituent beams have identical beams at the opposite sides from nodal point).

More realistic results can be derived by performing a 'rigid body nodal junction model', treating nodal junction as a rigid body with finite size. Figure 5-11 visualizes deformed shapes of the rigid body nodal junction model. Only the hexagonal lattice is shown for visualization. Triangular geometry at the intersection of the beams represents a rigid nodal junction. Figure 5-12 shows FE results comparing stiffness derived from the nodal point model (X) and the rigid body nodal junction model (square). It is shown that stiffnesses modelled with rigid body nodal junction are greater than those for the rigid point model, which was to be expected since the rigid body nodal junction model uses shorter constituent beams with effective beam length (see Fig. 5-1); it is in agreement with the results observed from the additive manufacturing community [75]. For our application (open area fraction of 0.82-0.92), the stiffness doesn't show much difference (maximum of 4-6% for the RVEs with lowest open area fraction) between the results since the RVEs of interest stand in the low-density regime.

Overall, the triangular lattice appears to be a reasonable choice for our applications on CAT grating structural support. For state-of-the-art CAT gratings (open area fraction of 0.82), we gain 44% improvement on in-plane stretch stiffness, 580% on shear stiffness, 23% on out-of-plane bending stiffness, and 96% on twisting stiffness according to Fig. 5-12. Improvements of all aspect of stiffness are encouraging since all modes of stiffness come into play when CAT gratings are deformed after bonding to metallic frames for assembly. Uniform heating experiment is taken as an example to help understand this idea.

Fig. 5-13a shows a meshed model of a CAT grating bonded on a titanium frame for assembly. Fig. 5-13b shows a partly meshed view for frame and cured epoxies at bonding points. The bonding points exist at the middle of four flexures. Assuming

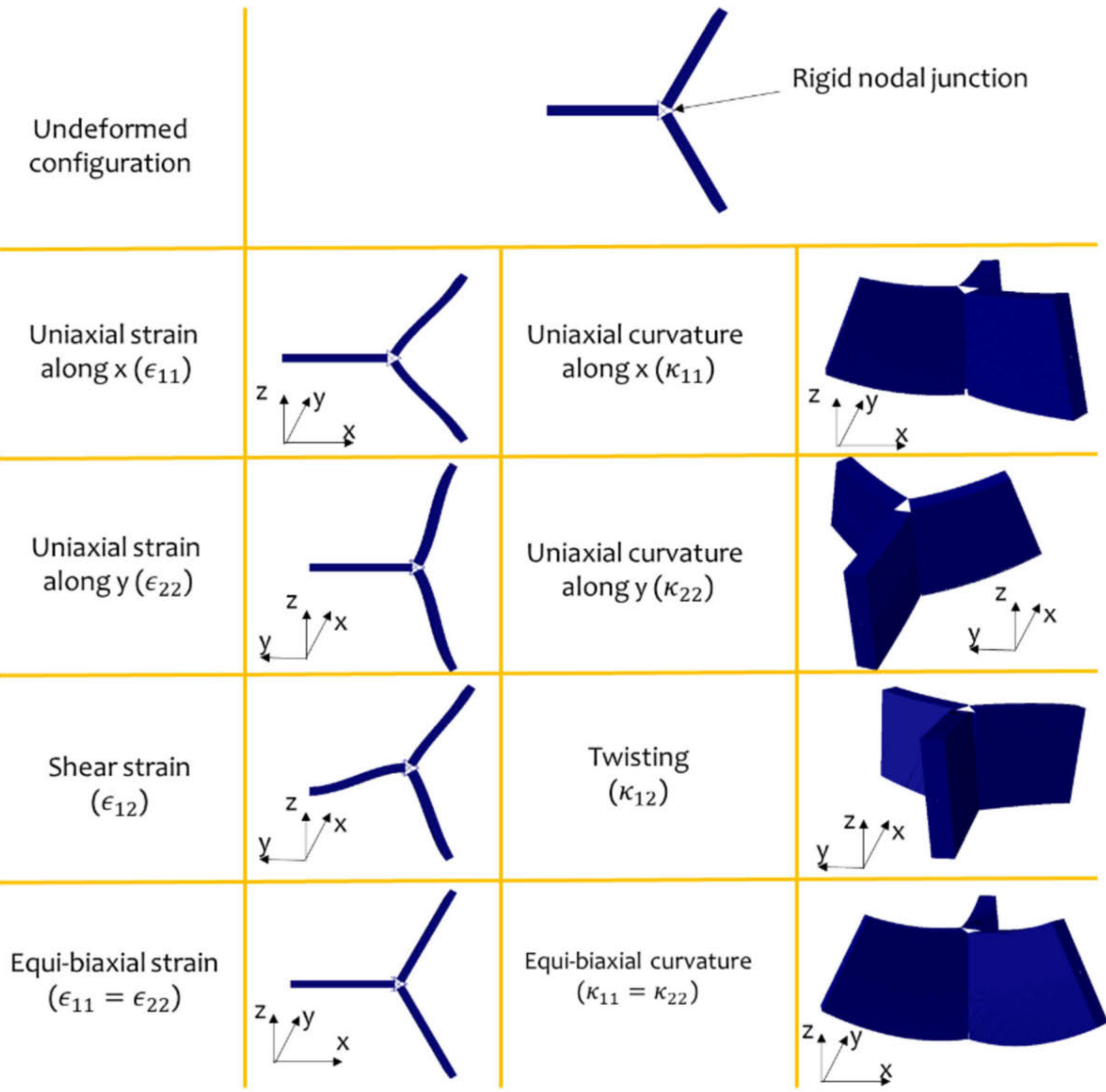

Figure 5-11: Visualization for in-plane and out-of-plane deformation of hexagonal lattice under different loading conditions (uniaxial strain, shear, equibiaxial strain, uniaxial curvature, twisting curvature, and equibiaxial curvature).

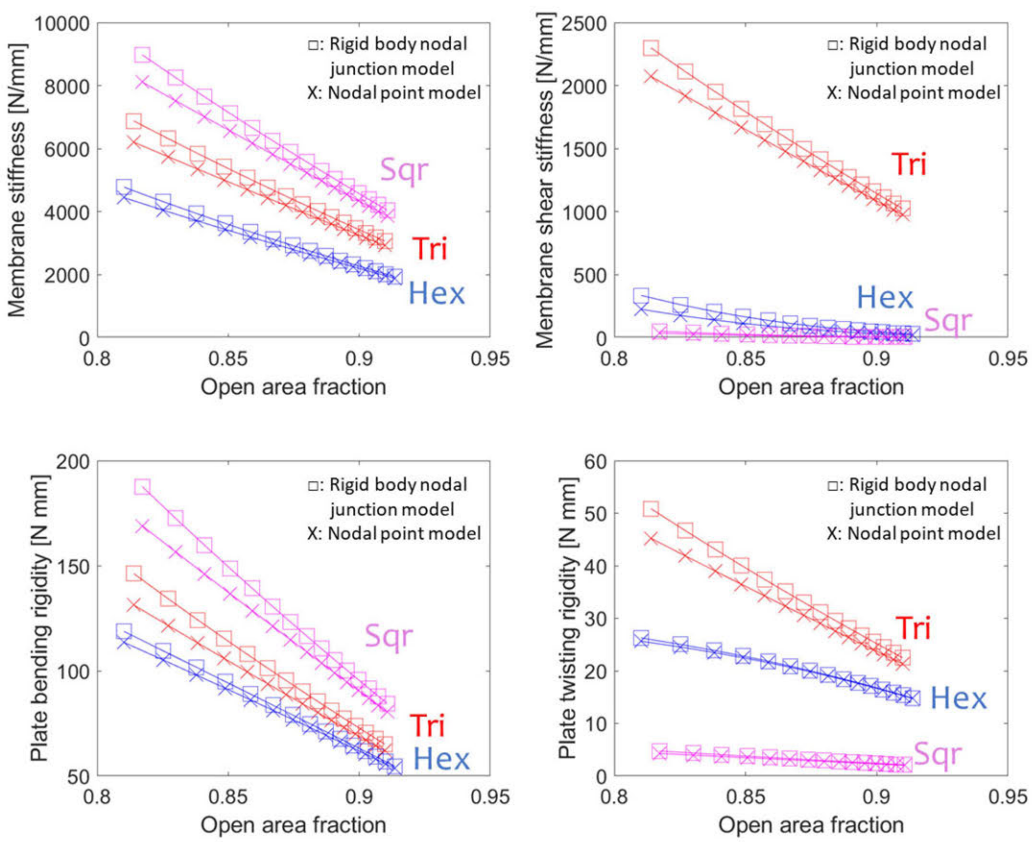

Figure 5-12: In-plane (top) and out-of-plane (bottom) stiffness modelled with nodal junction as a rigid point (X) and as a rigid body (square).

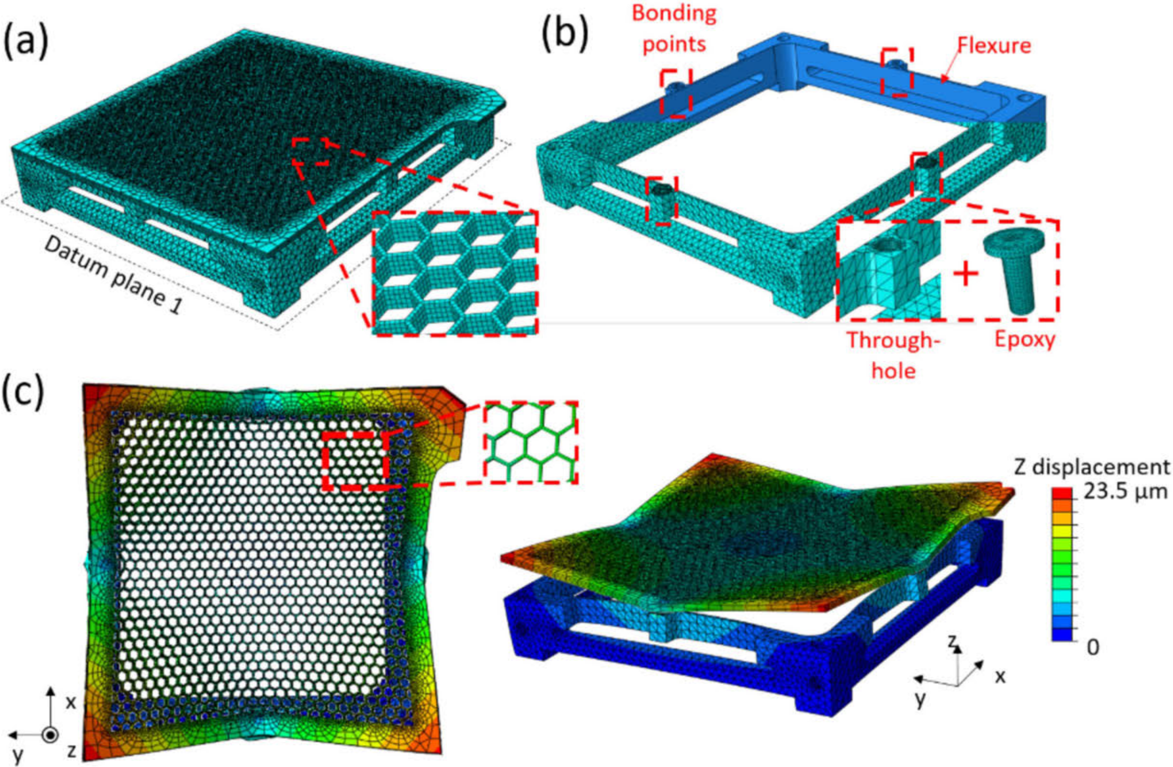

Figure 5-13: Full scale model of CAT gratings bonded to the frame with epoxy. (a) Meshed model of CAT grating attached to the frame with epoxy. Only the L2 hexagonal support and L3 aperture was included in the model with an assumption that thin CAT gratings and L1 membranes have negligible contribution to the overall stiffness of the structure. (b) Half geometrical and half meshed model to show detailed structures and mesh for titanium frame and epoxies. (c, d) Top (c) and inclined (d) view of deformed CAT grating facet when the whole assembly is uniformly heated by 30 degC. Color represents out-of-plane (z) displacement.

uniform heating of 30 degC applied to the whole assembly, CTE mismatch between the frame and a CAT grating constrains the grating, applying forces and moments at its bonding points (see Fig. 5-13b); the flexures at the titanium frame with higher CTE wants to expand more in x and y than the silicon grating with lower CTE (CTE for Si: $2.6e^{-6}$ and Ti: $8.6e^{-6}$ $degC^{-1}$). Center point of datum plane 1 was fixed (both translation and rotation) for simulation (see Fig. 5-13a). Fig. 5-13c shows exaggerated views for deformed shape of the grating (left: top view, right: inclined view). The gratings were not only stretched but bent out-of-plane since external loads were applied far from the neutral axis of the grating. Local variations of curvature (both in x, y and twist) are easily seen from the inclined view, indicating that portions of the hexagonal lattice are under twisting and out-of-plane bending moments. For the unit lattice near corners, the lattice underwent in-plane shear (see inset in red dotted line in Fig. 5-13c). For the lattice along the lines subtended by four bonding points, the lattice is under compression and bending out-of-plane. Though it is not clear from the images, the lattices at the center of the grating undergo equibiaxial compression and bending if the loads from four bonding points were applied to be symmetric.

5.6 Conclusion

In-plane and out-of-plane mechanical behavior of 2d-periodic lattices were analyzed based on analytical and numerical approaches in an effort to design optical structural supports with maximized optical area fraction-to-stiffness ratio. It is the first study on out-of-plane properties of 2d-periodic lattice to the author's knowledge, whereas in-plane analysis on 2d periodic lattices is common in aerospace community to investigate mechanics of cores in sandwich panels. First, analytical and FE solutions were derived by modelling lattices with Euler-Bernoulli beam elements adjoined at the nodal 'point'. The derived analytical and FE solutions show very close agreement. Stiffness contributions from deformation modes of the beam - whether it be

stretching-dominated, bending-dominated, or twisting-dominated - can be obtained from the analytical solution, as it derives total strain energy (and thus stiffness) by summing energy from stretching, bending, and twisting of the beams based on simple beam theory. Timoshenko beam theory better approximates the real-world behavior by allowing the beams to transversely shear. It is explicitly shown in one example; hexagonal RVE modelled with Timoshenko beam elements shows larger slope at its nodal junction than that from Euler-Bernoulli beam elements when uniaxial curvature was applied along x, implying transverse shear stress arose along the beam to minimize strain energy. Effect of nodal geometry was studied - treating a nodal junction as a 'rigid body' element and clamping adjoining beams to its cross-section - to understand the nodal contribution on overall stiffness. Stiffnesses were shown to deviate only by 4-6% from the nodal point model, as our lattices of interest lie on the low-density regime. Overall, triangular lattice was found to be the best lattice topology to populate the aperture of x-ray grating, with over 23-580% of gain in stiffness (depending on deformation modes) at the same open area fraction.

Chapter 6

Conclusion

The ability to manufacture products precisely has been fundamental for modern human inventions. Space telescopes, semiconductors equipment, and laser interferometric gravitational observatory (LIGO) are among many examples. For these technologies, what is seemingly an easy task in other fields requires decades of research. In the field of x-ray telescopes for example, precise alignment of gratings or mirror modules has been an issue for the last ∼30 years. Research is still ongoing to asymptotically achieve demanding requirements of few arc-minutes of tolerance (see Chap. 3 for example). However, as soon as the goal is achieved, its impact is enormous not only for its invention but because of derivative technologies developed along the effort of research and development.

Engineering space-based CAT grating spectrometers is one of the most challenging precision engineering problems. It can be roughly classified into two areas: optical engineering and mechanical engineering. The former focuses on development of metrologies for CD controls, precision alignment of gratings, diffraction efficiency modelling of CAT gratings, and ray tracing for tolerance analysis. The latter focuses on deformation aspects of optical components, treating them as structures made of thin shells or slender beams. Since optical and mechanical properties are inter-related

for scientific instruments in a spectrometer, the problems can't be solved if two themes are considered separately. This thesis takes a holistic approach to the manufacturing problem by considering both themes at the same time.

Precision metrologies for measuring critical dimensional parameters are one of the most fundamental technologies towards manufacturing future x-ray telescopes. Several metrologies were invented in this thesis to characterize grating period (chapter 2), misalignment (chapter 3), and grating bar tilt angle (chapter 4) to satisfy mission requirements. In chapter 2, a UV-based grating period metrology was invented - including concept development, modelling, construction, characterization, and testing - using simple UV reflection and diffraction principles. The developed metrology assessed feasibility of lithography (e.g., interference lithography, ArF semiconductor scanner) for patterning 200-nm gratings with period uniformity of $<$0.006 nm rms (see section 1.8 in chapter 1) towards future x-ray telescope missions. It is suited for fast ($\sim$1 hr per grating) and precise ($\sim$0.004 nm rms) characterization of grating period as compared to SEM imaging ($\sim$10 hrs per grating, $\sim$5 nm in precision). It achieved 2X better precision compared to the previous period measurement tool in Ref. [20]. It successfully characterized period variation of gratings patterned with traditional interference lithography to be $<$0.018 nm (1 ppm) in 30 x 30 mm window (corresponds to resolving power of $>$10000), which is sufficient for future x-ray telescope missions.

In chapter 3, a UV-based metrology and alignment procedures were developed for precision alignment of CAT gratings (see section 1.8 in chapter 1 for requirements). The metrology provides fast ($\sim$1hr per grating) and indirect way of measuring angular orientations between gratings using a UV laser, avoiding time-consuming ($\sim$one day per grating) x-ray characterization. It achieved a precision of 0.66 arcmin (requirement $<$1.8 arcmin), an accuracy of 3.18 arcmin (requirement $<$3 arcmin) for roll angle measurements with 'high-quality' CAT gratings (see section 3.2 in chapter 3). From a series of tests performed to align four CAT gratings to satisfy alignment requirements for Arcus mission (see section 1.8.3 in chapter 1 for requirements), four 'high-quality' CAT gratings were successfully aligned to satisfy the requirements in

test 1 (see sections 3.2.5 in chapter 3). It is the first demonstration to align CAT gratings to satisfy the alignment requirements, which set a milestone for manufacturing x-ray grating spectrometers for future x-ray telescope missions. In test 2, improvements were made in hardware design (i.e., facet frame and grating window) and alignment speed (~one day per grating for test 1 to ~1 hr per grating for test 2), and scalability of alignment process for high-volume alignment (>1000). The precision, accuracy, scalability, and speed attained from two tests are necessary since an actual high-volume (>1000) alignment for NASA missions needs to be done in limited amount of time (few months) reliably (see section 1.8.3 in chapter 1).

In chapter 4, a grating bar tilt metrology was invented using x-ray diffraction and laser reflection principles. Gratings were illuminated with a collimated x-ray beam (Cu Kα), similar to variable-angle small-angle x-ray scattering, to record changes of diffraction efficiency (DE) as a function of incidence angle. Simulations using scalar diffraction theory and rigorous coupled wave analysis predict extrema (0th order DE minimized, ±1st order DE maximized) when local grating bars are parallel to the incident x-ray beam. The surface normal was measured independently by reflecting a laser beam from the grating surface. The independent measurements using x rays and laser beams were referenced to each other via a slit reference axis to characterize the bar tilt angle relative to the surface normal. The developed metrology features a repeatability of <0.01 deg, an accuracy of ~0.08 deg (grating bar angle relative to surface normal), and a fast scan speed (~ 5 sec of integration time per point per sample), which are significant improvement over conventional cross-sectional SEM imaging (a repeatability ~0.1 deg, an accuracy ~0.5 deg, a speed of 0.5 hrs per sample). The fast x-ray measurements were repeated at arbitrary points across large gratings (3 x 3 cm^2) to study spatial variation of the bar tilt angle. It provided feedbacks in optimizing etch recipes to suppress grating bar tilt variations to be <0.1 deg (<6 arcmin), which are critical to achieve effective area requirements for Arcus (>350 cm^2) and Lynx (>4000 cm^2) missions. The proposed method can be expanded to characterize cross-sectional profiles of other high-aspect ratio nanostructures with

appropriate x-ray diffraction modelling, which may have envisioned impact in CD controls in manufacturing 3D electronic IC chips (e.g., FinFet, 3D-NAND, etc) in semiconductor manufacturing.

In chapter 5, structural analysis on several 2d periodic lattices (hexagon, triangle, square) were performed to design CAT grating structural supports that provide high optical area fraction at a given stiffness. With an assumption of infinite periodicity, analysis was performed on unit cell for chosen 2d lattices since length scale of aperture ($>$3 cm) is much larger than that for unit cells ($\sim$1 mm). Plane stress condition was assumed for unit cell analysis. As thin CAT gratings are more likely to deform in bending/twisting, not only in-plane stretching/shear but also out-of-plane bending/twisting stiffness of the lattices were studied. It is the first study to investigate out-of-plane bending/twisting response of 2d periodic unit cell to the author's knowledge. The triangular lattice was found to exhibit higher stiffness than (current) hexagonal lattice in all deformation modes (stretching, shear, out-of-plane bending, twisting). It is estimated that replacing current hexagon with triangular lattice is expected to increase optical area by 5% without compromising stiffness. Alternatively, triangular lattice is expected to increase stiffness by 23-580% (depending on loading modes) compared to current hexagonal lattice without compromising optical area. Back-of-the-envelope calculation implies 5% of increase in optical area corresponds to cost reduction of $\sim$500,000 US dollars for 290 million US dollar x-ray grating spectrometer mission (i.e., Arcus). It has envisioned impact in other applications including light-weight space sail [60], architecture, neutron optics, UV filters [24], honeycomb solid oxide fuel cells [80], and MEMS/NEMS sensors [18] to increase structural efficiencies.

6.1 Future work

While the UV metrology described in chapter 2 and 3 worked fine for period measurements of reflection gratings (see chapter 2) and alignment of CAT gratings (see chapter 3), the fact that it relies on measurements of reflected beams (not transmitted beams) limits reliable operations when 'low-quality' CAT gratings (i.e., those with few microns of out-of-plane buckling) are to be measured. It is because reflected beams are sensitive to surface profile unlike transmitted beams (see section 2.6 in chapter 2 and section 3.4 in chapter 3). It is desirable to develop more reliable metrology using 'transmitted' beams, similar to a geometry similar to that for x-ray grating spectrometer. For grating alignment (see section 3.4 in chapter 3), with ongoing shift from interference lithography to the 193 nm semiconductor scanner for grating patterning, it may be possible to use 'transmitted' diffraction orders of a visible (red) laser from 5-μm period L1 cross-support for alignment as L1 support and grating bars will have consistent angles for all the gratings as defined by photomask. It may eliminate the need for using 'reflected' beams of a UV laser for grating alignment. Improvements in kinematic alignment will need to be addressed as press-fitted pins degrade accuracy in grating alignment. Replacing it with monolithic structures defined during machining of grating window may provide better accuracy.

Further experiments can be performed to find shape of the grating bars using an x-ray (see chapter 4). In chapter 4, straight grating bars were assumed for modelling purpose since only the grating bar tilt angle was of interest. A more rigorous x-ray diffraction modelling can be done with varying shapes of grating bars (e.g., tapered bars, unsymmetric bars, hour-glass bars, etc.) to understand the shape of the bars.

Further studies on dynamic properties (e.g., phononic responses, resonance frequencies) of 2D lattices could be pursued to understand potential failure modes from vibrations or shocks during launch. A study on stress concentration effects at corners of adjoining beams may be needed to engineer fillets with appropriate radius. Tests on fabrication of triangular structural supports need to be done to understand its man-

ufacturability without suffering from taper or underetch near sharp corners (angles at corners are more acute for triangular lattice as compared to those for hexagonal lattice).

Appendix A

Example MATLAB scripts to calculate analytical solutions on stiffness of 2d periodic lattices

MATLAB functions to implement calculations of full analytical solutions (eqns. 5.36-5.46 in Chap. 5) on stiffness (both in-plane and out-of-plane) of 2d periodic lattices with varying beam length (i.e., open area fraction) are provided. Functions receive Young's modulus of material, length, width, and depth of the constituent beams, and output the stiffness components (in-plane stiffness tensor, C, and out-of-plane stiffness tensor, D) and values for free variables after deformation. Scripts for hexagonal lattice are provided as examples. The script written in section A.1 performs calculation of eqns. 5.36-5.39 to derive analytical solution for in-plane stiffness tensor, C. The script written in section A.2 perform calculation of eqns. 5.40-5.46 to derive analytical solution for out-of-plane stiffness tensor, D.

A.1 MATLAB script to calculate analytical solution on in-plane stiffness tensor for hexagonal lattice

```
1  function [LHex1, OAFRAC_H, CTENSOR_AX_H, CTENSOR_BD_H, CTENSOR_H, PHI, U1STAR, ...
       U2STAR]=fn_Analytical_Hex_Inplane(LHex1, E, w, t, indicator_LWT)
2  %% Hex Inplane Analytical
3  Abeam=w.*t; % Beam cross-sectional area [mm^2]
4  Ibeam=t.*w.^3/12; % Beam moment of inertia [mm^4]
5
6  AHex=3*sqrt(3)/2.*LHex1.^2; % Calculate area of unit cell
7
8  SYSM=[]; INVSYSM=[]; PHI=[]; U1STAR=[]; U2STAR=[];
9  CTENSOR_H=[]; CTENSOR_AX_H=[]; CTENSOR_BD_H=[];
10
11 for i=1:length(LHex1)
12     A.x=LHex1(i)*cosd(60); A.y=LHex1(i)*sind(60); A.n1=cosd(60); A.n2=sind(60);
13     xA=[A.x; A.y]; nA=[A.n1; A.n2]; mA=cross([0;0;1],[A.n1; A.n2; 0]); mA=mA(1:2);
14     B.x=LHex1(i)*cosd(180); B.y=LHex1(i)*sind(180); B.n1=-1; B.n2=0;
15     xB=[B.x; B.y]; nB=[B.n1; B.n2]; mB=cross([0;0;1],[B.n1; B.n2; 0]); mB=mB(1:2);
16     C.x=LHex1(i)*cosd(-60); C.y=LHex1(i)*sind(-60); C.n1=cosd(-60); C.n2=sind(-60);
17     xC=[C.x; C.y]; nC=[C.n1; C.n2]; mC=cross([0;0;1],[C.n1; C.n2; 0]); mC=mC(1:2);
18
```

```
19      % Calculate open area fraction
20      A_CELL(i) = 3*sqrt(3)/2*LHex1(i)^2;
21      OA_CELL(i) = 3*sqrt(3)/2*LHex1(i)^2-3*w*LHex1(i)+sqrt(3)/2*w^2;
22      OAFRAC_H(i) = OA_CELL(i)/A_CELL(i);
23
24      %% Deriving uStar1, uStar2, Phi
25      SysM=[3*LHex1(i), mA(1)+mB(1)+mC(1), mA(2)+mB(2)+mC(2);
26          12*E*Ibeam/LHex1(i)^2*(mA(1)+mB(1)+mC(1)),
27          E*Abeam/LHex1(i)*(nA(1)^2+nB(1)^2+nC(1)^2)...
28          +12*E*Ibeam/LHex1(i)^3*(mA(1)^2+mB(1)^2+mC(1)^2),
29          E*Abeam/LHex1(i)*(nA(2)*nA(1)+nB(2)*nB(1)+nC(2)*nC(1))...
30          +12*E*Ibeam/LHex1(i)^3*(mA(2)*mA(1)+mB(2)*mB(1)+mC(2)*mC(1));
31
32          12*E*Ibeam/LHex1(i)^2*(mA(2)+mB(2)+mC(2)),
33          E*Abeam/LHex1(i)*(nA(1)*nA(2)+nB(1)*nB(2)+nC(1)*nC(2))...
34          +12*E*Ibeam/LHex1(i)^3*(mA(1)*mA(2)+mB(1)*mB(2)+mC(1)*mC(2)),
35          E*Abeam/LHex1(i)*(nA(2)^2+nB(2)^2+nC(2)^2)...
36          +12*E*Ibeam/LHex1(i)^3*(mA(2)^2+mB(2)^2+mC(2)^2);];
37
38      SYSM=[SYSM, SysM]; % Concatenate the SysM matrix
39
40      invSysM=inv(SysM);
41      INVSYSM=[INVSYSM, invSysM]; % Concatenate the invSysM matrix
42
```

```
%%Calculating Phi, uStar
eps11=0.000; eps12=0.000; eps22=0.0005; % Change it for whatever strain you want to apply

eps=[eps11 eps12; eps12, eps22];
RHside=[dot(eps*xA,mA)+dot(eps*xB,mB)+dot(eps*xC,mC);
        E*Abeam/LHex1(i)*dot(eps*xA,nA)*nA(1)+12*E*Ibeam/LHex1(i)^3*dot(eps*xA,mA)*mA(1)...
        + E*Abeam/LHex1(i)*dot(eps*xB,nB)*nB(1)+12*E*Ibeam/LHex1(i)^3*dot(eps*xB,mB)*mB(1)...
        + E*Abeam/LHex1(i)*dot(eps*xC,nC)*nC(1)+12*E*Ibeam/LHex1(i)^3*dot(eps*xC,mC)*mC(1);
        E*Abeam/LHex1(i)*dot(eps*xA,nA)*nA(2)+12*E*Ibeam/LHex1(i)^3*dot(eps*xA,mA)*mA(2)...
        + E*Abeam/LHex1(i)*dot(eps*xB,nB)*nB(2)+12*E*Ibeam/LHex1(i)^3*dot(eps*xB,mB)*mB(2)...
        + E*Abeam/LHex1(i)*dot(eps*xC,nC)*nC(2)+12*E*Ibeam/LHex1(i)^3*dot(eps*xC,mC)*mC(2)];

FreeVar=invSysM*RHside;

PHI=[PHI, FreeVar(1)];
U1STAR=[U1STAR, FreeVar(2)];
U2STAR=[U2STAR, FreeVar(3)];

%Calculating dPhideps, duSalpha_deps
dPhideps=invSysM(1)*(kron(xA,mA)+kron(xB,mB)+kron(xC,mC));
duS1deps=invSysM(5)*(E*Abeam/LHex1(i)...
    *(kron(xA,nA)*nA(1)+kron(xB,nB)*nB(1)+kron(xC,nC)*nC(1))
    +12*E*Ibeam/LHex1(i)^3*(kron(xA,mA)*mA(1)+kron(xB,mB)*mB(1)+kron(xC,mC)*mC(1)));
```

```
67      duS2deps=invSysM(9)*(E*Abeam/LHex1(i)...
68          *(kron(xA,nA)*nA(2)+kron(xB,nB)*nB(2)+kron(xC,nC)*nC(2))
69          +12*E*Ibeam/LHex1(i)^3*(kron(xA,mA)*mA(2)+kron(xB,mB)*mB(2)+kron(xC,mC)*mC(2)));
70
71      %Calculate axial and bending component of the tensor
72      Ctensor_Ax_H=1/AHex(i)*(E*Abeam/LHex1(i)*(kron(kron(xA,nA)...
73          -duS1deps*nA(1)-duS2deps*nA(2),kron(xA,nA)-duS1deps*nA(1)-duS2deps*nA(2)) ...
74          +kron(kron(xB,nB)-duS1deps*nB(1)-duS2deps*nB(2),kron(xB,nB)-duS1deps*nB(1)-duS2deps*nB(2)) ...
75          +kron(kron(xC,nC)-duS1deps*nC(1)-duS2deps*nC(2),kron(xC,nC)-duS1deps*nC(1)-duS2deps*nC(2))));
76
77      CTENSOR_AX_H=[CTENSOR_AX_H, Ctensor_Ax_H];
78
79      Ctensor_Bd_H=1/AHex(i)*12*E*Ibeam/LHex1(i)^3 ...
80          *(kron(LHex1(i)*dPhideps-(kron(xA,mA)-duS1deps*mA(1)-duS2deps*mA(2))...
81          ,LHex1(i)*dPhideps-(kron(xA,mA)-duS1deps*mA(1)-duS2deps*mA(2))) ...
82          +kron(LHex1(i)*dPhideps-(kron(xB,mB)-duS1deps*mB(1)-duS2deps*mB(2))...
83          ,LHex1(i)*dPhideps-(kron(xB,mB)-duS1deps*mB(1)-duS2deps*mB(2))) ...
84          +kron(LHex1(i)*dPhideps-(kron(xC,mC)-duS1deps*mC(1)-duS2deps*mC(2))...
85          ,LHex1(i)*dPhideps-(kron(xC,mC)-duS1deps*mC(1)-duS2deps*mC(2))));
86
87      CTENSOR_BD_H=[CTENSOR_BD_H, Ctensor_Bd_H];
88
89      % Sum two components of the tensor
90      Ctensor_H=Ctensor_Ax_H+Ctensor_Bd_H;
```

```

    % Concatenate the tensors for each Length
    CTENSOR_H=[CTENSOR_H,Ctensor_H];
end


Anal_C11_H=CTENSOR_H(1,:);
Anal_C12_H=CTENSOR_H(4,:);
Anal_C66_H=CTENSOR_H(6,:);
```

A.2 MATLAB script to calculate analytical solution on out-of-plane stiffness tensor for hexagonal lattice

```matlab
function [DTENSOR_BD_H, DTENSOR_TW_H, DTENSOR_H, W_S_H, TH1_S_H, ...
    TH2_S_H]=fn_Analytical_Hex_outofplane(LHex1, E, w, t, indicator_LWT)
%% Hex Inplane Analytical
L=LHex1;  % Length [mm]
nu=0.265;
G=E/2/(1+nu);

Ibeam=t.^3*w./12; % Beam moment of inertia [mm^4]
beta=0.293; % Constant to be multiplied to calculate J_eff for the beam (a/b ratio =5.2)
Jbeam=t.*w.^3*beta;

AHex=3*sind(60).*(L./2).^2; % Calculate area of unit cell

DTENSOR_H=[]; DTENSOR_BD_H=[]; DTENSOR_TW_H=[]; W_S_H=[]; TH1_S_H=[]; TH2_S_H=[];

for i=1:length(L)
    A.x=L(i)/2*cosd(60); A.y=L(i)/2*sind(60); xA=[A.x; A.y];
    P_A  = [0.5*xA(1)^2; 0.5*xA(1)*xA(2); 0.5*xA(1)*xA(2); 0.5*xA(2)^2];
    R11_A=cosd(60); R12_A=sind(60); R1p_A = [R11_A; R12_A];
```

```
R21_A=-sind(60); R22_A=cosd(60); R2p_A = [R21_A; R22_A];

Bs.x=L(i)/2*cosd(180); Bs.y=L(i)/2*sind(180); xBs=[Bs.x; Bs.y];
P_Bs = [0.5*xBs(1)^2; 0.5*xBs(1)*xBs(2); 0.5*xBs(1)*xBs(2); 0.5*xBs(2)^2];
R11_B=cosd(0); R12_B=sind(0); R1p_B = [R11_B; R12_B];
R21_B=-sind(0); R22_B=cosd(0); R2p_B = [R21_B; R22_B];

C.x=L(i)/2*cosd(-60); C.y=L(i)/2*sind(-60); xC=[C.x; C.y];
P_C  = [0.5*xC(1)^2; 0.5*xC(1)*xC(2); 0.5*xC(1)*xC(2); 0.5*xC(2)^2];
R11_C=cosd(-60); R12_C=sind(-60); R1p_C = [R11_C; R12_C];
R21_C=-sind(-60); R22_C=cosd(-60); R2p_C = [R21_C; R22_C];

%% Deriving w_s, th1_s, th2_s (free variables)
kap11=0.001; kap12=0; kap21=kap12; kap22=0; % Change curvature to whatever you want to apply
kap=[kap11 kap12; kap21, kap22];

SysM=[6, L(i)/2*(R11_A-R11_B+R11_C), L(i)/2*(R12_A-R12_B+R12_C);

      24*E*Ibeam/L(i)^2*(R11_A-R11_B+R11_C),
      2*G*Jbeam/L(i)*(R21_A^2+R21_B^2+R21_C^2)...
      + E*Ibeam*8./L(i)*(R11_A^2+R11_B^2+R11_C^2),
      2*G*Jbeam/L(i)*(R21_A*R22_A+R21_B*R22_B+R21_C*R22_C)...
      + E*Ibeam*8./L(i)*(R11_A*R12_A+R11_B*R12_B+R11_C*R12_C);

```

```
43          24*E*Ibeam/L(i)^2*(R12_A-R12_B+R12_C),
44          2*G*Jbeam/L(i)*(R21_A*R22_A+R21_B*R22_B+R21_C*R22_C)... + ...
                E*Ibeam*8./L(i)*(R11_A*R12_A+R11_B*R12_B+R11_C*R12_C),
45          2*G*Jbeam/L(i)*(R22_A^2+R22_B^2+R22_C^2)...
46          + E*Ibeam*8./L(i)*(R12_A^2+R12_B^2+R12_C^2)];
47
48   invSysM=inv(SysM);
49
50   RHside=[2*(dot(reshape(kap,[4,1]),P_A)+dot(reshape(kap,[4,1]),P_Bs) ...
51            +dot(reshape(kap,[4,1]),P_C))-L(i)/2*(dot(R1p_A,0.5*(kap+kap')*xA)-dot(R1p_B,0.5*(kap+kap')*xBs)...
52            +dot(R1p_C,0.5*(kap+kap')*xC));
53
54            E*Ibeam*24/L(i)^2*(dot(reshape(kap,[4,1]),P_A)*R11_A-dot(reshape(kap,[4,1]),P_Bs)*R11_B...
55            +dot(reshape(kap,[4,1]),P_C)*R11_C)-4*E*Ibeam/L(i)*(R11_A*dot(R1p_A,0.5*(kap+kap')*xA)...
56            +R11_B*dot(R1p_B,0.5*(kap+kap')*xBs)+R11_C*dot(R1p_C,0.5*(kap+kap')*xC))...
57            +2*G*Jbeam/L(i)*(R21_A*dot(R2p_A,0.5*(kap+kap')*xA)+R21_B*dot(R2p_B,0.5*(kap+kap')*xBs)...
58            +R21_C*dot(R2p_C,0.5*(kap+kap')*xC));
59
60            E*Ibeam*24/L(i)^2*(dot(reshape(kap,[4,1]),P_A)*R12_A-dot(reshape(kap,[4,1]),P_Bs)*R12_B...
61            +dot(reshape(kap,[4,1]),P_C)*R12_C)-4*E*Ibeam/L(i)*(R12_A*dot(R1p_A,0.5*(kap+kap')*xA)...
62            +R12_B*dot(R1p_B,0.5*(kap+kap')*xBs)+R12_C*dot(R1p_C,0.5*(kap+kap')*xC))...
63            +2*G*Jbeam/L(i)*(R22_A*dot(R2p_A,0.5*(kap+kap')*xA)+R22_B*dot(R2p_B,0.5*(kap+kap')*xBs)...
64            +R22_C*dot(R2p_C,0.5*(kap+kap')*xC))];
65
```

```
66      FreeVar=invSysM*RHside;
67
68      W_S_H=[W_S_H, FreeVar(1)];
69      TH1_S_H=[TH1_S_H, FreeVar(2)];
70      TH2_S_H=[TH2_S_H, FreeVar(3)];
71
72      %% Deriving derivatives
73      Rhs_1=2*(P_A+P_Bs+P_C)-L(i)/2*(0.5*(kron(R1p_A,xA)+kron(xA,R1p_A)) ...
74          -0.5*(kron(R1p_B,xBs)+kron(xBs,R1p_B))+0.5*(kron(R1p_C,xC)+kron(xC,R1p_C)));
75      Rhs_2=E*Ibeam*(R11_A*(24/L(i)^2*P_A-4/L(i)*0.5*(kron(R1p_A,xA)+kron(xA,R1p_A))) ...
76          +R11_B*(24/L(i)^2*(-P_Bs)-4/L(i)*0.5*(kron(R1p_B,xBs)+kron(xBs,R1p_B)))...
77          +R11_C*(24/L(i)^2*P_C-4/L(i)*0.5*(kron(R1p_C,xC)+kron(xC,R1p_C))))...
78          +2*G*Jbeam/L(i)*(R21_A*0.5*(kron(R2p_A,xA)+kron(xA,R2p_A))...
79          +R21_B*0.5*(kron(R2p_B,xBs)+kron(xBs,R2p_B))+R21_C*0.5*(kron(R2p_C,xC)+kron(xC,R2p_C)));
80      Rhs_3=E*Ibeam*(R12_A*(24/L(i)^2*P_A-4/L(i)*0.5*(kron(R1p_A,xA)+kron(xA,R1p_A))) ...
81          +R12_B*(24/L(i)^2*(-P_Bs)-4/L(i)*0.5*(kron(R1p_B,xBs)+kron(xBs,R1p_B)))...
82          +R12_C*(24/L(i)^2*P_C-4/L(i)*0.5*(kron(R1p_C,xC)+kron(xC,R1p_C)))) ...
83          +2*G*Jbeam/L(i)*(R22_A*0.5*(kron(R2p_A,xA)+kron(xA,R2p_A))...
84          +R22_B*0.5*(kron(R2p_B,xBs)+kron(xBs,R2p_B))+R22_C*0.5*(kron(R2p_C,xC)+kron(xC,R2p_C)));
85
86      dw_sdkap = invSysM(1,1)*Rhs_1+invSysM(1,2)*Rhs_2+invSysM(1,3)*Rhs_3;
87      dth1_sdkap = invSysM(2,1)*Rhs_1+invSysM(2,2)*Rhs_2+invSysM(2,3)*Rhs_3;
88      dth2_sdkap = invSysM(3,1)*Rhs_1+invSysM(3,2)*Rhs_2+invSysM(3,3)*Rhs_3;
89
```

```
90      dPAdkap=8/L(i)^2*(3*P_A-L(i)/2*0.5*(kron(R1p_A,xA)+kron(xA,R1p_A))...
91          -3*dw_sdkap-L(i)*(R11_A*dth1_sdkap+R12_A*dth2_sdkap));
92      dQAdkap=48/L(i)^3*(-2*P_A+L(i)/2*0.5*(kron(R1p_A,xA)+kron(xA,R1p_A))...
93          +2*dw_sdkap+L(i)/2*(R11_A*dth1_sdkap+R12_A*dth2_sdkap));
94
95      dPBsdkap=8/L(i)^2*(3*P_Bs+L(i)/2*0.5*(kron(R1p_B,xBs)+kron(xBs,R1p_B))...
96          -3*dw_sdkap+L(i)*(R11_B*dth1_sdkap+R12_B*dth2_sdkap));
97      dQBsdkap=48/L(i)^3*(2*P_Bs+L(i)/2*0.5*(kron(R1p_B,xBs)+kron(xBs,R1p_B))...
98          -2*dw_sdkap+L(i)/2*(R11_B*dth1_sdkap+R12_B*dth2_sdkap));
99
100     dPCdkap=8/L(i)^2*(3*P_C-L(i)/2*0.5*(kron(R1p_C,xC)+kron(xC,R1p_C))...
101         -3*dw_sdkap-L(i)*(R11_C*dth1_sdkap+R12_C*dth2_sdkap));
102     dQCdkap=48/L(i)^3*(-2*P_C+L(i)/2*0.5*(kron(R1p_C,xC)+kron(xC,R1p_C))...
103         +2*dw_sdkap+L(i)/2*(R11_C*dth1_sdkap+R12_C*dth2_sdkap));
104
105     %% Calculate axial and bending component of the tensor
106     Dtensor_Bd_H=1/AHex(i)*E*Ibeam/2 ...
107         *(L(i)*kron(dPAdkap,dPAdkap)+L(i)^2/4*kron(dPAdkap,dQAdkap)...
108         +L(i)^2/4*kron(dPAdkap,dQAdkap)+L(i)^3/12*kron(dQAdkap,dQAdkap) ...
109         +L(i)*kron(dPBsdkap,dPBsdkap)-L(i)^2/4*kron(dPBsdkap,dQBsdkap)...
110         -L(i)^2/4*kron(dPBsdkap,dQBsdkap)+L(i)^3/12*kron(dQBsdkap,dQBsdkap) ...
111         +L(i)*kron(dPCdkap,dPCdkap)+L(i)^2/4*kron(dPCdkap,dQCdkap)...
112         +L(i)^2/4*kron(dPCdkap,dQCdkap)+L(i)^3/12*kron(dQCdkap,dQCdkap));
113
```

```
114     DTENSOR_BD_H=[DTENSOR_BD_H, Dtensor_Bd_H]; % Concatenate
115
116     Dtensor_Tw_H=1/AHex(i)*2*G*Jbeam/L(i) ...
117         *(kron(0.5*(kron(R2p_A,xA)+kron(xA,R2p_A))-R21_A*dth1_sdkap-R22_A*dth2_sdkap, ...
               0.5*(kron(R2p_A,xA)+kron(xA,R2p_A))-R21_A*dth1_sdkap-R22_A*dth2_sdkap)...
118         +kron(-0.5*(kron(R2p_B,xBs)+kron(xBs,R2p_B))+R21_B*dth1_sdkap+R22_B*dth2_sdkap, ...
               -0.5*(kron(R2p_B,xBs)+kron(xBs,R2p_B))+R21_B*dth1_sdkap+R22_B*dth2_sdkap)...
119         +kron(0.5*(kron(R2p_C,xC)+kron(xC,R2p_C))-R21_C*dth1_sdkap-R22_C*dth2_sdkap, ...
               0.5*(kron(R2p_C,xC)+kron(xC,R2p_C))-R21_C*dth1_sdkap-R22_C*dth2_sdkap));
120
121     DTENSOR_TW_H=[DTENSOR_TW_H, Dtensor_Tw_H];
122
123     % Sum two components of the tensor
124     Dtensor_H=Dtensor_Bd_H+Dtensor_Tw_H; % Concatenate
125
126     % Concatenate the tensors for each Length
127     DTENSOR_H=[DTENSOR_H,Dtensor_H];
128 end
129
130
131 Anal_D11_H=DTENSOR_H(1,:);
132 Anal_D12_H=DTENSOR_H(4,:);
133 Anal_D66_H=DTENSOR_H(6,:);
```

Appendix B

Python scripts for simulation of in-plane and out-of-plane stiffnesses

Python scripts that perform FE simulation using Abaqus commercial software are shown as examples. Scripts for both in-plane and out-of-plane stiffnesses are shown. Similar scripts were built for simulations of other 2D-lattices.

B.1 Script for FE simulation of in-plane stiffness for triangular lattice

```
1
2 '''
3 ==========================================================================...

4 Python code for Triangular lattice:
5 NB: The units are N and mm (SI small parts)
6 Code: Tri_Inplane.py
7 Authors: Jungki Song
```

```
8 Last update: March 13, 2020
9 MIT
10 email: jksong@mit.edu
11 ===================================================================...

12 '''
13 '''
14 -------------------------------------------------------------------...

15 Import Python-related libraries
16 -------------------------------------------------------------------...

17 '''
18 import numpy as np
19 import math
20 from math import cos, pi
21
22 '''
23 -------------------------------------------------------------------...

24 Import Abaqus-related libraries
25 -------------------------------------------------------------------...

26 '''
27 from part import *
28 from material import *
29 from section import *
30 from assembly import *
31 from step import *
32 from interaction import *
33 from load import *
34 from mesh import *
35 from optimization import *
36 from job import *
37 from sketch import *
38 from visualization import *
```

```
39 import mesh
40
41 '''
42 -------------------------------------------------------------------...
43 Simulation options
44 -------------------------------------------------------------------...
45 '''
46 # Parameters
47 width = np.array([0.096]) # mm
48 Length=np.array([1.7, 1.836, 1.971, 2.107, 2.243, 2.379, 2.514,...
       2.65, 2.786, 2.921, 3.057, 3.193, 3.329, 3.464, 3.6])
49 thickness = 0.5
50
51 # Meshing Parameters
52 numel = 50   # Number of elements for edge seeds
53 bias  = 200  # Bias to conenctrate mesh closer to the hole
54 tol   = 1e-6 # Tolerance for bounding box selection
55
56 '''
57 -----------------------------------------------------------------...
58 Pre-processing
59 -----------------------------------------------------------------...
60 '''
61
62 # Parameters to be used during pre-processing
63 seed_size=0.005
64
65 Young=169e3
66 Poisson=0.265
67
68 eps_M11 = [0.0005, 0,      0,      0.0005]
69 eps_M22 = [0,      0.0005, 0,      0.0005]
```

```
70 twoeps_M12 = [0,     0,     0.0005, 0]
71
72 SE=[]
73 FreeVar=[]
74
75 for L in Length:
76   for w in width:
77     Area = L*L*sin(pi/3)
78     OArea= sqrt(3)/2*L**2-3*w*L+3*sqrt(3)/2*w**2
79     OAreafrac = OArea/Area
80
81     EffL = L#-sqrt(3)*w # mm
82
83     for i in range(len(eps_M11)):
84
85       # Directories and Solving
86       basename = os.path.dirname(os.path.realpath('__file__')) ...
     # Getting current directory
87       os.chdir(basename)  # Change to this directory
88       ncpus = 1 # Number of cpus
89
90       # File Extensions to delete after simulation ends
91       FileDelList=['.023','.mdl', '.sim', '.stt', '.com', '.fil...
    ', '.ipm', '.lck', '.prt', '_tmp.inp',
92            '.sta','.jnl','.msg','.cae','.inp', '.dat']
93
94       # Use geometry to identify the model's features
95       session.journalOptions.setValues(replayGeometry=...
    COORDINATE, recoverGeometry=COORDINATE)
96
97       # Clear the model database
98       Mdb()
99       ModelName    = 'Model-1'
100      Model = mdb.models[ModelName] #Define Model as the ...
    current model's class
101
```

```
102     JobName = 'Tri_'+'L_'+str(int(EffL*1000))+'_W_'+str(int(w...
    *1000))+'_t_'+str(int(thickness*1000))+'TSSd0p005'+str(int(i...
    ));
103
104     x1A = EffL*0.5*cos(pi/3)
105     x2A = EffL*0.5*sin(pi/3)
106     x1B = EffL*0.5
107     x2B = 0
108     x1C = EffL*0.5*cos(pi/3)
109     x2C = -EffL*0.5*sin(pi/3)
110
111     x1A_star = -EffL*0.5*cos(pi/3)
112     x2A_star = -EffL*0.5*sin(pi/3)
113     x1B_star = -EffL*0.5
114     x2B_star = 0
115     x1C_star = -EffL*0.5*cos(pi/3)
116     x2C_star = EffL*0.5*sin(pi/3)
117
118     # Part...
    ------------------------------------------------------------------------...

119     # Make Rectangle
120     s=Model.ConstrainedSketch(name='__profile__', sheetSize...
    =3)
121
122     Model.sketches['__profile__'].Line(point1=(x1B_star, ...
    x2B_star), point2=(x1B, x2B))
123     Model.sketches['__profile__'].Line(point1=(x1C_star, ...
    x2C_star), point2=(x1C, x2C))
124     Model.sketches['__profile__'].Line(point1=(x1A, x2A), ...
    point2=(x1A_star, x2A_star))
125
126     Model.Part(
127       name='Part-1',
128       dimensionality=TWO_D_PLANAR,
129         type=DEFORMABLE_BODY)
```

```
130     Model.parts['Part-1'].BaseWire(sketch=s)
131     Model.ConstrainedSketch(name='__profile__', sheetSize=3)....
    unsetPrimaryObject()
132     session.viewports['Viewport: 1'].setValues(...
    displayedObject=Model.parts['Part-1'])
133     del Model.sketches['__profile__']
134 
135     # Material
136     session.viewports['Viewport: 1'].partDisplay.setValues(
137       sectionAssignments=ON,
138         engineeringFeatures=ON)
139     session.viewports['Viewport: 1'].partDisplay....
    geometryOptions.setValues(
140         referenceRepresentation=OFF)
141     Model.Material(name='Material-1')
142     Model.materials['Material-1'].Elastic(table=((Young, ...
    Poisson), ))
143 
144     #Profile
145     Model.RectangularProfile(
146       name='Profile-1',
147       a=thickness,
148       b=w)
149 
150     #Section
151     Model.BeamSection(name='Section-1',
152         integration=DURING_ANALYSIS,
153         poissonRatio=0.0,
154         profile='Profile-1',
155         material='Material-1',
156         temperatureVar=LINEAR,
157         consistentMassMatrix=False)
158 
159     #Section assignment (Make set)
160     edges = Model.parts['Part-1'].edges.findAt(((-EffL*0.25, ...
    0.0, 0.0), ), ((EffL*0.25, 0.0, 0.0), ),
```

```
161         ((-EffL*0.25*cos(pi/3), EffL*0.25*sin(pi/3), 0.0), ), ...
    ((EffL*0.25*cos(pi/3), -EffL*0.25*sin(pi/3), 0.0), ),
162         ((EffL*0.25*cos(pi/3), EffL*0.25*sin(pi/3), 0.0), ), ...
    ((-EffL*0.25*cos(pi/3), -EffL*0.25*sin(pi/3), 0.0), ), )
163       Model.parts['Part-1'].Set(
164         edges=edges,
165         name='Set-1')
166
167       #Beam orientation
168       mdb.models['Model-1'].parts['Part-1']....
    assignBeamSectionOrientation(
169         region=mdb.models['Model-1'].parts['Part-1'].sets['Set...
    -1'],
170         method=N1_COSINES,
171         n1=(0.0, 0.0, -1.0))
172
173
174       #Section assignment
175       Model.parts['Part-1'].SectionAssignment(
176         region=Model.parts['Part-1'].sets['Set-1'],
177         sectionName='Section-1',
178         offset=0.0,
179           offsetType=MIDDLE_SURFACE,
180           offsetField='',
181           thicknessAssignment=FROM_SECTION)
182
183       # Assembly
184       Model.rootAssembly.DatumCsysByDefault(CARTESIAN)
185       Model.rootAssembly.Instance(
186         name='Part-1-1',
187         part=Model.parts['Part-1'],
188         dependent=OFF)
189       session.viewports['Viewport: 1'].assemblyDisplay....
    setValues(
190           adaptiveMeshConstraints=ON)
191
```

```
192     # Meshing
193     mdb.models['Model-1'].rootAssembly.setElementType(
194       regions=(mdb.models['Model-1'].rootAssembly.instances['...
    Part-1-1'].edges.findAt(((0.5*x1A, 0.5*x2A, 0.0), ), ((0.5*...
    x1A_star, 0.5*x2A_star, 0.0), ),
195       ((0.5*x1B, 0.5*x2B, 0.0), ), ((0.5*x1B_star, 0.5*...
    x2B_star, 0.0), ), ((0.5*x1C, 0.5*x2C, 0.0), ), ((0.5*...
    x1C_star, 0.5*x2C_star, 0.0), )), ),
196       elemTypes=(mesh.ElemType(elemCode=B21, elemLibrary=...
    STANDARD), ))
197
198     Model.rootAssembly.seedPartInstance(
199       regions=(Model.rootAssembly.instances['Part-1-1'],),
200       size=seed_size,
201       deviationFactor=0.1,
202         minSizeFactor=0.1)
203     Model.rootAssembly.generateMesh(regions=(Model....
    rootAssembly.instances['Part-1-1'],))
204
205     #Constraint (make node sets)
206     Model.rootAssembly.Set(
207       vertices=Model.rootAssembly.instances['Part-1-1']....
    vertices.findAt(((x1A, x2A, 0.0), )),
208       name='A')
209     Model.rootAssembly.Set(
210       vertices=Model.rootAssembly.instances['Part-1-1']....
    vertices.findAt(((x1A_star, x2A_star, 0.0), )),
211       name='A*')
212     Model.rootAssembly.Set(
213       vertices=Model.rootAssembly.instances['Part-1-1']....
    vertices.findAt(((x1B, x2B, 0.0), )),
214       name='B')
215     Model.rootAssembly.Set(
216       vertices=Model.rootAssembly.instances['Part-1-1']....
    vertices.findAt(((x1B_star, x2B_star, 0.0), )),
217       name='B*')
```

```
218     Model.rootAssembly.Set(
219       vertices=Model.rootAssembly.instances['Part-1-1']....
    vertices.findAt(((x1C, x2C, 0.0), )),
220       name='C')
221     Model.rootAssembly.Set(
222       vertices=Model.rootAssembly.instances['Part-1-1']....
    vertices.findAt(((x1C_star, x2C_star, 0.0), )),
223       name='C*')
224 
225     #Constraint (Equations)
226     Model.Equation(
227       name='Constraint-1',
228       terms=((1.0, 'A', 6), (-1.0, 'A*', 6)))
229     Model.Equation(
230       name='Constraint-2',
231       terms=((1.0, 'B', 6), (-1.0, 'B*', 6)))
232     Model.Equation(
233       name='Constraint-3',
234       terms=((1.0, 'C', 6), (-1.0, 'C*', 6)))
235 
236     #Step
237     Model.StaticStep(
238       name='Step-1',
239       previous='Initial')
240     session.viewports['Viewport: 1'].assemblyDisplay....
    setValues(step='Step-1')
241 
242     # BC
243     Model.DisplacementBC(name='BC_A',
244       createStepName='Step-1',
245         region=Model.rootAssembly.sets['A'],
246         u1=eps_M11[i]*x1A+twoeps_M12[i]*0.5*x2A,
247         u2=twoeps_M12[i]*0.5*x1A+eps_M22[i]*x2A,
248         ur3=UNSET,
249         amplitude=UNSET,
250         fixed=OFF,
```

```
251             distributionType=UNIFORM,
252             fieldName='',
253             localCsys=None)
254 
255         Model.DisplacementBC(name='BC_A*',
256           createStepName='Step-1',
257             region=Model.rootAssembly.sets['A*'],
258             u1=eps_M11[i]*x1A_star+twoeps_M12[i]*0.5*x2A_star,
259             u2=twoeps_M12[i]*0.5*x1A_star+eps_M22[i]*x2A_star,
260             ur3=UNSET,
261             amplitude=UNSET,
262             fixed=OFF,
263             distributionType=UNIFORM,
264             fieldName='',
265             localCsys=None)
266 
267         Model.DisplacementBC(name='BC_B',
268           createStepName='Step-1',
269             region=Model.rootAssembly.sets['B'],
270             u1=eps_M11[i]*x1B+twoeps_M12[i]*0.5*x2B,
271             u2=twoeps_M12[i]*0.5*x1B+eps_M22[i]*x2B,
272             ur3=UNSET,
273             amplitude=UNSET,
274             fixed=OFF,
275             distributionType=UNIFORM,
276             fieldName='',
277             localCsys=None)
278 
279         Model.DisplacementBC(name='BC_B*',
280           createStepName='Step-1',
281             region=Model.rootAssembly.sets['B*'],
282             u1=eps_M11[i]*x1B_star+twoeps_M12[i]*0.5*x2B_star,
283             u2=twoeps_M12[i]*0.5*x1B_star+eps_M22[i]*x2B_star,
284             ur3=UNSET,
285             amplitude=UNSET,
286             fixed=OFF,
```

```
287             distributionType=UNIFORM,
288             fieldName='',
289             localCsys=None)
290
291         Model.DisplacementBC(name='BC_C',
292           createStepName='Step-1',
293             region=Model.rootAssembly.sets['C'],
294             u1=eps_M11[i]*x1C+twoeps_M12[i]*0.5*x2C,
295             u2=twoeps_M12[i]*0.5*x1C+eps_M22[i]*x2C,
296             ur3=UNSET,
297             amplitude=UNSET,
298             fixed=OFF,
299             distributionType=UNIFORM,
300             fieldName='',
301             localCsys=None)
302
303         Model.DisplacementBC(name='BC_C*',
304           createStepName='Step-1',
305             region=Model.rootAssembly.sets['C*'],
306             u1=eps_M11[i]*x1C_star+twoeps_M12[i]*0.5*x2C_star,
307             u2=twoeps_M12[i]*0.5*x1C_star+eps_M22[i]*x2C_star,
308             ur3=UNSET,
309             amplitude=UNSET,
310             fixed=OFF,
311             distributionType=UNIFORM,
312             fieldName='',
313             localCsys=None)
314
315         #Job and submit
316         mdb.Job(atTime=None, contactPrint=OFF, description='', ...
    echoPrint=OFF,
317           explicitPrecision=SINGLE, getMemoryFromAnalysis=True, ...
    historyPrint=OFF,
318           memory=10, memoryUnits=PERCENTAGE, model=ModelName, ...
    modelPrint=OFF,
```

```
319         multiprocessingMode=DEFAULT, name=JobName, ...
    nodalOutputPrecision=
320         SINGLE, numCpus=ncpus, numGPUs=0, queue=None, ...
    resultsFormat=ODB, scratch='',
321         type=ANALYSIS, userSubroutine='', waitHours=0, ...
    waitMinutes=0)
322 
323       mdb.jobs[JobName].submit(consistencyChecking=OFF)
324       mdb.jobs[JobName].waitForCompletion()
325 
326       '''
327       ...
    -------------------------------------------------------------------...

328       Post-processing
329       ...
    -------------------------------------------------------------------...

330       '''
331 
332       odb = session.openOdb(name=JobName+'.odb')
333       session.viewports[session.currentViewportName].setValues(...
    displayedObject=odb)
334       x0 = session.XYDataFromHistory(name='ALLSE Whole Model-3'...
    , odb=odb,
335         outputVariableName='Strain energy: ALLSE for Whole ...
    Model', steps=(
336         'Step-1', ), __linkedVpName__='Viewport: 1')
337 
338       SE.append(x0[1][1])
339 
340       if i==0:
341         C11=SE[i]/((0.5*Area)*eps_M11[i]**2)
342       elif i==1:
343         C22=SE[i]/((0.5*Area)*eps_M22[i]**2)
344       elif i==2:
```

```
345         C66=SE[i]/((0.5*Area)*twoeps_M12[i]**2)
346       elif i==3:
347         C12=(SE[i]/(0.5*Area)-C11*eps_M11[i]**2-C22*eps_M22[i...
    ]**2)/(2*eps_M11[i]*eps_M22[i])
348
349       x1 = session.xyDataListFromField(
350               odb=odb,
351               outputPosition=NODAL,
352               variable=(('UR3', NODAL), ),
353               nodeSets=('A', ))
354       FreeVar.append(x1)
355
356       odb.close()
357
358       # Clean Up after simulation
359       for indDel in FileDelList:
360         if os.path.exists(JobName+indDel):
361           os.remove(JobName+indDel)
362
363
364         nueff = C12/C11
365         Ceff=C11
366         #Geff=C66/2/thickness
367
368         fileID=open('TriInplane_'+'L_'+str(int(EffL*1000))+'_W_...
    '+str(int(w*1000))+'_t_'+str(int(thickness*1000))+'result TS...
     Sd0p005.txt','w')
369
370         fileID.write('Effective elasticity tensor C11, C22, C12...
    , C66 [N/mm]\n')
371         fileID.write('%f, %f, %f, %f\n' % (C11,C22,C12,C66))
372
373         fileID.write('Strain energy: uniaxial1, uniaxial2, ...
    shear, equibiaxial [mJ]\n')
374         fileID.write('%f, %f, %f, %f\n' % (SE[0], SE[1], SE[2],...
     SE[3]))
```

```
375
376         fileID.write('Ceff[N/mm] nueff \n')
377         fileID.write('%f, %f \n' % (Ceff, nueff))
378
379         fileID.write('MembraneAxialStiffness[N/mm] ...
    MembraneShearStiffness[N/mm] MembraneBiaxialStiffness[N/mm] ...
    \n')
380         fileID.write('%f, %f, %f \n' % (Ceff, 0.5*Ceff*(1-nueff...
    ), Ceff*(1+nueff)))
381
382         fileID.write('MembraneShearStiffness[N/mm] (calculated ...
    with C66) \n')
383         fileID.write('%f\n' % (C66))
384
385         fileID.write('MembraneBiaxialStiffness[N/mm] (...
    calculated with C11+C12) \n')
386         fileID.write('%f\n' % (C11+C12))
387
388         fileID.write('Unit cell area [mm^3]\n')
389         fileID.write('%f\n' % (Area))
390
391         fileID.write('Open optical area [mm^2]\n')
392         fileID.write('%f\n' % (OArea))
393
394         fileID.write('Open area fraction\n')
395         fileID.write('%f\n' % (OAreafrac))
396
397         #FreeVar[odb file index][U1,U2,UR3 index][Frame index][...
    x,y coordinate index (time=0) (variable=1)]
398         fileID.write('UR3 for uniaxial in 1 direction case\n')
399         fileID.write('%f\n' % (FreeVar[0][0][1][1]))
400
401         fileID.write('UR3 for uniaxial in 2 direction case\n')
402         fileID.write('%f\n' % (FreeVar[1][0][1][1]))
403
404         fileID.write('UR3 for shear case\n')
```

```
405         fileID.write('%f\n' % (FreeVar[2][0][1][1]))
406
407         fileID.write('UR3 for biaxial case\n')
408         fileID.write('%f\n' % (FreeVar[3][0][1][1]))
409
410         fileID.close()
411
412         #clear data
413         SE=[]
```

B.2 Script for FE simulation of out-of-plane stiffness for triangular lattice

```
1
2 '''
3 ================================================================...

4 Python code for Triangular lattice:
5 NB: The units are N and mm (SI small parts)
6 Code: Tri_outofplane.py
7 Authors: Jungki Song
8 Last update: March 13, 2020
9 MIT
10 email: jksong@mit.edu
11 ================================================================...

12 '''
13 '''
14 -----------------------------------------------------------------...

15 Import Python-related libraries
```

```
16 ------------------------------------------------------------------...

17 '''
18 import numpy as np
19 import math
20
21 from math import cos, pi
22
23 '''
24 ------------------------------------------------------------------...

25 Import Abaqus-related libraries
26 ------------------------------------------------------------------...

27 '''
28 from part import *
29 from material import *
30 from section import *
31 from assembly import *
32 from step import *
33 from interaction import *
34 from load import *
35 from mesh import *
36 from optimization import *
37 from job import *
38 from sketch import *
39 from visualization import *
40 import mesh
41
42
43 '''
44 ------------------------------------------------------------------...

45 Simulation options
46 ------------------------------------------------------------------...

```

```
47 '''
48 # Parameters
49 width = np.array([0.096]) # mm
50 Length=np.array([1.7, 1.836, 1.971, 2.107, 2.243, 2.379, 2.514,...
     2.65, 2.786, 2.921, 3.057, 3.193, 3.329, 3.464, 3.6])
51 thickness = 0.5
52
53 # Meshing Parameters
54 numel = 50   # Number of elements for edge seeds
55 bias  = 200  # Bias to conenctrate mesh closer to the hole
56 tol   = 1e-6 # Tolerance for bounding box selection
57
58 '''
59 ------------------------------------------------------------------...

60 Pre-processing
61 ------------------------------------------------------------------...

62 '''
63
64 # Parameters to be used during pre-processing
65 seed_size=0.005
66
67 Young=169e3
68 Poisson=0.265
69
70 Kap_M11 = [0.001, 0,     0,     0.001]
71 Kap_M22 = [0,     0.001, 0,     0.001]
72 twoKap_M12 = [0,     0,     0.001, 0]
73
74 SE=[]
75 FreeVar=[]
76
77 for L in Length:
78     for w in width:
79         Area = L*L*sin(pi/3)
```

```
80        OArea= sqrt(3)/2*L**2-3*w*L+3*sqrt(3)/2*w**2
81        OAreafrac = OArea/Area
82        EffL = L#-(sqrt(3)/2*w)*2 # mm
83
84        for i in range(len(Kap_M11)):
85
86            # Directories and Solving
87            basename = os.path.dirname(os.path.realpath('...
    __file__'))  # Getting current directory
88            os.chdir(basename)  # Change to this directory
89            ncpus = 1 # Number of cpus
90
91            # File Extensions to delete after simulation ends
92            FileDelList=['.023','.mdl', '.sim', '.stt', '.com',...
     '.fil', '.ipm', '.lck', '.prt', '_tmp.inp',
93                '.sta','.jnl','.msg','.cae', '.inp','.dat']
94
95            # Use geometry to identify the model's features
96            session.journalOptions.setValues(replayGeometry=...
    COORDINATE, recoverGeometry=COORDINATE)
97
98            # Clear the model database
99            Mdb()
100           ModelName    = 'Model-1'
101           Model = mdb.models[ModelName] #Define Model as the ...
    current model's class
102
103           JobName = 'Tri_'+'L_'+str(int(EffL*1000))+'_W_'+str...
    (int(w*1000))+'_t_'+str(int(thickness*1000))+'TSSd0p005'+str...
    (int(i));
104
105           x1A = EffL*0.5*cos(pi/3)
106           x2A = EffL*0.5*sin(pi/3)
107           x1B = EffL*0.5
108           x2B = 0
109           x1C = EffL*0.5*cos(pi/3)
```

```
110             x2C = -EffL*0.5*sin(pi/3)
111
112             x1A_star = -EffL*0.5*cos(pi/3)
113             x2A_star = -EffL*0.5*sin(pi/3)
114             x1B_star = -EffL*0.5
115             x2B_star = 0
116             x1C_star = -EffL*0.5*cos(pi/3)
117             x2C_star = EffL*0.5*sin(pi/3)
118
119             # Part...
    ----------------------------------------------------------------------...

120             # Make Rectangle
121             s=Model.ConstrainedSketch(name='__profile__', ...
    sheetSize=3)
122
123             Model.sketches['__profile__'].Line(point1=(x1B_star...
    , x2B_star), point2=(x1B, x2B))
124             Model.sketches['__profile__'].Line(point1=(x1C_star...
    , x2C_star), point2=(x1C, x2C))
125             Model.sketches['__profile__'].Line(point1=(x1A, x2A...
    ), point2=(x1A_star, x2A_star))
126
127             Model.Part(
128                 name='Part-1',
129                 dimensionality=THREE_D,
130                 type=DEFORMABLE_BODY)
131             Model.parts['Part-1'].BaseWire(sketch=s)
132             Model.ConstrainedSketch(name='__profile__', ...
    sheetSize=3).unsetPrimaryObject()
133             session.viewports['Viewport: 1'].setValues(...
    displayedObject=Model.parts['Part-1'])
134             del Model.sketches['__profile__']
135
136             # Material
```

```
137            session.viewports['Viewport: 1'].partDisplay....
     setValues(
138                sectionAssignments=ON,
139                engineeringFeatures=ON)
140            session.viewports['Viewport: 1'].partDisplay....
     geometryOptions.setValues(
141                referenceRepresentation=OFF)
142            Model.Material(name='Material-1')
143            Model.materials['Material-1'].Elastic(table=((Young...
     , Poisson), ))
144
145
146            #Profile
147            Model.RectangularProfile(
148                name='Profile-1',
149                a=thickness,
150                b=w)
151
152            #Section
153            Model.BeamSection(name='Section-1',
154                integration=DURING_ANALYSIS,
155                poissonRatio=0.0,
156                profile='Profile-1',
157                material='Material-1',
158                temperatureVar=LINEAR,
159                consistentMassMatrix=False)
160
161            #Section assignment (Make set)
162            edges = Model.parts['Part-1'].edges.findAt(((-EffL...
     *0.25, 0.0, 0.0), ), ((EffL*0.25, 0.0, 0.0), ),
163                ((-EffL*0.25*cos(pi/3), EffL*0.25*sin(pi/3), ...
     0.0), ), ((EffL*0.25*cos(pi/3), -EffL*0.25*sin(pi/3), 0.0), ...
     ),
164                ((EffL*0.25*cos(pi/3), EffL*0.25*sin(pi/3), ...
     0.0), ), ((-EffL*0.25*cos(pi/3), -EffL*0.25*sin(pi/3), 0.0),...
      ), )
```

```
165            Model.parts['Part-1'].Set(
166                edges=edges,
167                name='Set-1')
168
169            #Beam orientation
170            mdb.models['Model-1'].parts['Part-1']....
    assignBeamSectionOrientation(
171                region=mdb.models['Model-1'].parts['Part-1']....
    sets['Set-1'],
172                method=N1_COSINES,
173                n1=(0.0, 0.0, -1.0))
174
175            #Section assignment
176            Model.parts['Part-1'].SectionAssignment(
177                region=Model.parts['Part-1'].sets['Set-1'],
178                sectionName='Section-1',
179                offset=0.0,
180                offsetType=MIDDLE_SURFACE,
181                offsetField='',
182                thicknessAssignment=FROM_SECTION)
183
184            # Assembly
185            Model.rootAssembly.DatumCsysByDefault(CARTESIAN)
186            Model.rootAssembly.Instance(
187                name='Part-1-1',
188                part=Model.parts['Part-1'],
189                dependent=OFF)
190            session.viewports['Viewport: 1'].assemblyDisplay....
    setValues(
191                adaptiveMeshConstraints=ON)
192
193            mdb.models['Model-1'].rootAssembly.setElementType(
194                regions=(mdb.models['Model-1'].rootAssembly....
    instances['Part-1-1'].edges.findAt(((-EffL*0.25, 0.0, 0.0), ...
    ), ((EffL*0.25, 0.0, 0.0), ),
```

```
195                         ((-EffL*0.25*cos(pi/3), EffL*0.25*sin(...
pi/3), 0.0), ), ((EffL*0.25*cos(pi/3), -EffL*0.25*sin(pi/3),...
 0.0), ),
196                         ((EffL*0.25*cos(pi/3), EffL*0.25*sin(pi...
/3), 0.0), ), ((-EffL*0.25*cos(pi/3), -EffL*0.25*sin(pi/3), ...
0.0), ), ), ),
197                 elemTypes=(mesh.ElemType(elemCode=B31, ...
elemLibrary=STANDARD), ))
198
199             # Meshing
200             Model.rootAssembly.seedPartInstance(
201                 regions=(Model.rootAssembly.instances['Part-1-1...
'],),
202                 size=seed_size,
203                 deviationFactor=0.1,
204                 minSizeFactor=0.1)
205             Model.rootAssembly.generateMesh(regions=(Model....
rootAssembly.instances['Part-1-1'],))
206
207             #Step
208             Model.StaticStep(
209                 name='Step-1',
210                 previous='Initial')
211             session.viewports['Viewport: 1'].assemblyDisplay....
setValues(step='Step-1')
212
213             #BCs (make node sets)
214             Model.rootAssembly.Set(
215                 vertices=Model.rootAssembly.instances['Part-1-1...
'].vertices.findAt(((x1A, x2A, 0.0), )),
216                 name='A')
217             Model.rootAssembly.Set(
218                 vertices=Model.rootAssembly.instances['Part-1-1...
'].vertices.findAt(((x1A_star, x2A_star, 0.0), )),
219                 name='A*')
220             Model.rootAssembly.Set(
```

```
221                 vertices=Model.rootAssembly.instances['Part-1-1...
    '].vertices.findAt(((x1B, x2B, 0.0), )),
222                 name='B')
223             Model.rootAssembly.Set(
224                 vertices=Model.rootAssembly.instances['Part-1-1...
    '].vertices.findAt(((x1B_star, x2B_star, 0.0), )),
225                 name='B*')
226             Model.rootAssembly.Set(
227                 vertices=Model.rootAssembly.instances['Part-1-1...
    '].vertices.findAt(((x1C, x2C, 0.0), )),
228                 name='C')
229             Model.rootAssembly.Set(
230                 vertices=Model.rootAssembly.instances['Part-1-1...
    '].vertices.findAt(((x1C_star, x2C_star, 0.0), )),
231                 name='C*')
232             Model.rootAssembly.Set(
233                 vertices=Model.rootAssembly.instances['Part-1-1...
    '].vertices.findAt(((0.0, 0.0, 0.0), )),
234                 name='Star')
235 
236             # BC
237             mdb.models['Model-1'].DisplacementBC(
238                 name='BC_A',
239                 createStepName='Step-1',
240                 region=Model.rootAssembly.sets['A'],
241                 u1=0.0,
242                 u2=0.0,
243                 u3=0.5*Kap_M11[i]*x1A**2 + 0.5*Kap_M22[i]*x2A...
    **2 + twoKap_M12[i]*0.5*x1A*x2A,
244                 ur1=Kap_M22[i]*x2A+twoKap_M12[i]*0.5*x1A,
245                 ur2=-Kap_M11[i]*x1A-twoKap_M12[i]*0.5*x2A,
246                 ur3=0.0,
247                 amplitude=UNSET,
248                 fixed=OFF,
249                 distributionType=UNIFORM,
250                 fieldName='',
```

```
251                 localCsys=None)
252
253             mdb.models['Model-1'].DisplacementBC(
254                 name='BC_A*',
255                 createStepName='Step-1',
256                 region=Model.rootAssembly.sets['A*'],
257                 u1=0.0,
258                 u2=0.0,
259                 u3=0.5*Kap_M11[i]*x1A_star**2 + 0.5*Kap_M22[i]*...
    x2A_star**2 + twoKap_M12[i]*0.5*x1A_star*x2A_star,
260                 ur1=Kap_M22[i]*x2A_star+twoKap_M12[i]*0.5*...
    x1A_star,
261                 ur2=-Kap_M11[i]*x1A_star-twoKap_M12[i]*0.5*...
    x2A_star,
262                 ur3=0.0,
263                 amplitude=UNSET,
264                 fixed=OFF,
265                 distributionType=UNIFORM,
266                 fieldName='',
267                 localCsys=None)
268
269             mdb.models['Model-1'].DisplacementBC(
270                 name='BC_B',
271                 createStepName='Step-1',
272                 region=Model.rootAssembly.sets['B'],
273                 u1=0.0,
274                 u2=0.0,
275                 u3=0.5*Kap_M11[i]*x1B**2 + 0.5*Kap_M22[i]*x2B...
    **2 + twoKap_M12[i]*0.5*x1B*x2B,
276                 ur1=Kap_M22[i]*x2B+twoKap_M12[i]*0.5*x1B,
277                 ur2=-Kap_M11[i]*x1B-twoKap_M12[i]*0.5*x2B,
278                 ur3=0.0,
279                 amplitude=UNSET,
280                 fixed=OFF,
281                 distributionType=UNIFORM,
282                 fieldName='',
```

```
283                 localCsys=None)
284 
285             mdb.models['Model-1'].DisplacementBC(
286                 name='BC_B*',
287                 createStepName='Step-1',
288                 region=Model.rootAssembly.sets['B*'],
289                 u1=0.0,
290                 u2=0.0,
291                 u3=0.5*Kap_M11[i]*x1B_star**2 + 0.5*Kap_M22[i]*...
    x2B_star**2 + twoKap_M12[i]*0.5*x1B_star*x2B_star,
292                 ur1=Kap_M22[i]*x2B_star+twoKap_M12[i]*0.5*...
    x1B_star,
293                 ur2=-Kap_M11[i]*x1B_star-twoKap_M12[i]*0.5*...
    x2B_star,
294                 ur3=0.0,
295                 amplitude=UNSET,
296                 fixed=OFF,
297                 distributionType=UNIFORM,
298                 fieldName='',
299                 localCsys=None)
300 
301             mdb.models['Model-1'].DisplacementBC(
302                 name='BC_C',
303                 createStepName='Step-1',
304                 region=Model.rootAssembly.sets['C'],
305                 u1=0.0,
306                 u2=0.0,
307                 u3=0.5*Kap_M11[i]*x1C**2 + 0.5*Kap_M22[i]*x2C...
    **2 + twoKap_M12[i]*0.5*x1C*x2C,
308                 ur1=Kap_M22[i]*x2C+twoKap_M12[i]*0.5*x1C,
309                 ur2=-Kap_M11[i]*x1C-twoKap_M12[i]*0.5*x2C,
310                 ur3=0.0,
311                 amplitude=UNSET,
312                 fixed=OFF,
313                 distributionType=UNIFORM,
314                 fieldName='',
```

```
315                 localCsys=None)
316
317             mdb.models['Model-1'].DisplacementBC(
318                 name='BC_C*',
319                 createStepName='Step-1',
320                 region=Model.rootAssembly.sets['C*'],
321                 u1=0.0,
322                 u2=0.0,
323                 u3=0.5*Kap_M11[i]*x1C_star**2 + 0.5*Kap_M22[i]*...
        x2C_star**2 + twoKap_M12[i]*0.5*x1C_star*x2C_star,
324                 ur1=Kap_M22[i]*x2C_star+twoKap_M12[i]*0.5*...
        x1C_star,
325                 ur2=-Kap_M11[i]*x1C_star-twoKap_M12[i]*0.5*...
        x2C_star,
326                 ur3=0.0,
327                 amplitude=UNSET,
328                 fixed=OFF,
329                 distributionType=UNIFORM,
330                 fieldName='',
331                 localCsys=None)
332
333
334             #Job and submit
335             mdb.Job(atTime=None, contactPrint=OFF, description=...
        '', echoPrint=OFF,
336                 explicitPrecision=SINGLE, getMemoryFromAnalysis...
        =True, historyPrint=OFF,
337                 memory=20, memoryUnits=PERCENTAGE, model=...
        ModelName, modelPrint=OFF,
338                 multiprocessingMode=DEFAULT, name=JobName, ...
        nodalOutputPrecision=
339                 SINGLE, numCpus=ncpus, numGPUs=0, queue=None, ...
        resultsFormat=ODB, scratch='',
340                 type=ANALYSIS, userSubroutine='', waitHours=0, ...
        waitMinutes=0)
341
```

```
342             mdb.jobs[JobName].submit(consistencyChecking=OFF)
343             mdb.jobs[JobName].waitForCompletion()
344 
345             '''
346             ...
    --------------------------------------------------------------------...
347             Post-processing
348             ...
    --------------------------------------------------------------------...
349             '''
350 
351             odb = session.openOdb(name=JobName+'.odb')
352             session.viewports[session.currentViewportName]....
    setValues(displayedObject=odb)
353             x0 = session.XYDataFromHistory(name='ALLSE Whole ...
    Model-3', odb=odb,
354                 outputVariableName='Strain energy: ALLSE for ...
    Whole Model', steps=(
355                 'Step-1', ), __linkedVpName__='Viewport: 1')
356 
357             SE.append(x0[1][1])
358 
359             if i==0:
360                 D11=SE[i]/((0.5*Area)*Kap_M11[i]**2)
361             elif i==1:
362                 D22=SE[i]/((0.5*Area)*Kap_M22[i]**2)
363             elif i==2:
364                 D66=SE[i]/((0.5*Area)*twoKap_M12[i]**2)
365             elif i==3:
366                 D12=(SE[i]/(0.5*Area)-D11*Kap_M11[i]**2-D22*...
    Kap_M22[i]**2)/(2*Kap_M11[i]*Kap_M22[i])
367 
368             x3 = session.xyDataListFromField(
369                 odb=odb,
```

```
370                 outputPosition=NODAL,
371                 variable=(('U', NODAL, ((COMPONENT, 'U1'), (...
    COMPONENT, 'U2'), (COMPONENT, 'U3'), )), ('UR', NODAL, ((...
    COMPONENT, 'UR1'), (COMPONENT, 'UR2'), (COMPONENT, 'UR3'),))...
    , ),
372                 nodeSets=('STAR', ))
373             FreeVar.append(x3)
374 
375             odb.close()
376 
377             # Clean Up after simulation
378             for indDel in FileDelList:
379                 if os.path.exists(JobName+indDel):
380                     os.remove(JobName+indDel)
381 
382         Deff  = D11
383         nueff= D12/D11
384 
385         fileID=open('TriCurvature_'+'L_'+str(int(EffL*1000))+'...
    _W_'+str(int(w*1000))+'_t_'+str(int(thickness*1000))+'result...
     TS Sd0p005.txt','w')
386         #fileID=open('TriInplane_'+'L_'+str(int(L*1000))+'_W_'+...
    str(int(w*1000))+'_t_'+str(int(thickness*1000))+'result (Eff...
    ).txt','w')
387 
388         fileID.write('Effective elasticity tensor for curvature...
     D11, D22, D12, D66 [N mm]\n')
389         fileID.write('%f, %f, %f, %f \n' % (D11,D22,D12,D66))
390 
391         fileID.write('Strain energy: uniaxial1, uniaxial2, ...
    shear, equibiaxial [mJ]\n')
392         fileID.write('%f, %f, %f, %f\n' % (SE[0], SE[1], SE[2],...
     SE[3]))
393 
394         fileID.write('Deff[N mm/mm] nueff \n')
395         fileID.write('%f, %f \n' % (Deff, nueff))
```

```
396
397         fileID.write('PlateBendingRigidity[N mm] ...
    PlateTwistingRigidity[N mm] BiaxialPlateBendingRigidity[N mm...
    ] \n')
398         fileID.write('%f, %f, %f \n' % (Deff, 0.5*Deff*(1-nueff...
    ), Deff*(1+nueff)))
399
400         fileID.write('PlateTwistingRigidity[N mm] (calculated ...
    with D66) \n')
401         fileID.write('%f\n' % (D66))
402
403         fileID.write('MembraneBiaxialStiffness[N mm] (...
    calculated with D11+D12) \n')
404         fileID.write('%f\n' % (D11+D12))
405
406         fileID.write('Area [mm^2]\n')
407         fileID.write('%f\n' % (Area))
408
409         fileID.write('Open optical area [mm^2]\n')
410         fileID.write('%f\n' % (OArea))
411
412         fileID.write('Open area fraction\n')
413         fileID.write('%f\n' % (OAreafrac))
414
415         #FreeVar[odb file index][U3,UR1,UR2 index][Frame index...
    ][x,y coordinate index (time=0) (variable=1)]
416         fileID.write('U1, U2, U3, UR1, UR2, UR3 for uniaxial in...
     1 direction case\n')
417         fileID.write('%6f, %6f, %6f, %6f, %6f, %6f\n' % (...
    FreeVar[0][0][1][1], FreeVar[0][1][1][1], FreeVar...
    [0][2][1][1], FreeVar[0][3][1][1], FreeVar[0][4][1][1], ...
    FreeVar[0][5][1][1]))
418
419         fileID.write('U1, U2, U3, UR1, UR2, UR3 for uniaxial in...
     2 direction case\n')
```

```
420         fileID.write('%6f, %6f, %6f, %6f, %6f, %6f\n' % (...
    FreeVar[1][0][1][1], FreeVar[1][1][1][1], FreeVar...
    [1][2][1][1], FreeVar[1][3][1][1], FreeVar[1][4][1][1], ...
    FreeVar[1][5][1][1]))
421
422         fileID.write('U1, U2, U3, UR1, UR2, UR3 for shear case\...
    n')
423         fileID.write('%6f, %6f, %6f, %6f, %6f, %6f\n' % (...
    FreeVar[2][0][1][1], FreeVar[2][1][1][1], FreeVar...
    [2][2][1][1], FreeVar[2][3][1][1], FreeVar[2][4][1][1], ...
    FreeVar[2][5][1][1]))
424
425         fileID.write('U1, U2, U3, UR1, UR2, UR3 for biaxial ...
    case\n')
426         fileID.write('%6f, %6f, %6f, %6f, %6f, %6f\n' % (...
    FreeVar[3][0][1][1], FreeVar[3][1][1][1], FreeVar...
    [3][2][1][1], FreeVar[3][3][1][1], FreeVar[3][4][1][1], ...
    FreeVar[3][5][1][1]))
427
428         fileID.close()
429
430         SE=[]
431         FreeVar=[]
```

Bibliography

[1] 2020 International Roadmap for Devices and Systems (IRDS) — Beyond CMOS. Technical report, IEEE, Piscataway, 2018.

[2] 2020 International Roadmap for Devices and Systems (IRDS) — Metrology. Technical report, IEEE, Piscataway, 2018.

[3] 2020 International Roadmap for Devices and Systems (IRDS) — Moore More. Technical report, IEEE, Piscataway, 2018.

[4] M. Ahn, R. K. Heilmann, and M. L. Schattenburg. Fabrication of ultrahigh aspect ratio freestanding gratings on silicon-on-insulator wafers. *J. Vac. Sci. Technol. B*, 25(2593), 2007.

[5] M. Ahn, R. K. Heilmann, and M. L. Schattenburg. Fabrication of 200 nm-period blazed transmission gratings on silicon-on-insulator wafers. *J. Vac. Sci. Technol. B*, 26:2179–2182, 2008.

[6] E. H. Anderson, A. M. Levine, and M. L. Schattenburg. Transmission x-ray diffraction grating alignment using a photoelastic modulator. *Appl. Opt.*, 27(16), 1988.

[7] R. D. Barnett, D. Thomas, Y. Song, D. A. Tossell, T. Barrass, and O. Ansell. A new plasma source for next generation MEMS deep si etching: minimal tilt, improved profile uniformity and higher etch rates. *Electric Components and Technology Conference*, pages 1056–1059, 2010.

[8] K. P. Beuermann, H. Bräuninger, and J. Trümper. Aberrations of a facet-type transmission grating for cosmic x-ray and XUV spectroscopy. *Appl. Opt.*, 17(15):2304–2309, 1978.

[9] A. Bruccoleri, R. K. Heilmann, and M. L. Schattenburg. Fabrication process for 200 nm-pitch polished freestanding ultrahigh aspect ratio gratings. *J. Vac. Sci. Technol. B*, 34(06), 2016.

[10] A. Bruccoleri, P. Mukherjee, R. K. Heilmann, J. Yam, M. L. Schattenburg, and F. DiPiazza. Fabrication of nanoscale, high throughput, high aspect ratio freestanding gratings. *J. Vac. Sci. Technol. B*, 30(06), 2012.

[11] W. Cash. X-ray optics: a technique for high-resolution imaging. *Appl. Opt.*, 26(14):2915–2920, 1987.

[12] H. N. Chapman and K. A. Nugent. Coherent lensless x-ray imaging. *Nature Photonics*, 4:833–839, 2010.

[13] C. G. Chen, R. K. Heilmann, C. Joo, P. T. Konkola, G. S. Pati, and M. L. Schattenburg. Beam alignment for scanning beam interference lithography. *J. Vac. Sci. Technol. B*, 20(6):3071–3074, 2016.

[14] C. G. Chen, P. T. Konkola, R. K. Heilmann, G. S. Pati, and M. L. Schattenburg. Image metrology and system controls for scanning beam interference lithography. *J. Vac. Sci. Technol. B*, 19(6):2335–2341, 2001.

[15] P. Cizmar, A. E. Vladár, and M. T. Postek. Real-time scanning charged-particle microscope image composition with correction of drift. *Microsc. Microanal.*, 17:302–308, 2011.

[16] J. Cottam, W. Cash, K. A. Flanagan, R. K. Heilmann, G. Y. Prigozhin, A. P. Rasmussen, G. R. Ricker, M. L. Schattenburg, and E. Schindhelm. The Constellation-X reflection grating spectrometer. *Proc. SPIE*, 6266(62661), 2006.

[17] M. Danielsson, D. M. Parks, , and M. C. Boyce. Three-dimensional micromechanical modeling of voided polymeric materials. *J. Mech. Phys. Solids*, 50(2), 2002.

[18] K. Davami, L. Zhao, E. Lu, J. Cortes, C. Lin, D. E. Lilley, P. K. Purohit, and I. Bargatin. Ultralight shape-recovering plate mechanical metamaterials. *Nat. Comm.*, 6(10019), 2015.

[19] V.S. Deshpande, M.F. Ashby, and N.A. Fleck. Foam topology bending versus stretching dominated architectures. *Acta Materialia*, 49(6):1035–1040, 2001.

[20] D. Dewey, D. N. Humphries, G. Y. McLean, and D. A. Moschella. Laboratory calibration of x-ray transmission diffraction gratings. *Proc. SPIE*, 2280:257–271, 1994.

[21] B. D. Donovan, R. L. McEntaffer, J. H. Tutt, C. T. DeRoo, R. Allured, J. A. Gaskin, and J. J. Kolodziejczak. X-ray verification of an optically aligned off-plane grating module. *Appl. Opt.*, 57(3):454–464, 2018.

[22] I. Doytchinov, P. Shore, B. Nicquevert, X. Tonnellier, A. Heather, and M. Modena. Thermal effects compensation and associated uncertainty for large magnet assembly precision alignment. *Precision Engineering*, 59:134–149, 2019.

[23] B. D. Donovan et al. An updated optical design of the off-plane grating rocket experiment. *Proc. SPIE*, 11119(1111911), 2019.

[24] C. A. Kilbourne et al. Design, implementation, and performance of the Astro-H soft x-ray spectrometer aperture assembly and blocking filters. *J. Astro. Tel. Instr. Syst.*, 4, 2018.

[25] C. R. Canizares et al. The chandra high-energy transmission grating: design, fabrication, ground calibration, and 5 years of filght. *PASP*, 117(836):1144–1171, 2005.

[26] Maximilien J. Collon et. al. Development of ATHENA mirror modules. *Proc. SPIE*, 10399(10399), 2017.

[27] R. K. Smith et al. Arcus: The soft x-ray grating explorer. *Proc. SPIE*, 11118(11118), 2019.

[28] J. Ferrera, M. L. Schattenburg, and H. I. Smith. Analysis of distortion in interference lithography. *J. Vac. Sci. Technol. B*, 14(4009), 1996.

[29] K. F. Fischbach, A. M. Levine, M. L. Schattenburg, D. Dewey, R. L. Renshaw, J. Dalcanton, R. Newman, and W. Fissell. Performance of high spatial frequency x-ray transmission gratings. *Proc. SPIE*, 0982, 1988.

[30] C. R. Forest, M. L. Schattenburg, C. G. Chen, R. K. Heilmann, P. T. Konkola, J. Przbylowski, Y. Sun, J. You, S. M. Kahn, and D.Golini. Precision shaping, assembly, and metrology of foil optics for x-ray reflection gratings. *Proc. SPIE*, 4851:538–548, 2003.

[31] J. A. Gaskin, D. Swartz, A. Vikhlinin, F. Özel, K. Gelmis, J. Arenberg, S. Bandler, M. W. Bautz, M. Civitani, A. Dominguez, M. Eckart, A. Falcone, E. Figueroa-Feliciano, H. M. Günther, R. K. Heilmann, K. Kilaru, R. Kraft, K. McCarley, R. McEntaffer, G. Pareschi, P. Reid, M. L. Schattenburg, D. Schwartz, H. Tananbaum, G. Tremblay, W. Zhang, and J. Zuhone. Lynx x-ray observatory: An Overview. *J. Astron. Telesc. Instrum. Syst.*, 5:021001, 2019.

[32] L. J. Gibson and M. F. Ashby. *Cellular Solids: Structure and Properties*. Cambridge University Press, 1997.

[33] J. W. Goodman. *Introduction to Fourier Optics*. W. H. Freeman, 2017.

[34] A. Goy, G. Rughoobur, S. Li, K. Arthur, A. I. Akinwande, and G. Barbastathis. High-resolution limited-angle phase tomography of dense layered objects using deep neural networks. *Proc. Natl. Acad. Sci.*, 116, 2019.

[35] H. M. Günther, M. W. Bautz, R. K. Heilmann, D. P. Huenemoerder, H. L. Marshall, M. A. Nowak, and N. S. Schulz. Ray-tracing critical-angle transmission gratings for the x-ray surveyor and explorer-size missions. *Proc. SPIE*, 9905(990556):1–10, 2016.

[36] H. M. Günther, C. deRoo, R. K. Heilmann, E. Hertz, R. K. Smith, J. Wilms, and Arcus Collaboration. Ray-tracing Arcus in phase A. *Proc. SPIE*, 10699(106996), 2018.

[37] H. M. Günther, J. Frost, and A. Theriault-Shay. MARXS: A modular software to ray-trace x-ray instrumentation. *Astron. J.*, 154(6), 2017.

[38] H. M. Günther and R. K. Heilmann. Design progress on the Lynx soft x-ray critical-angle transmission grating spectrometer. *Proc. SPIE*, 11118(111181), 2019.

[39] H. M. Günther and R. K. Heilmann. Lynx soft x-ray critical-angle transmission grating spectrometer. *J. Astron. Telesc. Instrum. Syst.*, 5(021003), 2019.

[40] H. M. Günther, R. K. Heilmann, P. Cheimets, and R. K. Smith. Performance of a double tilted-rowland-spectrometer on Arcus. *Proc. SPIE*, 10397(103970), 2017.

[41] J. E. Harvey and C. L. Vernold. Description of diffraction grating behavior in direction cosine space. *Appl. Opt.*, 37(34):8158–8159, 1998.

[42] R. K. Heilmann, M. Ahn, E. M. Gullikson, and M. L. Schattenburg. Blazed high-efficiency x-ray diffraction via transmission through arrays of nanometer-scale mirrors. *Opt. Express*, 16(12):8658–8669, 2008.

[43] R. K. Heilmann, M. Ahn, E. M. Gullikson, and M. L. Schattenburg. Diffraction efficiency of 200 nm period critical-angle transmission gratings in the soft x-ray and extreme ultraviolet wavelength bands. *Appl. Opt.*, 50(11):1364–1373, 2011.

[44] R. K. Heilmann, M. Akilian, C.-H. Chang, C. R. Fores, C. Joo, A. Lapsa, J. C. Montoya, and M. L. Schattenburg. Thin-foil reflection gratings for Constellation-X. *Proc. SPIE*, 5488(283), 2004.

[45] R. K. Heilmann, M. Akilian, C.-H. Chang, R. Hallock, E. Cleaveland, and M. L. Schattenburg. Shaping of thin grazing incidence reflection grating substrates via magnetorheological finishing. *Proc. SPIE*, 5900(590009), 2005.

[46] R. K. Heilmann, A. Bruccoleri, P. Mukherjee, J. Yam, and M. L. Schattenburg. Fabrication update on critical-angle transmission gratings for soft x-ray grating spectrometers. *Proc. SPIE*, 8147(81471), 2011.

[47] R. K. Heilmann, A. Bruccoleri, P. Mukherjee, J. Yam, and M. L. Schattenburg. Nanofabrication advances for high efficiency critical-angle transmission gratings. *Proc. SPIE*, 8861(886119), 2013.

[48] R. K. Heilmann, A. R. Bruccoleri, and M. L. Schattenburg. High-efficiency blazed transmission gratings for high-resolution soft x-ray spectroscopy. *Proc. SPIE*, 9603(960314):1–12, 2015.

[49] R. K. Heilmann, A. R. Bruccoleri, J. Song, C. deRoo, P. Cheimets, E. Hertz, R. K. Smith, V. Burwitz, G. Hartner, M.-M. La Caria, C. Pelliciari, H. M. Günther, S. N. T. Heine, B. LaMarr, H. L. Marshall, N. S. Schulz, E. M. Gullikson, and M. L. Schattenburg. Blazed transmission grating technology development for the Arcus x-ray spectrometer explorer. *Proc. SPIE*, 10699(106996), 2018.

[50] R. K. Heilmann, A. R. Bruccoleri, J. Song, J. Kolodziejczak, J. A. Gaskin, S. L. O'Dell, P. Cheimets, E. Hertz, R. K. Smith, V. Burwitz, G. Hartner, M.-M. La Caria, and M. L. Schattenburg. Critical-angle transmission grating technology development for high resolving power soft x-ray spectrometers on Arcus and Lynx. *Proc. SPIE*, 10399(1039914):1–15, 2017.

[51] R. K. Heilmann, C. G. Chen, P. T. Konkola, and M. L. Schattenburg. Dimensional metrology for nanometer-scale science and engineering: Towards subnanometer accurate encoders. *Nanotechnology*, 15:5504, 2004.

[52] R. K. Heilmann, J. Kolodziejczak, A. R. Bruccoleri, J. A. Gaskin, and M. L. Schattenburg. Demonstration of resolving power $\lambda/\delta\lambda > 10{,}000$ for a space-based x-ray transmission grating spectrometer. *Appl. Opt.*, 58:1223+, 2019.

[53] J. Hohe and W. Becker. Effective elastic properties of triangular grid structures. *Compos. Struct.*, 45(2):131–145, 1999.

[54] J. Hohe and W. Becker. A mechanical model for two-dimensional cellular sandwich cores with general geometry. *Comput. Mater. Sci.*, 19(1), 2000.

[55] J. Hohe and W. Becker. A refined analysis of the effective elasticity tensor for general cellular sandwich cores. *Int. J. Solids Struct.*, 38(21):3689–3717, 2001.

[56] M. Holler, M. Guizar-Sicairos, E. H. R. Tsai, R. Dinapoli, E. Müller, O. Bunk, J. Raabe, and G. Aeppli. High-resolution non-destructive three-dimensional imaging of integrated circuits. *Nature*, 543:402–406, 2017.

[57] T. Hu, R. L. Jones, W. L. Wua, and E. K. Lin. Small angle x-ray scattering metrology for sidewall angle and cross section of nanometer scale line gratings. *J. of Appl. Phys.*, 96(1983), 2004.

[58] H.-T. Huang and F. L. Terry Jr. Spectroscopic ellipsometry and reflectometry from gratings (Scatterometry) for critical dimension measurement and in situ, real-time process monitoring. *Thin Solid Films*, 455, 2004.

[59] J. Huo, N. v. Dijk, and E. K. Gamstedt. Elastic properties of rhombic mesh structures based on computational homogenisation. *Eng. Struct.*, 172:66–75, 2018.

[60] O. Ilic, C. M. Went, and H. A. Atwater. Nanophotonic heterostructures for efficient propulsion and radiative cooling of relativistic light sails. *Nano Lett.*, 18(9):5583–5589, 2018.

[61] C. Joo, G. S. Pati, C. G. Chen, P. T. Konkola, R. K. Heilmann, and M. L. Schattenburg. Precision fringe metrology using a fresnel zone plate. *J. Vac. Sci. Technol. B*, 20(6):3075–309, 2002.

[62] P. T. Konkola, C. G. Chen, R. K. Heilmann, C. Joo, J. C. Montoya, C.-H. Chang, and M. L. Schattenburg. Nanometer-level repeatable metrology using the nanoruler. *J. Vac. Sci. Technol. B*, 21(6):3097–3101, 2016.

[63] R. S. Kumar and D. L. McDowell. Generalized continuum modeling of 2-d periodic cellular solids. *Int. J. Solids Struct.*, 41(26):7399–7422, 2004.

[64] M. LaPedus. 3D NAND metrology challenges growing. https://semiengineering.com/3d-nand-metrology-challenges-growing/.

[65] I. G. Masters and K. E. Evans. Models for the elastic deformation of honeycombs. *Compos. Struct.*, 35(4):403–422, 1996.

[66] L. R. Meza, G. P. Phlipot, C. M. Portela, A. Maggi, L. C. Montemayor, A. Comella, D. M. Kochmann, and J. R. Greer. Re-examining the mechanical property space of three-dimensional lattice architectures. *Acta Materialia*, 140:424–432, 2017.

[67] H. Miao, A. A. Gomella, N. Chedid, L. Chen, and H. Wen. Fabrication of 200 nm period hard x-ray phase gratings. *Nano Lett.*, 14(6):3453–3458, 2014.

[68] J. Miao, P. Charalambous, J. Kirz, and D. Sayre. Extending the methodology of x-ray crystallography to allow imaging of micrometre-sized non-crystalline specimens. *Nature*, 400:342–344, 1999.

[69] M. G. Moharam and T. K. Gaylord. Rigorous coupled-wave analysis of planar-grating diffraction. *J. Opt. Soc. Am. A*, 71(7):811–818, 1981.

[70] J. C. Montoya, C.-H. Chang, R. K. Heilmann, and M. L. Schattenburg. Doppler writing and linewidth control for scanning beam interference lithography. *J. Vac. Sci. Technol. B*, 23(6):2640–2645, 2005.

[71] P. Mukherjee, A. Bruccoleri, R. K. Heilmann, M. L. Schattenburg, A. F. Kaplan, and L. J. Guo. Plasma etch fabrication of 60:1 aspect ratio silicon nanogratings with 200 nm pitch. *J. Vac. Sci. Technol. B*, 28, 2010.

[72] *General Environmental Verification Standard (GEVS).*

[73] N. G. Orji, M. Badaroglu, B. M. Barnes, C. Beitia, B. D. Bunday, U. Celano, R. J. Kline, M. Neisser, Y. Obeng, and A. E. Vladar. Metrology for the next generation of semiconductor devices. *Nature Electronics*, 1:532–547, 2018.

[74] G. G. Pavlov, V. E. Zavlin, B. Aschenbach, J. Trümper, and D. Sanwal. The compact central object in Cassiopeia A: A neutron star with hot polar caps or a black hole? *Astrophys. J. Lett.*, 531(1), 2000.

[75] C. M. Portela, J. R. Greer, and D. M. Kochmann. Impact of node geometry on the effective stiffness of non-slender three-dimensional truss lattice architectures. *Extreme Mech. Lett.*, 22:138–148, 2018.

[76] M. T. Postek and A. E. Vladár. Nanomanufacturing concerns about measurements made in the SEM part IV: charging and its mitigation. *Proc. SPIE*, 9556:95560Q, 2015.

[77] M. T. Postek, A. E. Vladár, and P. Cizmar. Nanomanufacturing concerns about measurements made in the SEM part III: vibration and drift. *Proc. SPIE*, 9173:917306, 2014.

[78] S. I. Ranganathan and M. Ostoja-Starzewski. Universal elastic anisotropy index. *Phys. Rev. Lett.*, 101(055504), 2008.

[79] C. J. Raymond, M. R. Murnane, S. L. Prins, S. Sohail, H. Naqvi, J. R. McNeil, and J. W. Hosch. Multiparameter grating metrology using optical scatterometry. *J. Vac. Sci. Technol. B*, 15(361), 1997.

[80] J. C. Ruiz-Morales, D. M.-López, J. P.-Martínez, J. C.-Vázquez, J. J. Roa, M. Segarra, S. N.Savvin, and P. Núñeza. Performance of a novel type of electrolyte-supported solid oxide fuel cell with honeycomb structure. *J. Power Sources*, 195(2):516–521, 2010.

[81] S. Fang S. Murakawa and J. P. McVittie. Ion trajectory distortion and profile tilt by surface charging in plasma etching. *Appl. Phys. Lett.*, 64(1558), 1994.

[82] D. Sayre. Imaging processes and coherence in physics. *Springer Lecture Notes in Physics*, 112(229), 1980.

[83] M. L. Schattenburg, R. J. Aucoin, R. C. Fleming, I. Plotnik, J. Porter, and H. I. Smith. Fabrication of high energy x-ray transmission gratings for AXAF. *Proc. SPIE*, 2280(4009):181–190, 1994.

[84] M. L. Schattenburg, C. R. Canizares, D. Dewey, A. M. Levine, T. H. Markert, and H. I. Smith. Transmission grating spectroscopy and the Advanced X-ray Astrophysics Facility (AXAF). *Proc. SPIE*, 0982, 1988.

[85] M.L. Schattenburg and H.I. Smith. The critical role of metrology in nanotechnology. *Proc. SPIE*, 4608:116–124, 2001.

[86] C. M. Settens, A. Cordes, B. D. Bunday, A. F. Bello, V. K. Kamineni, A. Paul, J. Fronheiser, and R. J. Matyi. Assessment of critical dimension small-angle x-ray scattering measurement approaches for FinFET fabrication process monitoring. *J. of Micro/Nanolithography, MEMS, and MOEMS*, 13(4), 2014.

[87] M. M. Shulaker, T. F. Wu, M. M. Sabry, H. Wei, H. S. Philip Wong, and S. Mitra. Monolithic 3D integration: a path from concept to reality. In *Proceedings of the 2015 Design, Automation and Test in Europe Conference Exhibition*, 2015.

[88] M. Soccio, N. Alayo, I. Martín-Fabiani, D. R. Rueda, M. C. García-Gutiérrez, E. Rebollar, D. E. Martínez-Tong, F. Pérez-Murano, and T. A. Ezquerra. On the assessment by grazing-incidence small-angle x-ray scattering of replica quality in polymer gratings fabricated by nanoimprint lithography. *J. Appl. Cryst.*, 47, 2014.

[89] J. Song, R. K. Heilmann, A. R. Bruccoleri, E. Hertz, and M. L. Schattenburg. Scanning laser reflection tool for alignment and period measurement of critical-angle transmission gratings. *Proc. SPIE*, 10399(1039915):1–10, 2017.

[90] J. Song, R. K. Heilmann, A. R. Bruccoleri, E. Hertz, and M. L. Schattenburg. Metrology for quality control and alignment of CAT grating spectrometers. *Proc. SPIE*, 10699(106990), 2018.

[91] J. Song, R. K. Heilmann, A. R. Bruccoleri, and M. L. Schattenburg. Characterizing profile tilt of nanoscale deep-etched gratings via x-ray diffraction. *J. Vac. Sci. Technol. B*, 37(062917), 2019.

[92] D. F. Sunday, S. List, J. S. Chawla, and R. J. Kline. Determining the shape and periodicity of nanostructures using small-angle x-ray scattering. *J. Appl. Cryst.*, 48:1355–1363, 2015.

[93] D. Mohr T. Tancogne-Dejean. Stiffness and specific energy absorption of additively-manufactured metallic BCC metamaterials composed of tapered beams. *Int. J. Mech. Sci.*, 141:101–116, 2018.

[94] T. Tancogne-Dejean, A. B. Spierings, and D. Mohr. Additively-manufactured metallic micro-lattice materials for high specific energy absorption under static and dynamic loading. *Acta Materialia*, 116:14–28, 2016.

[95] A. Vigliotti and D. Pasini. Linear multiscale analysis and fintie element validation of stretching and bending dominated lattice materials. *Mechanics of Materials*, 46:57–68, 2012.

[96] D. Vukobratovich and P. Yoder. *Fundamentals of Optomechanics*. CRC Press, 2018.

[97] M. E. Walsh. *On the design of lithographic interferometers and their application*. PhD thesis, Massachusetts Institute of Technology (MIT), 2004.

[98] A.-J. Wang and D. L. McDowell. In-plane stiffness and yield strength of periodic metal honeycombs. *J. Eng. Mater. Technol.*, 126(2):137–156, 2004.

[99] C. Wang, R. L. Jones, E. K. Lin, and W. L. Wua. Small angle x-ray scattering measurements of lithographic patterns with sidewall roughness from vertical standing waves. *Appl. Phys. Lett.*, 90(193122), 2007.

[100] M. C. Weisskopf, J. J. Hester, A. F. Tennant, R. F. Elsner, N. S. Schulz, H. L. Marshall, M. Karovska, J. S. Nichols, D. A. Swartz, and J. J. Kolodziejczak. Discovery of spatial and spectral structure in the x-ray emission from the Crab Nebula. *Astrophys. J. Lett.*, 536(2), 2000.

[101] W. L. Wu and E. K. Lin. Small angle neutron scattering measurements of nanoscale lithographic features. *J. of Appl. Phys.*, 88(7298), 2000.

[102] B. Wua, A. Kumar, and S. Pamarthy. High aspect ratio silicon etch: A review. *J. Appl. Phys.*, 108(5):051101, 2010.

[103] P. Yeh. *Optical waves in layered media*. Wiley-Interscience, 2005.

[104] W. W. Zhang, K. D. Allgood, M. P. Biskach, K. W. Chan, M. Hlinka, J. D. Kearney, J. R. Mazzarella, R. S. McClelland, A. Numata, L. G. Olsen, R. E. Riveros, T. T. Saha, and P. M. Solly. Monocrystalline silicon and the meta-shell approach to building x-ray astronomical optics. *Proc. SPIE*, 10399(10399), 2017.

[105] Y. Zhao, C.-H. Chang, R. K. Heilmann, and M. L. Schattenburg. Phase control in multiexposure spatial frequency multiplication. *J. Vac. Sci. Technol. B*, 25(6):2439–2443, 2007.